STUDY REPORT

SR 206 (2009)

Heat Flux Measurements:

Experiments and Modelling

A.P. Robbins and P.C.R. Collier

The work reported here was funded by the Building Research Levy.

ISSN: 1178-4938

Preface

This report was prepared during research into the use of plate thermometers for heat flux measurements and how these measurements can subsequently be used in terms of modelling and estimating other conditions or parameters.

Appendices are included in a separate document.

Acknowledgments

This work was funded by the Building Research Levy.

Note

This report is intended for researchers, fire engineers and designers.

Heat Flux Measurements: Experiments and Modelling

BRANZ Study Report SR 206

A.P. Robbins and P.C.R. Collier

Reference

Robbins A. P. and Collier P. C. R. 2009. 'Heat Flux Measurements: Experiments and Modelling'. *BRANZ Study Report 206*. BRANZ Ltd, Judgeford, New Zealand.

Abstract

Plate thermometers for estimating incident radiative flux were investigated using a range of experiments: cone calorimeter tests, furniture calorimeter tests using a burner or a mattress as the heat source, and ISO room experiments also using a burner or a mattress as the heat source. A series of experiments in the ISO room were also performed with the door of the ISO room sealed off. The results from these experiments and the subsequent analysis are summarised in this report.

Overall reasonable agreement was found between Gardon gauge results and the estimates of incident radiative heat flux for steady sources of heat once the results of each type of instrument reached a quasi steady state or when the heat source was increased relatively slowly compared to a distinct stepped increase.

When considering the use of plate thermometers for non-steady state heat sources, care must be applied when analysing and applying the results. For non-steady state heat sources, it is recommended that particular aspects of the theory used in the calculation of the estimated incident radiative heat flux be considered or an alternative approach be developed. Such aspects include: the parameters affecting the response time of the plate thermometer to a stepped change in heat source; the different errors associated with the estimates based on plate thermometer temperatures for the initial rise and then (when or if a quasi steady state value is reached) effective convective and conductive coefficients for different orientations and local conditions; and observed oscillatory behaviour of the recorded temperature data and subsequent incident radiation estimates. This is discussed in detail in this report.

Experimental results were compared to Computational Fluid Dynamics (CFD) using the Fire Dynamics Simulator (FDS) model predictions for an example ISO room test. The results showed reasonable agreement for the incident radiative heat flux.

Contents Page

Figures

Page

Tables Page

Nomenclature

$C_{P,plate}$	specific heat of the metal plate (J/kg K)
H_{conv}	effective convective heat transfer coefficient of the plate thermometer (W/m² K)
k_{plate}	thermal conductivity of the metal plate (W/m² K)
K_{cond}	effective conduction heat transfer coefficient for the plate thermometer (W/m² K)
L_{plate}	characteristic length of the plate thermometer (m)
$\dot{q}''_{rad,net}$	net radiation flux received at the surface of the plate $\left(= \dot{q}''_{\mathrm{rad,inc}} - \dot{q}''_{\mathrm{rad,reflect}} - \dot{q}''_{\mathrm{rad,emit}}\right)$ (W/m²)
$\dot{q}''_{rad,inc}$	incident radiation heat flux received at the surface of the plate thermometer (W/m²)
$\dot{q}''_{rad,reflect}$	incident radiation heat flux reflected at the surface of the plate thermometer (W/m²)
$\dot{q}''_{rad,emit}$	emitted radiation heat flux from the surface of the plate thermometer to the surrounds (W/m²)
$\dot{q}''_{conv}$	convective heat flux from the hot surrounding gases to the surface of the plate (W/m²)
$\dot{q}''_{store}$	energy stored in the material of the plate per unit area of the surface of the plate thermometer (W/m²)
$\dot{q}''_{cond}$	conductive heat flux through the metal plate thickness (W/m²)
$\dot{q}''_{cond,1}$	conductive heat flux losses attributed to the geometry (length and width) of the plate (W/m²)
$\dot{q}''_{cond,2}$	conductive heat flux losses to the mineral insulation (W/m²)
t	time (s)
$T_{local\ gas}$	local gas temperature (K)
$T_{insluation}$	temperature of the backing insulation (K)
T_{PT}	temperature measured at the surface of the plate thermometer adjacent to the mineral insulation (K)
T_S	temperature at the surface of the plate thermometer adjacent to air (K)
T_∞	ambient temperature (K)
δ_{plate}	thickness of the plate thermometer (m)
ε_{plate}	emissivity of the plate thermometer (dimensionless)
σ	Stefan-Boltzmann constant (5.669 x 10^{-8} W/m² K^4)
ρ_{plate}	density of the metal plate (kg/m³)

1. INTRODUCTION

Heat transfer to fire-exposed structures is a topic drawing broad interest. The fire severity is central in estimating the thermal structural response during a fire event. Suggested descriptions of fire severity have taken the form of:

- the integrated heat flux absorbed by a structure (Gross and Robertson 1965)
- the normalised heat load (Harmathy 1993), and
- the incident heat flux (Lennon and Silcock 2006).

In most cases heat flux has been identified as an important variable.

In this research project a few well-defined experiments were carried out where temperature and heat flux are measured at locations around a heat source. The thermal impact is measured at various positions by plate thermometers and Gardon gauges.

The plate thermometer was chosen for the focus of this study to allow comparison of results to other projects that were being conducted around a similar timeframe to provide a more diverse set of data using a common measurement technique. Gardon gauges were also used to allow comparison to the plate thermometer estimate of the incident radiative heat flux.

In addition, an example is provided for this same thermal impact as calculated using a Computational Fluid Dynamics (CFD) model, Fire Dynamics Simulator (FDS). This example provides comparison of experimental results to modelled predictions.

1.1 Objectives

In summary, the objectives of the project that this report summarises were:

1. To determine by practical measurements the ability to quantitatively characterise the thermal challenge of a fire independently of the presence and response of a construction element using plate thermometers. The success of the measurements of the thermal insult depends on how well these measurements can be used to compute/predict the heat transfer to the exposed specimens and the consequent temperature development of them.
2. To provide data to contribute to the evaluation, in cooperation with code developers, of the ability of CFD codes to predict this thermal insult.

The objective of this report is to summarise the experimental set-ups used and results, and to present the discussion of the analysis of these results in terms of the objectives of the research project.

1.2 Scope

The focus of this project is on the use of plate thermometers to estimate the incident radiative heat fluxes and to assess the appropriateness of these estimates and/or the conditions in which the results would be appropriate using reduced scale testing.

The results from CFD modelling are used as an example for the comparison of experimental results with modelled predictions.

2. SUMMARY LITERATURE REVIEW

2.1 Heat flux measurement devices

Equipment for directly measuring heat fluxes included Gardon gauges and Schmidt Boelter gauges, where the measured voltage is directly proportional to the heat flux absorbed by the gauge And provides a continuous in-situ measurement.

The water-cooled Gardon gauge is of interest, since two were used in the experiments and results were compared to plate thermometer estimates as part of this investigation. Gardon gauges have a short response time (<1 s) and have been demonstrated to reach a steady irradiance measurement within 10 s when subjected to fluxes of up to 100 kW/m² (Ballestrin et al 2006). Measurement error for a Gardon gauge is expected to be approximately ±10% (Pitts et al 2006).

Gardon and Schmidt Boelter gauges are relatively expensive and fragile in the exposure conditions during a fire in a compartment. Therefore there is value in a inexpensive, robust and accurate heat flux measurement device to withstand repeated exposure to enclosed fire conditions. Alternative devices have therefore been developed over the years.

Plate thermometers were developed in the 1980s by Wickstrom as a robust method to indirectly measure the incident heat flux within furnaces. The use of plate thermometers in full-scale fire resistance tests was suggested as a way to harmonise the heat exposure for different fire furnaces (Wickstrom 1994). Assumptions about the system were used to calculate the incident radiation from the plate thermometer measurements. It was noted that the plate thermometers had a slower response than a thermocouple. Assuming a linear heat transfer rate for a lumped parameter system for the plate thermometer, the time constants were estimated as 40 s and 5 s for the plate thermometer and the shielded thermocouple respectively (Wickstrom 1994).

Other heat flux measuring devices have been developed, such as a thermal capacitance slug calorimeter (Pitts et al 2006) or devices utilising thin painted discs with different emissivities, steel billets with embedded thermocouples along the major axis, or a differential thermopile separated by a thin section of semiconductor insulator (Lennon and Silcock 2006).

2.2 Experiments

2.2.1 Plate thermometers

The published experiment results summarised here are for studies involving plate thermometers.

Wickstrom (1994) reported on the use of plate thermometers and thermocouples in furnaces for a range of standard heat exposure curves and for various international test facilities. Conclusions included that using plate thermometers to control a furnace according to the curve of an ISO 834 standard temperature to time plot would be appropriate. The estimated time constant of the plate thermometer was suggested to be negligible after 5 min into the standard test, where the plate thermometer measurement approximated the temperature of the standard curve.

Sultan (2006) investigated the impact of using either plate thermometers or shielded thermocouples to drive a furnace to fit a temperature versus time curve. Plate thermometer, shielded thermocouple and (water-cooled) Gardon gauge results during standard fire resistance tests in the floor and wall configurations were compared. Six

tests were conducted in each configuration. Three duplicate tests were performed using the shielded thermocouples to control the furnace (in accordance with (*Can/Ulc-S101-M89* 1989)/(*Astm E119-88* 1995)) and three duplicate tests were performed using the plate thermometers to control the furnace (in accordance with (*ISO 834-1* 1999) and (*EN 1363-1* 1999)). However heat flux estimates based on the plate thermometer measurements were not directly compared to Gardon gauge measurements. The temperature differences between the measurements of the plate thermometers and shielded thermocouples were not significant. For both orientations of the furnace tested, for approximately the first 8 min of each test, the average temperature reported for the plate thermometers was slightly higher than the average of the shielded thermocouples. Then the average temperature reported for the plate thermometers was consistently (~5%) lower than the average of the shielded thermocouples. The range of heat flux measured by the Gardon gauge was up to approximately 150 kW/m².

Ingason and Wickstrom (2007) presented theory for estimating the incident radiative heat flux from plate thermometer measurements (Ingason and Wickstrom 2007; Wickstrom 2004). As this theory is used as the basis for the estimation of incident radiative heat flux in this study, details of this theory is presented in Section 3.2.1, where it is used and discussed. Tests were performed in a cone calorimeter (*ISO 5660* 2002) over a range of incident heat fluxes from 10 to 45 kW/m² that were set using a Schmidt Boelter gauge. A steady state temperature was reached within 2 to 3 min. The test results were used to determine the correction factor related to conductive losses to the surrounds of 5 W/m²K. Good agreement was found between the plate thermometer estimates and the total heat flux measured by the Schmidt Boelter gauge (Ingason and Wickstrom 2007).

The results for plate thermometers and Schmidt Boelter gauge measurements in pool fires (nominally of 1, 2, 3.5 and 6 MW) and spray fire (nominally of 1, 2 and 3.5 MW) scenarios were also reported by Ingason and Wickstrom (2007). The fire scenario tests were at near steady state levels of heat release rate (HRR) and performed in free burning (open) conditions. Heat flux measurement instruments were positioned 1 m above the floor at 2 and 4 m from the fire. Comparison of Schmidt Boelter gauge measurements and incident radiation estimates from plate thermometer measurements provided a correction factor related to the conductive losses to the surrounds of 22 W/m²K. The higher correction factor associated with the pool and spray fire tests than the cone calorimeter tests was attributed to greater convective cooling of the back of the plate thermometer when in a vertical orientation.

Results for tests of free burning cartons recording plate thermometers and Schmidt Boelter gauge measurements were also reported by Ingason and Wickstrom (2007). Good agreement was reported for the comparison of Schmidt Boelter gauge measurements and estimates of incident radiative heat flux from plate thermometer measurements.

Wickstrom (2008) subsequently conducted tests in a ISO 9705 room with a constant yield (of about 450 kW) gas burner located in the corner to investigate the use of plate thermometers to measure Adiabatic Surface Temperature (AST) and the concept of using AST for estimating the heat transfer to structural members. Two steel beams were used in the tests with (welded and shielded) thermocouples measuring gas temperatures around as well as within the beam. Temperatures within the beam were measured using quick tip thermocouples that had been peened into drilled holes in the steel beam. Plate thermometers were placed on all four sides of the beam. Tests were performed with the instruments at three locations along the beam. Results of tests indicated that after the first five minutes, the plate thermometer temperature is very close to the AST even though the gas phase temperatures developed relatively fast. Two-dimensional finite element calculations were performed. It was demonstrated that

plate thermometer measurements could be successfully used as boundary conditions for the structural element calculations.

It was noted that future tests investigating the use of plate thermometer measurements to be used in estimating structural element temperatures are planned to be carried out in a fire resistance furnace (Wickstrom 2008).

2.2.2 Room-scale heat flux measurements

Dillon (1998) used steel plates, with 32 thermocouples fixed to the unexposed surface, to measure the heat flux to the walls and ceiling in ISO 9705 room/corner tests. The C-1018 carbon steel plates were 1.2 x 0.6 m x 5 mm thick. Three plates were used on the back wall (two above the burner and one beside) and two plates were located on the ceiling over the burner. Propane burner HRRs from 100 to 300 kW were tested. During each test gas temperatures and wall and ceiling surface temperatures increased, which provided incident heat flux in addition to the burner, as shown in Figure 1 (Dillon 1998). It was suggested that the measured heat flux could be corrected by removing estimated room feedback effects to calculate the incident heat flux received from the burner fire plume.

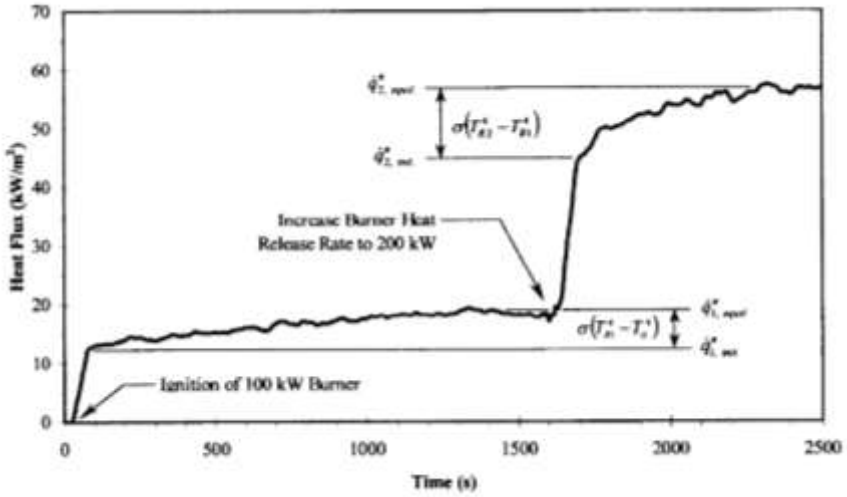

Figure 1: An example of incident heat flux added from the room during a 100 and 300 kW ISO 9705 room test. Extracted from (Dillon 1998).

Reduced-scale (0.95 x 0.98 m wide x 1.42 m high, 2/5-scale model of an ISO 9705 room) compartment fire tests were conducted to provide a database of comprehensive and accurate experimental measurements that could be used to improve fundamental understanding and modelling (Bundy et al 2007; Johnsson, Bundy and Hamins 2007). Fifty-six combinations of the experiments were performed. Seven fuels were used centrally in the compartment to produce approximately steady HRRs up to 400 kW. Two water-cooled Schmidt Boelter heat flux gauges were located in the floor facing upward and flush with the upper surface of the floor. The gauges were located approximately halfway between the walls and the burner at either side of the burner, one to the front of the enclosure and one to the back. Measurement uncertainty was associated with calibration, soot and dust deposition, and movement of the gauge surface to below the level of the floor. A conservative estimate of uncertainty was suggested as ±6%.

From experiment results, it was noted that fuels with high soot yields were associated with high heat flux levels (>100 kW/m²). For clean burning fuels, the heat flux was noted to be relatively constant for HRRs greater than 200 kW. Heat flux measurements greater than 150 kW/m² were recorded for under-ventilated toluene and some heptane fires (Bundy et al 2007; Johnsson, Bundy and Hamins 2007). An example of the results

for total heat flux measurements at the floor locations during a heptane spray test is included in Figure 2 (Bundy et al 2007). A summary of steady state measurements of total heat flux to the floor location at the rear of the enclosure is shown in Figure 3 (Bundy et al 2007).

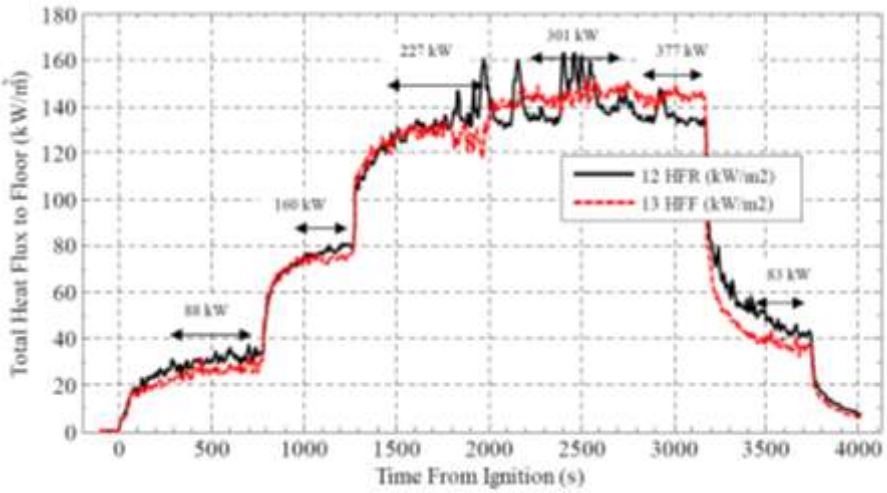

Figure 2: An example of total heat flux gauge measurements located on the floor of the enclosure using a heptane spray burner. Extracted from (Bundy et al 2007).

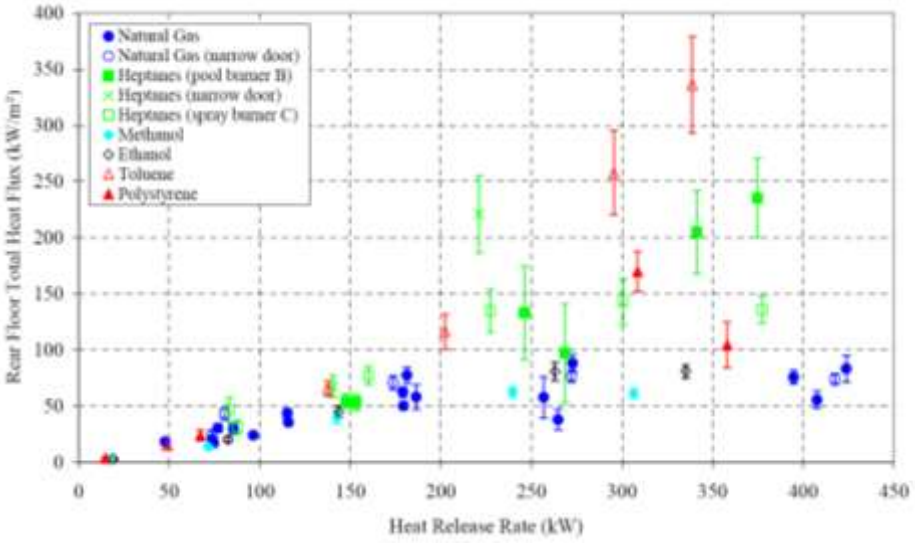

Figure 3: Steady state total heat flux measurements from the rear floor location. Extracted from (Bundy et al 2007).

2.3 Modelling

Compartment tests were performed with three types of steel members where the results were compared to FDS (a computational fluid dynamics model) and ANSYS (a commercial finite element package) estimations (Wickstrom, Duthinh and McGrattan 2007). Spray fires were used at approximately steady HRRs. FDS was used to estimate ASTs that were then used in the ANSYS calculations. For unprotected and protected steel elements, comparison of the FDS (using one-dimensional solid phase heat conduction) and ANSYS (using three-dimensional analysis) results showed good agreement in locations where uniform heating of the structural elements was expected. Comparison of the FDS and ANSYS estimates to experimental results for the steel

temperatures showed reasonable agreement. Therefore the use of AST was assumed to adequately transfer information to the finite element analysis. It was suggested that from a numerical point of view, the use of the AST reduces the amount of data that is required to be passed from a CFD model to a structural model.

3. HEAT TRANSFER MEASUREMENTS

3.1 Plate thermometer construction

The plate thermometers were constructed in accordance with ISO 834-1 (1999) and EN1363-1 (1999).

The plate thermometers are made from a 0.7±0.1 mm thick nickel alloy (INCONEL® 600) sheet. The 150 x 100 mm sheet is folded to form a plate thermometer with a face of 100 x 100 mm, as shown in Figure 4.

A K-type thermocouple was secured to the centre of the back face of the nickel alloy sheet by a small (25 x 6 mm) steel strip and two 2 mm diameter screws. A (97 x 97 mm x 10 mm thick) pad of inorganic insulation material (Kaowool™ VF board) was fitted behind the thermocouple.

The completed plate thermometer was conditioned by exposure in a fire resistance furnace for the first 90 min of the standard time/temperature curve.

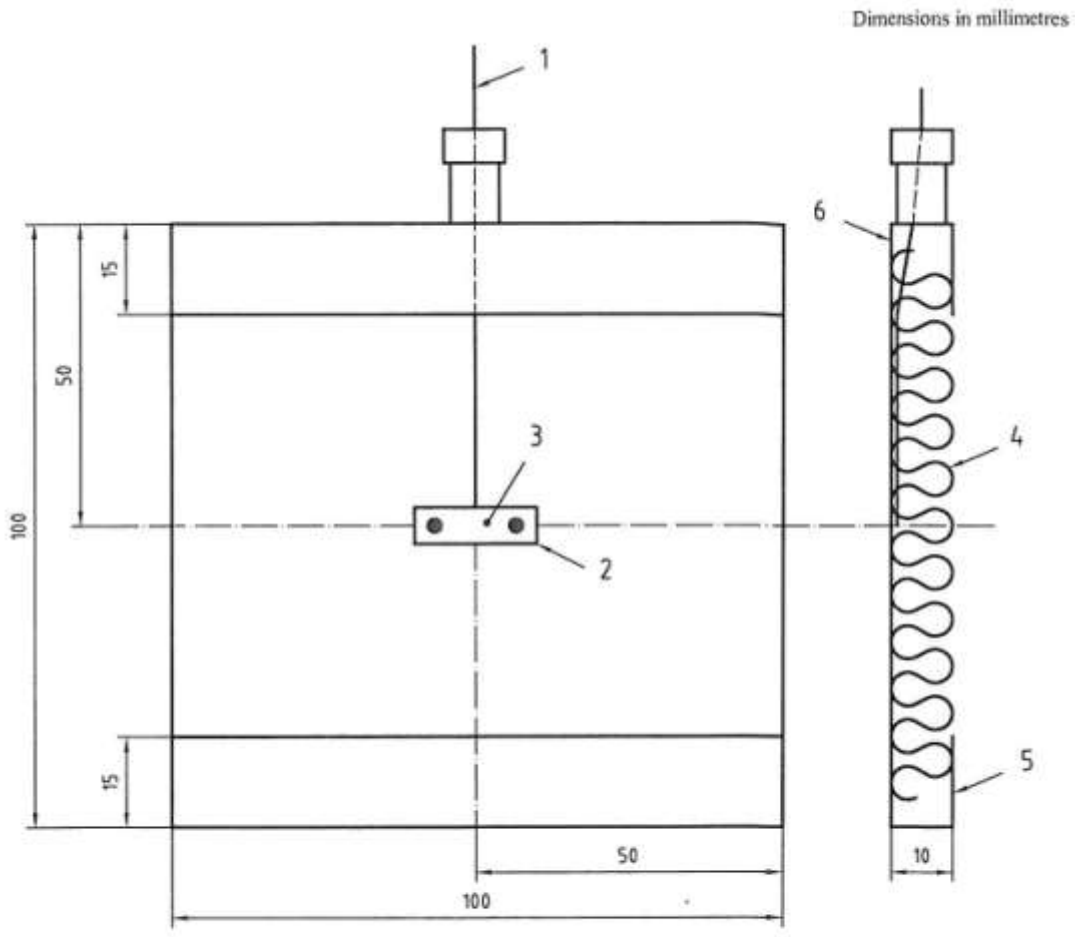

Key
1 Sheathed thermocouple with insulated hot junction
2 Spot-welded or screwed steel strip
3 Hot junction of thermocouple
4 Insulation material
5 Nickel alloy strip (0,7 ± 0,1) mm thick
6 Face A

Figure 4: Schematic of the back and side of a plate thermocouple. Extracted from (*ISO 834-1* 1999) and (*EN 1363-1* 1999).

3.2 Modelling theory

3.2.1 Estimation of the incident radiation for a plate thermometer

For the purposes of estimating the incident radiation that a plate thermometer is subject to, following the same approach as Ingason and Wickstron (2007), the INCONEL® 600 plate is assumed to be infinitely long and wide (i.e. an infinite plate) in air on one side and adjacent to mineral insulation on the other. A schematic of the assumed heat transfer associated with a plate thermometer is shown in Figure 5. Where:

- T_{PT} refers to the temperature measured at the surface of the plate thermometer adjacent to the mineral insulation (K)
- T_S refers to the temperature at the surface of the plate thermometer adjacent to air (K)
- δ_{plate} refers to thickness of the plate thermometer (m)
- $\dot{q}''_{rad,net} = \dot{q}''_{rad,inc} - \dot{q}''_{rad,reflect} - \dot{q}''_{rad,emit}$ refers to the net radiation flux received at the surface of the plate (W/m²)
- $\dot{q}''_{rad,inc}$ refers to the incident radiation flux received at the surface of the plate thermometer (W/m²)
- $\dot{q}''_{rad,reflect}$ refers to the incident radiation flux reflected at the surface of the plate thermometer (W/m²)
- $\dot{q}''_{rad,emit}$ refers to the emitted radiation flux from the surface of the plate thermometer to the surrounds (W/m²)
- $\dot{q}''_{conv}$ refers to the convective heat flux from the hot surrounding gases to the surface of the plate (W/m²)
- $\dot{q}''_{store}$ refers to the energy stored in the material of the plate per unit area of the surface of the plate thermometer (W/m²)
- $\dot{q}''_{cond}$ refers to the conductive heat flux through the metal plate thickness (W/m²)
- $\dot{q}''_{cond,1}$ refers to the conductive heat flux losses attributed to the geometry (length and width) of the plate (W/m²), and
- $\dot{q}''_{cond,2}$ refers to the conductive heat flux losses to the mineral insulation (W/m²).

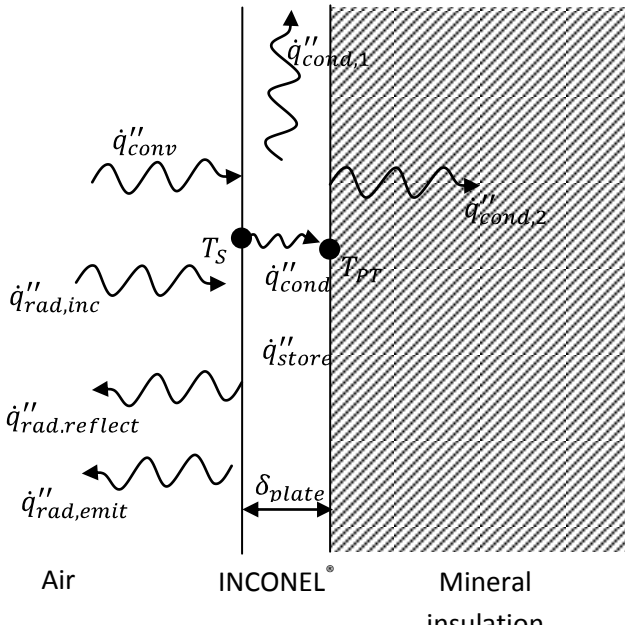

Figure 5: Schematic of heat transfer concerning a plate thermometer. Not to scale.

Balancing the energy for the situation shown in Figure 5 provides:

$$\dot{\mathbf{q}}''_{\mathbf{tot}} = \dot{\mathbf{q}}''_{\mathbf{rad,net}} + \dot{\mathbf{q}}''_{\mathbf{conv}} = \dot{\mathbf{q}}''_{\mathbf{cond}} + \dot{\mathbf{q}}''_{\mathbf{store}} + \dot{\mathbf{q}}''_{\mathbf{cond,1}} + \dot{\mathbf{q}}''_{\mathbf{cond,2}}$$

Equation 1

Which can be rewritten as:

$$\dot{\boldsymbol{q}}''_{\boldsymbol{rad,inc}} - \dot{\boldsymbol{q}}''_{\boldsymbol{rad,reflect}} - \dot{\boldsymbol{q}}''_{\boldsymbol{rad,emit}} = \dot{\boldsymbol{q}}''_{\boldsymbol{cond}} + \dot{\boldsymbol{q}}''_{\boldsymbol{store}} + \dot{\boldsymbol{q}}''_{\boldsymbol{cond,losses}} - \dot{\boldsymbol{q}}''_{\boldsymbol{conv}}$$

Equation 2

Where $\dot{q}''_{cond,losses}$ refers to an estimate of the combined thermal losses attributed to the plate geometry and the non-adiabatic properties of the mineral insulation.

$$\dot{\boldsymbol{q}}''_{\boldsymbol{rad,inc}} - (\mathbf{1} - \boldsymbol{\varepsilon}_{\boldsymbol{plate}})\dot{\boldsymbol{q}}''_{\boldsymbol{rad,inc}} - \boldsymbol{\sigma T_S^4} = \dot{\boldsymbol{q}}''_{\boldsymbol{cond}} + \dot{\boldsymbol{q}}''_{\boldsymbol{store}} + \dot{\boldsymbol{q}}''_{\boldsymbol{cond,losses}} - \dot{\boldsymbol{q}}''_{\boldsymbol{conv}}$$

Equation 3

$$\dot{\boldsymbol{q}}''_{\boldsymbol{rad,inc}} = \frac{\mathbf{1}}{\boldsymbol{\varepsilon}_{\boldsymbol{plate}}}\left(\dot{\boldsymbol{q}}''_{\boldsymbol{cond}} + \dot{\boldsymbol{q}}''_{\boldsymbol{store}} + \dot{\boldsymbol{q}}''_{\boldsymbol{cond,losses}} - \dot{\boldsymbol{q}}''_{\boldsymbol{conv}}\right) + \boldsymbol{\sigma T_S^4}$$

Equation 4

Where:

- ε_{plate} refers to the emissivity of the plate thermometer (dimensionless), and
- σ refers to the Stefan-Boltzmann constant (W/m² K^4).

This is in agreement with the theory presented by (Ingason and Wickstrom 2007).

If it is assumed that the temperatures associated with the convection between the plate and the surrounding gas and the conduction losses associated are ambient (T_∞), then Equation 4 can be rewritten as:

$$\dot{q}''_{rad,inc} = \frac{1}{\varepsilon_{plate}}\left(k_{plate}(T_S - T_{PT}) + \rho_{plate} C_{P,plate} \delta_{plate} \frac{\Delta\left(\frac{T_{PT}+T_S}{2}\right)}{\Delta t} + \mathrm{K_{cond}}(T_{PT} - T_\infty) - H_{conv}(T_S - T_\infty)\right) + \sigma T_S^4$$

Equation 5

Where:

- k_{plate} refers to the thermal conductivity of the metal plate (W/m² K)
- ρ_{plate} refers to the density of the metal plate (kg/m³)
- $C_{P,plate}$ refers to the specific heat of the metal plate (J/kg K)
- t refers to time (s)
- K_{cond} represents an estimate for the combined conduction heat transfer coefficients and path length for the conductive heat losses attributed to the geometry of the plate and the non-adiabatic conditions of the mineral insulation (W/m² K), and
- H_{conv} represents the estimated convective heat transfer coefficient of the Plate Associated with heat transfer from the surrounding hot gases to the plate thermometer (W/m² K).

Where the heat transfer coefficient $\mathrm{K_{cond}}$ is estimated based on experimental results for the calibration of the plate thermometers, and H_{conv} is estimated based on theory for a horizontal plate exposed to natural convection (using the approach described by (Ingason and Wickstrom 2007)), where:

$$H_{conv} = 4.0\left(\frac{(T_S - T_\infty)}{L_{plate}}\right)^{1/4}(T_S + T_\infty)^{-0.16}$$

Equation 6

Where L_{plate} refers to the characteristic length of the plate thermometer.

Furthermore assuming that the surface temperature of the plate is the same as the temperature between the plate and the insulation ($T_S = T_{PT}$), then Equation 5 can be rewritten as (Ingason and Wickstrom 2007):

$$\dot{q}''_{rad,inc} = \frac{1}{\varepsilon_{plate}}\left(\rho_{plate} C_{P,plate} \delta_{plate} \frac{\Delta T_{PT}}{\Delta t} + \mathrm{K_{cond}}(T_{PT} - T_\infty) - H_{conv}(T_{PT} - T_\infty)\right) + \sigma T_{PT}^4$$

Equation 7

In summary, the error associated with this approach is dependent on the assumptions:

- The surface temperature is the same as the temperature between the metal plate and the backing insulation ($T_S = T_{PT}$),
- The convection heat transfer coefficient (H_{conv}) can be estimated by a horizontal plate under natural convection conditions (Equation 6) (although the experiments performed here use the plate thermometers in a vertical orientation and some mixing) resulting in localised turbulent flow, which is expected in the ISO room experiments compared to a theoretically isolated plate,
- The local gas temperature is assumed to be ambient ($T_{local\ gas} = T_\infty$),

- The temperature of the backing insulation is assumed to be ambient ($T_{insluation} = T_{\infty}$),
- The loss of heat to the insulation and the non-one-dimensional heat transfer through the metal Plate Can be estimated by an effective lumped conduction heat transfer coefficient (K_{cond}). This lumped coefficient is assumed to be temperature independent and is estimated using experimental data from a calibration phase.

The impacts of these assumptions on the estimated incident radiation flux are discussed in more detail in Section 8.5.

3.2.2 Estimation of the incident radiation for a Gardon gauge

Gardon gauges absorb heat at a thin metallic circular section of foil. The heat is transferred to the heat sink welded around the outer edge of the foil. The voltage output is generated by a differential thermocouple, measuring the difference between the temperature at the centre back of the foil and the foil edge. The voltage output from a Gardon gauge is directly proportional to the absorbed heat flux ($\dot{q}''_{tot,Gardon}$). The absorbed heat flux by the Gardon gauge is:

$$\dot{\boldsymbol{q}}''_{\boldsymbol{tot,Gardon}} = \dot{\boldsymbol{q}}''_{\boldsymbol{rad,net,Gardon}} + \dot{\boldsymbol{q}}''_{\boldsymbol{conv,Gardon}}$$

Equation 8

$$\dot{\boldsymbol{q}}''_{\boldsymbol{tot,Gardon}} = \dot{\boldsymbol{q}}''_{\boldsymbol{rad,inc,Gardon}} - \dot{\boldsymbol{q}}''_{\boldsymbol{rad,reflect,Gardon}} - \dot{\boldsymbol{q}}''_{\boldsymbol{rad,emit,Gardon}} + \dot{\boldsymbol{q}}''_{\boldsymbol{conv,Gardon}}$$

Equation 9

$$\dot{\boldsymbol{q}}''_{\boldsymbol{tot,Gardon}} = \dot{\boldsymbol{q}}''_{\boldsymbol{rad,inc,Gardon}} - (\mathbf{1} - \boldsymbol{\varepsilon}_{\boldsymbol{Gardon}})\dot{\boldsymbol{q}}''_{\boldsymbol{rad,inc,Gardon}} - \boldsymbol{\sigma T}^{\mathbf{4}}_{\boldsymbol{Gardon,body}} + \dot{\boldsymbol{q}}''_{\boldsymbol{conv,Gardon}}$$

Equation 10

This simplifies to:

$$\dot{\boldsymbol{q}}''_{\boldsymbol{tot,Gardon}} = \boldsymbol{\varepsilon}_{\boldsymbol{Gardon}}\dot{\boldsymbol{q}}''_{\boldsymbol{rad,inc,Gardon}} - \boldsymbol{\sigma T}^{\mathbf{4}}_{\boldsymbol{Gardon,body}} + \dot{\boldsymbol{q}}''_{\boldsymbol{conv,Gardon}}$$

Equation 11

Therefore the incident radiation received by the Gardon gauge is:

$$\dot{\boldsymbol{q}}''_{\boldsymbol{rad,inc,Gardon}} = \frac{\mathbf{1}}{\boldsymbol{\varepsilon}_{\boldsymbol{Gardon}}}\left(\dot{\boldsymbol{q}}''_{\boldsymbol{tot,Gardon}} + \boldsymbol{\sigma T}^{\mathbf{4}}_{\boldsymbol{Gardon,body}} - \dot{\boldsymbol{q}}''_{\boldsymbol{conv,Gardon}}\right)$$

Equation 12

The calibration of the Gardon gauges assumes the form of:

$$\dot{\boldsymbol{q}}''_{\boldsymbol{rad,inc,Gardon}} = \boldsymbol{C}_{\boldsymbol{Gardon}}\boldsymbol{V}_{\boldsymbol{Gardon}}$$

Equation 13

Where:

- $\dot{q}''_{rad,net,Gardon}$ net radiative heat flux to the Gardon gauge
- $\dot{q}''_{rad,inc,Gardon}$ incident radiative heat flux to the Gardon gauge
- $\dot{q}''_{rad,reflect,Gardon}$ reflected radiative heat flux from the Gardon gauge
- $\dot{q}''_{rad,emit,Gardon}$ emitted radiative heat flux from the Gardon gauge
- $\dot{q}''_{conv,Gardon}$ convection heat flux to the Gardon gauge, and
- $T_{Gardon,body}$ temperature of the Gardon gauge copper, water-cooled body, which is approximated by the cooling water temperature.

- ε_{Gardon} refers to the emissivity of the Gardon gauge, which is approximately 0.92 (*64 Series, Hfm* 2002),
- $V_{Gardon} \propto \dot{q}''_{tot,Gardon}$ refers to the output voltage of the Gardon gauge, and
- C_{Gardon} refers to the calibration constant.

Therefore care must be taken when considering the results for small incident radiation values where the absorbed heat flux $\left(\dot{q}''_{tot,Gardon}\right)$ is of the same order of magnitude as the emitted radiation flux $\left(\dot{q}''_{rad,emit,Gardon} = \sigma T^4_{Gardon,body} \approx 0.6\ \mathrm{kW/m^2}\right)$ or for high incident heat flux scenarios where the influence of the convective component $\left(\dot{q}''_{conv,Gardon}\right)$ becomes significant (e.g. >> 55 kW/m²).

4. MODELLING PLATE THERMOMETER PARAMETER VALUES

4.1 Nickel-based alloy properties

The nickel-based alloy used for the plate thermometers was INCONEL® 600. Average emissivity values for INCONEL® 600 are presented in Table 1. The variation of the specific heat of INCONEL® 600 with temperature is shown in Figure 6. The average density, at 300 K, is presented in Table 2.

Table 1: Average emissivity values for INCONEL® 600.Extracted from (*Inconel® Alloy 600* 2008).

	Temperature (K)					
	588	**753**	**923**	**1088**	**1253**	**1363**
As-rolled and oxidised [a]	-	0.85	0.87	0.9	0.95	0.98
Sand-blasted and oxidised [b]	-	0.86	0.9	0.93	0.96	0.97

Notes:
[a] Oxidised by heating for 13 min in air at 1363 K.
[b] Oxidised by heating for 15 min at 1088 K, 15 min at 1253 K, and 15 min at 1423 K.

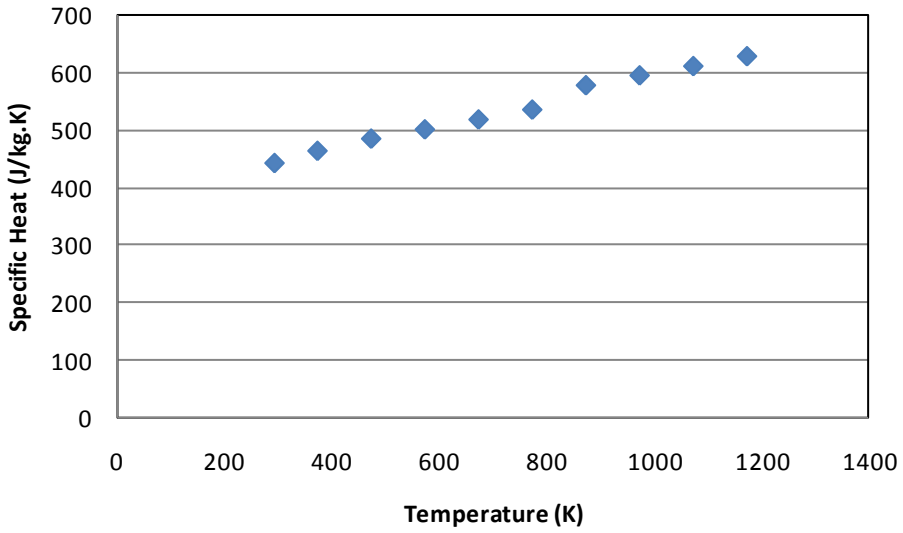

Figure 6: Variation of INCONEL® 600 specific heat with temperature. Adapted from (*Inconel® Alloy 600* 2008).

Table 2: Average material property values used for INCONEL® 600

Material Property	INCONEL® 600
Emissivity	0.85
Specific heat (J/kg.K) *	444
Density (kg/m^3) *	8470

Note: * at a temperature of 300 K.

4.2 Summary of parameter values used in analysis

A summary of the parameter values used in the analysis of the plate thermocouple data is presented in Table 3.

Table 3: Example of the input parameters used in the calculation of the heat flux from Plate A using INCONEL® 600 parameter values

	Minimum	Best	Maximum
Plate emissivity (ε_{plate})	0.8	0.85	0.9
Plate thickness (δ_{plate}) **(mm)**	0.6	0.7	0.8
Plate density (ρ_{plate}) **(kg/m³)**	8000	8500	9000
Plate Characteristic length (m)	0.09	0.10	0.11
Effective thermal conductivity constant $(\mathbf{K_{cond}})$ **(W/m².K)**	0	4	5
Average specific heat $(C_{P,plate})$ **(kJ/kg.K)**	300	440	500

5. EXPERIMENTAL SET-UP

5.1 Equipment

The measuring equipment used included:

1. K-type thermocouples
2. Plate thermometers
3. Gardon gauges.

The K-type thermocouples were located on the front surface of each cage for sample material on the equipment trees (Figure 8). Thermocouples were also located on the ceiling of the ISO room and the geometric centre, at the mid-point between the centre and each wall, and over the centre of the burner. A thermocouple tree was located in the corner of the ISO room.

The equipment trees consisted of three plate thermometers and three cages for sample materials, as shown in Figure 7. The plate thermometers and cages were located on equipment trees at 500, 1,000 and 1,400 mm from the floor. The trunk of the equipment tree consisted of a stainless steel tube which was secured using clamps to a weighted laboratory stand. Holes were drilled at appropriate heights for locating the plate thermometers and cages using concrete reinforcing wire to attach the sensors (Figure 8). Holes were also drilled in the back of the tube to pass thermocouple wires through to provide protection.

The sample material used for these tests was cotton pads, as used for the testing of integrity in accordance with (*EN 1363-1* 1999; *ISO 834-1* 1999). The cages for the sample material were hinged at the top front for easy replacement of the specimen between tests.

Gardon gauges were also located on two of the equipment trees using clamps to position the gauge directly above any selected plate thermometer. Calibration was performed using the cone calorimeter apparatus in the vertical orientation. Results for the calibration coefficient values are shown in Figure 383 and average values used in the analysis are presented in Table 15.

The ISO room, according to ISO 9705 (*ISO 9705* 1993) (3.6 x 2.4 x 2.4 m high), was used for a series of tests, with either a (300 x 300 mm) propane burner or a mattress on a load cell located in a corner. The layout of equipment is described in Section 5.2.

5.2 Description of tests

Six types of tests were performed:

1. Calibration, using the cone calorimeter,
2. Investigation of the plate thermometer measurements and analysis,
3. Furniture calorimeter with a burner,
4. Furniture calorimeter with a mattress,
5. ISO room with a burner in the corner,
6. ISO room with a mattress in the corner, and
7. ISO room with a mattress in the corner and the door opening sealed.

Summaries of the lists of tests and description of the layout of equipment is presented in this section. An example of results for each of the types of tests is included in Section 6, with detailed results included in Appendix A.

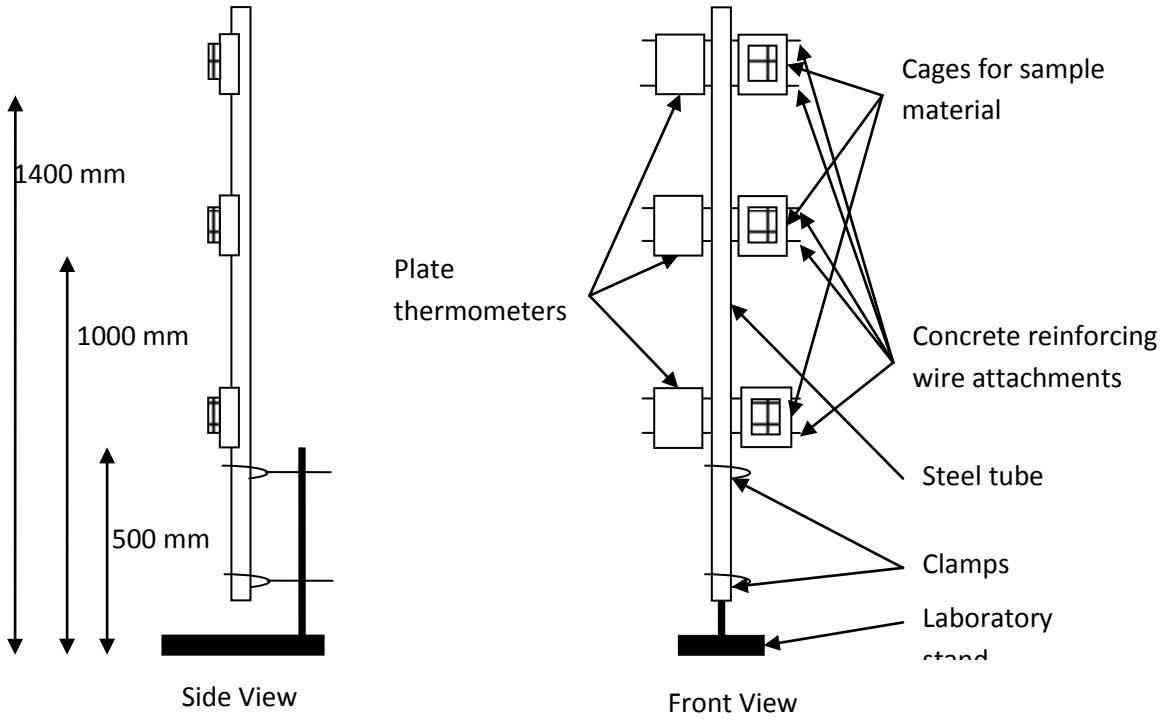

Figure 7: Schematic of the equipment trees. Not to scale.

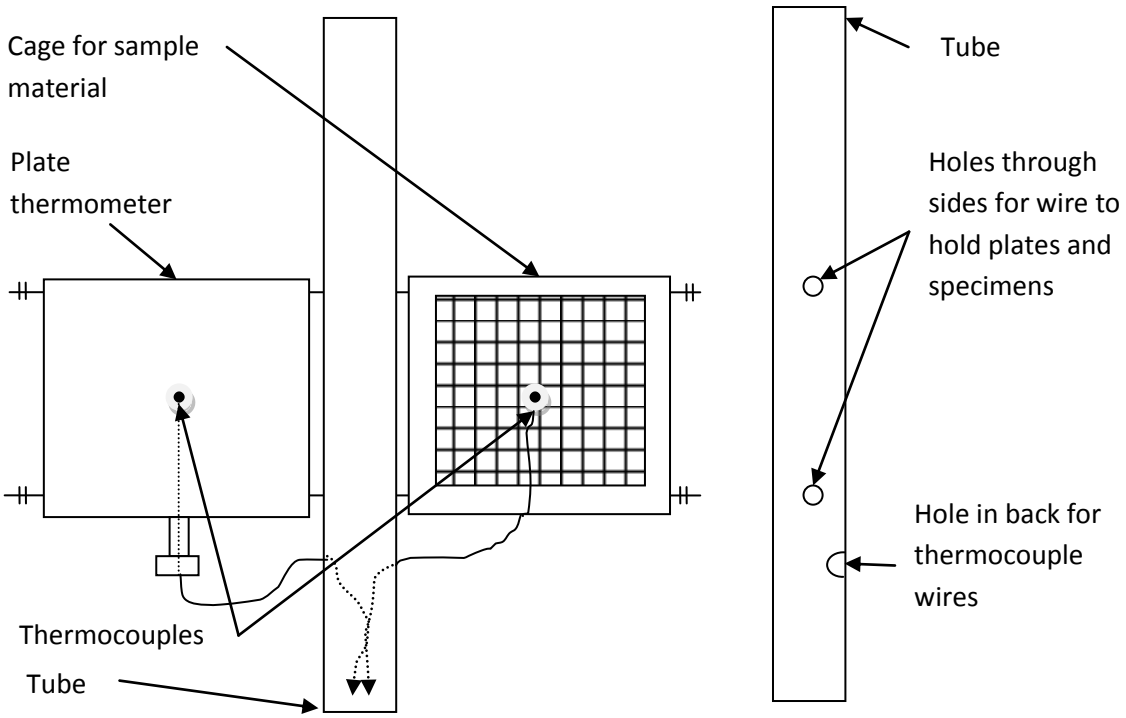

Figure 8: Schematic of the plate thermometer and cage for sample material located on the equipment trees. Not to scale.

5.2.1 Calibration

The response of the plate thermometers under the cone calorimeter was recorded for a range of target radiation levels from 1 to 30 kW/m². Nine tests were performed in the cone calorimeter with the plate thermometers in the horizontal orientation, with a target incident radiation from 0.5 to 25 kW/m². A summary of the tests is presented in Table 5. Five tests were performed in the in the cone calorimeter with the plate thermometer in the vertical orientation, with a target incident radiation from 2 to 30 kW/m². A summary of the tests is presented in Table 4. Data was recorded at 1 s intervals.

Note that the target radiation level was set using a calibrated radiation gauge located at the centre, at the same height as the surface of the plate thermometers. It is expected that the radiation level delivered by the cone calorimeter varies over the radius from the centre of the target area. This variation is ±2% kW/m² in the horizontal and ±10% kW/m² in the vertical directions, in accordance with (*AS/NZs 3837* 1998).

The range of heat flux values (e.g. Figure 89) and sensitivities (e.g. Figure 90) were calculated using PERT distributed values for input parameters (of Equation 7 with values presented in Table 3) using @Risk. The sampling of the input parameters was performed using the Latin Hypercube technique with a randomly generated seed and 10,000 iterations were used to calculate the results.

Three plate thermometers were chosen for use in the horizontally-oriented calibration tests. A range of surface finishes were chosen to assess the influence of surface damage (from oxidisation or impingement of other molten materials from previous tests). An image of the three plate thermometers is included in Figure 9. Only Plate A was used in the vertically oriented tests.

Table 4: Summary of tests performed in the cone calorimeter in the vertical orientation

Test Number	Target Incident Radiation (kW/m²)
Test 1	29.5
Test 2	21.9
Test 3	15.9
Test 4	6.6
Test 5	2.2

Table 5: Summary of tests performed in the cone calorimeter in the horizontal orientation

Test Number	Target Incident Radiation (kW/m²)
Test 1	25.0
Test 2	24.8
Test 3	19.0
Test 4	18.0
Test 5	14.8
Test 6	9.0
Test 7	3.5
Test 8	1.0
Test 9	0.5

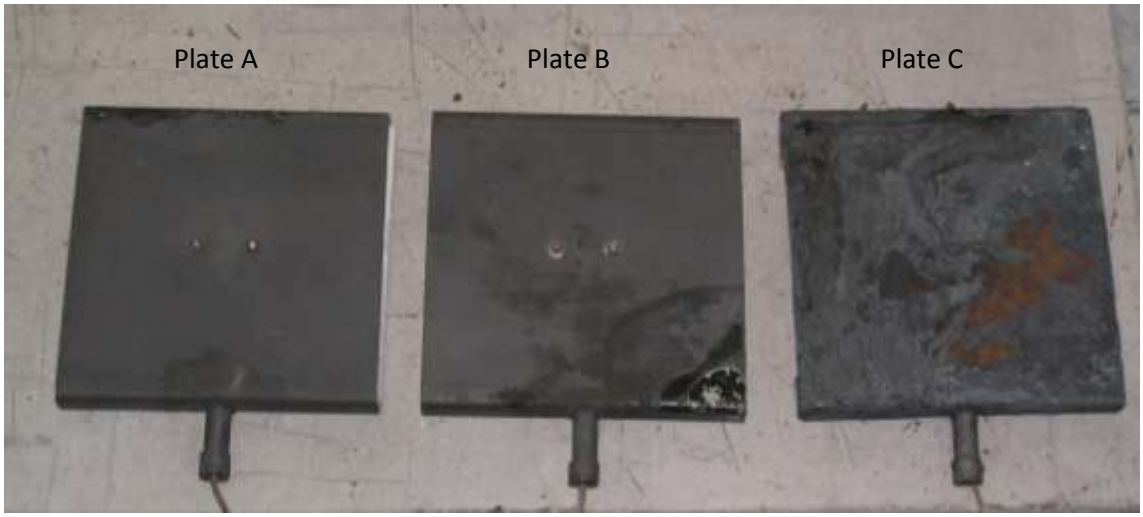

Figure 9: The three plate thermometers used in calibration tests.

5.2.2 Investigation of plate thermometer set-up

Seven tests were performed in the cone calorimeter on a plate that was modified with the spot-welded thermocouples on the front (labelled as the surface thermocouple) and back of the plate (labelled as the plate thermocouple, which is the location of the typical set-up). A range of target incident radiation from 5 to 27 kW/m² was used. Data was recorded at 1 s intervals. The strip at the back of the metal plate, used to locate the thermocouple, was not included for these sets of tests in order to assess the influence of the uneven spread of plate thickness directly surrounding the plate thermocouple. A summary of the tests is presented in Table 6.

Table 6: Summary of tests performed in the cone calorimeter with spot-welded thermocouples on back and front of plate

Test Number	Target Incident Radiation (kW/m²)
Test 1	5.0
Test 2	7.2
Test 3	9.3
Test 4	14.4
Test 5	19.4
Test 6	22.9
Test 7	27.3

During the calibration tests, as listed in Table 5, some of the tests were performed with one plate thermocouple located directly below the plate thermometer that was subjected to the target heat flux. For example, during Test 3 of Table 5, Plate B was placed on top of Plate A and then the stacked plates were taken from ambient conditions to expose Plate B to the target heat flux at the appropriate distance from the radiative coil. Therefore the plate on the bottom (Plate A in this example) was exposed to the heat flux from the back of the top plate (Plate B in this example). This provided an estimate of heat lost through the mineral insulation of the plate thermometer from the comparison of the estimate of the heat loss component of the top plate from the theory and the incident heat flux of the bottom plate.

5.2.3 Furniture calorimeter with a burner

Eight tests were performed in the furniture calorimeter with a gas burner. A summary of the tests is presented in Table 7, where the orientation of the equipment trees is also described. Data was recorded at 10 s intervals.

Table 7: Summary of tests performed under the furniture calorimeter using a gas burner

Test Number	Equipment Tree Locations	Heat Flux Gauge Locations
Test 1	All 4 at 1000 mm from centre of burner, at 0, 45, 90 & 135°	A: 4bot B: not working
Test 2	All 4 at 600 mm from centre of burner, at 0, 45, 90 & 135°	A: 4mid B: not used
Test 3	All 4 at 600 mm from centre of burner, at 0, 45, 90 & 135°	A: 4top B: 2mid
Test 4	All 4 at 1500 mm from centre of burner, at 0, 45, 90 & 135°	A: 4top B: 2top
Test 5	All 4 at 1300 mm from centre of burner, 1 diametrically opposite to 4 & 2 diametrically opposite to 3	A: 4mid B: 2mid
Test 6	All 4 at 1000 mm from centre of burner, 1 diametrically opposite to 4 & 2 diametrically opposite to 3	A: 4top B: 2top
Test 7	All 4 at 1300 mm from centre of burner, 1 diametrically opposite to 4 & 2 diametrically opposite to 3	A: 4top B: 2top
Test 8	All 4 at 1300 mm from centre of burner, 1 diametrically opposite to 4 & 2 diametrically opposite to 3	A:4top B:2top

5.2.4 Furniture calorimeter with a mattress

Two tests were performed with a burning mattress under the furniture calorimeter. A summary of the tests is presented in Table 8, where the orientation of the equipment trees is also described. Data was recorded at 10 s intervals.

Table 8: Summary of tests performed under the furniture calorimeter with a burning mattress

Test Number	Equipment Tree Locations	Heat Flux Gauge Locations
Test 1	Each at 1 m from centre of folded mattress 1: behind mattress 2: left hand side of mattress 3: in front of mattress 4: right hand side of mattress	Not used
Test 2	Each at 1 m from centre of folded mattress 1: behind mattress 2: left hand side of mattress 3: in front of mattress 4: right hand side of mattress	Not used

5.2.5 ISO room with a burner in the corner

Six tests were performed in the ISO room using a gas burner in the corner of the room. A summary of the tests and the orientation of the equipment is presented in Table 10. Data was recorded at 10 s intervals.

The layout within the ISO room is shown schematically in Figure 10 for the situation of the gas burner located in one corner. The distances shown are related to the location of the centre pole of each of the four equipment trees. The locations are also described in Table 11.

Table 9: Summary of tests performed in ISO room using a gas burner

Test Number	Equipment Tree Locations	Gardon gauge Locations
Test 1	Orientation A	A: 4top B: 2top
Test 2	Orientation A	A: 4mid B: 2mid
Test 3	Orientation B	A: 4mid B: 2mid
Test 4	Orientation B	A: 4mid B: 2mid
Test 5	Orientation B	A: 4mid B: 2mid
Test 6	Orientation B	A: 4mid B: 2mid

Table 10: Descriptions of equipment tree orientations used in ISO room experiments

Stand Orientation	Tree Number	Equipment Tree Locations (location of the centre of stand) (mm)	
		Radial Distance from Centre of the Burner or Mattress	Location Relative to the Bottom Left Corner of the ISO Room (using orientation shown in Figure 10 and Figure 11) (x,y)
Orientation A	1	800	150,1480
	2	2000	910, 620
	3	2500	2200, 1200
	4	3000	3115, 1900
Orientation B	1	1750	300, 500
	2	2783	2150, 210
	3	3383	3300, 730
	4	3175	3470, 2160
Orientation C	1	1910	210, 2160
	2	3210	3450, 500
	3	2790	2350, 2080
	4	3570	3470, 1790

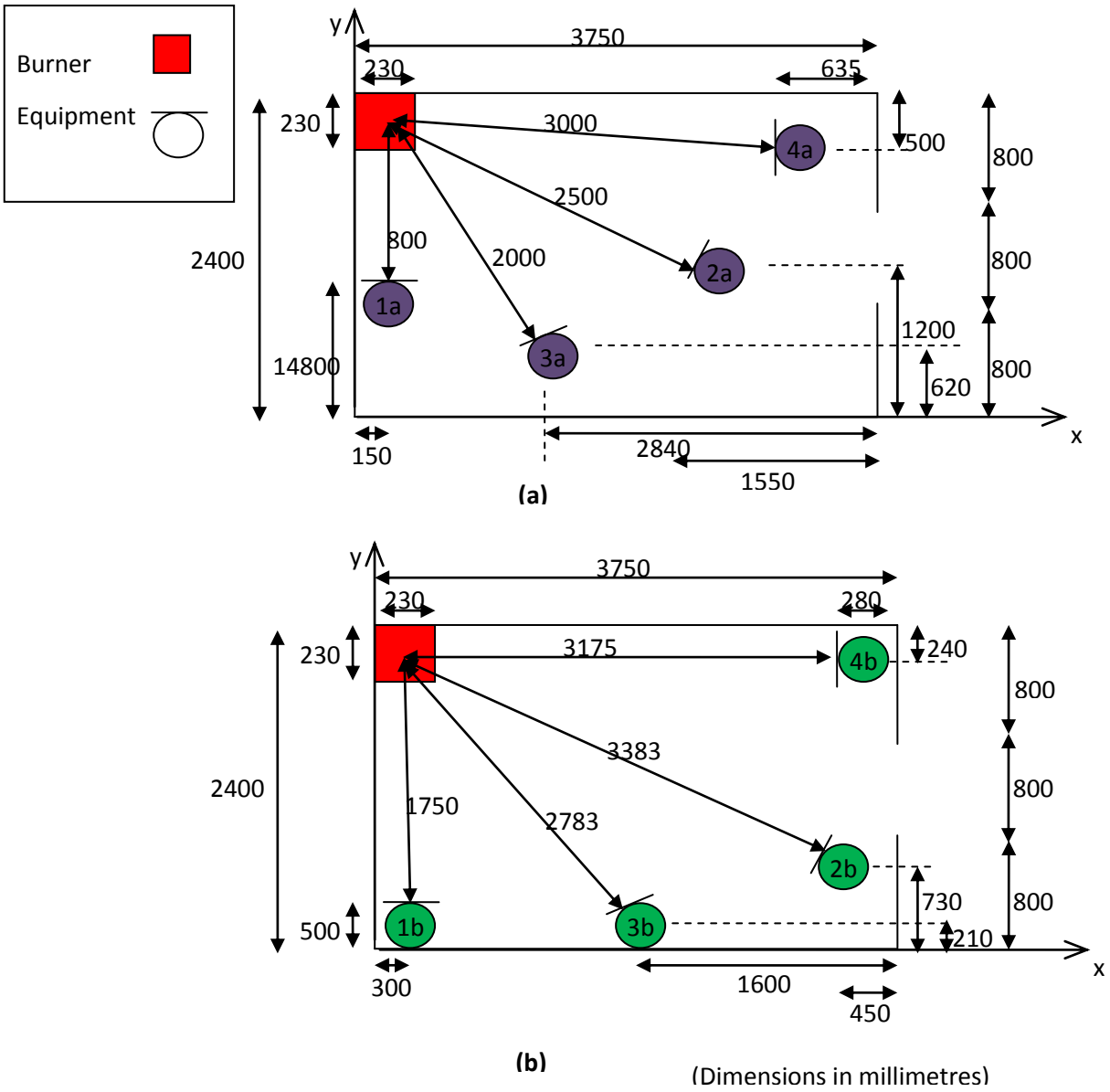

Figure 10: Schematic of various layouts of the equipment stands used within the ISO room for the mattress tests in (a) Orientation A and (b) Orientation B. Not to scale.

5.2.6 ISO room with a mattress in the corner

Six tests were performed in the ISO room where a mattress was burned in the corner of the room. A summary of the tests and the orientation of the equipment is presented in Table 11. Data was recorded at 10 s intervals.

The layout within the ISO room is shown schematically in Figure 11 for the situation of the burning mattress on the load cell located in one corner. The distances shown are related to the location of the centre pole of each of the four equipment trees. The locations are also described in Table 11.

Table 11: Summary of tests performed in ISO room using a mattress in the corner of the room (with the door open)

Test Number	Stand locations	Heat Flux Gauge locations
Test 1	Orientation C	A: 4mid B: 2mid
Test 2	Orientation C	A: 4mid B: 2mid
Test 3	Orientation C	A: 4mid B: 2mid
Test 4	Orientation C	A: 4mid B: 2mid
Test 5	Orientation C	A: 4mid B: 2mid
Test 6	Orientation C	A: 4mid B: 2mid

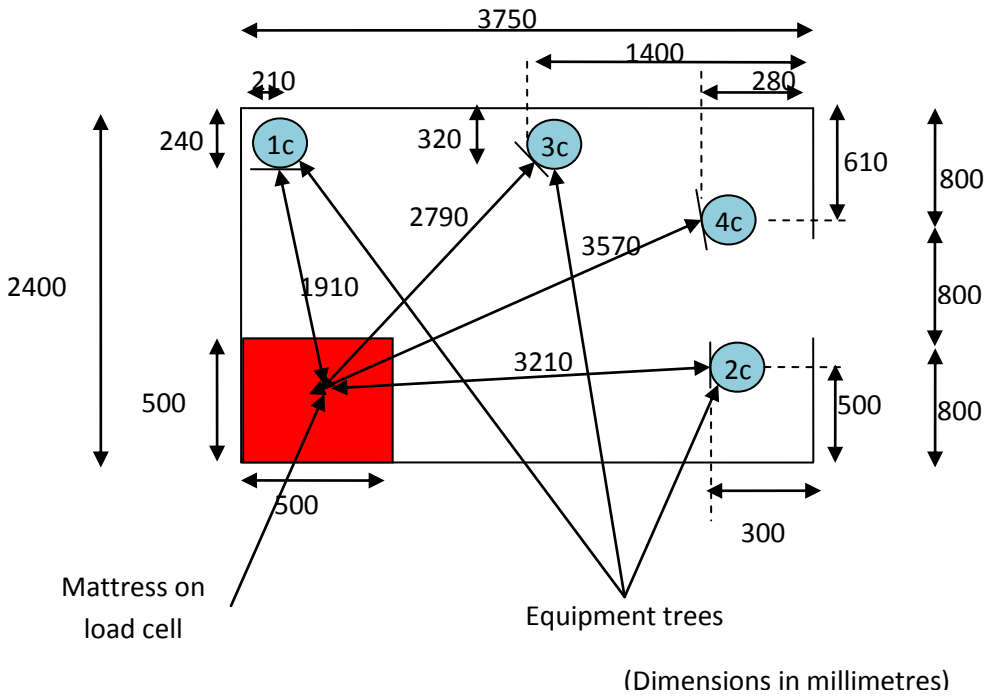

Figure 11: Schematic of the layout of the equipment stands used within the ISO room for Orientation C. Not to scale.

5.2.7 ISO room with a mattress in the corner and the room opening sealed

Four tests were performed in the ISO room with a mattress in the corner and the door opening of the room was sealed during the test.

A summary of the tests is presented in Table 12. The orientation of the equipment trees was Orientation C, as shown in Figure 11. In each test the Gardon gauges were used in the same positions, directly above the plate thermometers located at the middle height of equipment tree number 2 and 4. Data was recorded at 10 s intervals.

Table 12: Summary of tests performed in ISO room using a mattress in the corner of the room where the door opening of the room was sealed

Test Number	Equipment Tree Locations	Gardon gauge Locations
Test 1	Orientation C	A: 4mid B: 2mid
Test 2	Orientation C	A: 4mid B: 2mid
Test 3	Orientation C	A: 4mid B: 2mid
Test 4	Orientation C	A: 4mid B: 2mid

6. EXPERIMENT RESULTS

6.1 Calibrating plate thermometers

An example of the results of the tests used in the calibration of the plate thermometers, as discribed in Section 5.2.1, is presented in this section. The incident radiative heat flux was calculated using Equation 7, and the measured plate thermometer temperature (T_{PT}) and best-fit parameter values summarised in Table 3, such that Equation 7 can be rewritten as:

$$\dot{q}''_{rad,inc} = \frac{1}{0.85}\left(8500 \times 440 \times 0.7 \times \frac{\Delta T_{PT}}{\Delta t} + 4(T_{PT} - T_{\infty}) - 4.0\left(\frac{(T_{PT} - T_{\infty})}{0.1}\right)^{1/4}(T_{PT} + T_{\infty})^{-0.16}(T_{PT} - T_{\infty})\right) + 5.669 \times 10^{-8} T_{PT}^4$$

Equation 14

Detailed results are presented in Appendix A. Analysis of these tests is discussed and presented in Section 7.1.

6.1.1 Horizontal orientation - Test 3

The target incident radiation level for this example was 19 kW/m².

An example of the calculated heat flux based on plate thermometer measurements for based on 'best' input parameters (presented in Table 3) is shown in Figure 12 for the three example plate thermometers tested. The plate thermometers were in the horizontal orientation.

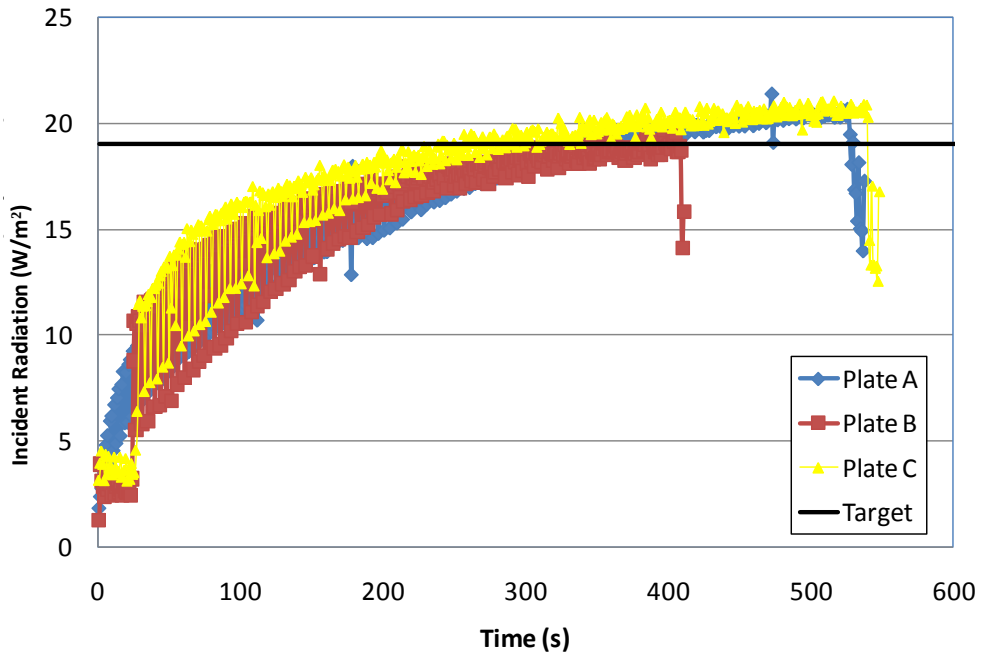

(a)

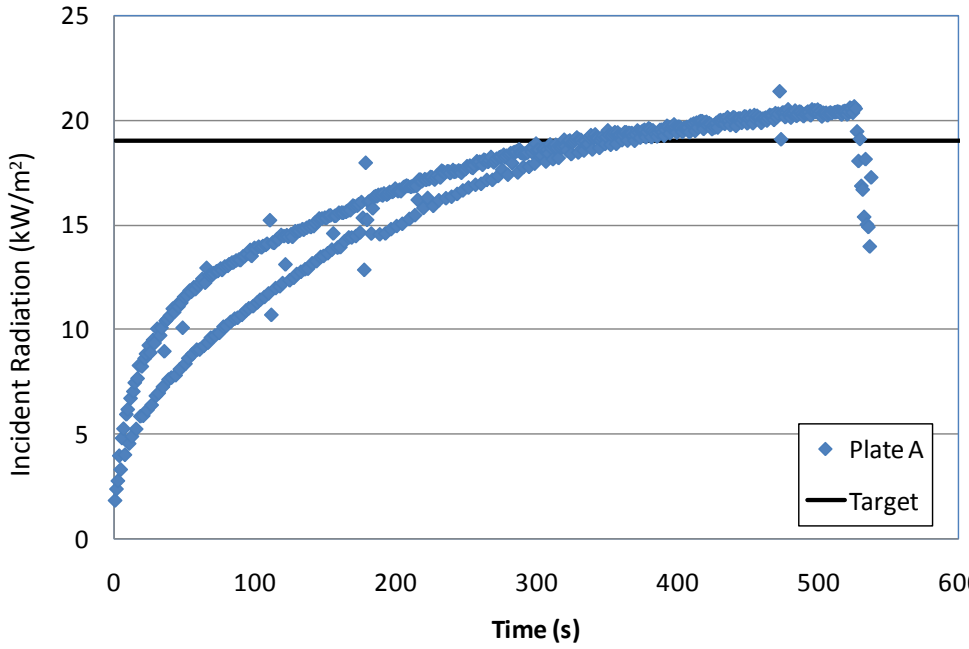
25
20
15
10
5
0
Incident Radiation (kW/m²)
0
100
200
300
400
500
600
Time (s)
Plate A
Target

(b)

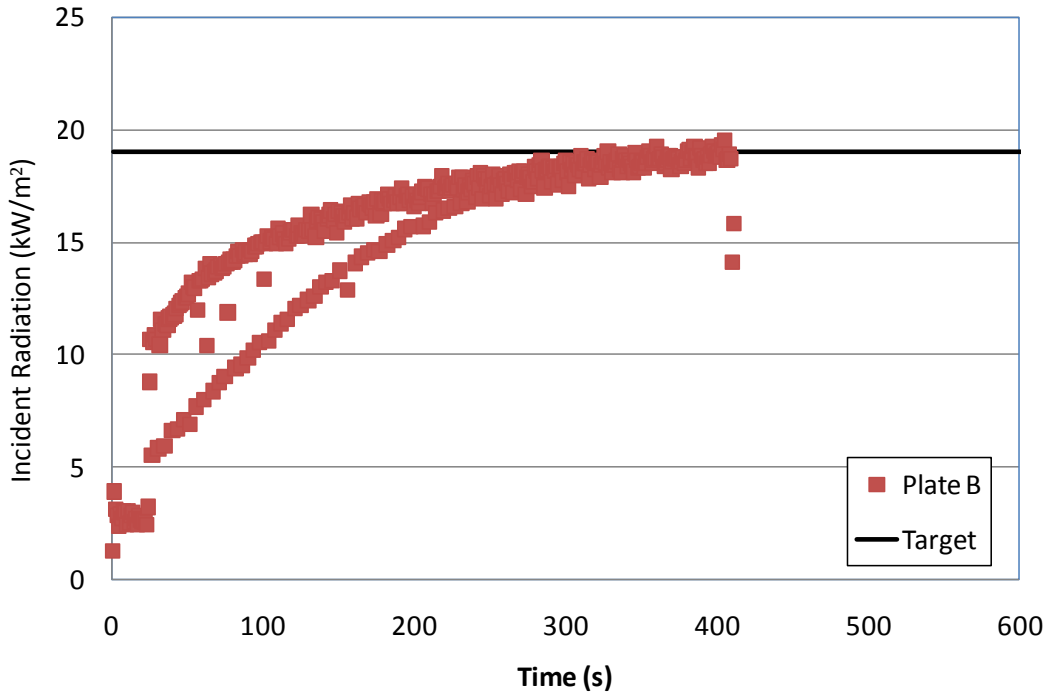
25
20
15
10
5
0
Incident Radiation (kW/m²)
0
100
200
300
400
500
600
Time (s)
Plate B
Target

(c)

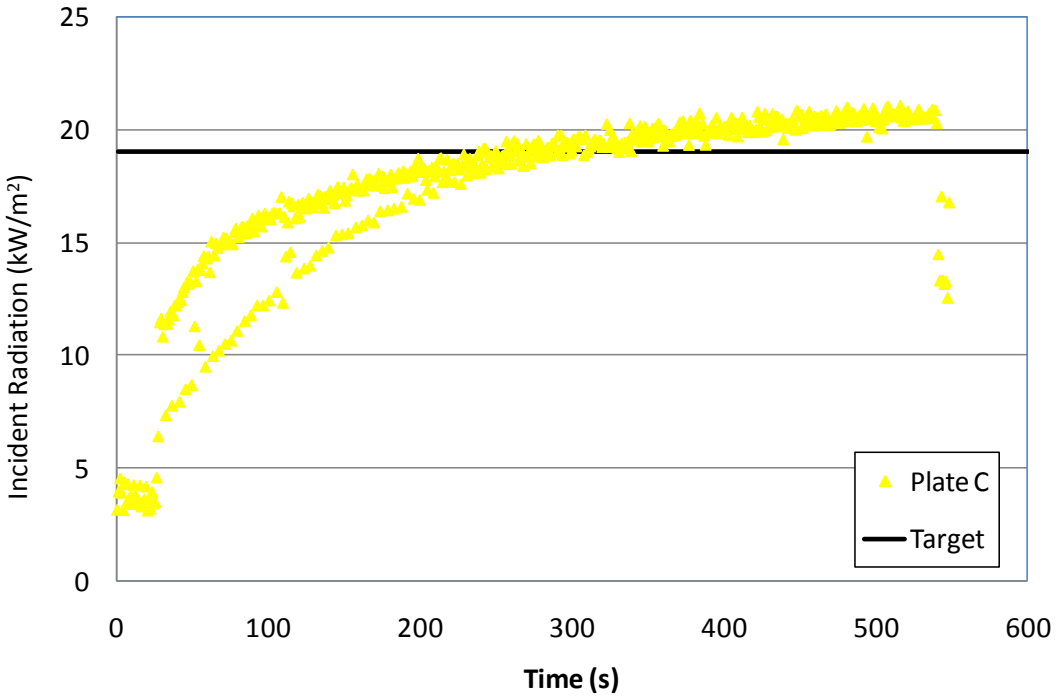

(d)

Figure 12: Calculated heat flux based on plate thermometer measurements for (a) all plates tested, (b) Plate A, (c) Plate B and (d) Plate C, based on 'best' input parameters presented in Table 3, with a target radiation level of 19 kW/m².

6.1.2 Vertical orientation summary

A summary of the results for effective thermal conductivity coefficient values for the cone calorimeter tests performed with the plate thermometers in the vertical orientation is presented in Table 13.

Table 13: Summary of results for the average effective thermal conductivity coefficient calculated for tests performed in the cone calorimeter in the vertical orientation

Test Number	Target Incident Radiation (kW/m²)	Effective Thermal Conductivity Coefficient (W/m².K)
Test 1	29.5	4
Test 2	21.9	6
Test 3	15.9	8
Test 4	6.6	5
Test 5	2.2	1

6.2 Investigation of plate thermometer set-up

An example of the results of the tests used to investigate the plate thermometer set-up and the analysis used for estimating the incident radiation, as discussed in Section 5.2.2, is presented in this section. Detailed results are presented in Appendix A.

6.2.1 Test 5

The target incident radiation for this example was 19.4 kW/m².

The results for the estimation of incident radiation using the plate thermometer temperature (located at the back of the plate only) and using the plate thermometer and (front of plate) surface temperatures is shown in Figure 13. The difference in the values of the estimated incident radiation using the two calculation methods (one using one temperature measurement and the second using two temperature measurements) is shown in Figure 14. The temperature difference between the plate thermometer thermocouple and the surface thermocouple is shown in Figure 15. The results for the radiative, convective, conductive and storage components for the estimation of the incident radiative heat flux are shown in Figure 16. A comparison of the estimated incident radiative heat flux calculated for a plate thermometer with a spot-welded thermocouple on the back of the plate (target of 19.4 kW/m², Test 5) and a plate thermometer with a thermocouple located by a strip of metal and two screws (target of 19 kW/m², Tests 3 of Section 6.1.1) is shown in Figure 17.

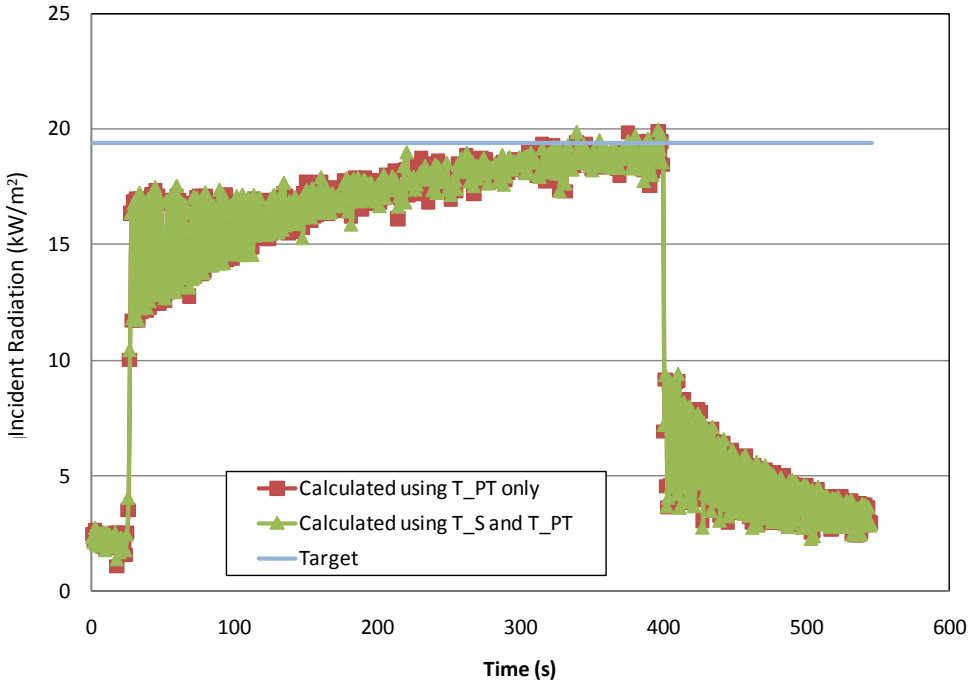

Figure 13: Estimation of incident radiation using the plate thermometer temperature only and using the plate thermometer and surface temperatures, with a target incident radiation of 19.4 kW/m².

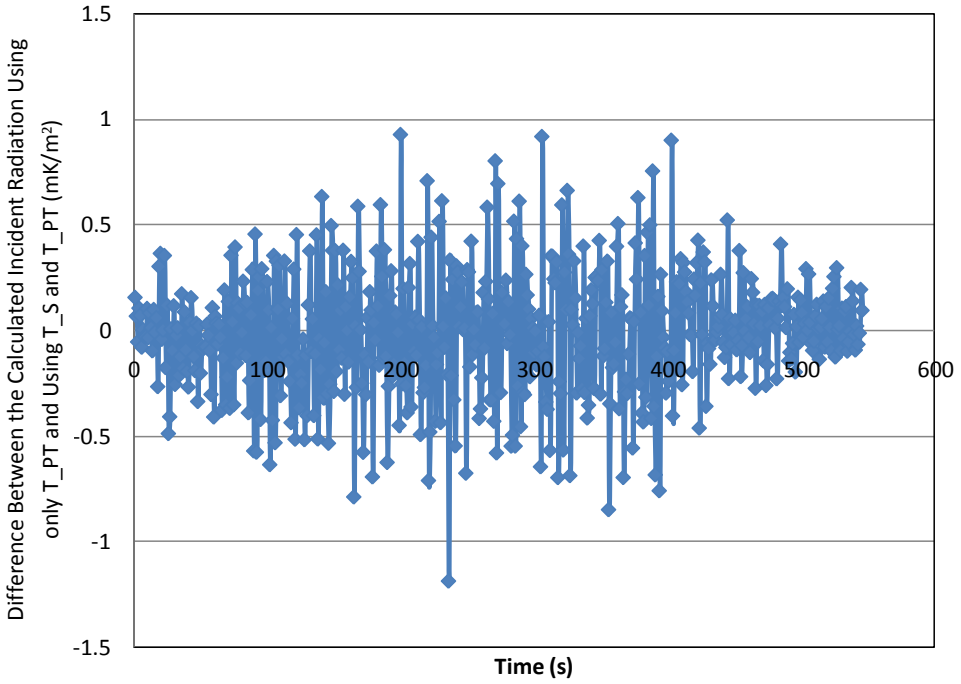

Figure 14: Difference in estimated incident radiation using the two calculation methods (i.e. using the one temperature measurement at the back of the metal plate assuming $(T_S = T_{PT})$, and using two temperatures – one at the front surface of the plate and the one at the back surface of the plate thermometer assuming $(T_S \neq T_{PT})$).

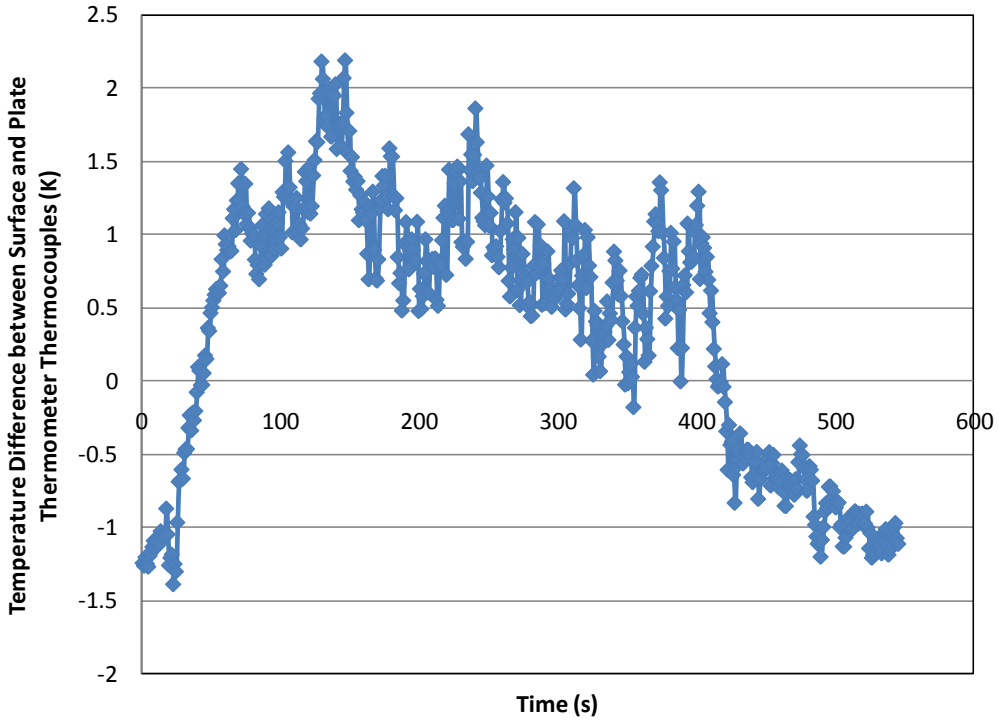

Figure 15: Difference in measured temperature between the plate thermometer thermocouple and the surface thermocouple.

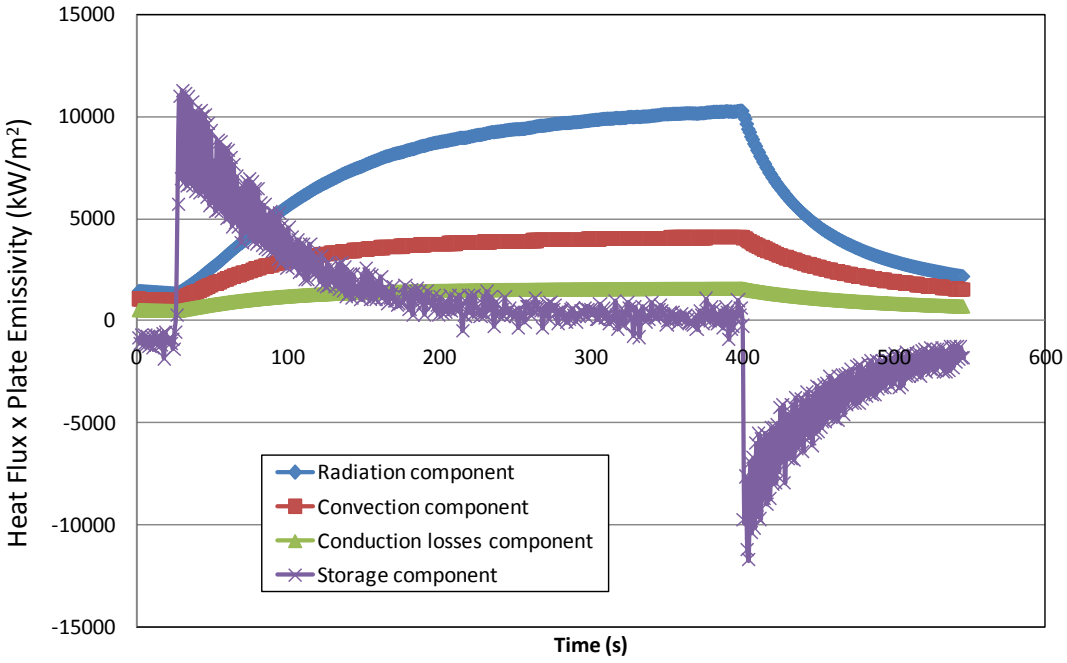

Figure 16: Component values for the estimation of the incident radiative heat flux.

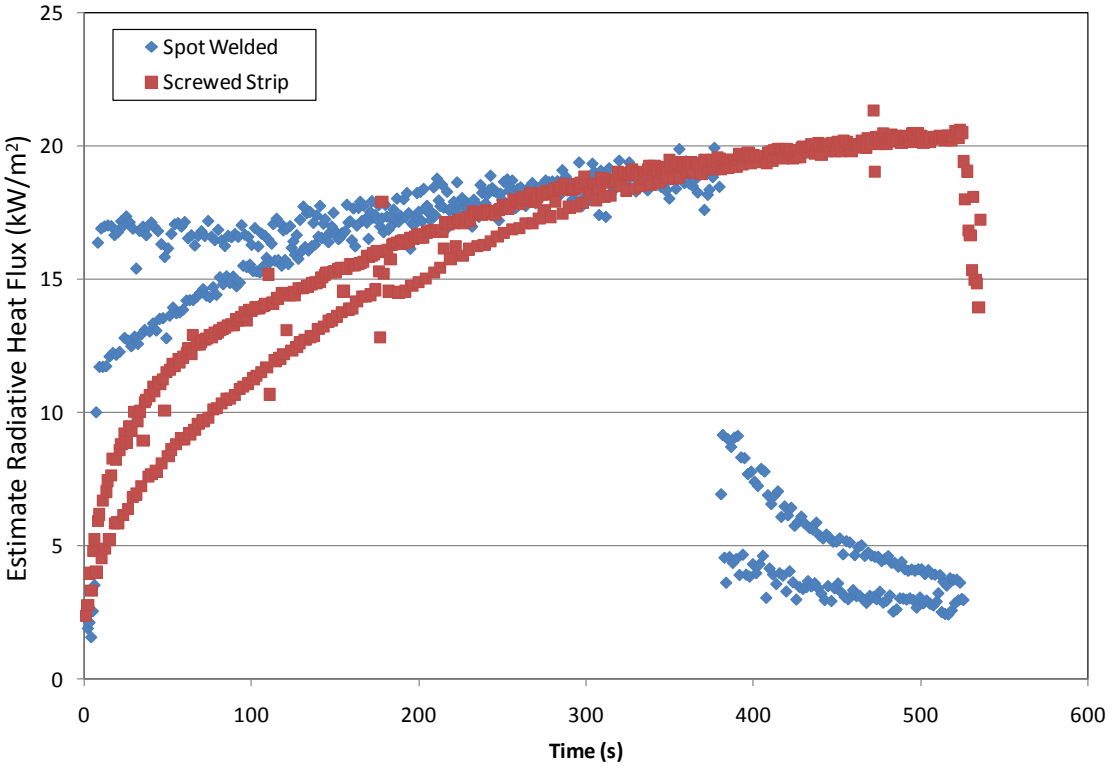

Figure 17: Comparison of the estimated incident radiative heat flux for a plate thermometer with a spot-welded thermocouple on the back of the plate (target of 19.4 kW/m², Test 5) and a plate thermometer with a thermocouple located by a strip of metal and two screws (target of 19 kW/m², Test 3 of Section 6.1.1).

6.2.2 Test 3 of Section 6.1/Section 5.2.1

An example of the cone calorimeter tests where one plate thermometer was placed directly below the plate exposed to the target incident heat flux is shown in Figure 18. In this example, Plate B was exposed to the target heat source (19 kW/m^2) at the standard distance, and Plate A was located directly below Plate B. The comparison of the radiative, convective, conductive and storage components of the heat flux of Plate B and the incident heat flux of Plate A is shown in Figure 19. In this example the effective thermal conductivity associated with the losses to the mineral insulation was 4 W/m^{2}K.

More detailed results are included in Appendix A.2.8.

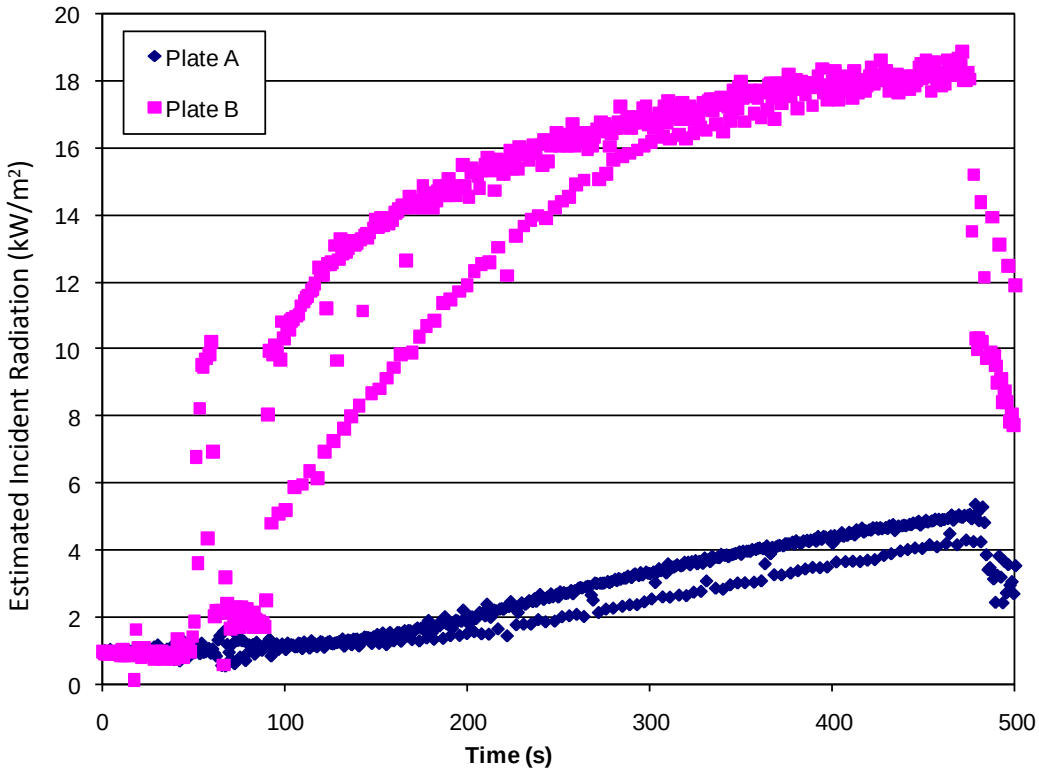

Figure 18: Cone calorimeter tests where Plate B is exposed to the target heat source (19 kW/m^2) at the standard distance, with Plate A located directly below Plate B.

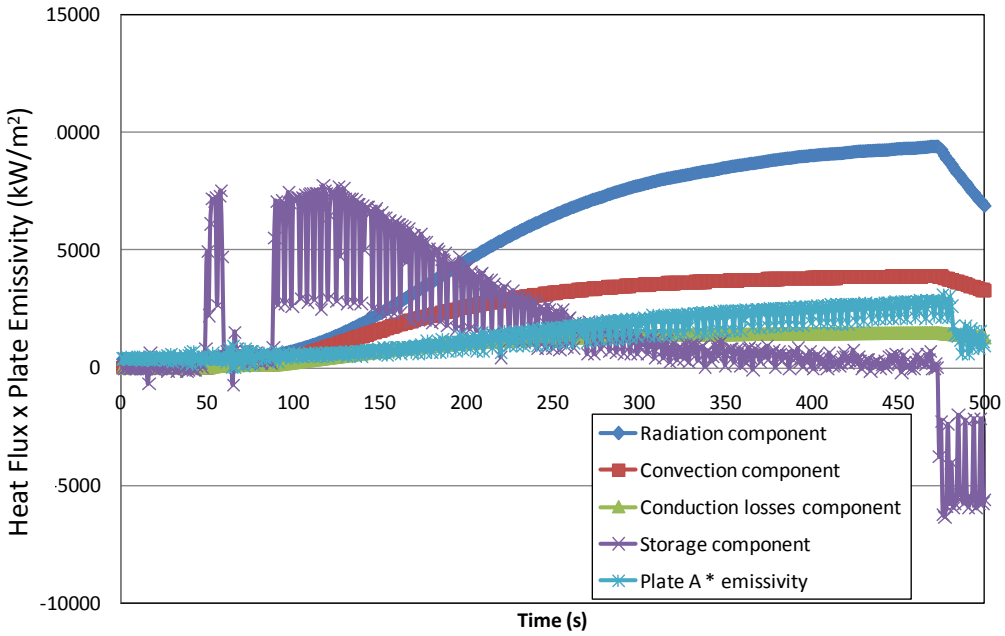

Figure 19: Comparison of components of the heat flux of Plate B and the incident heat flux of Plate A, located directly behind Plate B, where K_{cond}= 4 W/m²K.

6.3 Furniture calorimeter experiments with burner only

Examples of the results of the tests using the furniture calorimeter and a propane burner, as discussed in Section 5.2.3, are presented in this section. Detailed results are presented in Appendix A.

6.3.1 Test 5

This furniture calorimeter example had all four equipment trees location at a distance of 1.3 m from the centre of the burner. The equipment trees were located diametrically opposite to each other, where equipment trees 1 and 4 faced each other and equipment trees 2 and 3 faced each other. The Gardon gauges A and B were located directly above the plate thermometers located at the mid-height of equipment trees 4 and 2 respectively.

The HRR, as calculated by oxygen calorimetry and by the fuel mass flow rate of the burner, is compared to the incident radiant heat flux calculated from Gardon gauge A measurements in Figure 20. Where plate thermometers were in adjacent locations to the two Gardon gauges, estimates of the incident radiative heat flux from plate thermometer measurements were compared to the Gardon gauge measurements, as shown in Figure 21. In this case the top plate location of equipment tree 4 and the middle plate location of equipment tree 2 were directly below the locations of the Gardon gauges.

For all the plate thermometer measurements at each location on each equipment tree, the estimates of the incident radiative heat flux are shown in Figure 22 and the temperatures over each of the adjacent sample materials are shown in Figure 23. For clarity these results are shown for each of the equipment trees in Figure 24. The estimated incident radiative heat fluxes at each of the heights above the floor are shown in Figure 25.

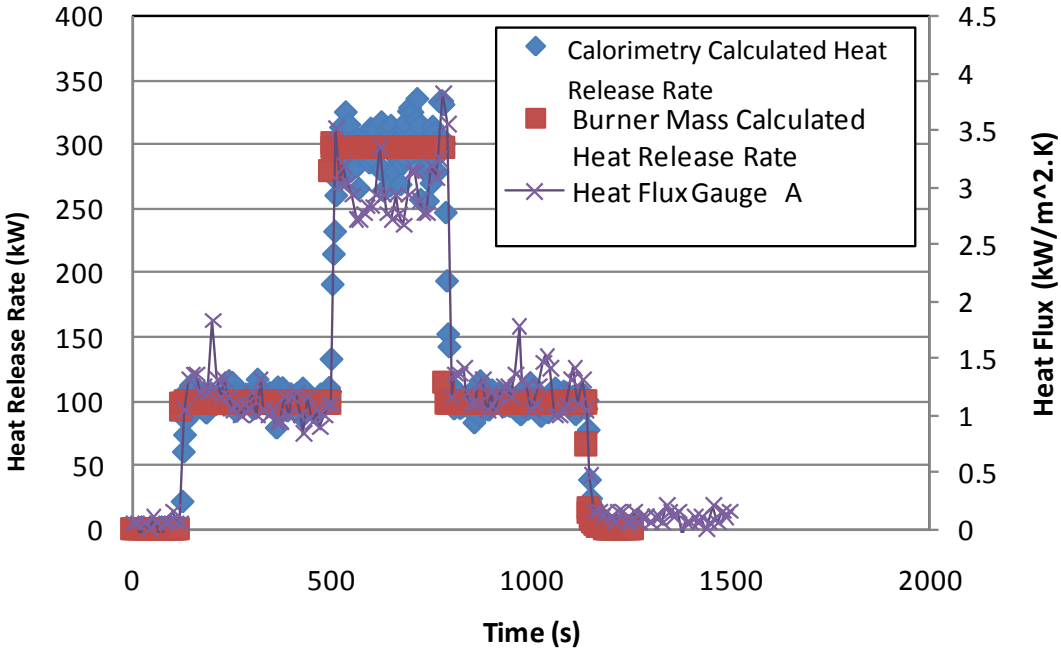

Figure 20: HRR, as calculated by oxygen calorimetry and by the fuel mass flow rate of the burner, and incident radiant heat flux estimated from Gardon gauge A measurements.

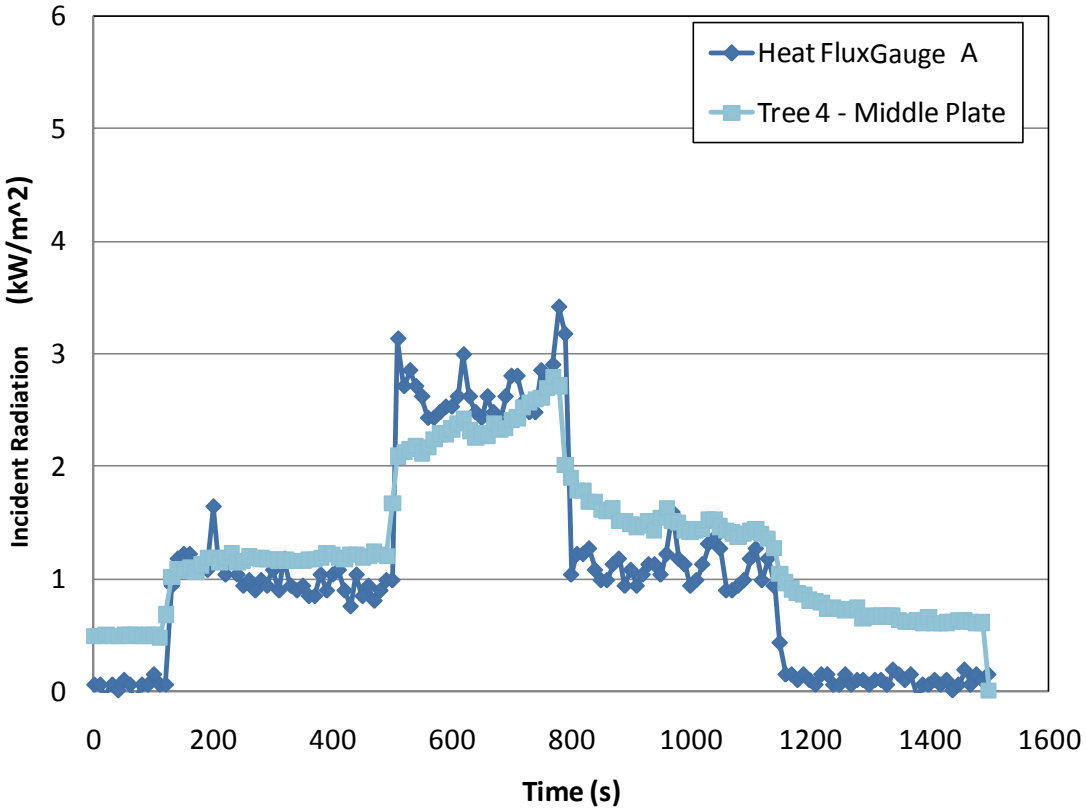

(a)

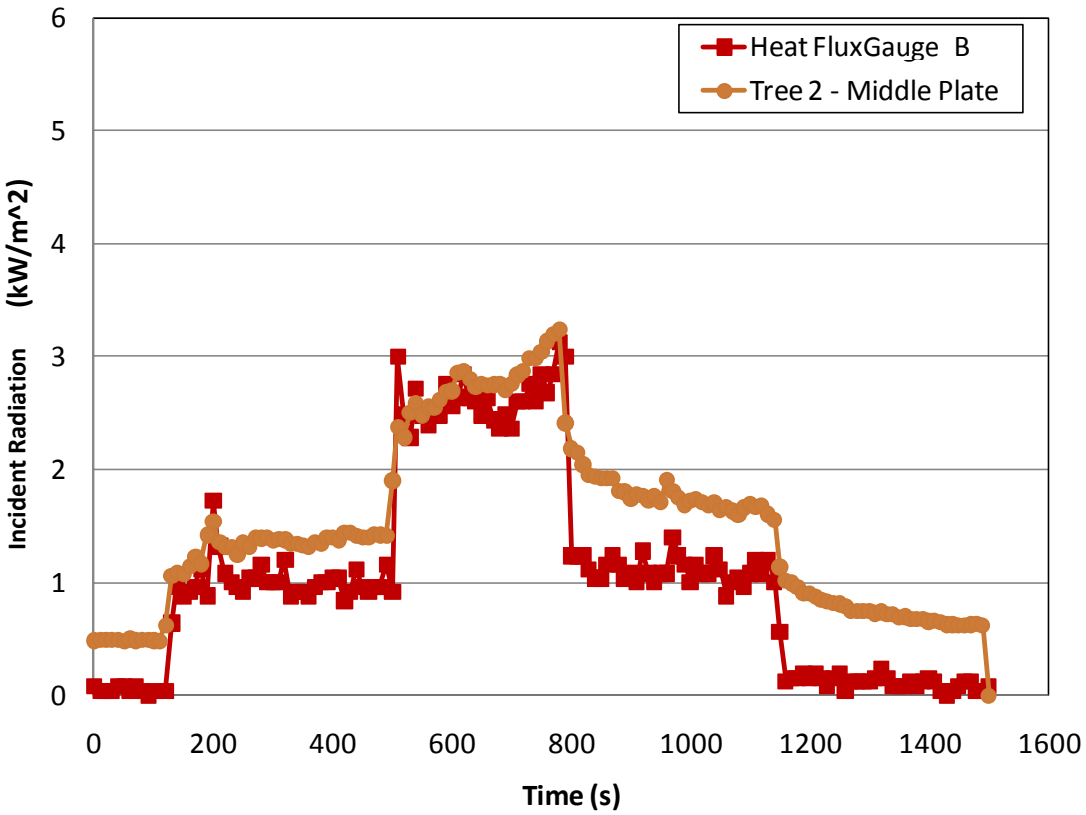

(b)

Figure 21: Estimates of the incident radiative heat flux at the (a) top plate location of tree 4 and (b) middle plate location of tree 2 from plate thermometer and Gardon gauge measurements.

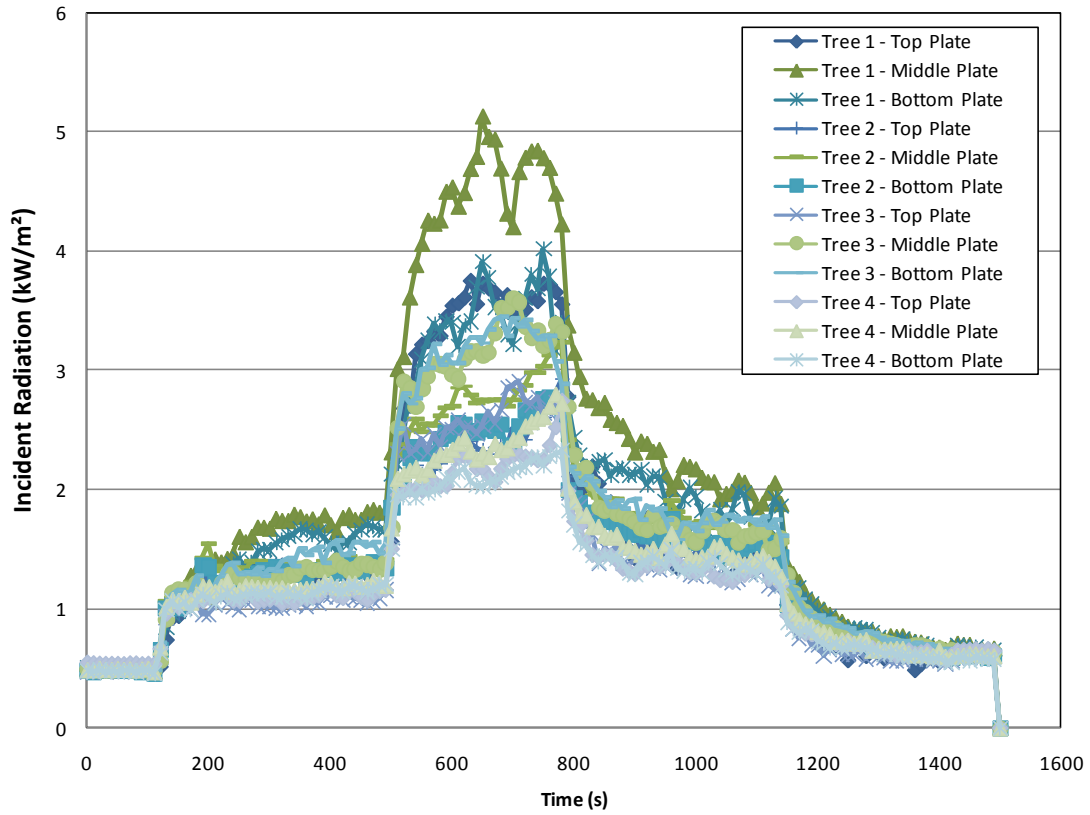

Figure 22: Estimates of the incident radiative heat flux from the plate thermometer measurements at each location on each tree.

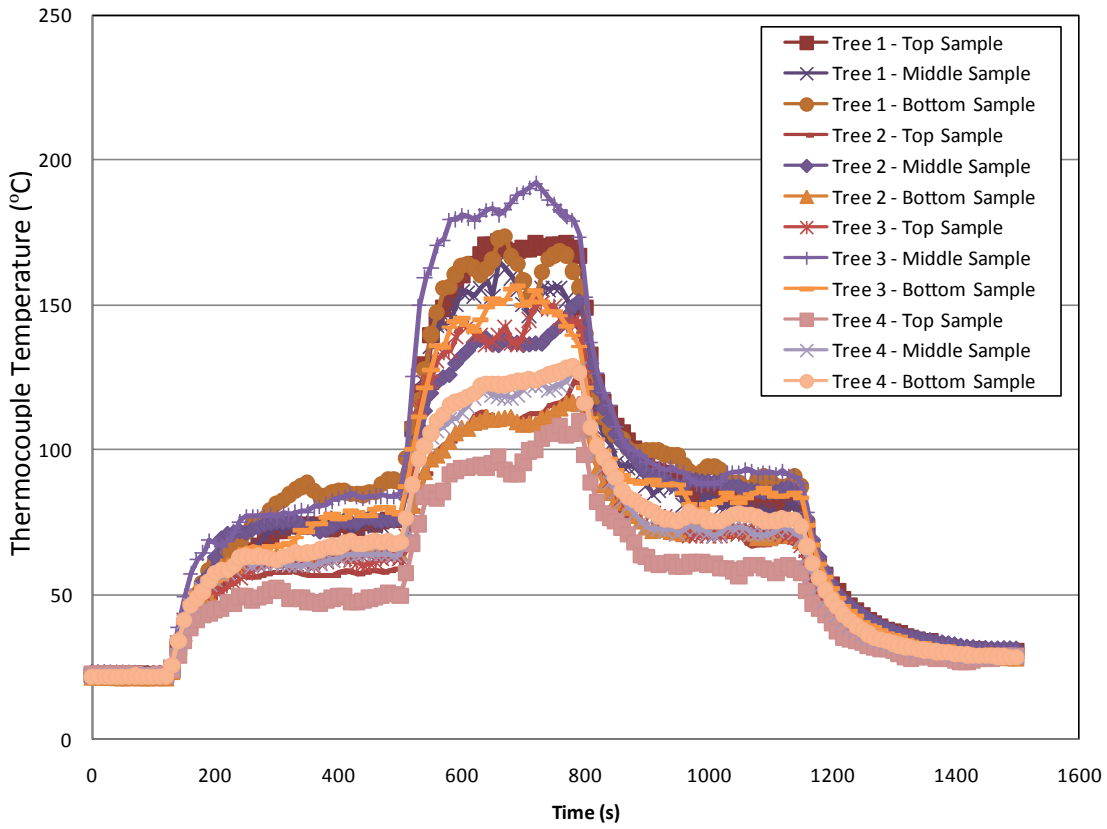

Figure 23: Thermocouple measurements at each sample location on each tree.

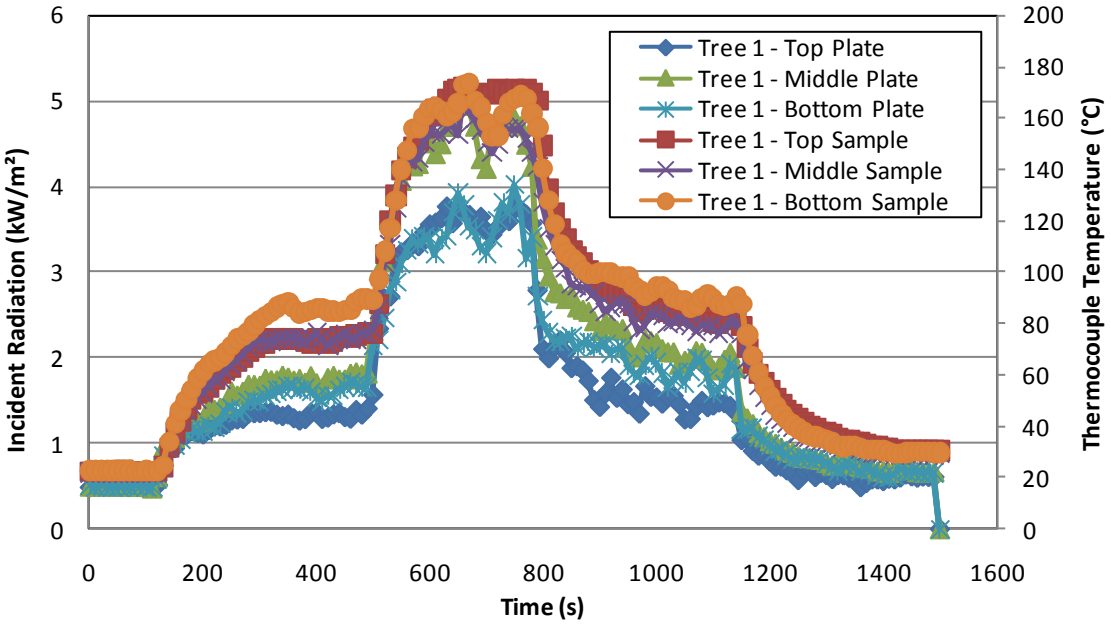
Tree 1 - Top Plate
Tree 1 - Middle Plate
Tree 1 - Bottom Plate
Tree 1 - Top Sample
Tree 1 - Middle Sample
Tree 1 - Bottom Sample
Incident Radiation (kW/m²)
Thermocouple Temperature (°C)
Time (s)
0
1
2
3
4
5
6
0
20
40
60
80
100
120
140
160
180
200
0
200
400
600
800
1000
1200
1400
1600

(a)

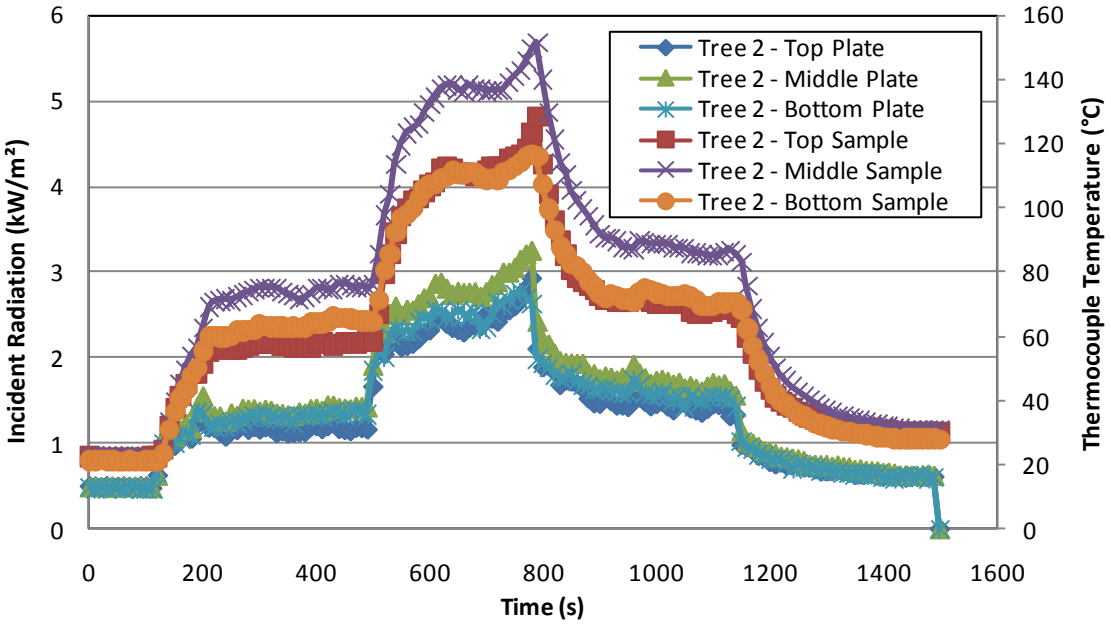
Tree 2 - Top Plate
Tree 2 - Middle Plate
Tree 2 - Bottom Plate
Tree 2 - Top Sample
Tree 2 - Middle Sample
Tree 2 - Bottom Sample
Incident Radiation (kW/m²)
Thermocouple Temperature (°C)
Time (s)
0
1
2
3
4
5
6
0
20
40
60
80
100
120
140
160
0
200
400
600
800
1000
1200
1400
1600

(b)

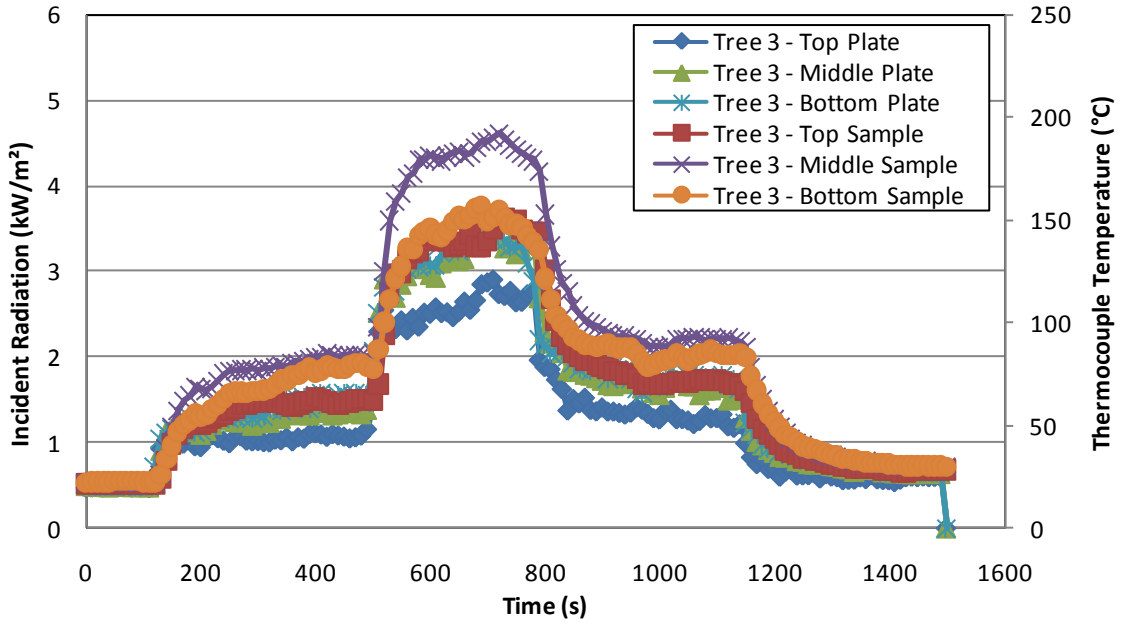

(c)

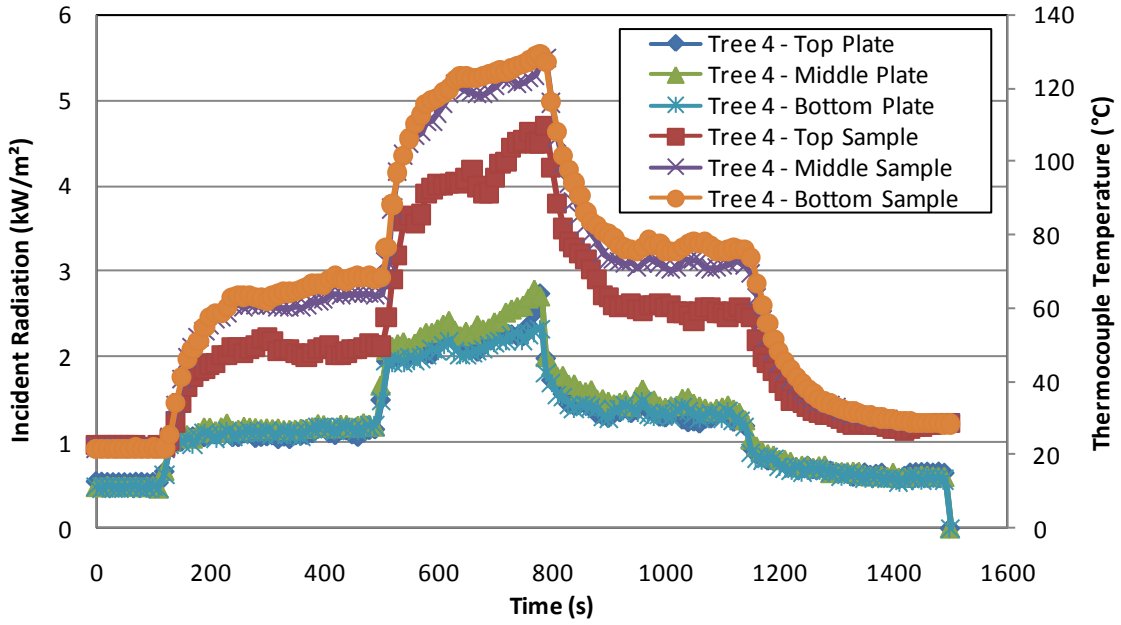

(d)

Figure 24: Thermocouple measurements and estimates of the incident radiation calculated from plate thermometer measurements for each location on each equipment tree: (a) tree 1, (b) tree 2, (c) tree 3 and (d) tree 4.

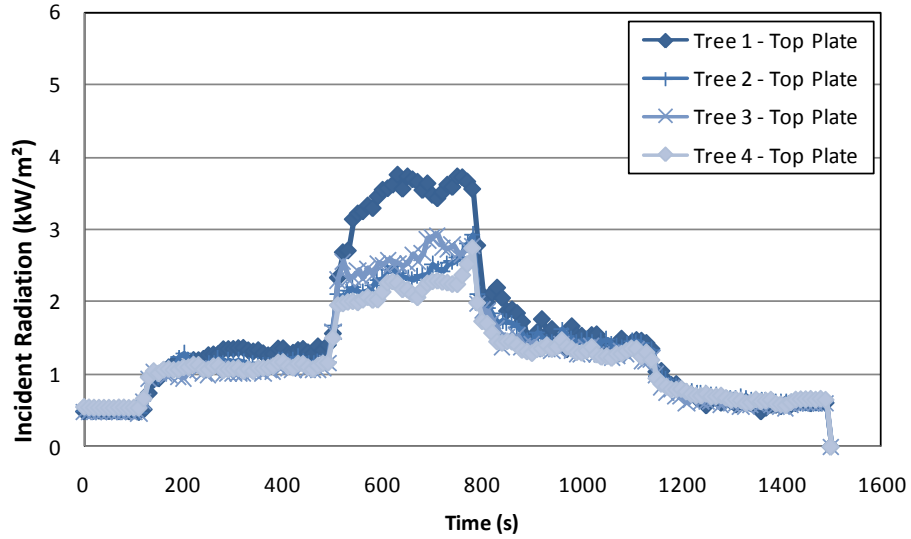

(a)

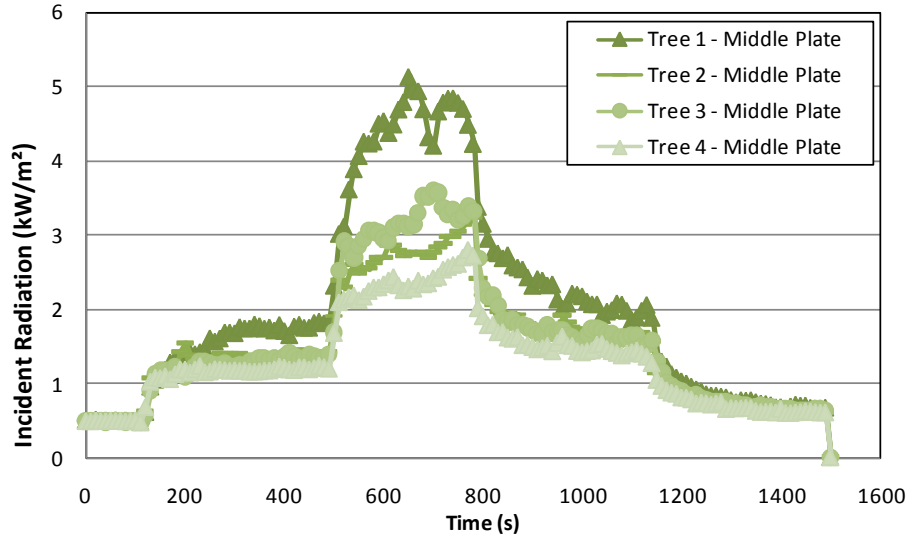

(b)

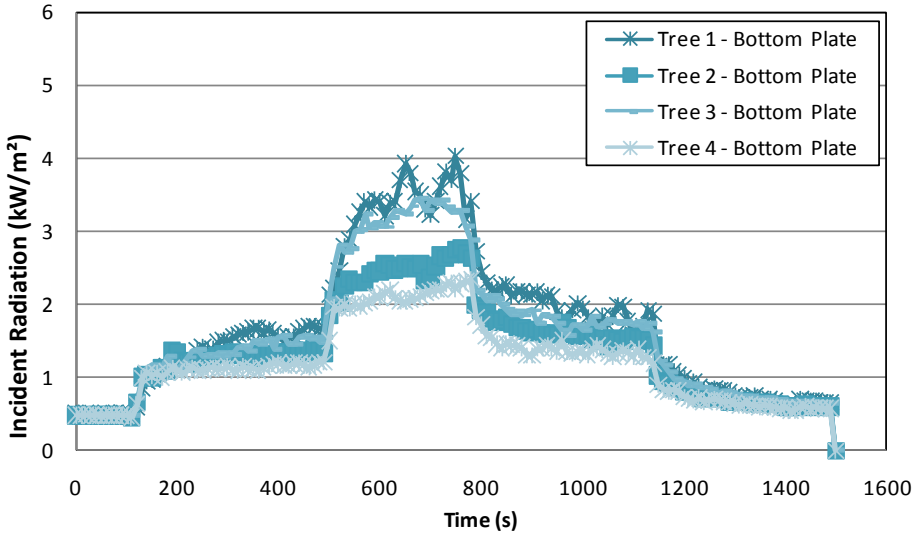

(c)

Figure 25: Estimates of the incident radiation flux calculated from plate thermometer measurements for the (a) top, (b) middle and (c) bottom locations of each of the equipment trees.

6.3.2 Test 6

This furniture calorimeter example had all four equipment trees location at a distance of 1.0 m from the centre of the burner. The equipment trees were located diametrically opposite to each other, where equipment trees 1 and 4 faced each other and equipment trees 2 and 3 faced each other. The Gardon gauges A and B were located directly above the plate thermometers located at the top-height of equipment trees 4 and 2 respectively.

Similarly as presented for Test 5 in the previous section, the HRR, as calculated by oxygen calorimetry and by the fuel mass flow rate of the burner, is compared to the incident radiant heat flux calculated from Gardon gauge A measurements in Figure 26. Where plate thermometers were in adjacent locations to the two Gardon gauges, estimates of the incident radiative heat flux from plate thermometer measurements were compared to the Gardon gauge measurements, as shown in Figure 27. In this case the top plate location of equipment tree 4 and the middle plate location of equipment tree 2 were directly below the locations of the Gardon gauges.

For all the plate thermometer measurements at each location on each equipment tree, the estimates of the incident radiative heat flux are shown in Figure 28 and the temperatures over each of the adjacent sample materials are shown in Figure 29. For clarity these results are shown for each of the equipment trees in Figure 30. The estimated incident radiative heat fluxes at each of the heights above the floor are shown in Figure 31.

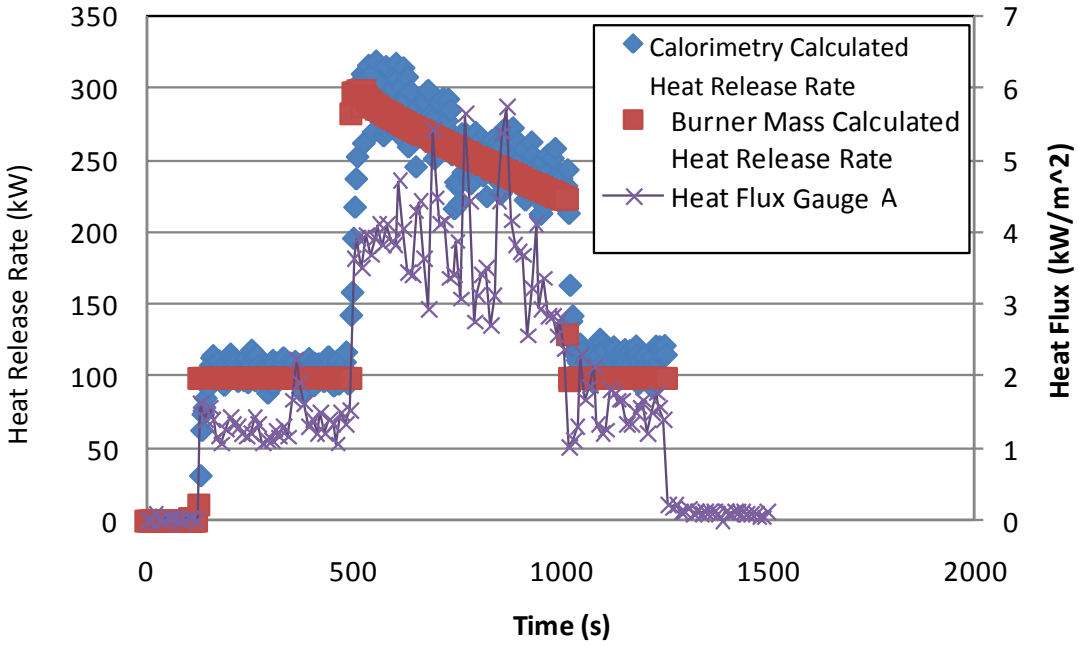

Figure 26: HRR, as calculated by oxygen calorimetry and by the fuel mass flow rate of the burner, and incident radiant heat flux estimated from Gardon gauge A measurements.

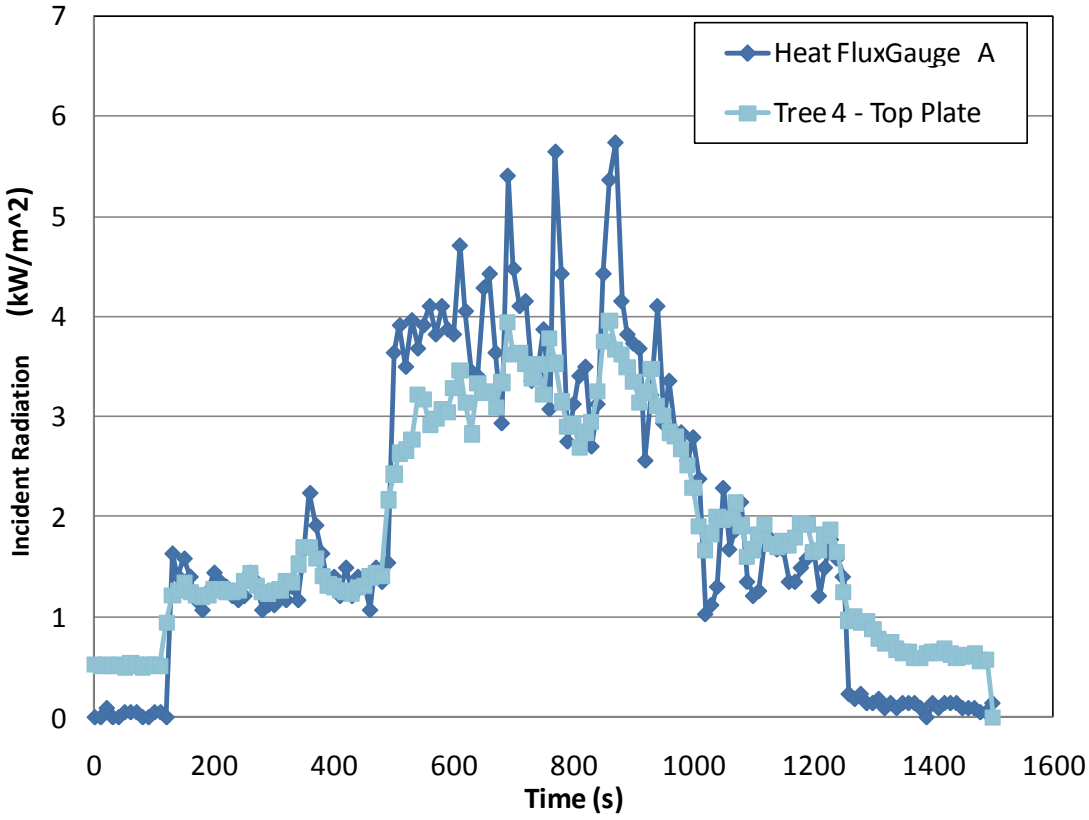

(a)

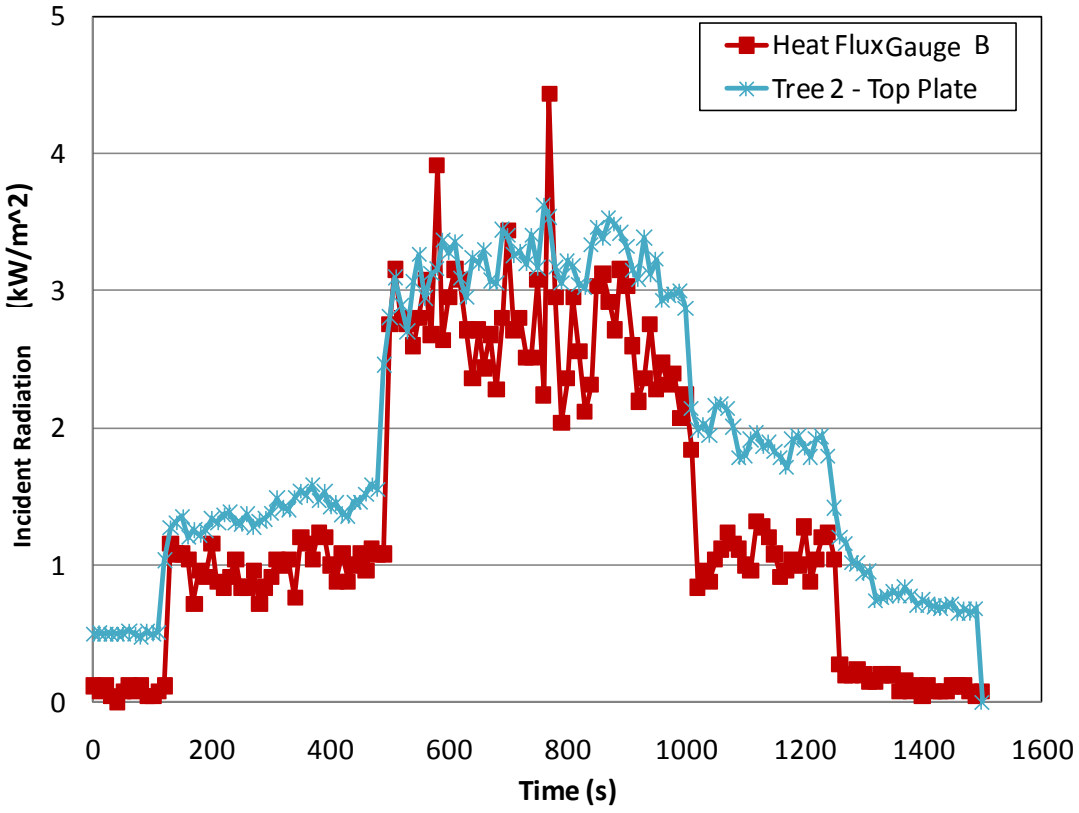

(b)

Figure 27: Estimates of the incident radiative heat flux at the (a) top plate location of tree 4 and (b) top plate location of tree 2 from plate thermometer and Gardon gauge measurements.

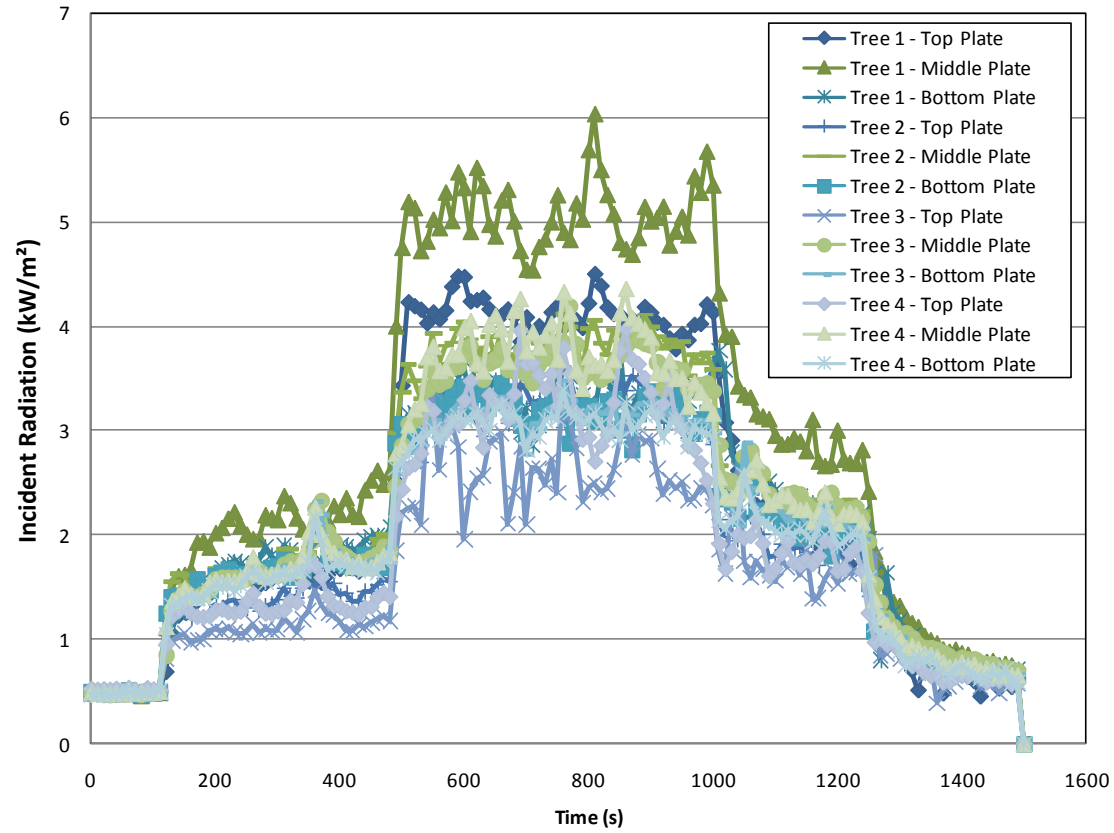

Figure 28: Estimates of the incident radiative heat flux from the plate thermometer measurements at each location on each tree.

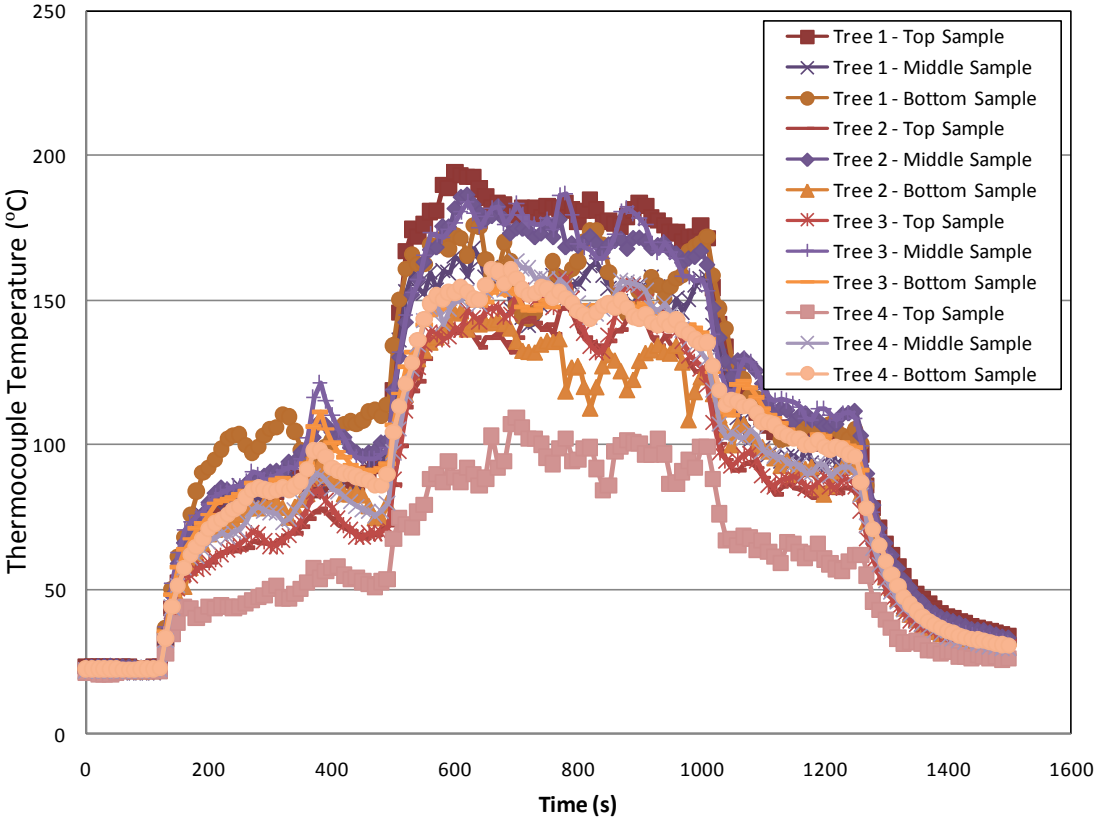

Figure 29: Thermocouple measurements at each sample location on each tree.

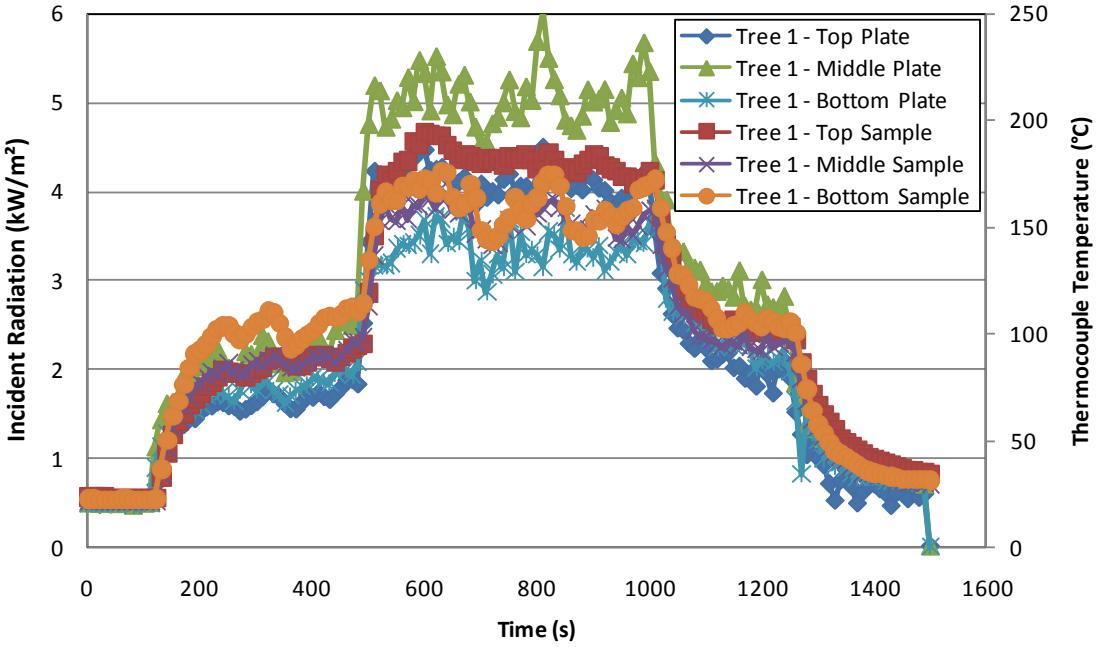
Tree 1 - Top Plate
Tree 1 - Middle Plate
Tree 1 - Bottom Plate
Tree 1 - Top Sample
Tree 1 - Middle Sample
Tree 1 - Bottom Sample
Incident Radiation (kW/m²)
Thermocouple Temperature (°C)
Time (s)
0
1
2
3
4
5
6
0
50
100
150
200
250
0
200
400
600
800
1000
1200
1400
1600

(a)

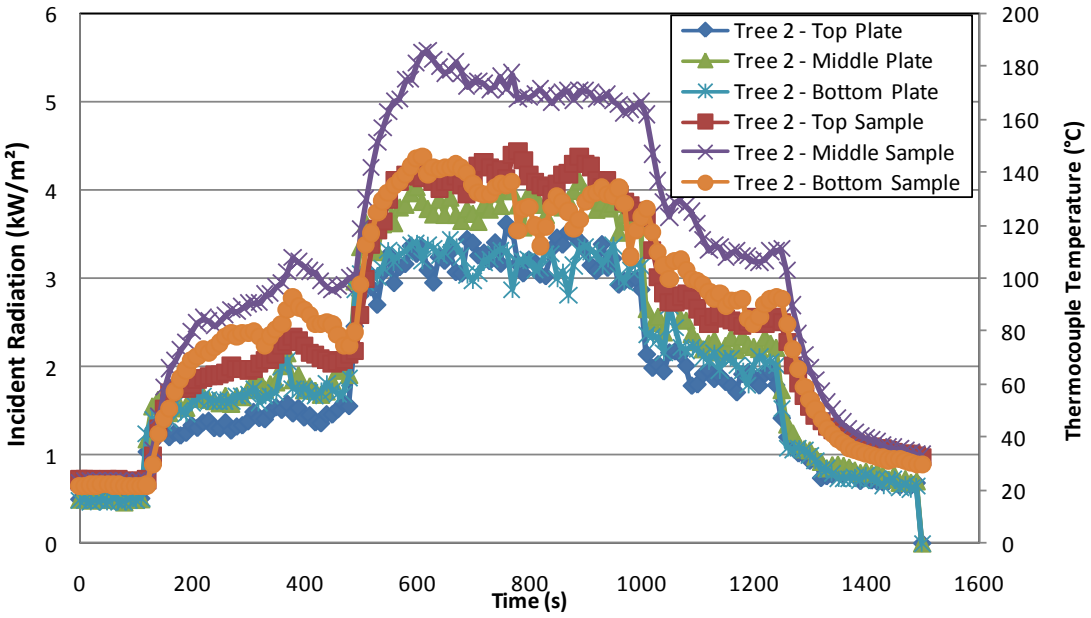
Tree 2 - Top Plate
Tree 2 - Middle Plate
Tree 2 - Bottom Plate
Tree 2 - Top Sample
Tree 2 - Middle Sample
Tree 2 - Bottom Sample
Incident Radiation (kW/m²)
Thermocouple Temperature (°C)
Time (s)
0
1
2
3
4
5
6
0
20
40
60
80
100
120
140
160
180
200
0
200
400
600
800
1000
1200
1400
1600

(b)

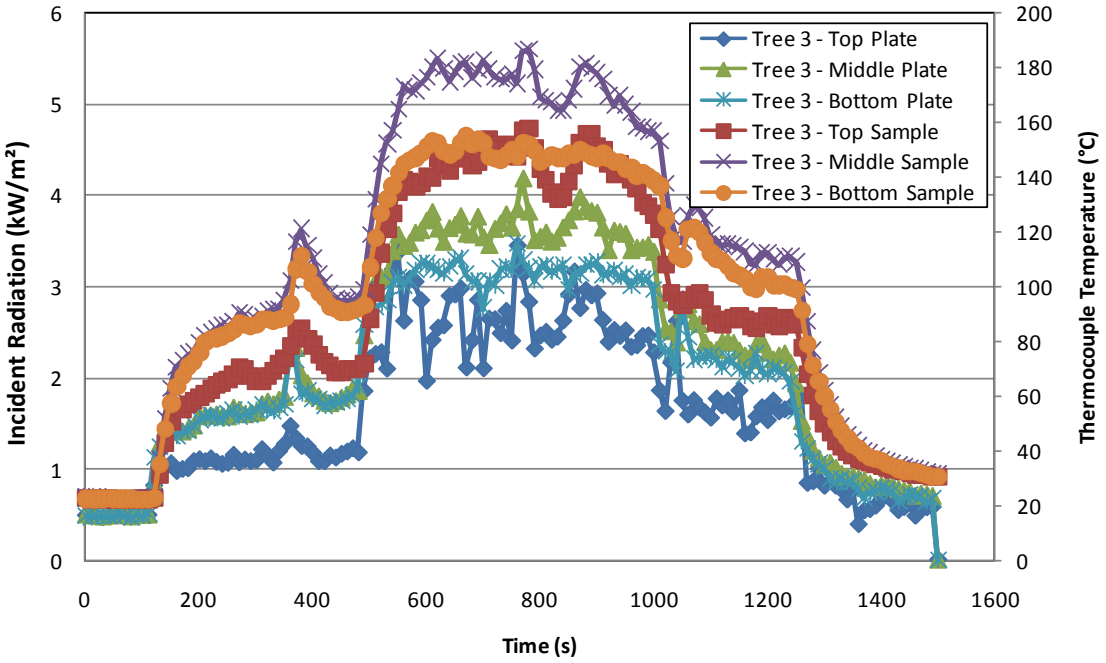

(c)

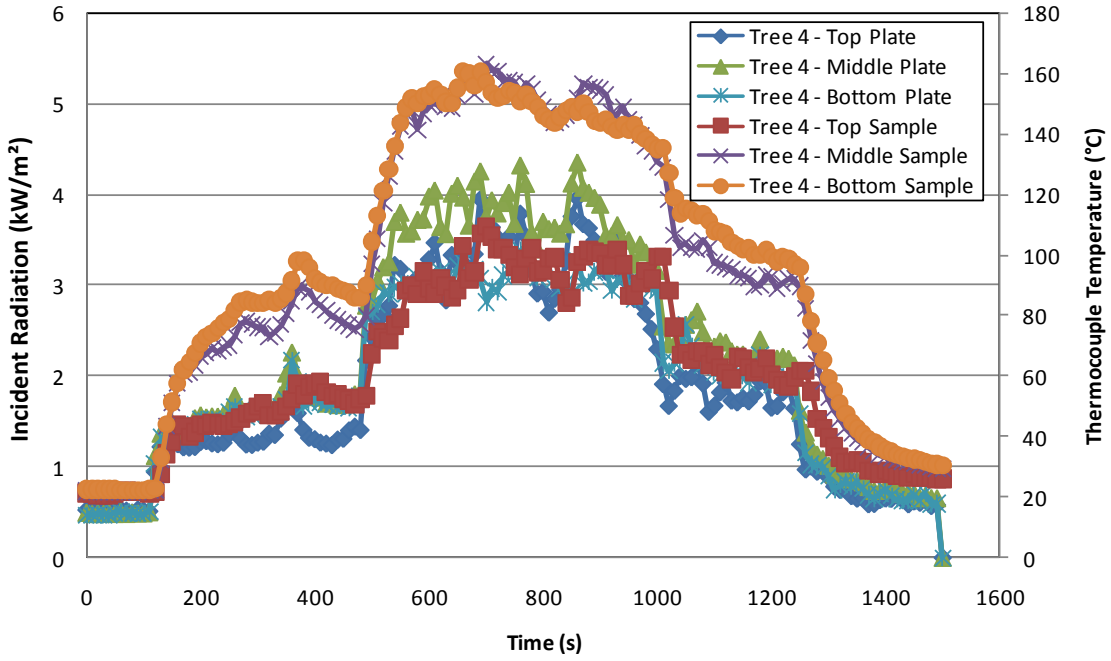

(d)

Figure 30: Thermocouple measurements and estimates of the incident radiation calculated from plate thermometer measurements for each location on each equipment tree: (a) tree 1, (b) tree 2, (c) tree 3 and (d) tree 4.

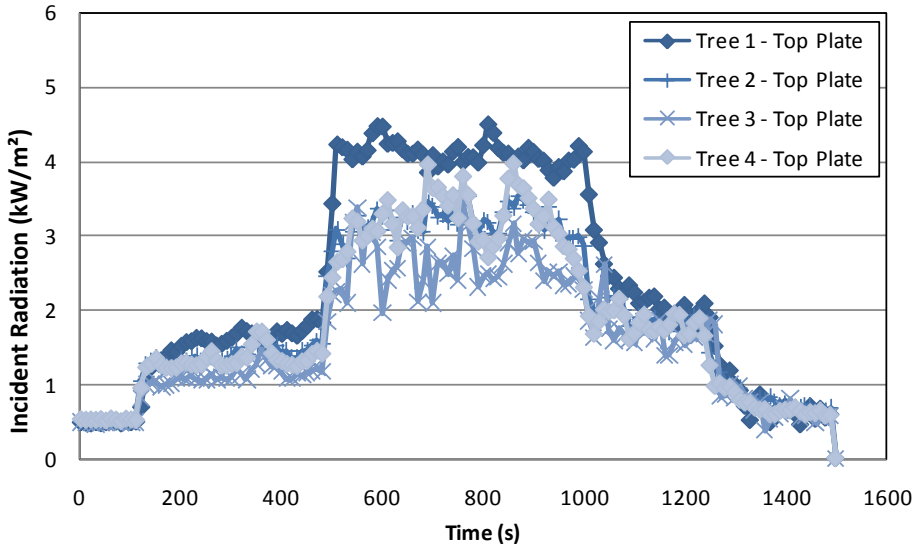

(a)

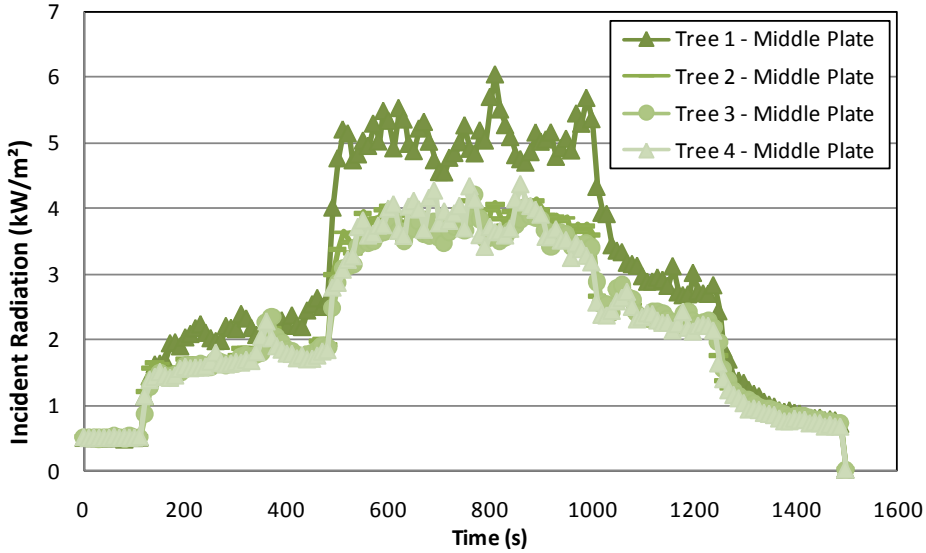

(b)

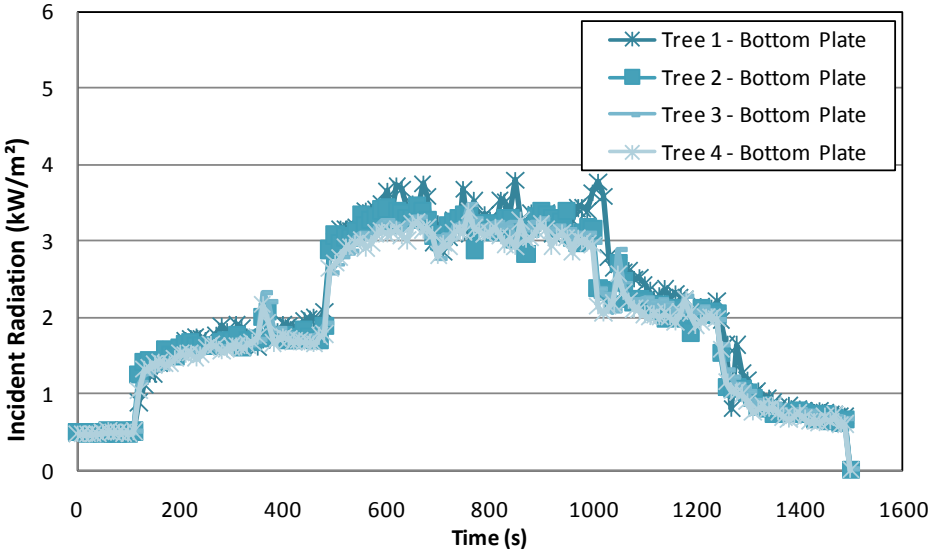

(c)

Figure 31: Estimates of the incident radiation flux calculated from plate thermometer measurements for the (a) top, (b) middle and (c) bottom locations of each of the equipment trees.

6.4 Furniture calorimeter experiments with mattress

An example of the results of the tests using the furniture calorimeter and a flaming mattress, as discussed in Section 5.2.4, is presented in this section. Detailed results are presented in Appendix A.

6.4.1 Test 1

This furniture calorimeter example had all four equipment trees location at a distance of 1.0 m from the centre of the folded mattress. Equipment tree 1 as located to be back of the folded mattress, equipment tree 3 was located in front of the mattress and equipment trees 2 and 4 were located to the left and right of the mattress respectively. No Gardon gauges were used during this set of tests.

The HRR, as calculated by oxygen calorimetry and estimated from the fuel mass loss (measured using a load cell), is compared to the incident radiant heat flux calculated from Gardon gauge A measurements in Figure 32Figure 20.

For all the plate thermometer measurements at each location on each equipment tree, the estimates of the incident radiative heat flux are shown in Figure 33 and the temperatures over each of the adjacent sample materials are shown in Figure 34. For clarity these results are shown for each of the equipment trees in Figure 35. The estimated incident radiative heat fluxes at each of the heights above the floor are shown in Figure 36.

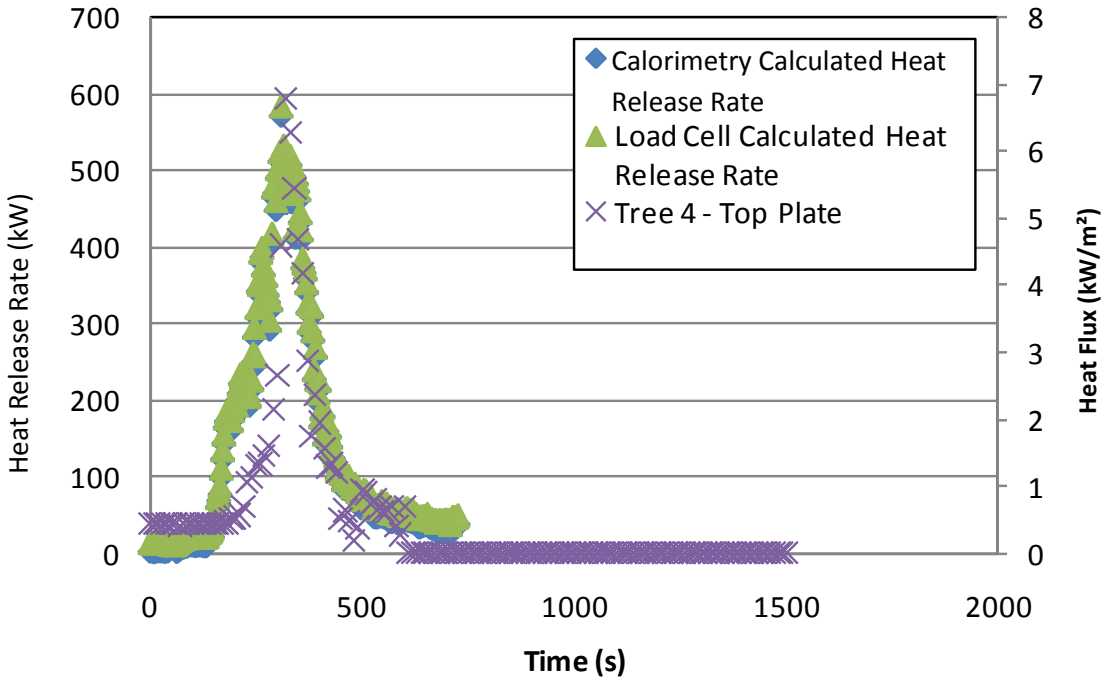

Figure 32: HRR, as calculated by oxygen calorimetry and by the fuel mass rate of the mattress on a load cell, and incident radiant heat flux estimated from the plate thermometer at the top of tree 4.

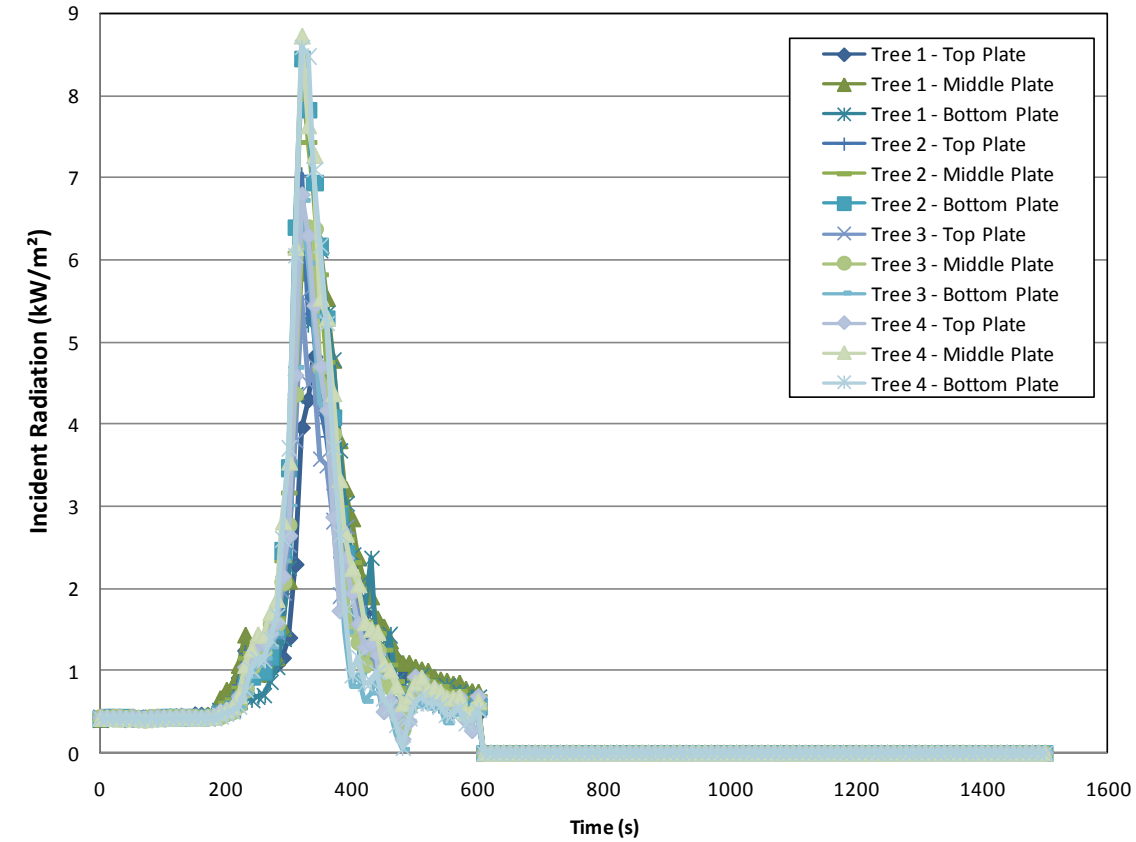

Figure 33: Estimates of the incident radiative heat flux from the plate thermometer measurements at each location on each tree.

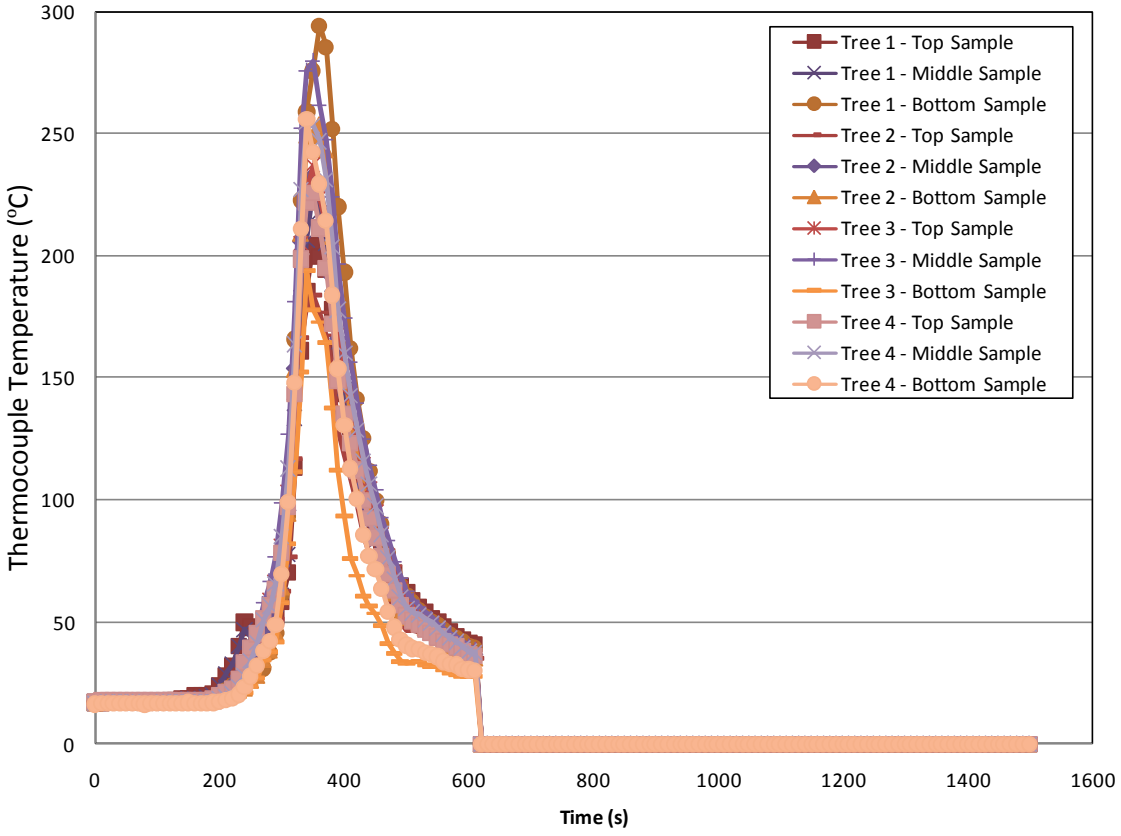

Figure 34: Thermocouple measurements at each sample location on each tree.

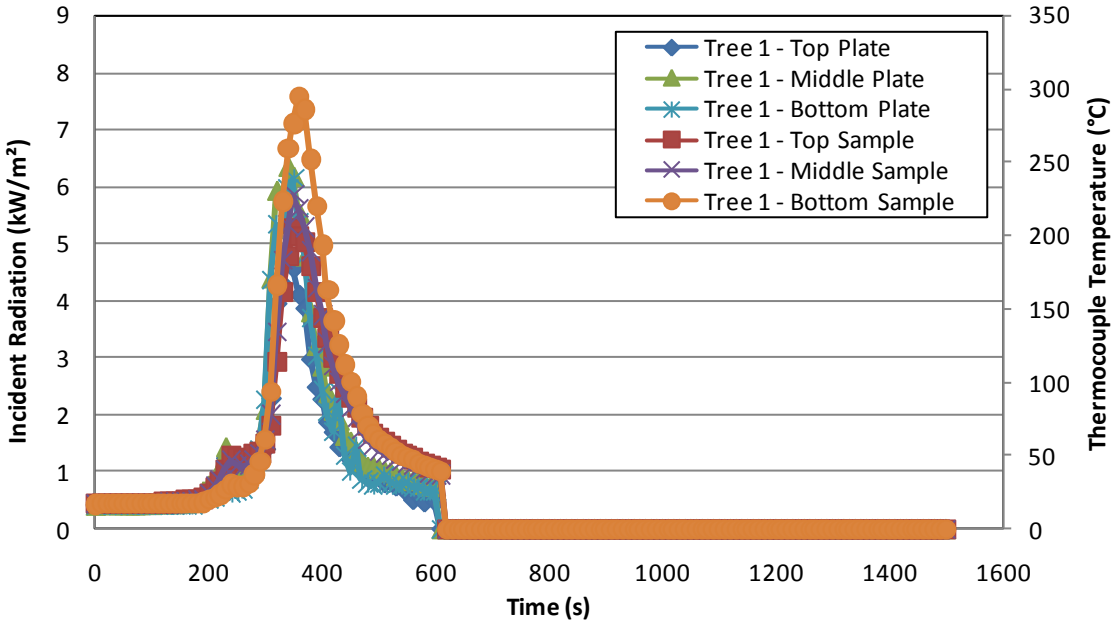
Tree 1 - Top Plate
Tree 1 - Middle Plate
Tree 1 - Bottom Plate
Tree 1 - Top Sample
Tree 1 - Middle Sample
Tree 1 - Bottom Sample
Incident Radiation (kW/m²)
Thermocouple Temperature (°C)
Time (s)
0
1
2
3
4
5
6
7
8
9
0
50
100
150
200
250
300
350
0
200
400
600
800
1000
1200
1400
1600

(a)

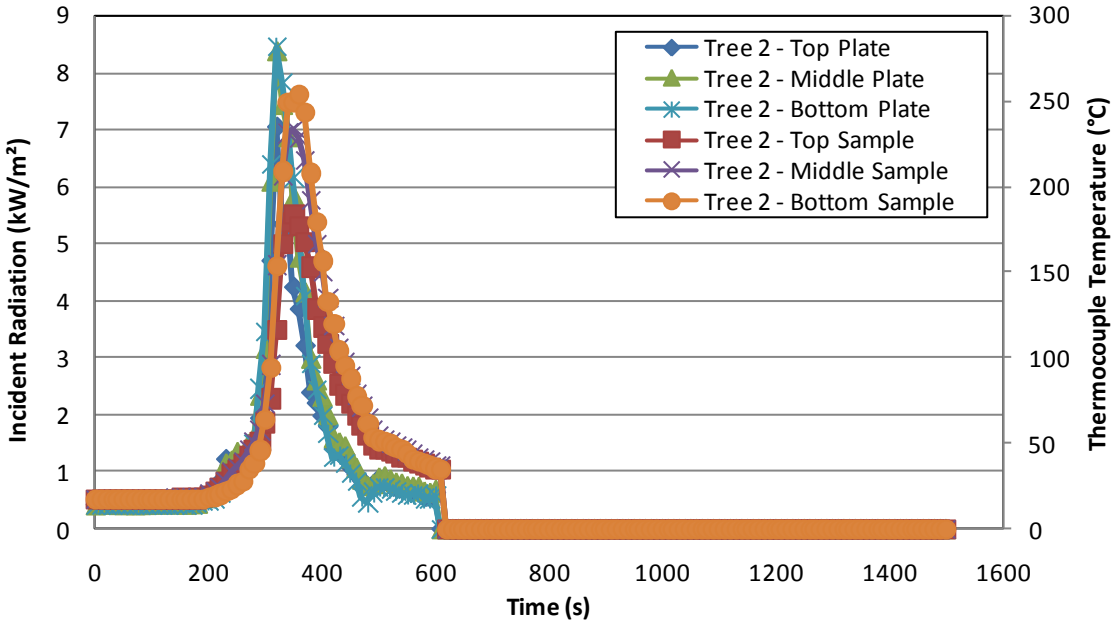
Tree 2 - Top Plate
Tree 2 - Middle Plate
Tree 2 - Bottom Plate
Tree 2 - Top Sample
Tree 2 - Middle Sample
Tree 2 - Bottom Sample
Incident Radiation (kW/m²)
Thermocouple Temperature (°C)
Time (s)
0
1
2
3
4
5
6
7
8
9
0
50
100
150
200
250
300
0
200
400
600
800
1000
1200
1400
1600

(b)

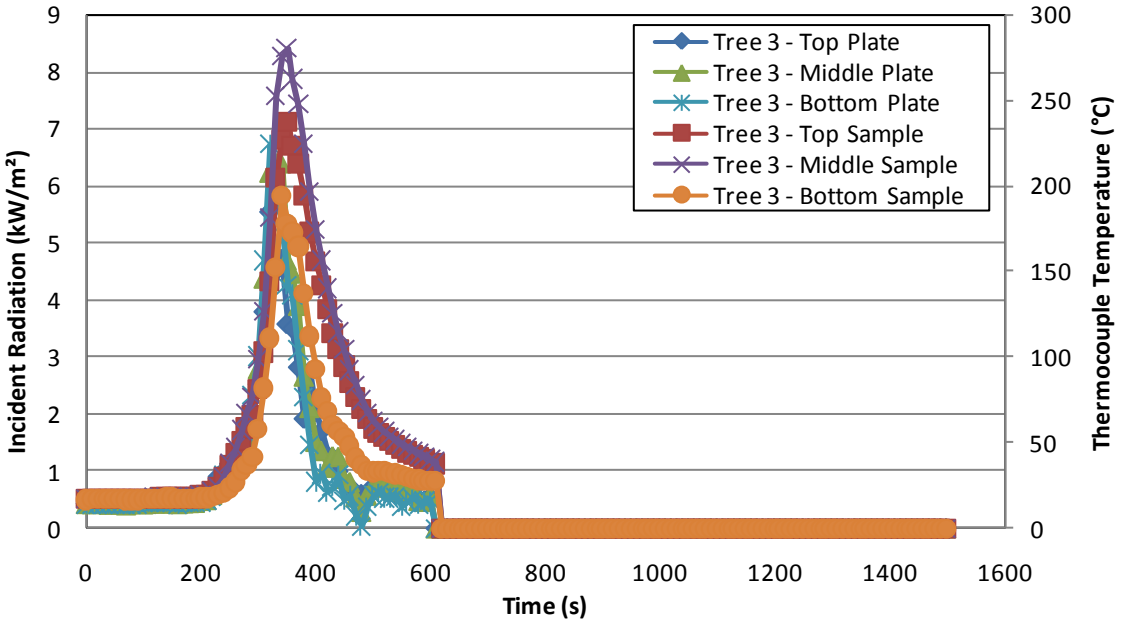

(c)

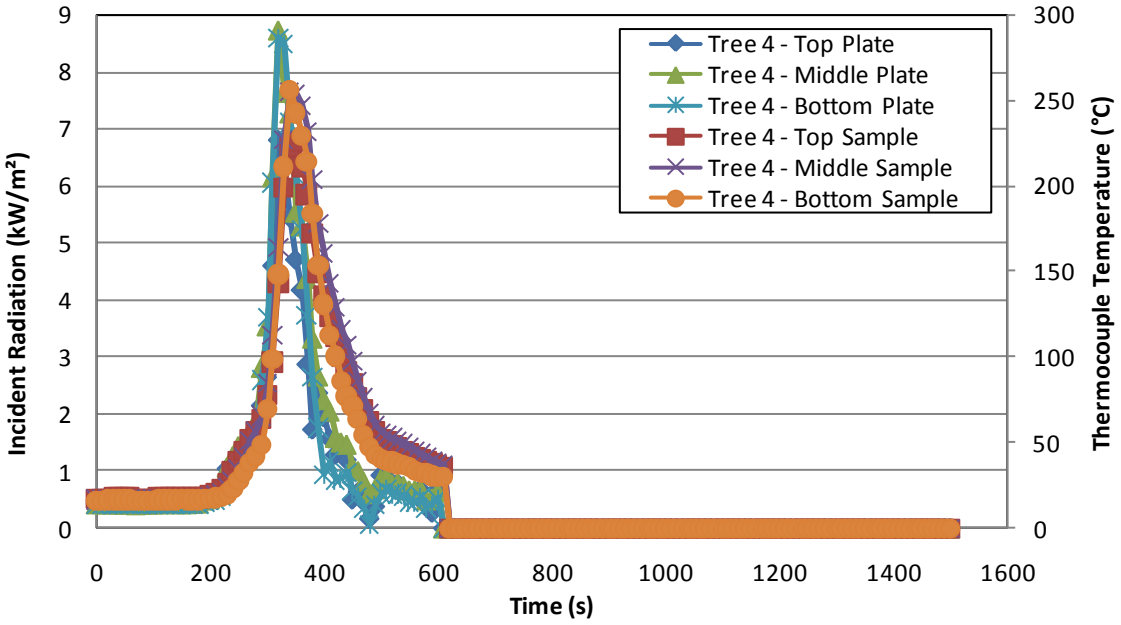

(d)

Figure 35: Thermocouple measurements and estimates of the incident radiation calculated from plate thermometer measurements for each location on each equipment tree: (a) tree 1, (b) tree 2, (c) tree 3 and (d) tree 4.

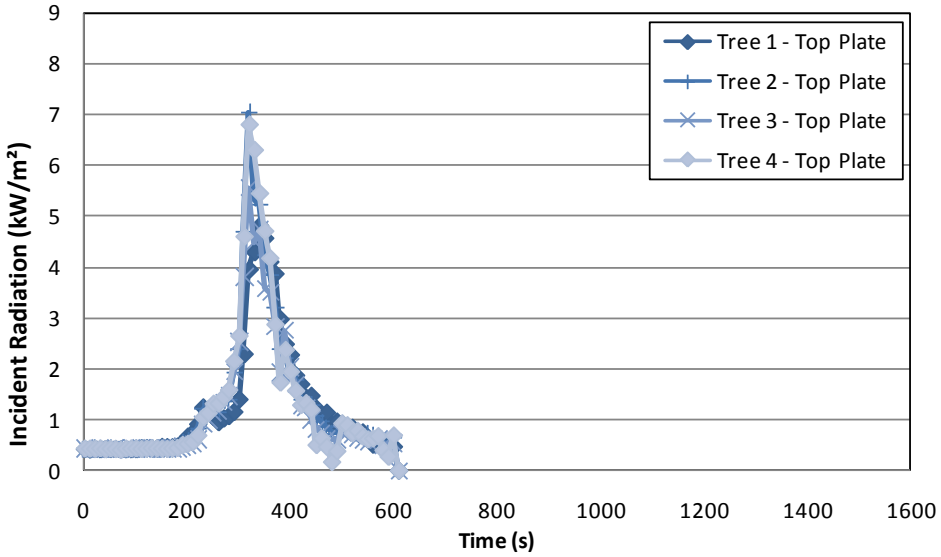

(a)

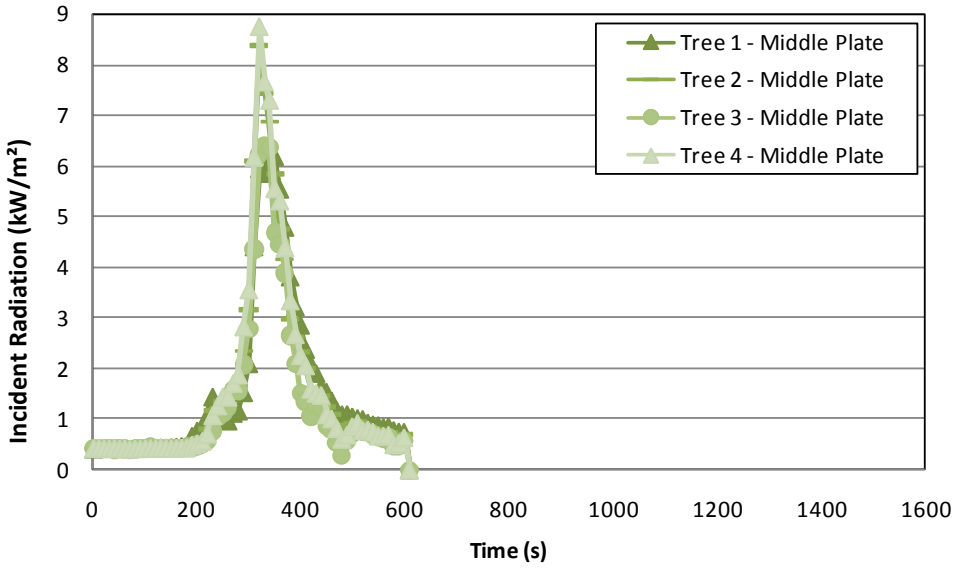

(b)

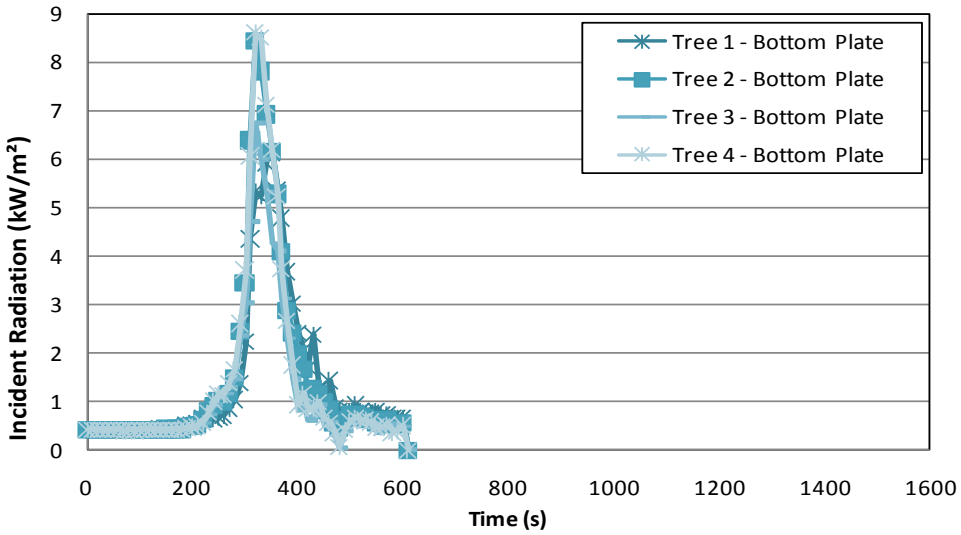

(c)

Figure 36: Estimates of the incident radiation flux calculated from plate thermometer measurements for the (a) top, (b) middle and (c) bottom locations of each of the equipment trees.

6.5 ISO room experiments with burner only

Examples of the results of the tests using the ISO room and a gas burner in the corner, as discussed in Section 5.2.5, are presented in this section. Detailed results are presented in Appendix A.

6.5.1 Test 1

This ISO room test with burner example had the equipment trees in the Orientation A set-up (Figure 10(a)).

The HRR, as calculated by oxygen calorimetry and by the fuel mass flow rate of the burner, is compared to the incident radiant heat flux calculated from Gardon gauge A measurements in Figure 37. From the temperature measurements in the corner of the ISO room (Figure 39), the layer height and average upper and lower layer temperatures were estimated, as shown in Figure 38. Temperatures just below the ceiling were also measured (Figure 40).

Where plate thermometers were in adjacent locations to the two Gardon gauges, estimates of the incident radiative heat flux from plate thermometer measurements were compared to the Gardon gauge measurements, as shown in Figure 41. In this case the top plate locations of equipment tree 4 and 2 were directly below the locations of the Gardon gauges.

For all the plate thermometer measurements at each location on each equipment tree, the estimates of the incident radiative heat flux are shown in Figure 42 and the temperatures over each of the adjacent sample materials are shown in Figure 43. For clarity these results are shown for each of the equipment trees in Figure 44. The estimated incident radiative heat fluxes at each of the heights above the floor of the ISO room are shown in Figure 45.

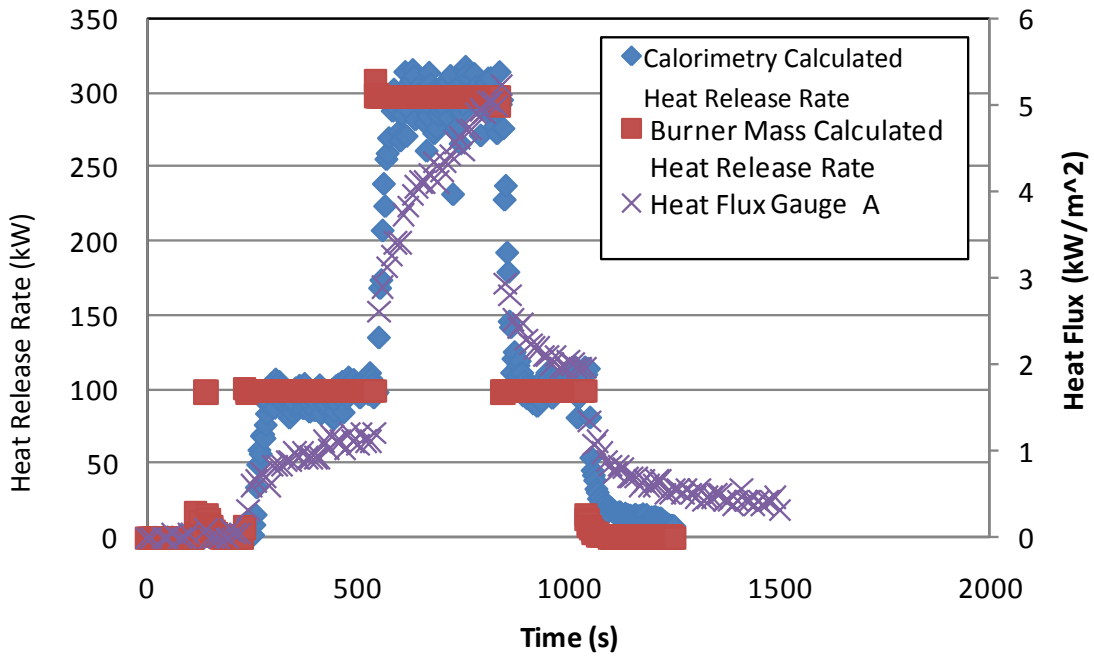

Figure 37: HRR, as calculated by oxygen calorimetry and by the fuel mass flow rate of the burner, and incident radiant heat flux estimated from Gardon gauge A measurements.

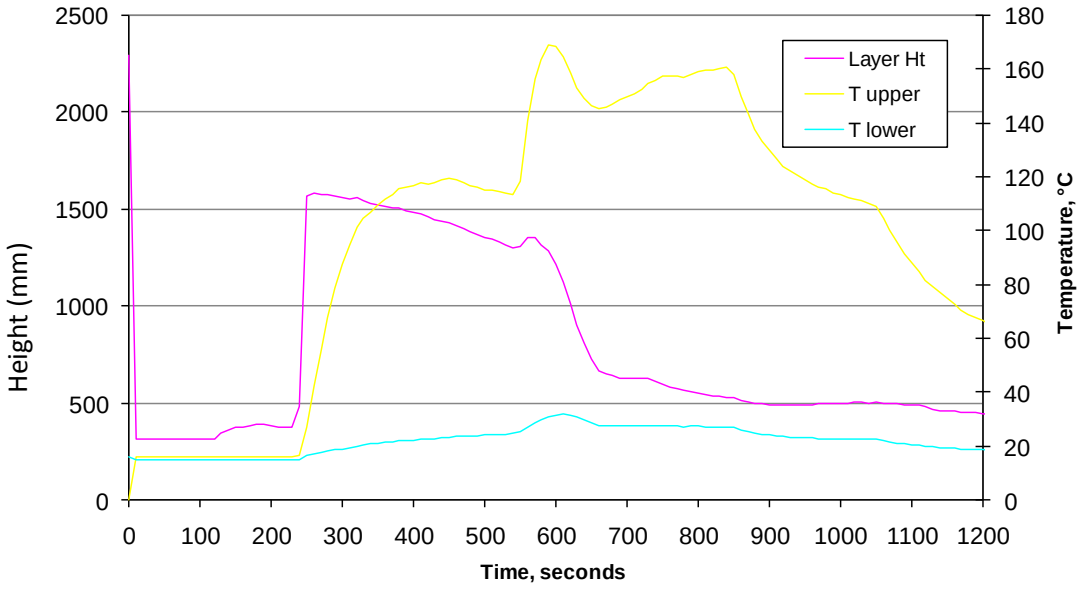

Figure 38: Estimate of the interface height and average upper and lower layer temperatures.

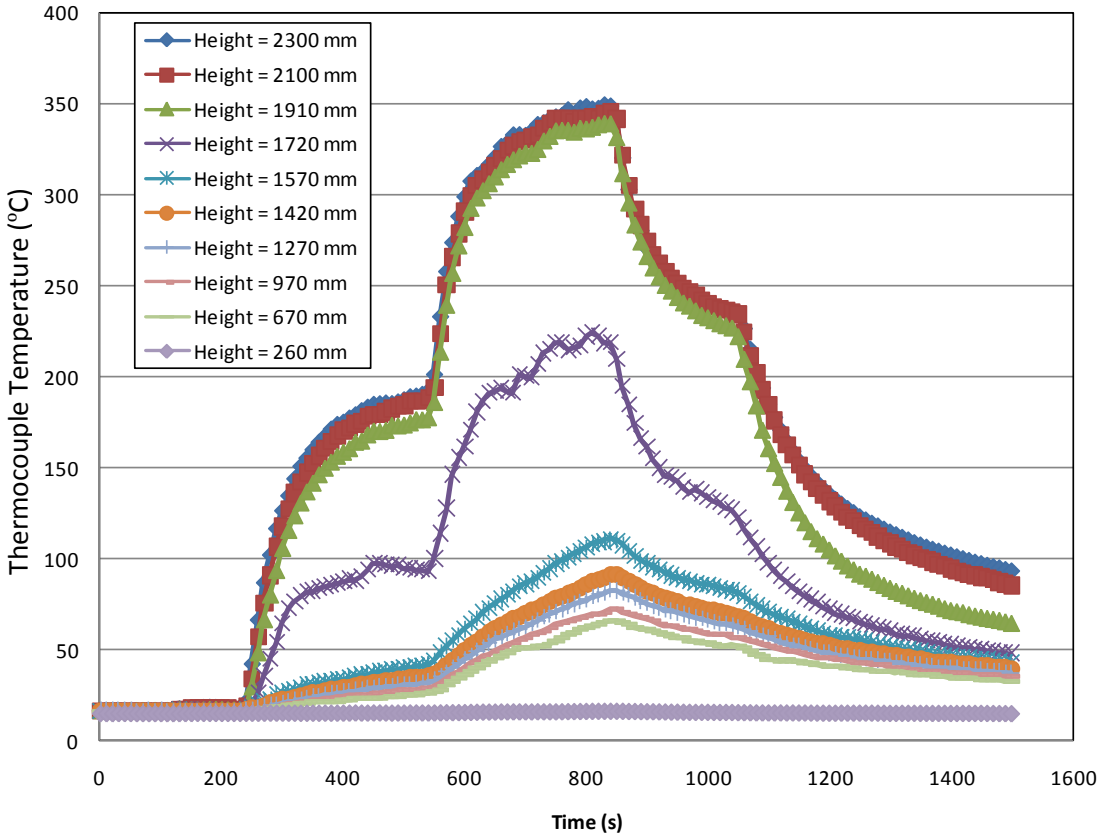

Figure 39: ISO room corner temperatures (°C) at various heights.

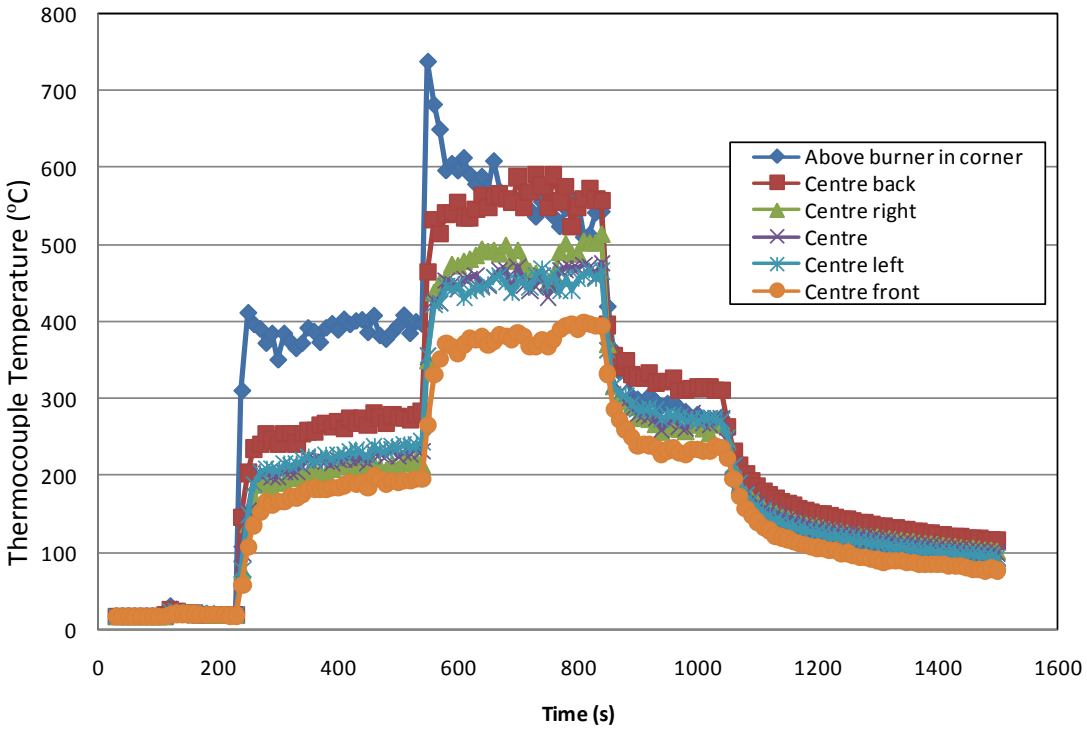

Figure 40: ISO room ceiling temperatures (°C).

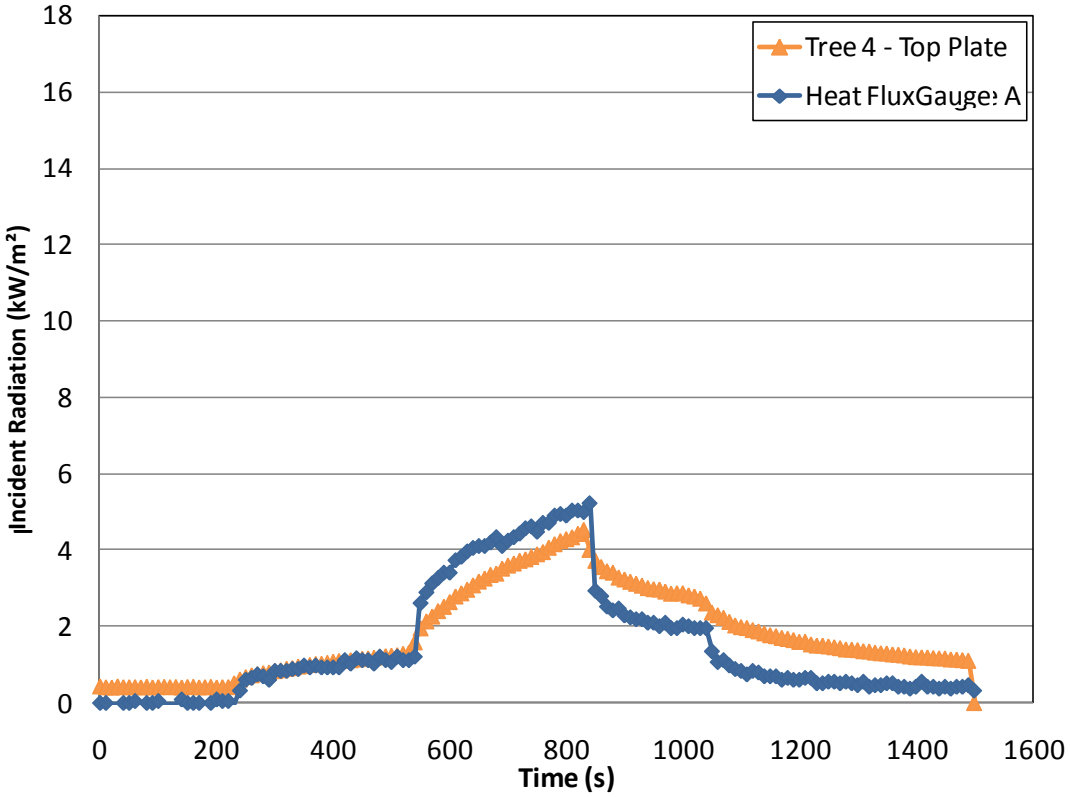

(a)

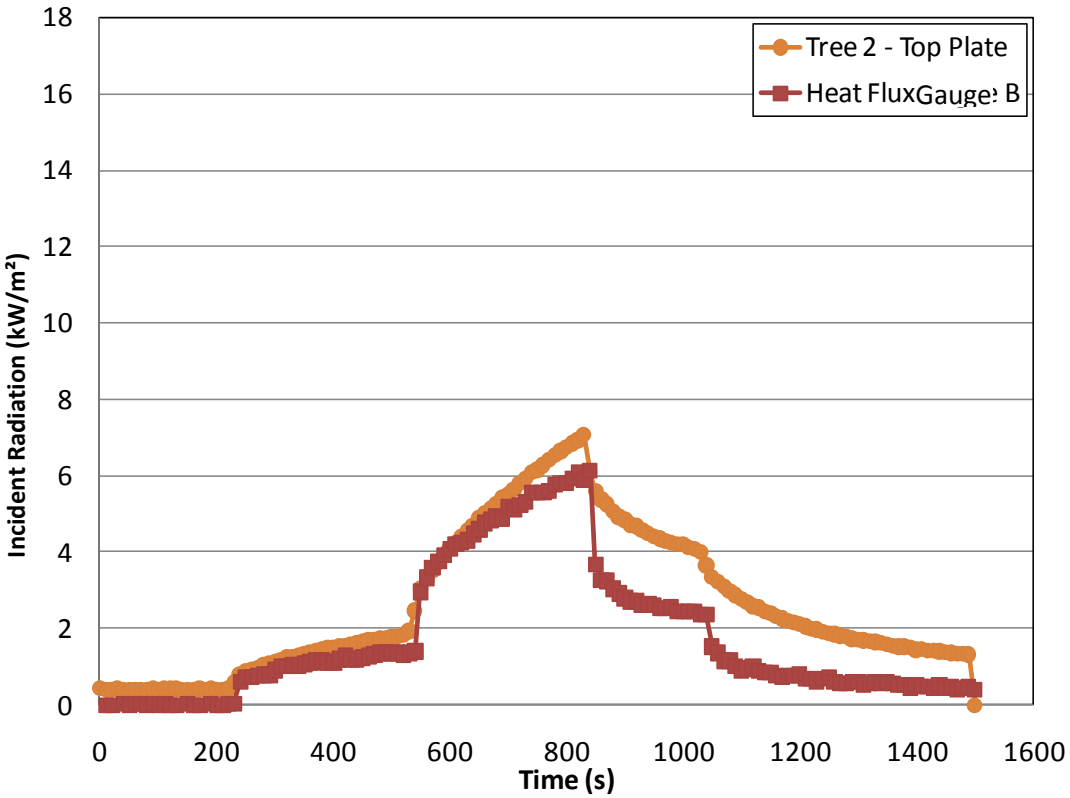

(b)

Figure 41: Estimates of the incident radiative heat flux at the (a) top plate location of tree 4 and (b) top plate location of tree 2 from plate thermometer and Gardon gauge measurements.

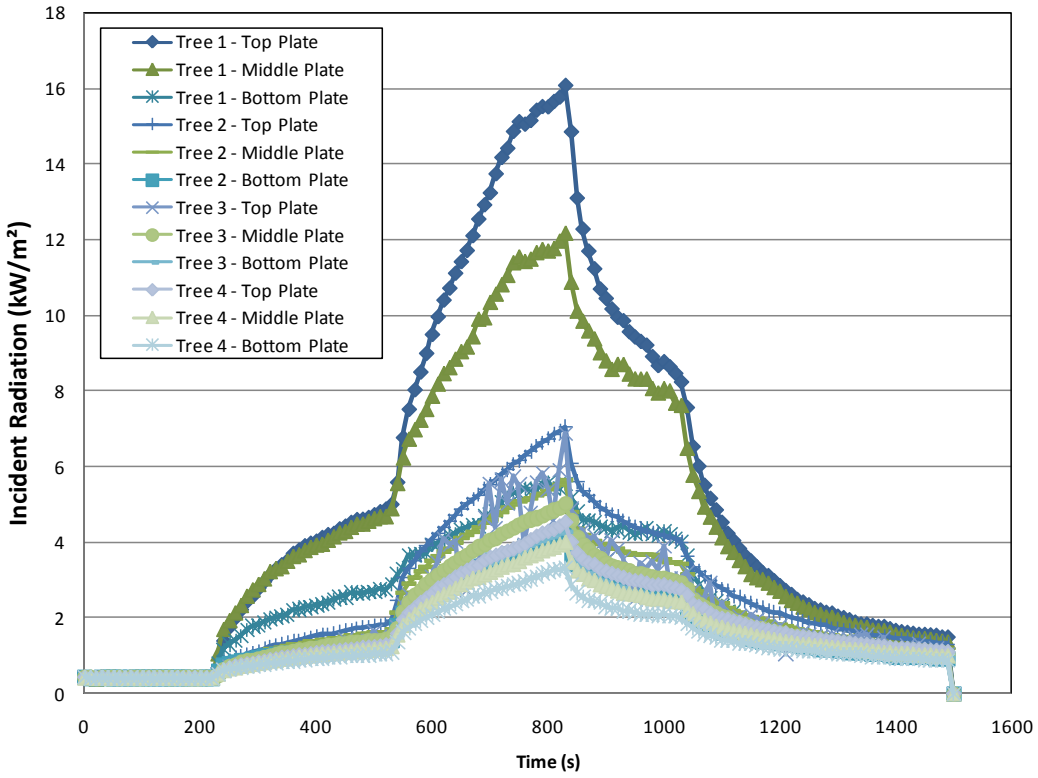

Figure 42: Estimates of the incident radiative heat flux from the plate thermometer measurements at each location on each tree.

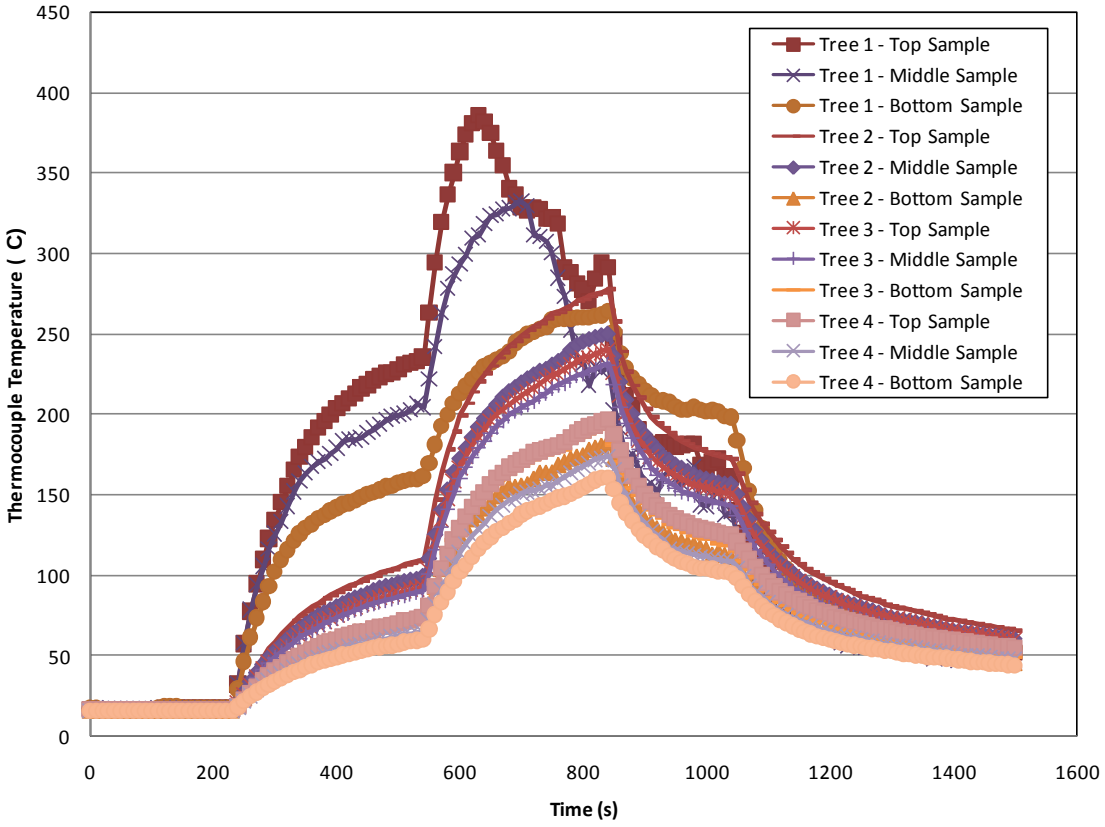

Figure 43: Thermocouple measurements at each sample location on each tree.

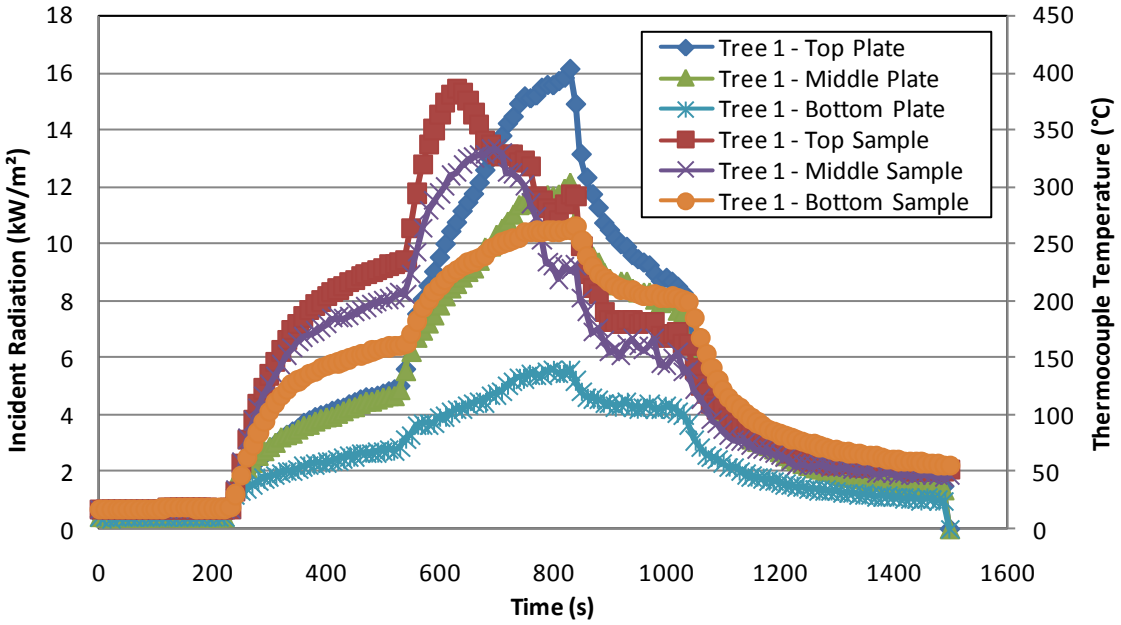
Tree 1 - Top Plate
Tree 1 - Middle Plate
Tree 1 - Bottom Plate
Tree 1 - Top Sample
Tree 1 - Middle Sample
Tree 1 - Bottom Sample
Incident Radiation (kW/m²)
Thermocouple Temperature (°C)
Time (s)
0
2
4
6
8
10
12
14
16
18
0
50
100
150
200
250
300
350
400
450
0
200
400
600
800
1000
1200
1400
1600

(a)

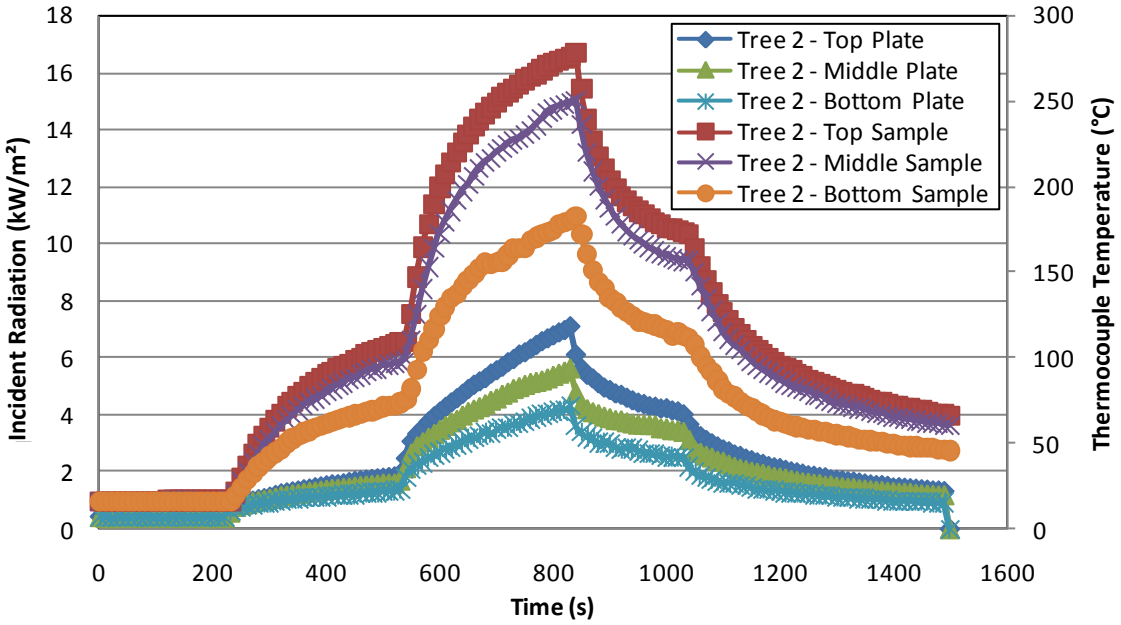
Tree 2 - Top Plate
Tree 2 - Middle Plate
Tree 2 - Bottom Plate
Tree 2 - Top Sample
Tree 2 - Middle Sample
Tree 2 - Bottom Sample
Incident Radiation (kW/m²)
Thermocouple Temperature (°C)
Time (s)
0
2
4
6
8
10
12
14
16
18
0
50
100
150
200
250
300
0
200
400
600
800
1000
1200
1400
1600

(b)

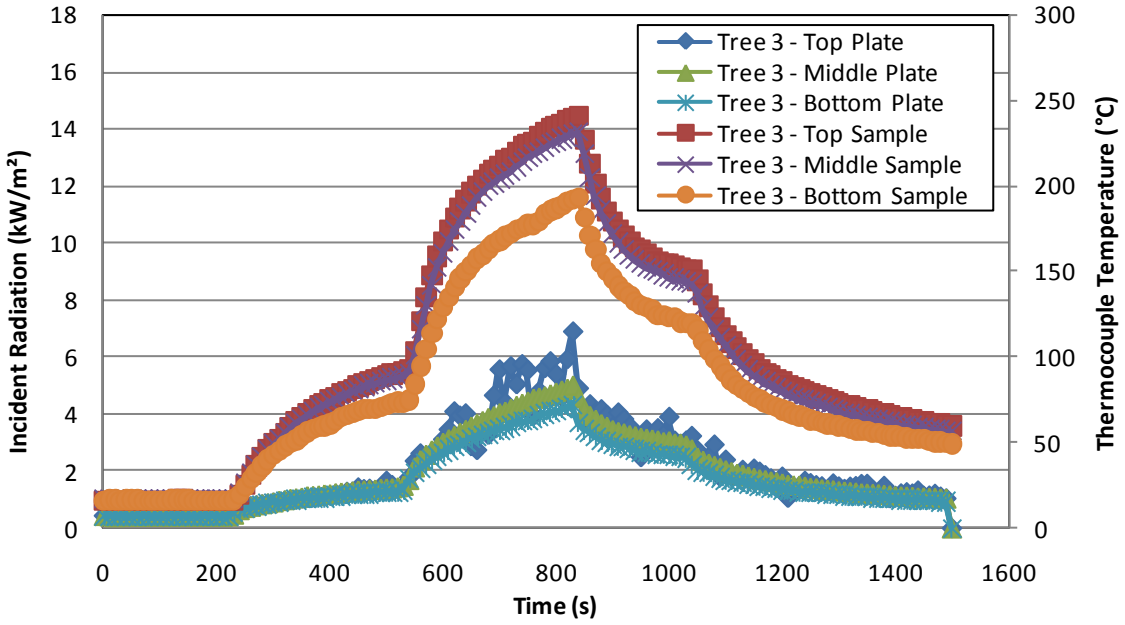

(c)

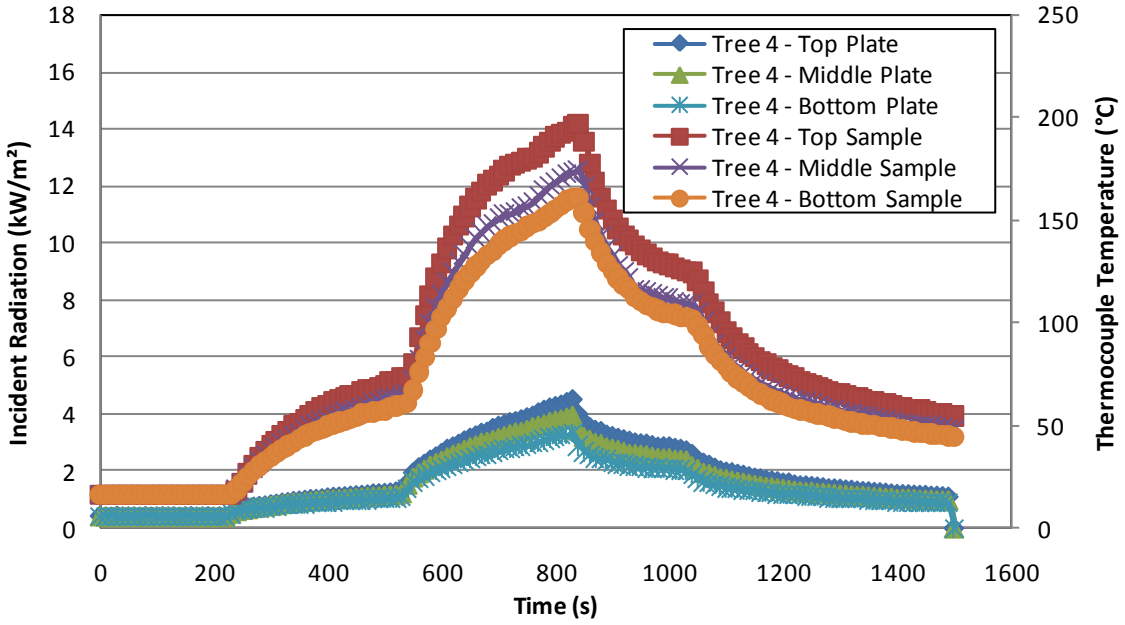

(d)

Figure 44: Thermocouple measurements and estimates of the incident radiation calculated from plate thermometer measurements for each location on each equipment tree: (a) tree 1, (b) tree 2, (c) tree 3 and (d) tree 4.

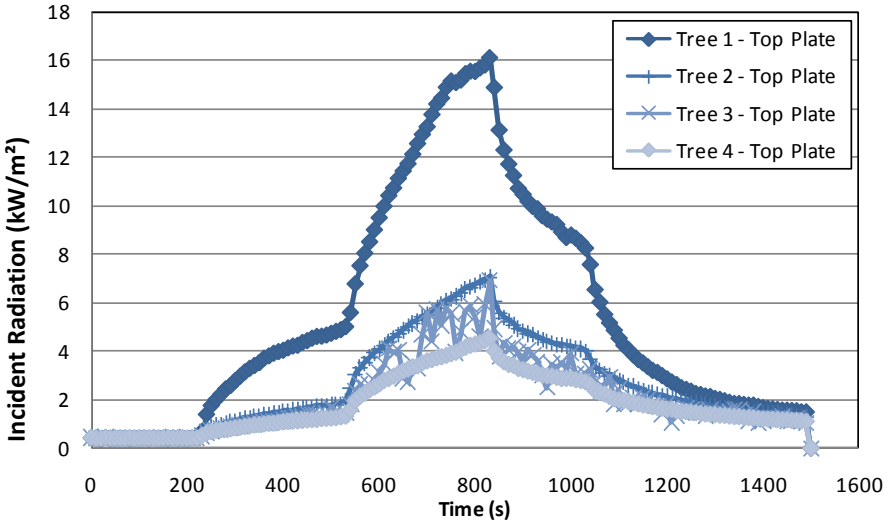

(a)

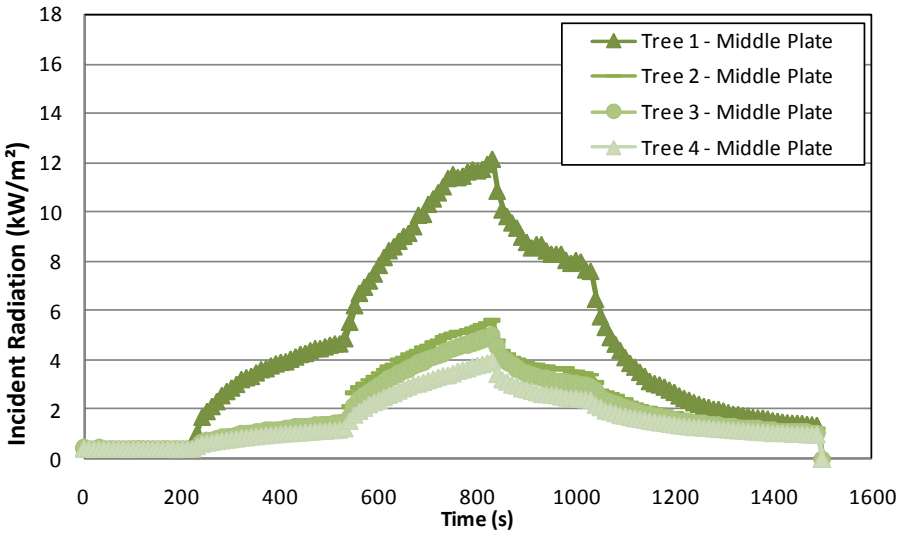

(b)

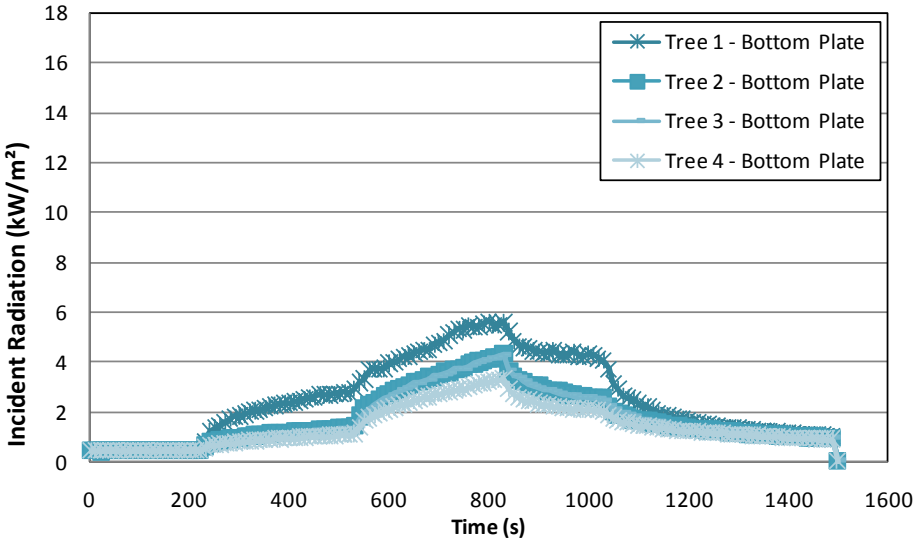

(c)

Figure 45: Estimates of the incident radiation flux calculated from plate thermometer measurements for the (a) top, (b) middle and (c) bottom locations of each of the equipment trees.

6.5.2 Test 6

This ISO room test with burner example had the equipment trees in the Orientation B set-up (Figure 10(b)).

Similarly to Test 1 in the previous section, the HRR, as calculated by oxygen calorimetry and by the fuel mass flow rate of the burner, is compared to the incident radiant heat flux calculated from Gardon gauge A measurements in Figure 46. From the temperature measurements in the corner of the ISO room (Figure 48), the layer height and average upper and lower layer temperatures were estimated, as shown in Figure 47. Temperatures just below the ceiling were also measured (Figure 49).

Where plate thermometers were in adjacent locations to the two Gardon gauges, estimates of the incident radiative heat flux from plate thermometer measurements were compared to the Gardon gauge measurements, as shown in Figure 50. In this case the top plate locations of equipment tree 4 and 2 were directly below the locations of the Gardon gauges.

For all the plate thermometer measurements at each location on each equipment tree, the estimates of the incident radiative heat flux are shown in Figure 51 and the temperatures over each of the adjacent sample materials are shown in Figure 52. For clarity these results are shown for each of the equipment trees in Figure 53. The estimated incident radiative heat fluxes at each of the heights above the floor of the ISO room are shown in Figure 54.

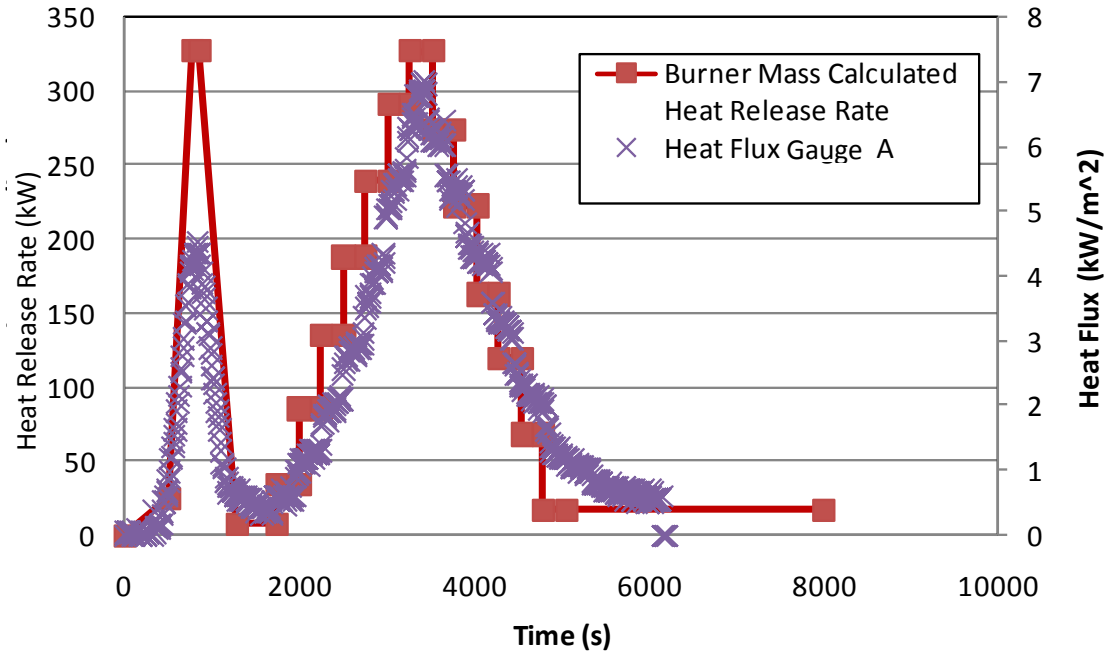

Figure 46: HRR, as estimated by the fuel mass flow rate of the burner, and incident radiant heat flux estimated from Gardon gauge A measurements.

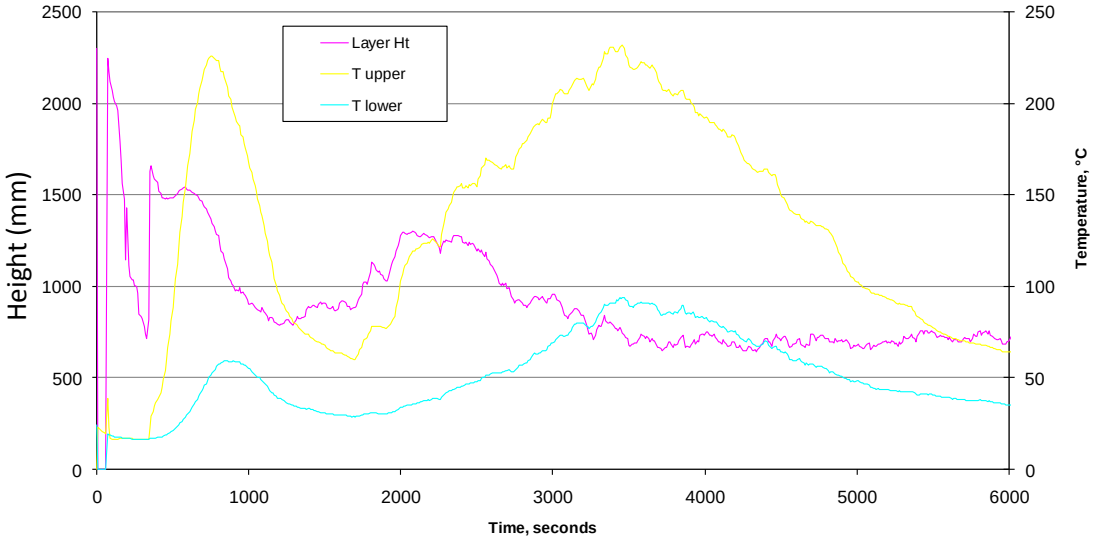

Figure 47: Estimate of the interface height and average upper and lower layer temperatures.

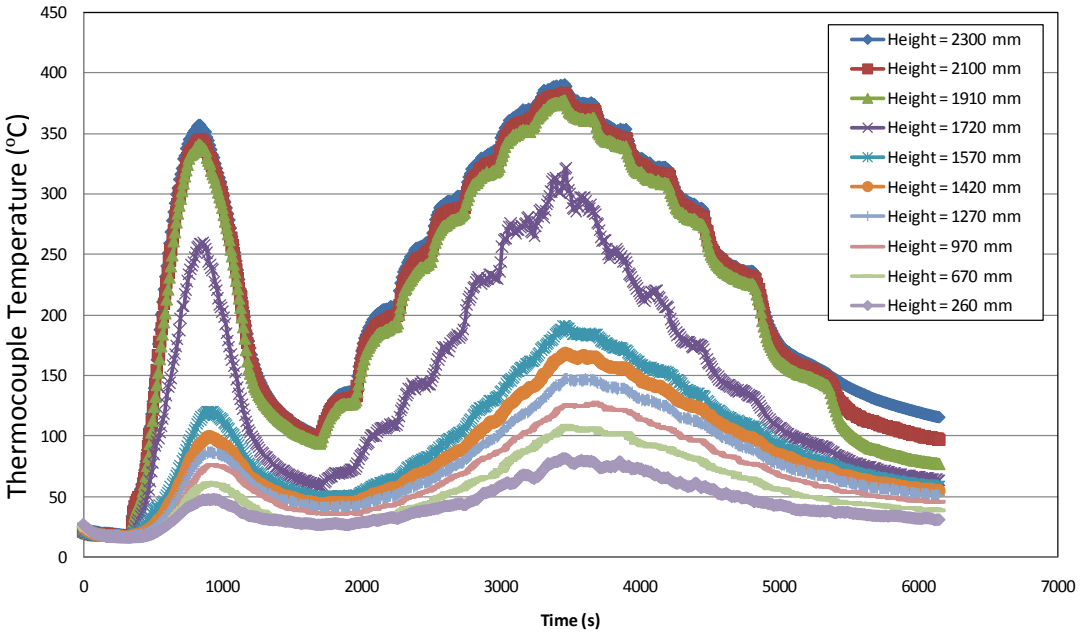

Figure 48: ISO room corner temperatures (°C) at various heights.

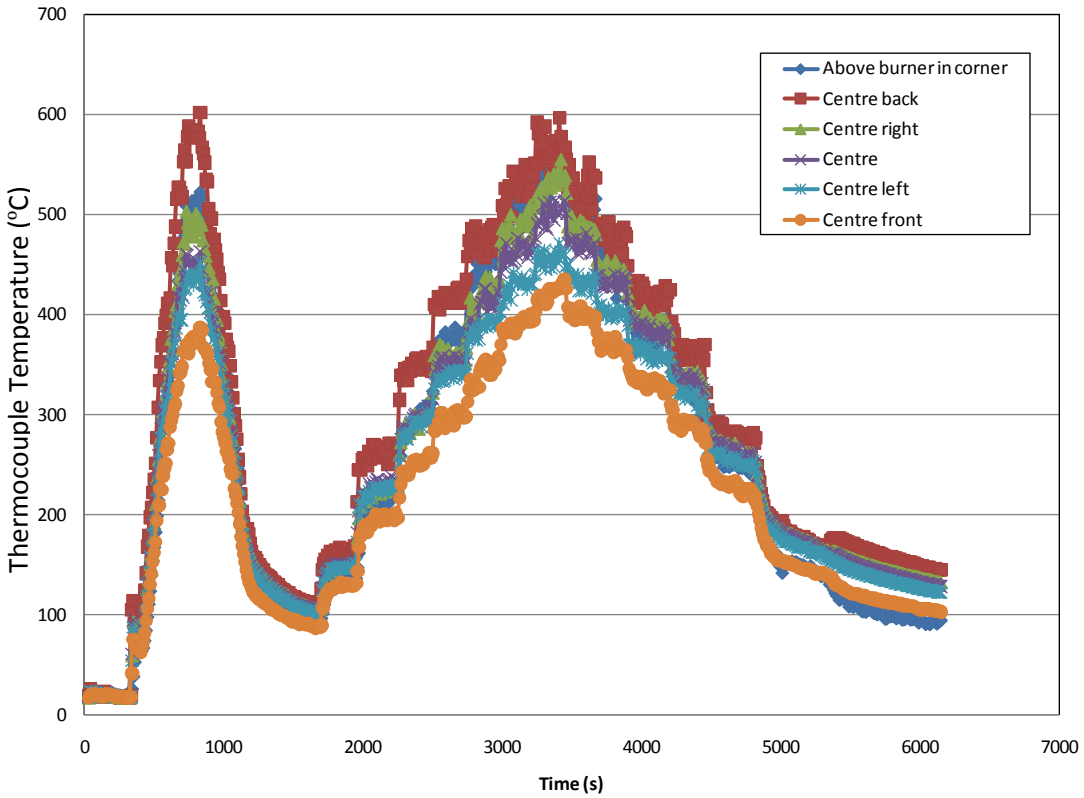

Figure 49: ISO room ceiling temperatures (°C).

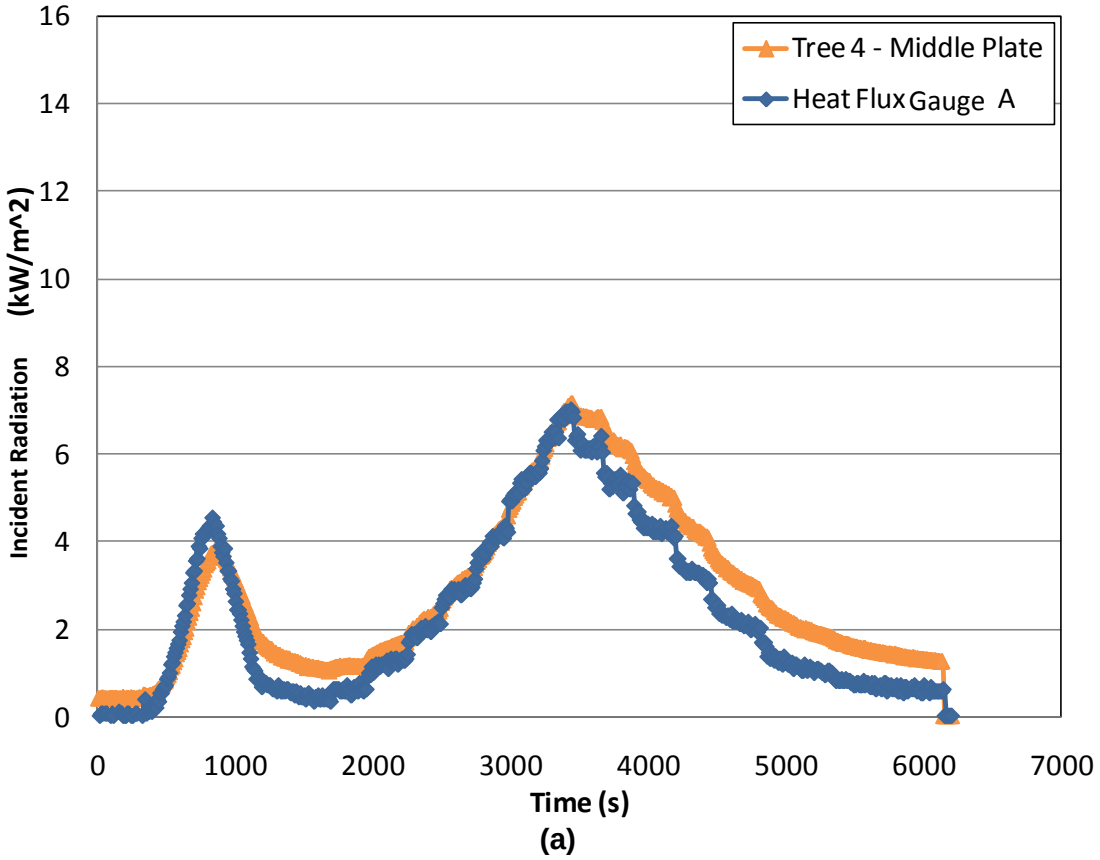

(a)

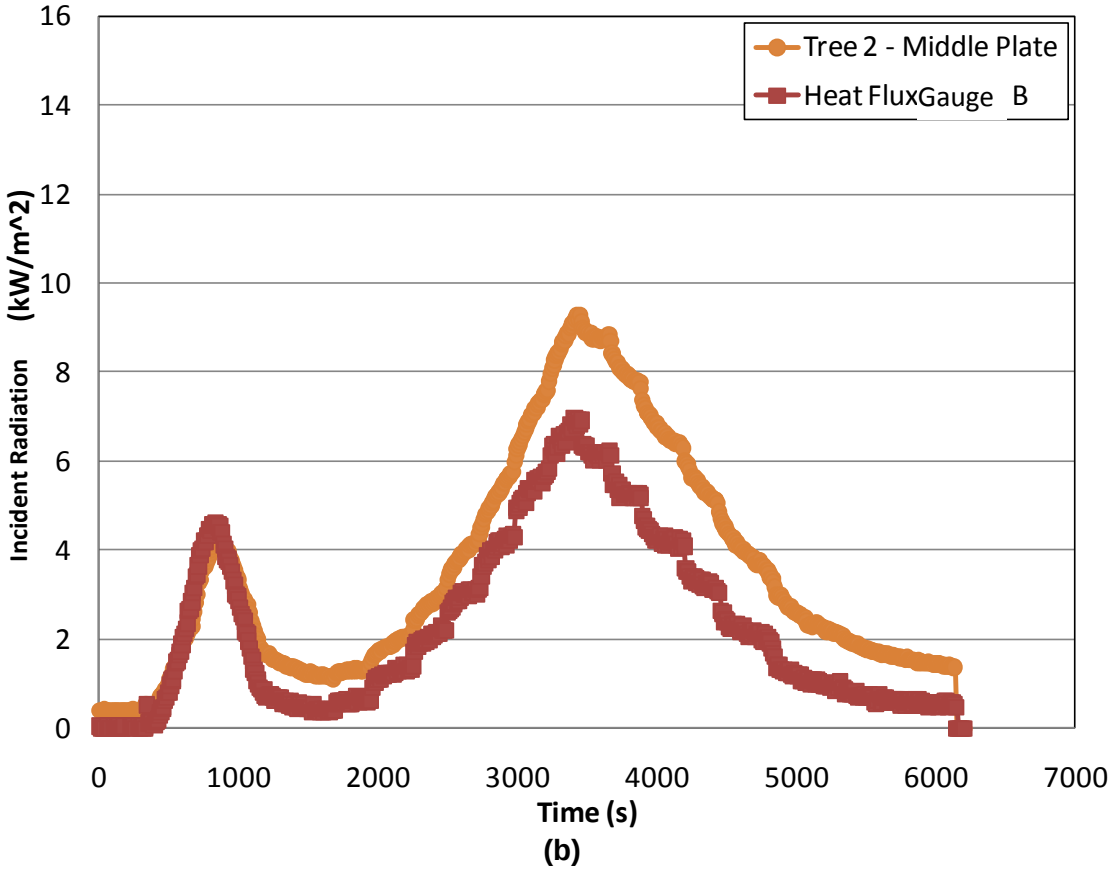

(b)

Figure 50: Estimates of the incident radiative heat flux at the (a) top plate location of tree 4 and (b) top plate location of tree 2 from plate thermometer and Gardon gauge measurements.

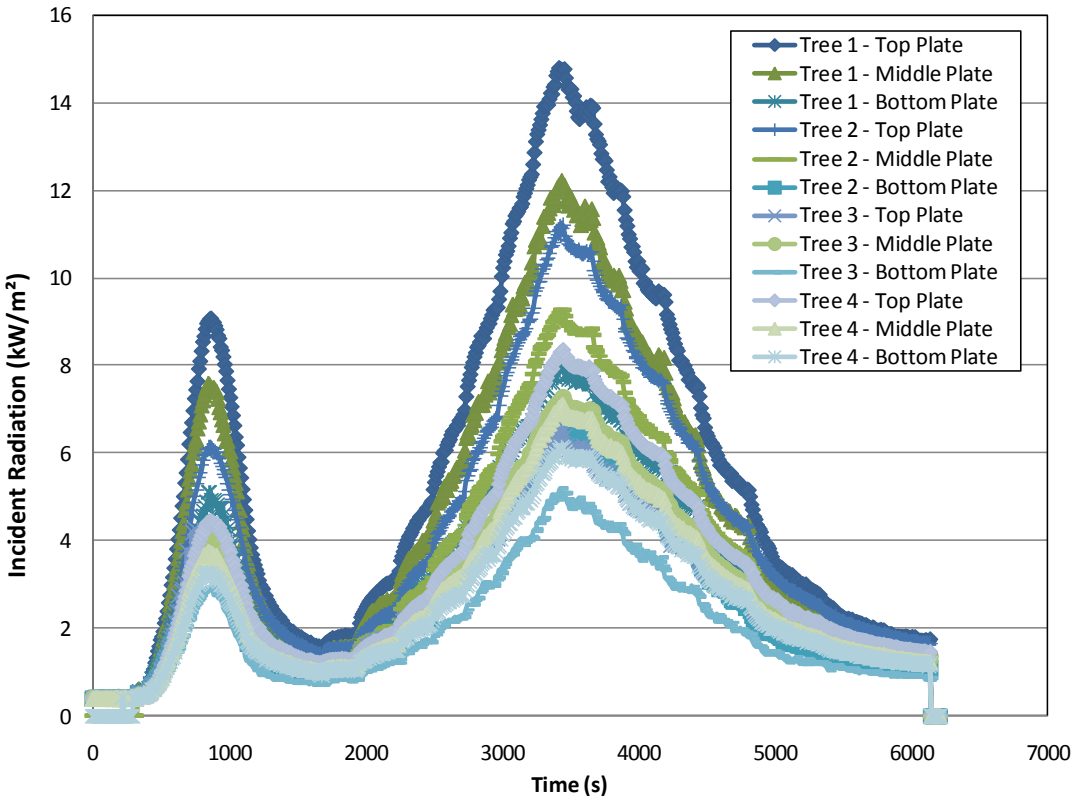

Figure 51: Estimates of the incident radiative heat flux from the plate thermometer measurements at each location on each tree.

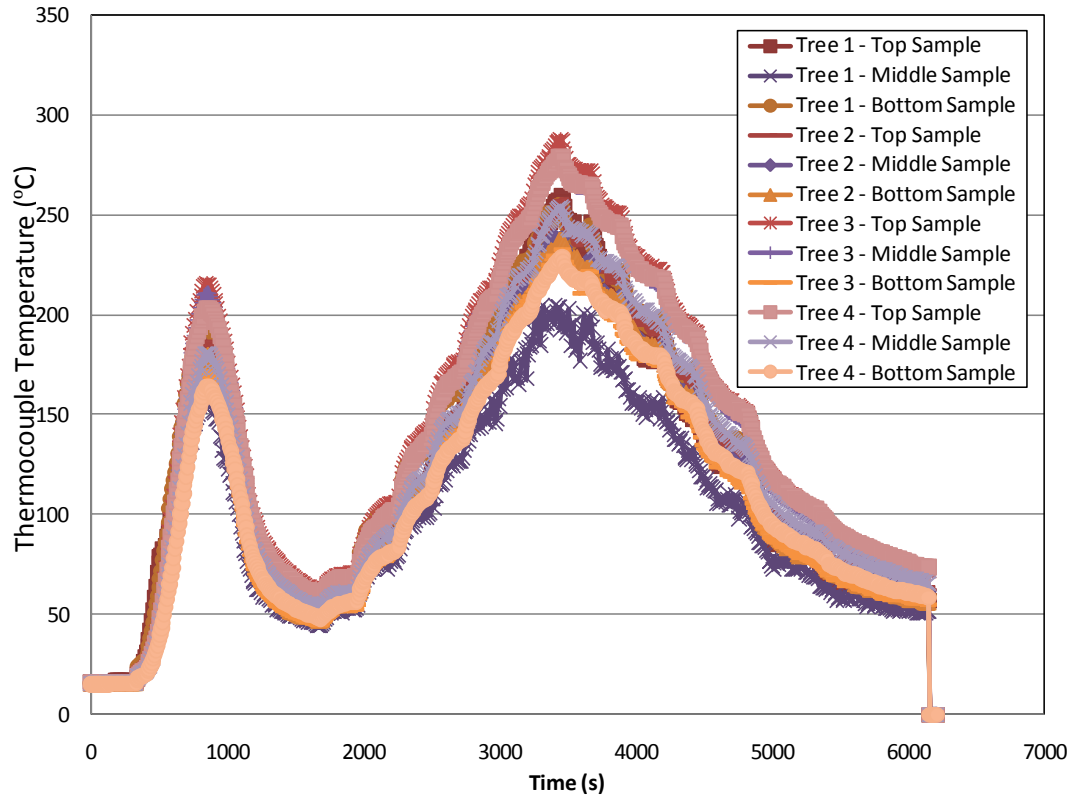

Figure 52: Thermocouple measurements at each sample location on each tree.

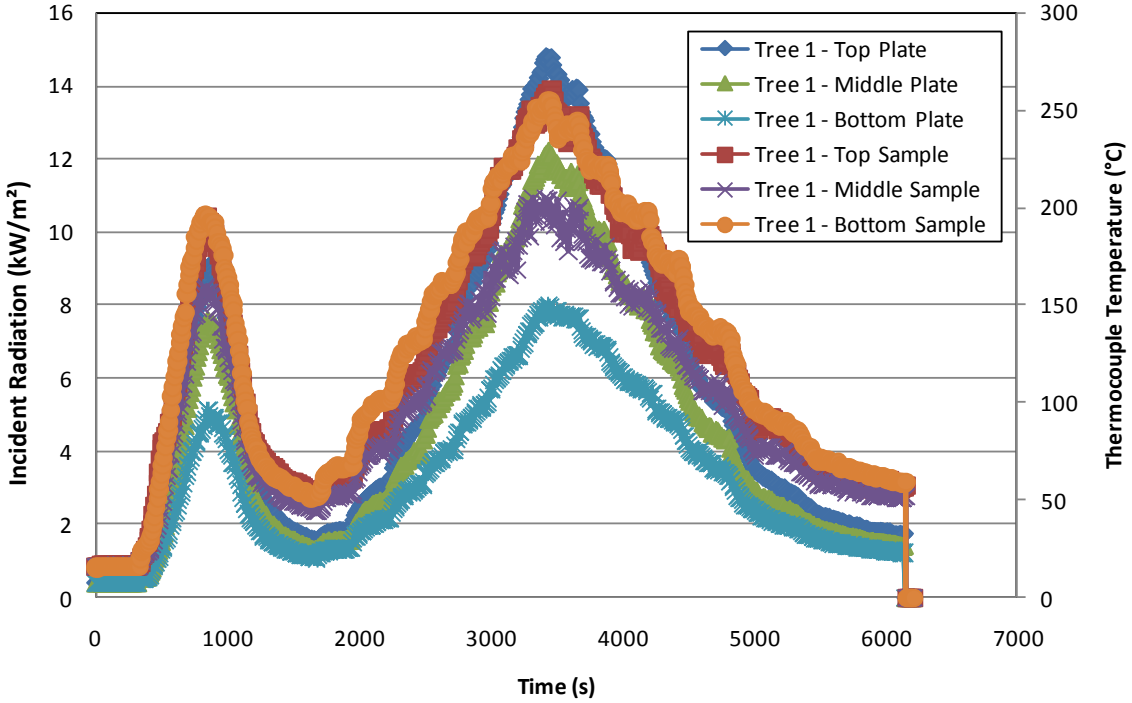
Tree 1 - Top Plate
Tree 1 - Middle Plate
Tree 1 - Bottom Plate
Tree 1 - Top Sample
Tree 1 - Middle Sample
Tree 1 - Bottom Sample
Incident Radiation (kW/m²)
Thermocouple Temperature (°C)
Time (s)
0
2
4
6
8
10
12
14
16
0
50
100
150
200
250
300
0
1000
2000
3000
4000
5000
6000
7000

(a)

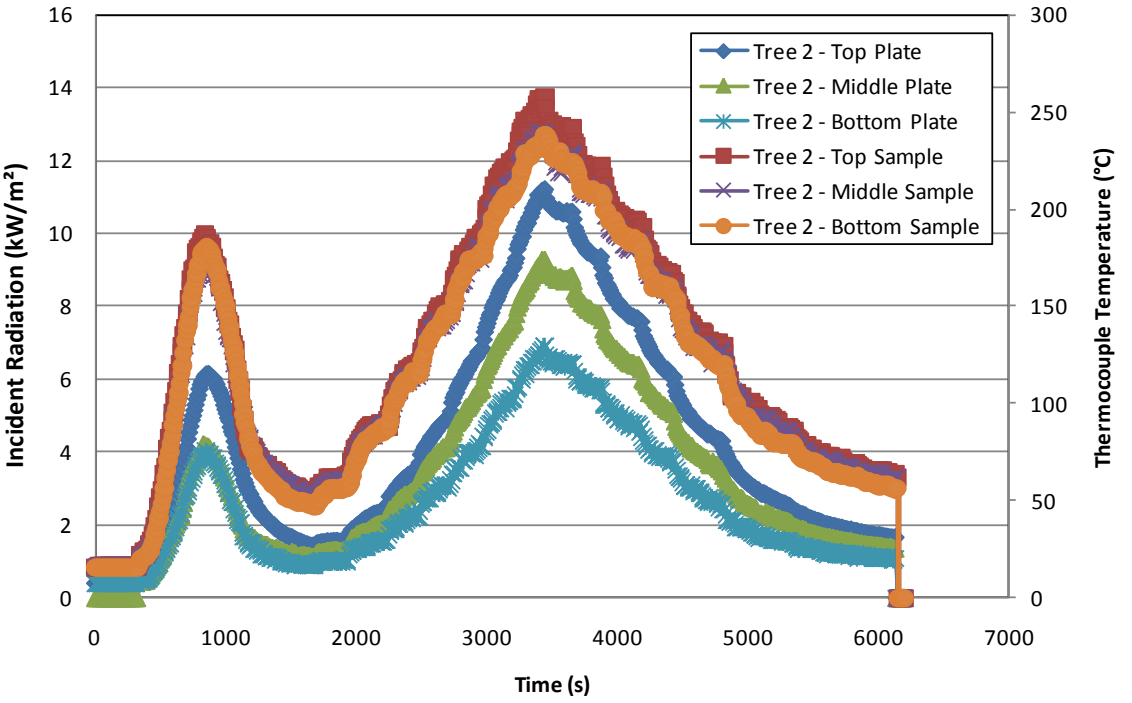
Tree 2 - Top Plate
Tree 2 - Middle Plate
Tree 2 - Bottom Plate
Tree 2 - Top Sample
Tree 2 - Middle Sample
Tree 2 - Bottom Sample
Incident Radiation (kW/m²)
Thermocouple Temperature (°C)
Time (s)
0
2
4
6
8
10
12
14
16
0
50
100
150
200
250
300
0
1000
2000
3000
4000
5000
6000
7000

(b)

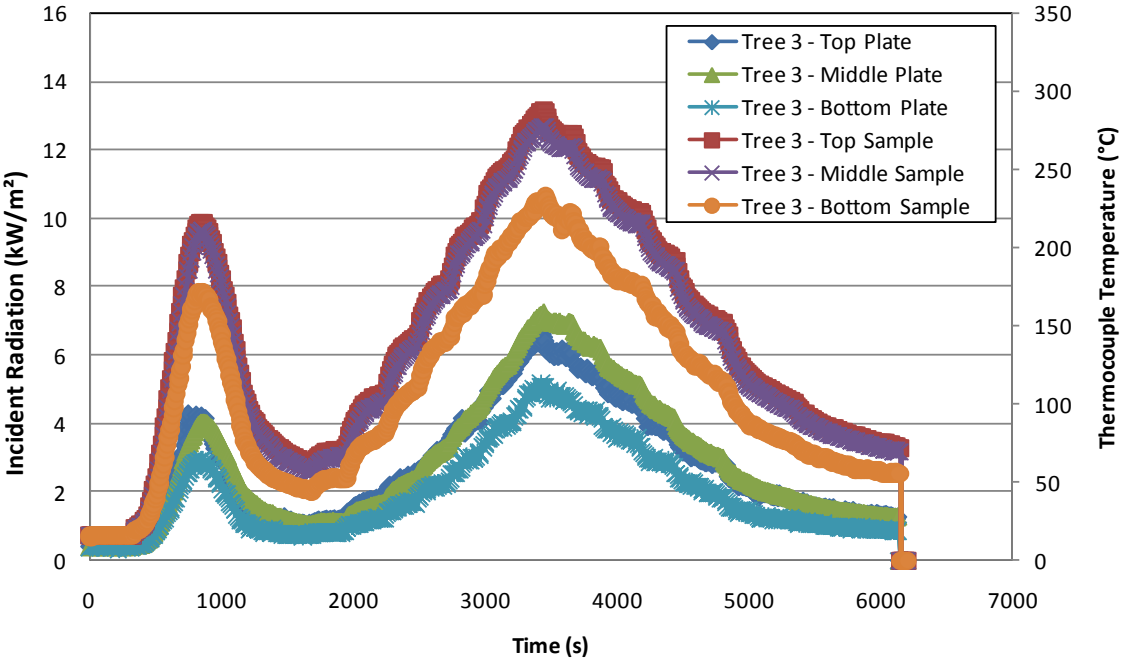

(c)

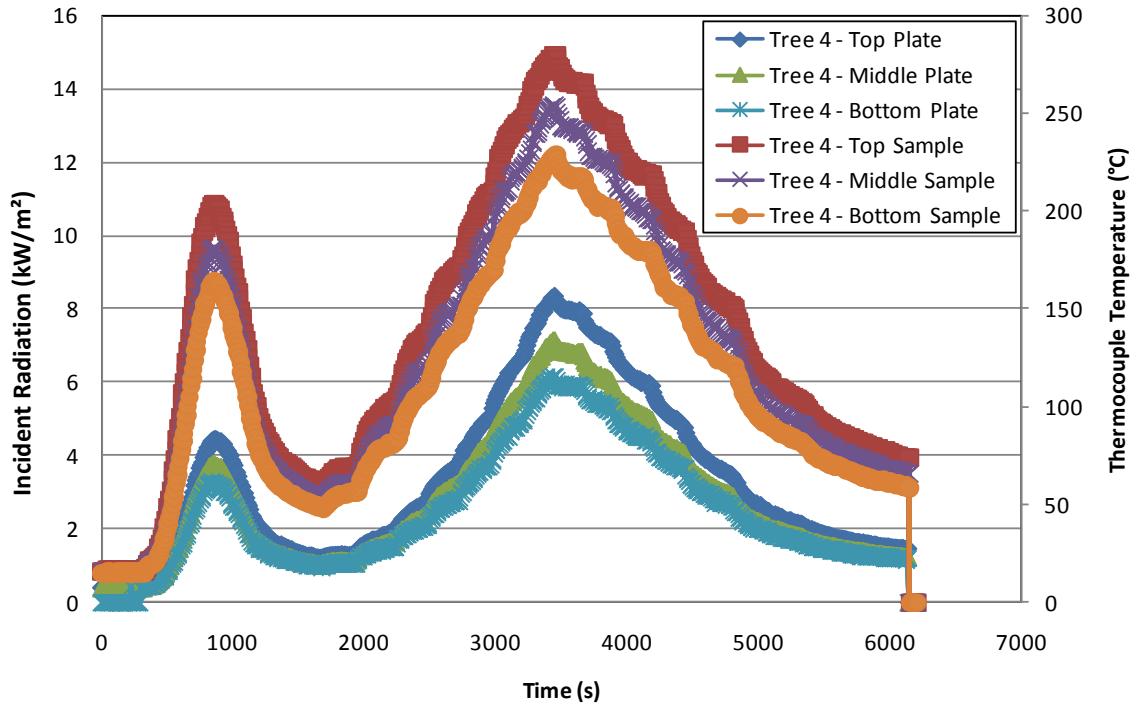

(d)

Figure 53: Thermocouple measurements and estimates of the incident radiation calculated from plate thermometer measurements for each location on each equipment tree: (a) tree 1, (b) tree 2, (c) tree 3 and (d) tree 4.

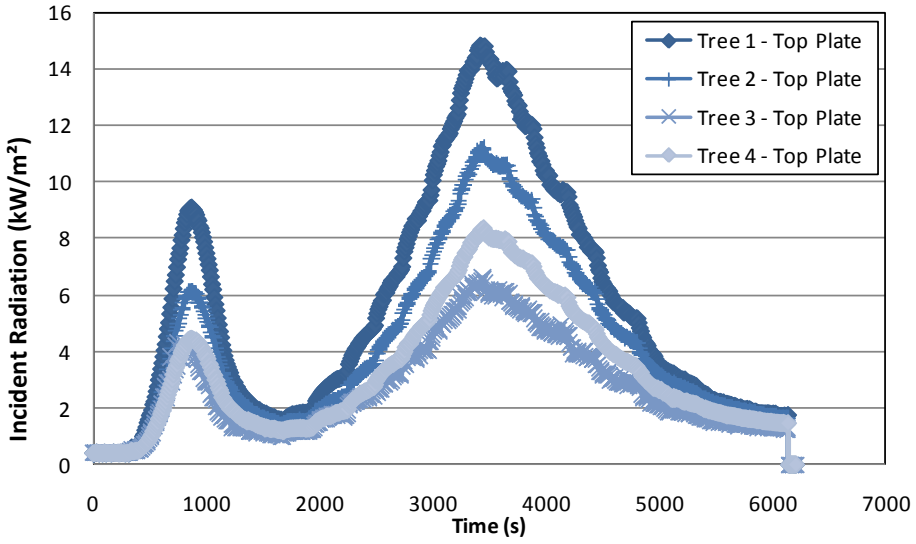

(a)

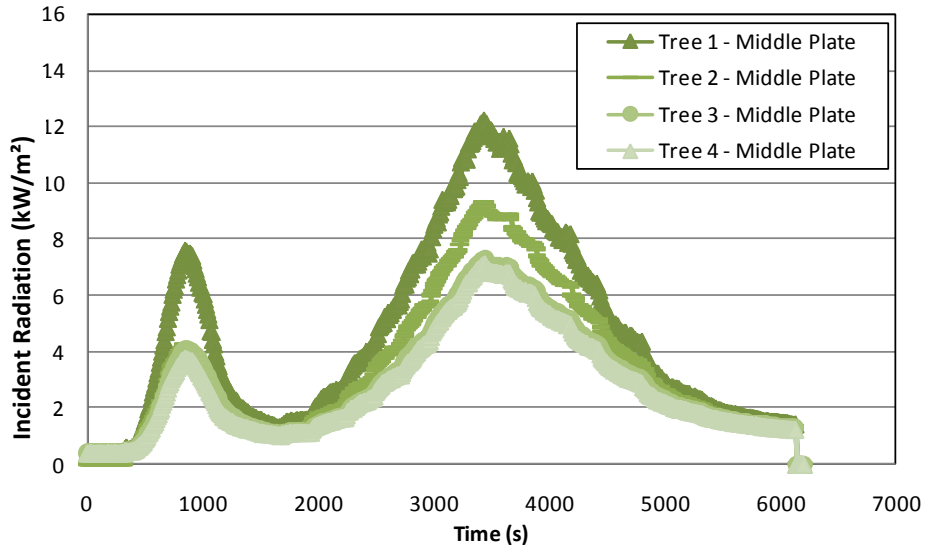

(b)

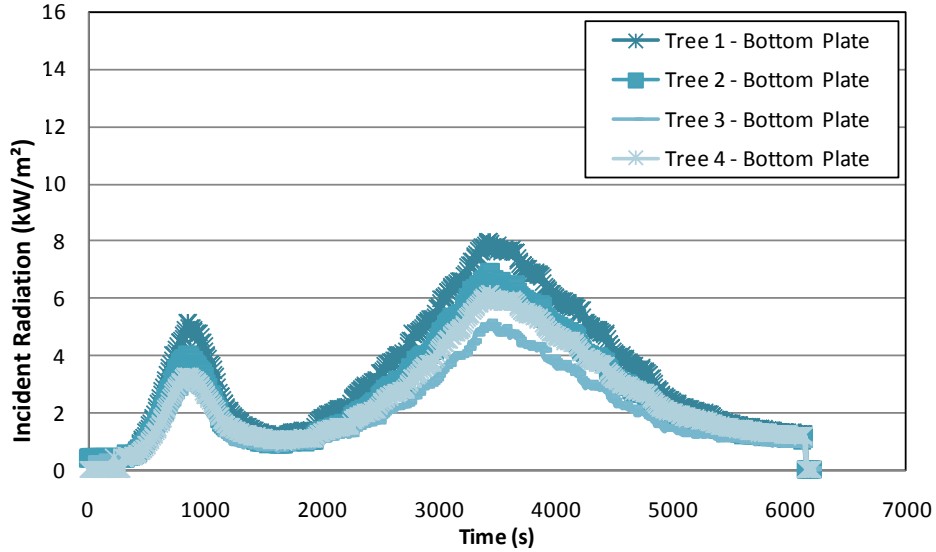

(c)

Figure 54: Estimates of the incident radiation flux calculated from plate thermometer measurements for the (a) top, (b) middle and (c) bottom locations of each of the equipment trees.

6.6 ISO room experiments with mattress

Examples of the results of the tests using the ISO room and a burning mattress on a load cell in the corner, as discussed in Section 5.2.6, are presented in this section. Detailed results are presented in Appendix A.

6.6.1 Test 3

This ISO room test with a folded mattress example had the equipment trees in the Orientation C set-up (Figure 11).

The HRR, as calculated by oxygen calorimetry and estimated from the fuel mass loss (measured using a load cell), is compared to the incident radiant heat flux calculated from Gardon gauge A measurements in Figure 55. From the temperature measurements in the corner of the ISO room (Figure 57), the layer height and average upper and lower layer temperatures were estimated, as shown in Figure 56. Temperatures just below the ceiling were also measured (Figure 58).

Where plate thermometers were in adjacent locations to the two Gardon gauges, estimates of the incident radiative heat flux from plate thermometer measurements were compared to the Gardon gauge measurements, as shown in Figure 59. In this case the middle plate locations of equipment tree 4 and 2 were directly below the locations of the Gardon gauges.

For all the plate thermometer measurements at each location on each equipment tree, the estimates of the incident radiative heat flux are shown in Figure 60 and the temperatures over each of the adjacent sample materials are shown in Figure 61. For clarity these results are shown for each of the equipment trees in Figure 62. The estimated incident radiative heat fluxes at each of the heights above the floor of the ISO room are shown in Figure 63.

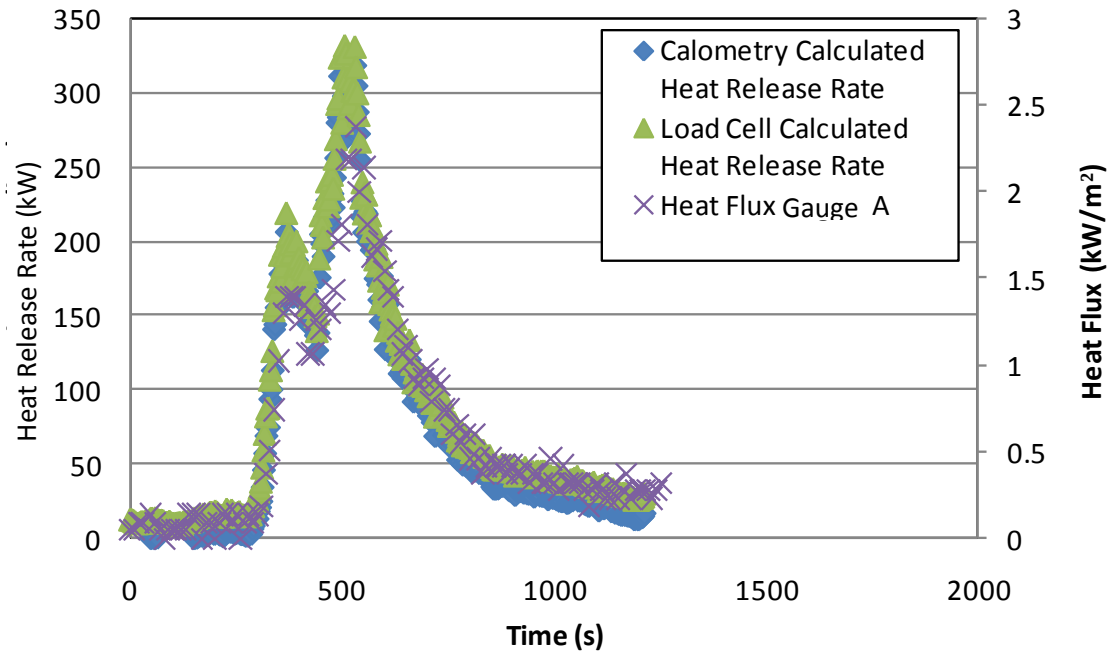

Figure 55: HRR, as calculated by oxygen calorimetry and by the fuel mass rate of the mattress on a load cell, and incident radiant heat flux estimated from the plate thermometer at the top of tree 4.

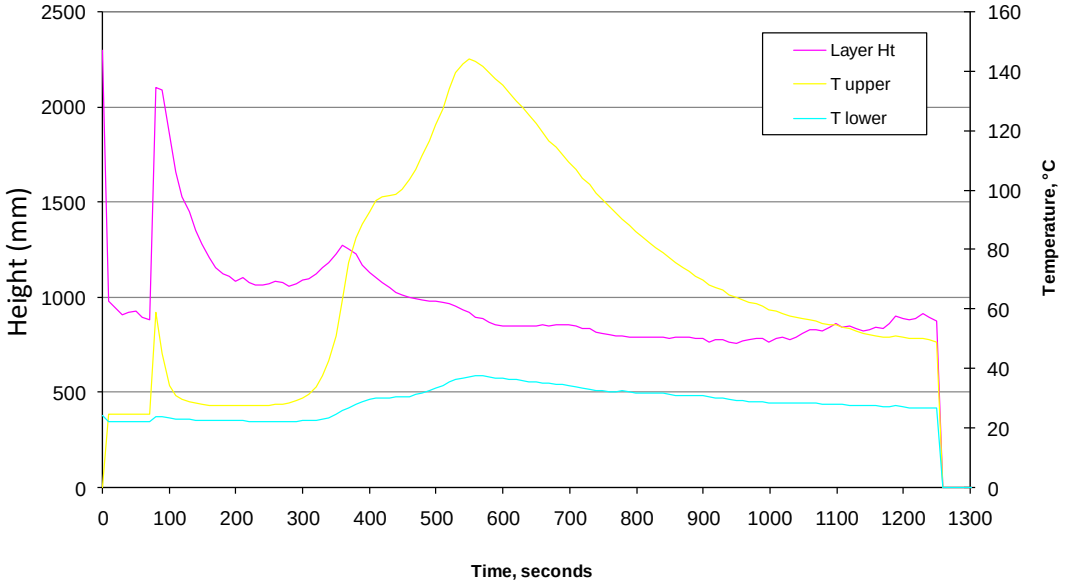

Figure 56: Estimate of the interface height and average upper and lower layer temperatures.

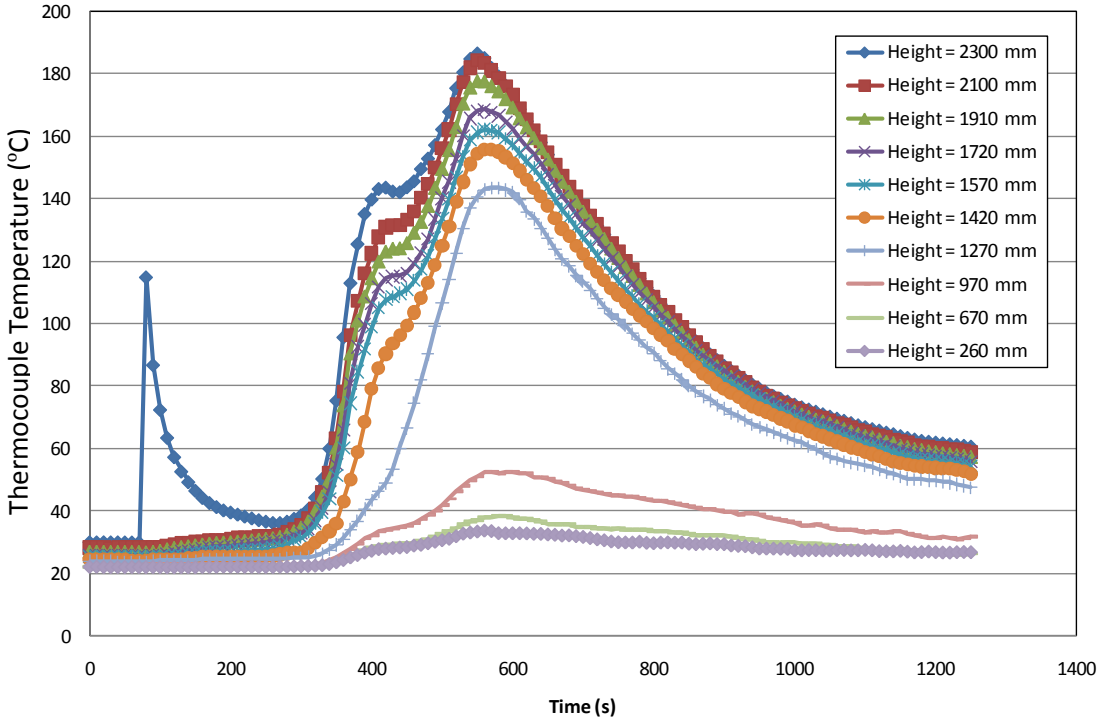

Figure 57: ISO room corner temperatures (°C) at various heights.

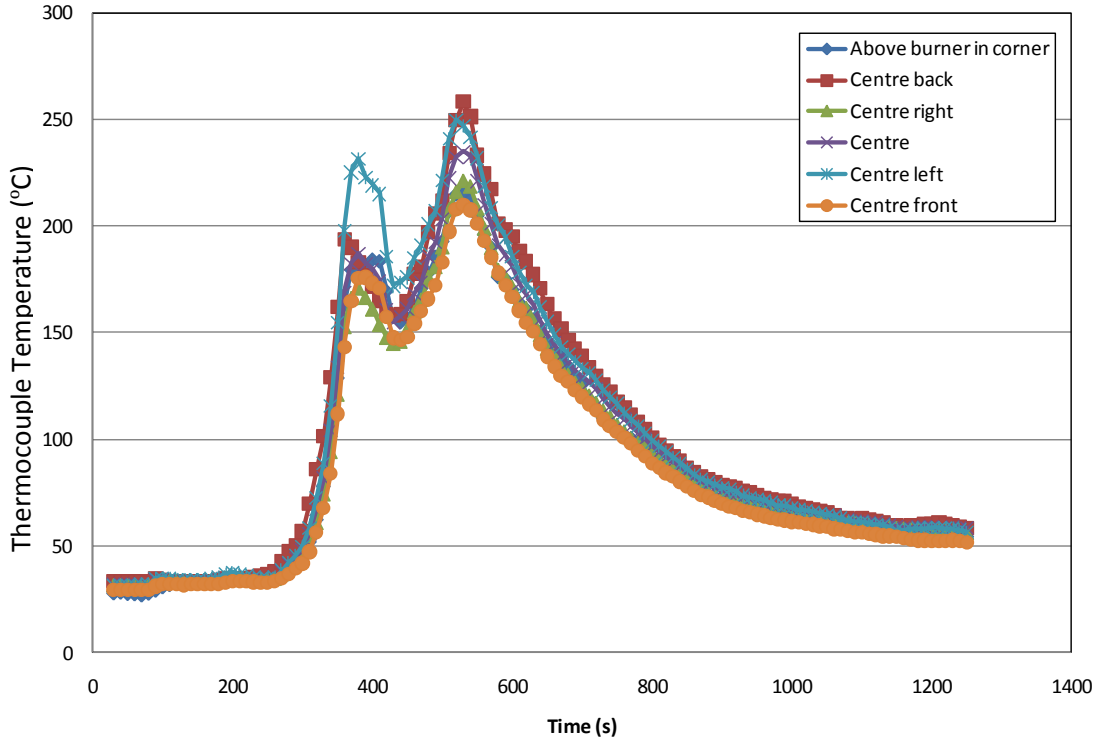

Figure 58: ISO room ceiling temperatures (°C).

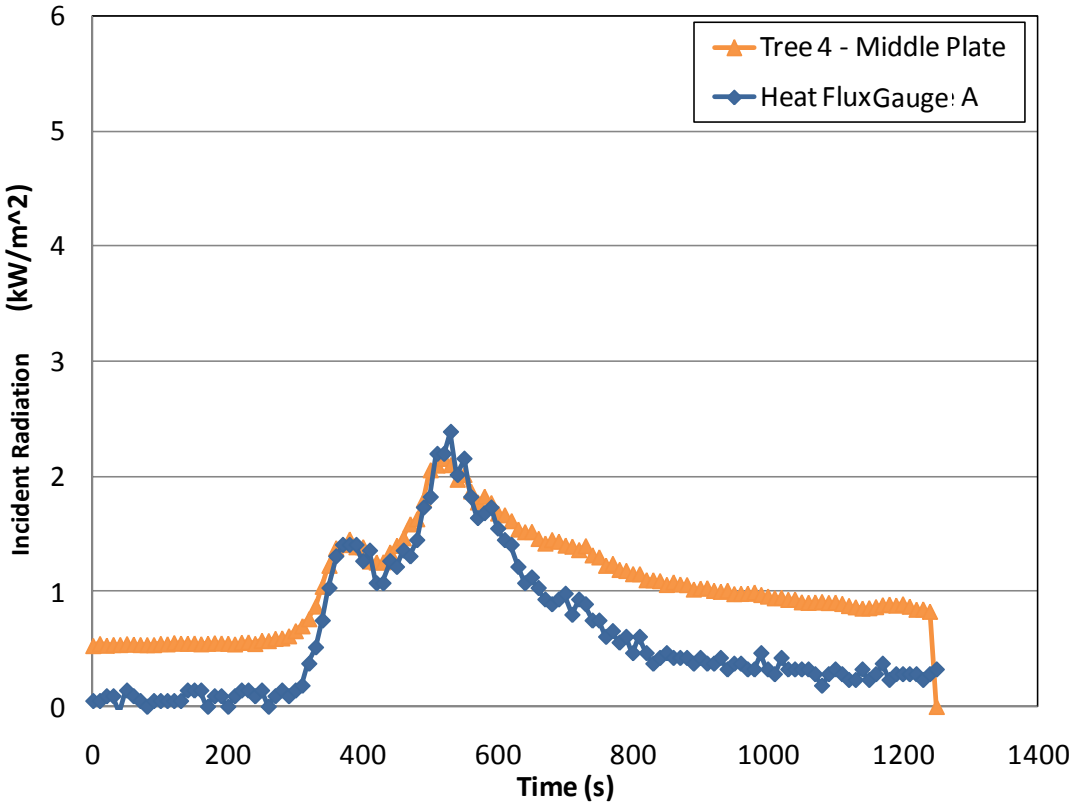

(a)

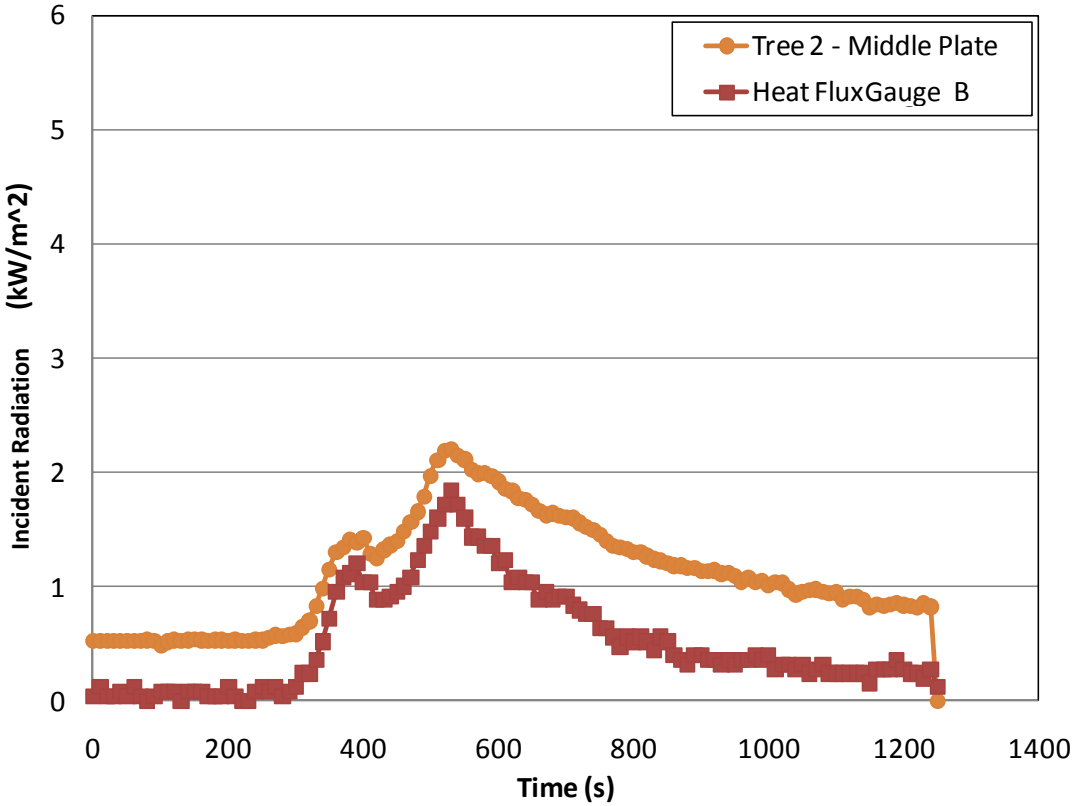

(b)

Figure 59: Estimates of the incident radiative heat flux at the (a) middle plate location of tree 4 and (b) middle plate location of tree 2 from plate thermometer and Gardon gauge measurements.

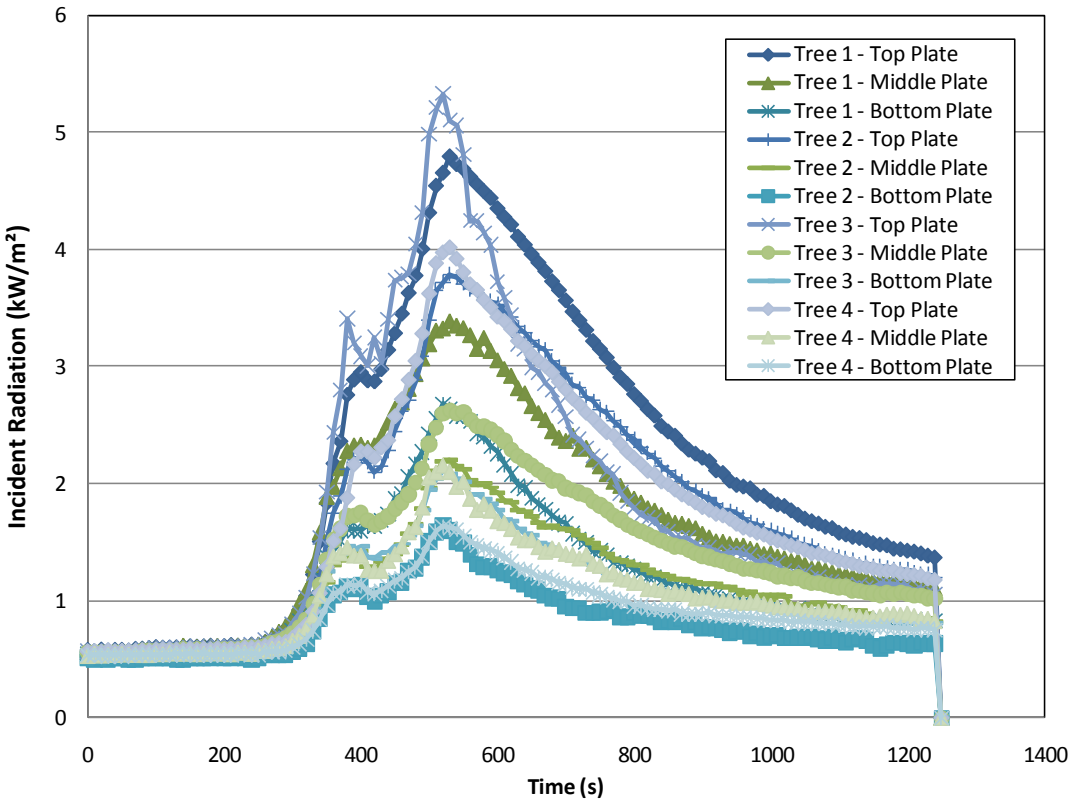

Figure 60: Estimates of the incident radiative heat flux from the plate thermometer measurements at each location on each tree.

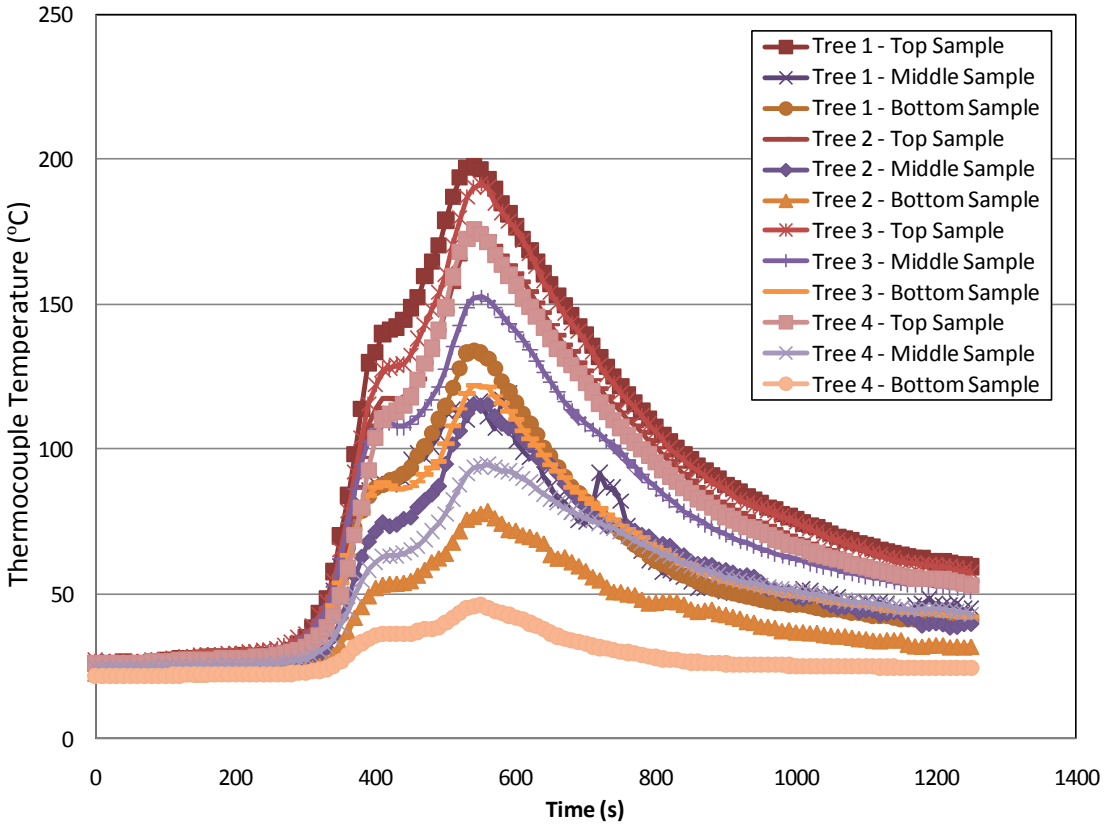

Figure 61: Thermocouple measurements at each sample location on each tree.

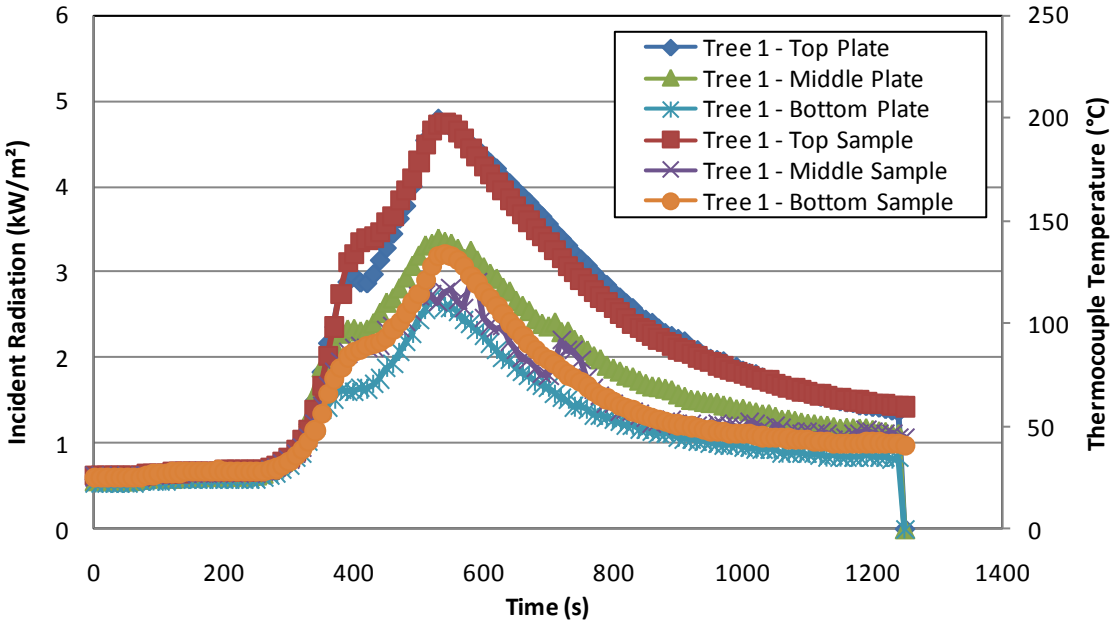
Tree 1 - Top Plate
Tree 1 - Middle Plate
Tree 1 - Bottom Plate
Tree 1 - Top Sample
Tree 1 - Middle Sample
Tree 1 - Bottom Sample
Incident Radiation (kW/m²)
Thermocouple Temperature (°C)
Time (s)
0
1
2
3
4
5
6
0
50
100
150
200
250
0
200
400
600
800
1000
1200
1400

(a)

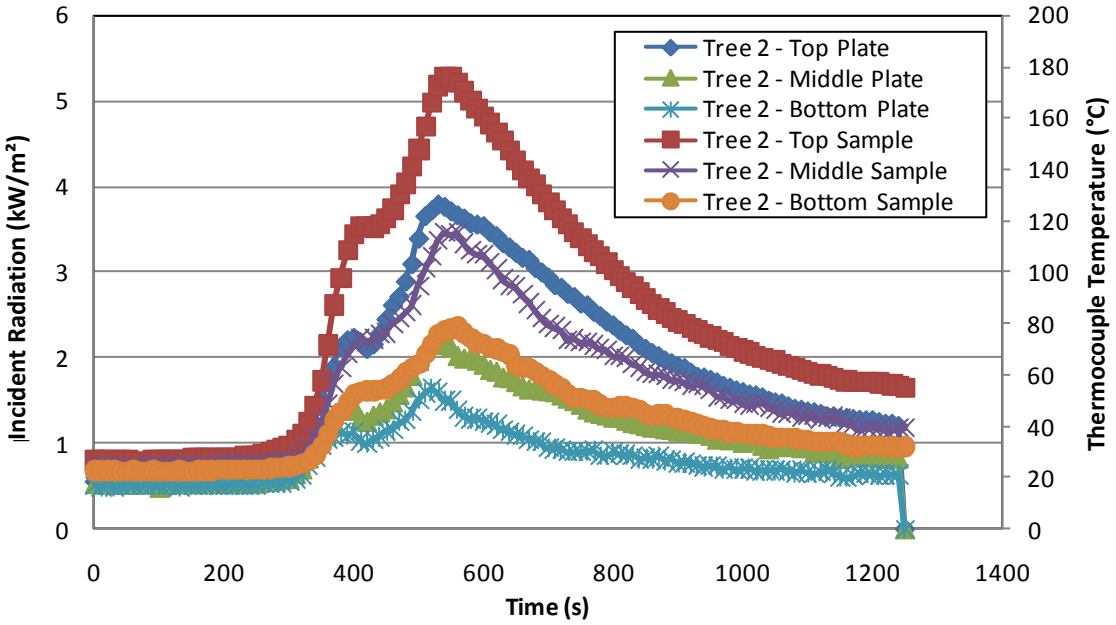
Tree 2 - Top Plate
Tree 2 - Middle Plate
Tree 2 - Bottom Plate
Tree 2 - Top Sample
Tree 2 - Middle Sample
Tree 2 - Bottom Sample
Incident Radiation (kW/m²)
Thermocouple Temperature (°C)
Time (s)
0
1
2
3
4
5
6
0
20
40
60
80
100
120
140
160
180
200
0
200
400
600
800
1000
1200
1400

(b)

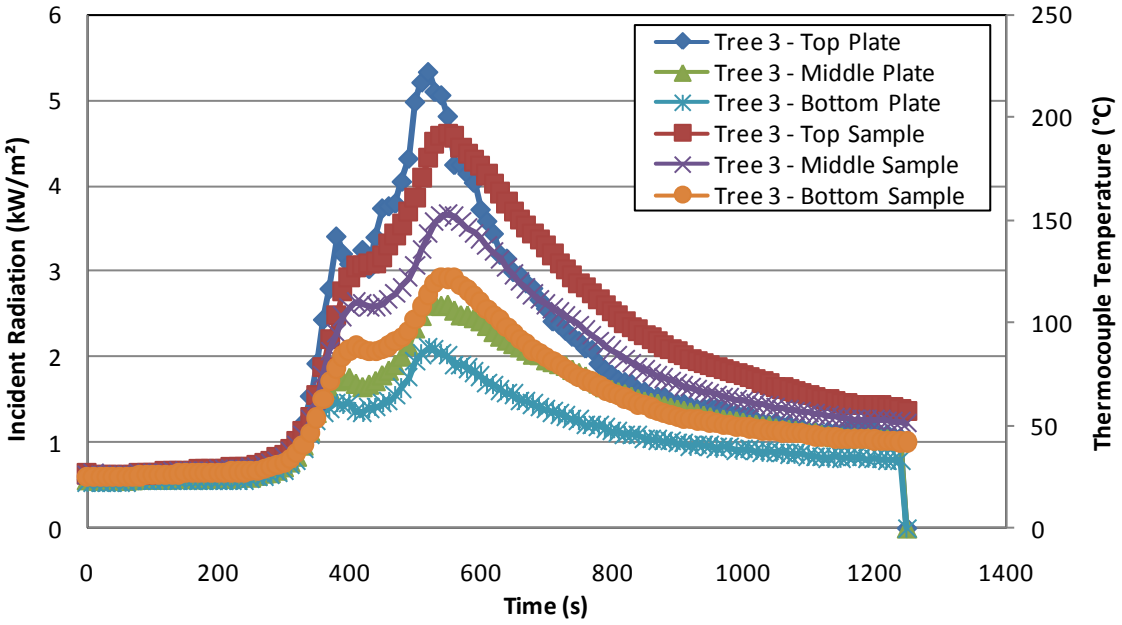

(c)

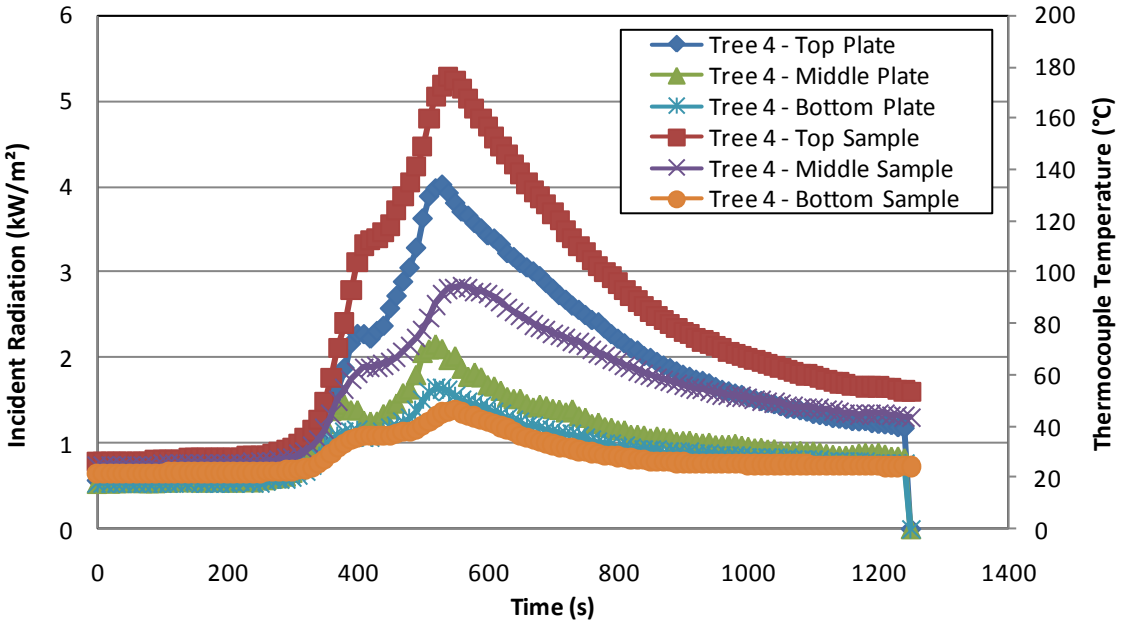

(d)

Figure 62: Thermocouple measurements and estimates of the incident radiation calculated from plate thermometer measurements for each location on each equipment tree: (a) tree 1, (b) tree 2, (c) tree 3 and (d) tree 4.

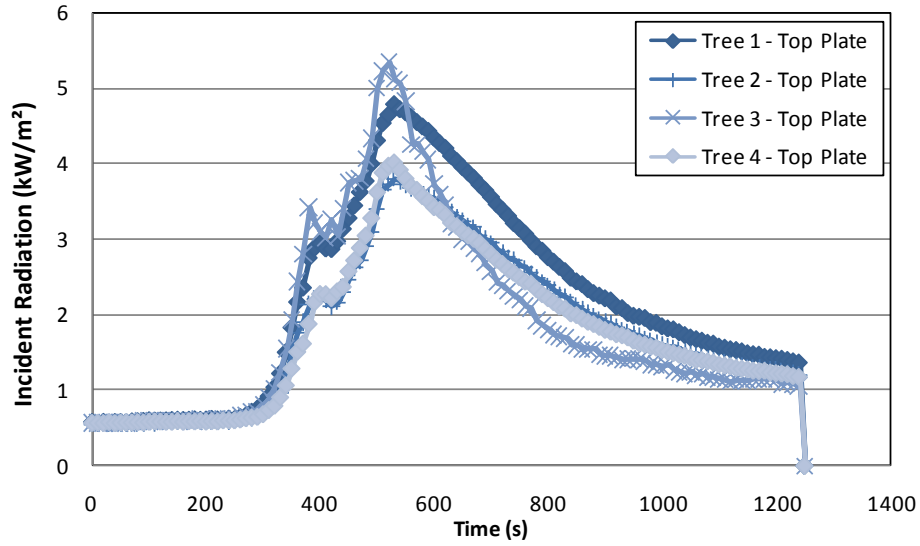

(a)

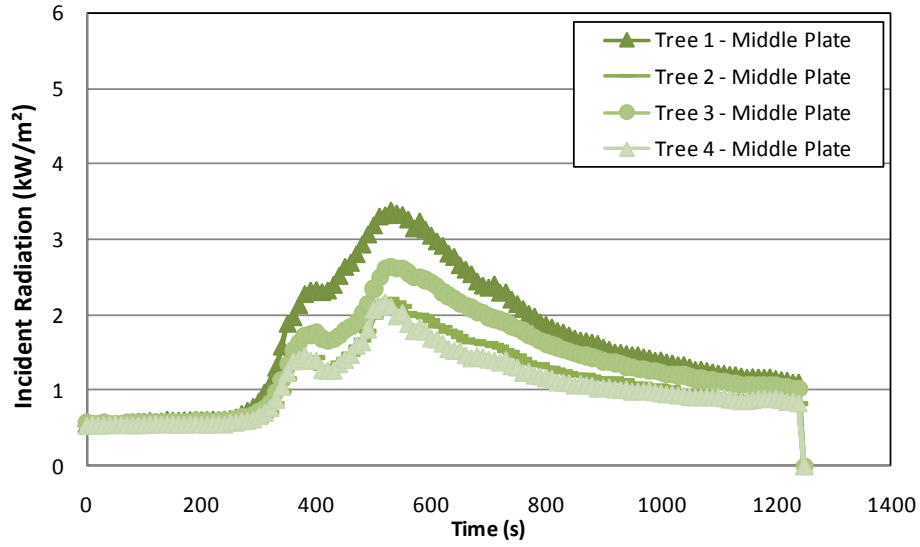

(b)

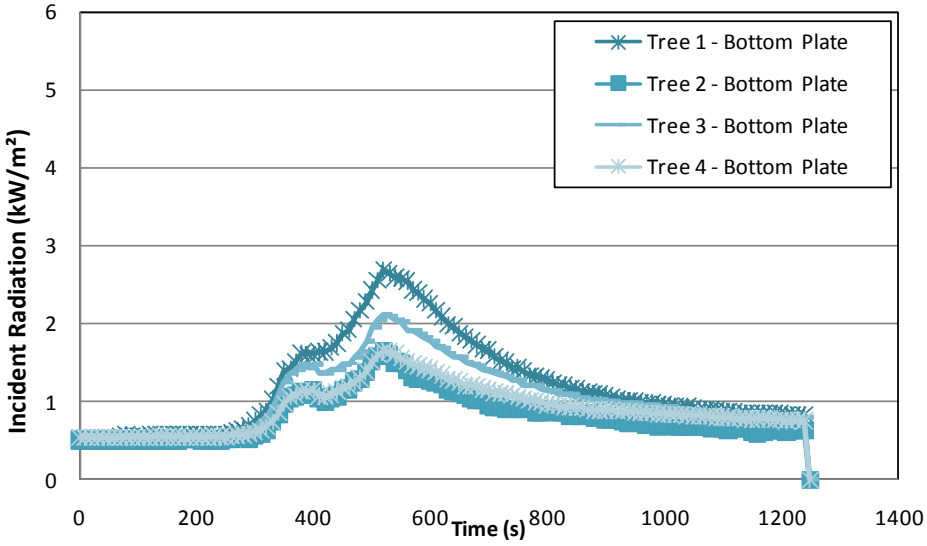

(c)

Figure 63: Estimates of the incident radiation flux calculated from plate thermometer measurements for the (a) top, (b) middle and (c) bottom locations of each of the equipment trees.

6.6.2 Test 4

Similar to Test 3, as presented in the previous section , this ISO room test with a folded mattress example had the equipment trees in the Orientation C set-up (Figure 11).

The HRR, as calculated by oxygen calorimetry and estimated from the fuel mass loss (measured using a load cell), is compared to the incident radiant heat flux calculated from Gardon gauge A measurements in Figure 64. From the temperature measurements in the corner of the ISO room (Figure 66), the layer height and average upper and lower layer temperatures were estimated, as shown in Figure 65. Temperatures just below the ceiling were also measured (Figure 67).

Where plate thermometers were in adjacent locations to the two Gardon gauges, estimates of the incident radiative heat flux from plate thermometer measurements were compared to the Gardon gauge measurements, as shown in Figure 68. In this case the middle plate locations of equipment tree 4 and 2 were directly below the locations of the Gardon gauges.

For all the plate thermometer measurements at each location on each equipment tree, the estimates of the incident radiative heat flux are shown in Figure 69 and the temperatures over each of the adjacent sample materials are shown in Figure 70. For clarity these results are shown for each of the equipment trees in Figure 71. The estimated incident radiative heat fluxes at each of the heights above the floor of the ISO room are shown in Figure 72.

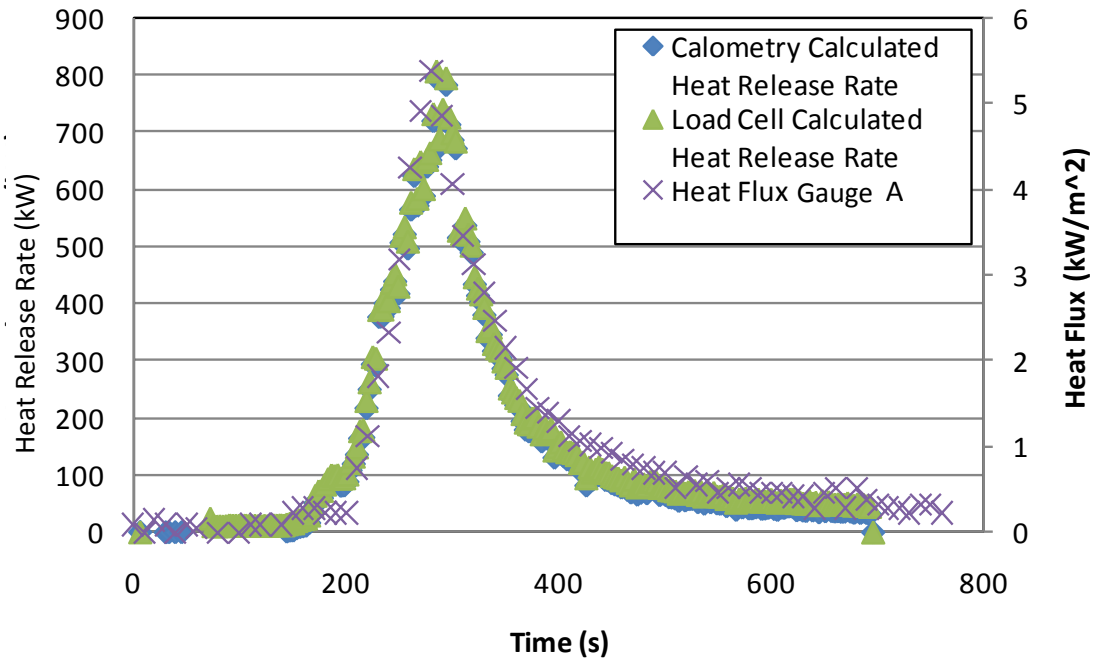

Figure 64: HRR, as calculated by oxygen calorimetry and by the fuel mass rate of the mattress on a load cell, and incident radiant heat flux estimated from the plate thermometer at the top of tree 4.

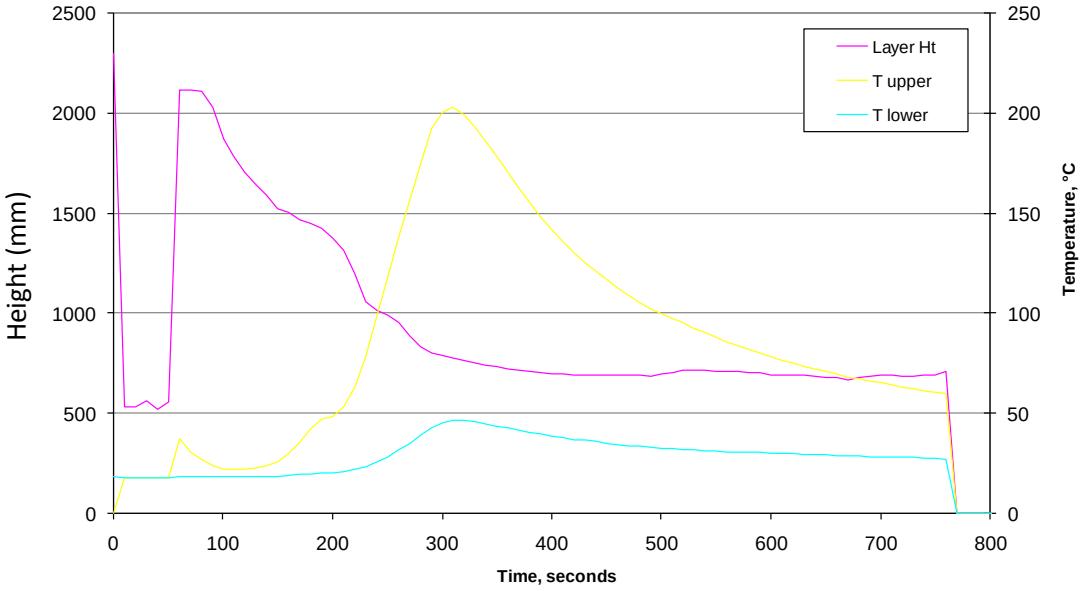

Figure 65: Estimate of the interface height and average upper and lower layer temperatures.

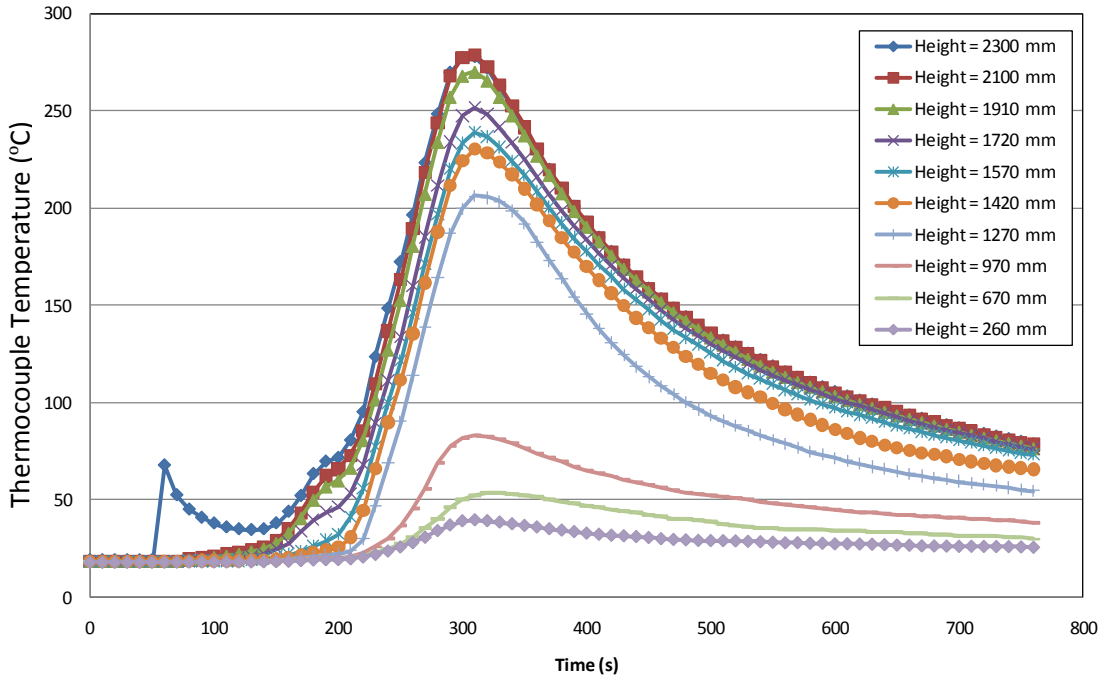

Figure 66: ISO room corner temperatures (°C) at various heights.

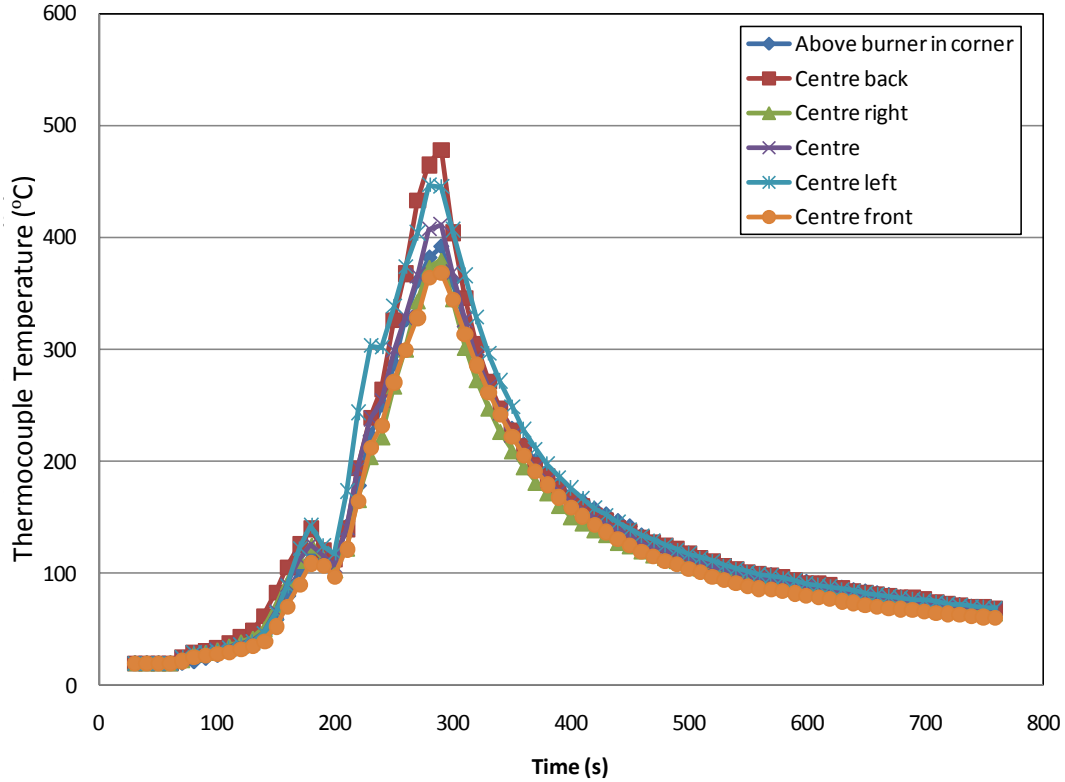

Figure 67: ISO room ceiling temperatures (°C).

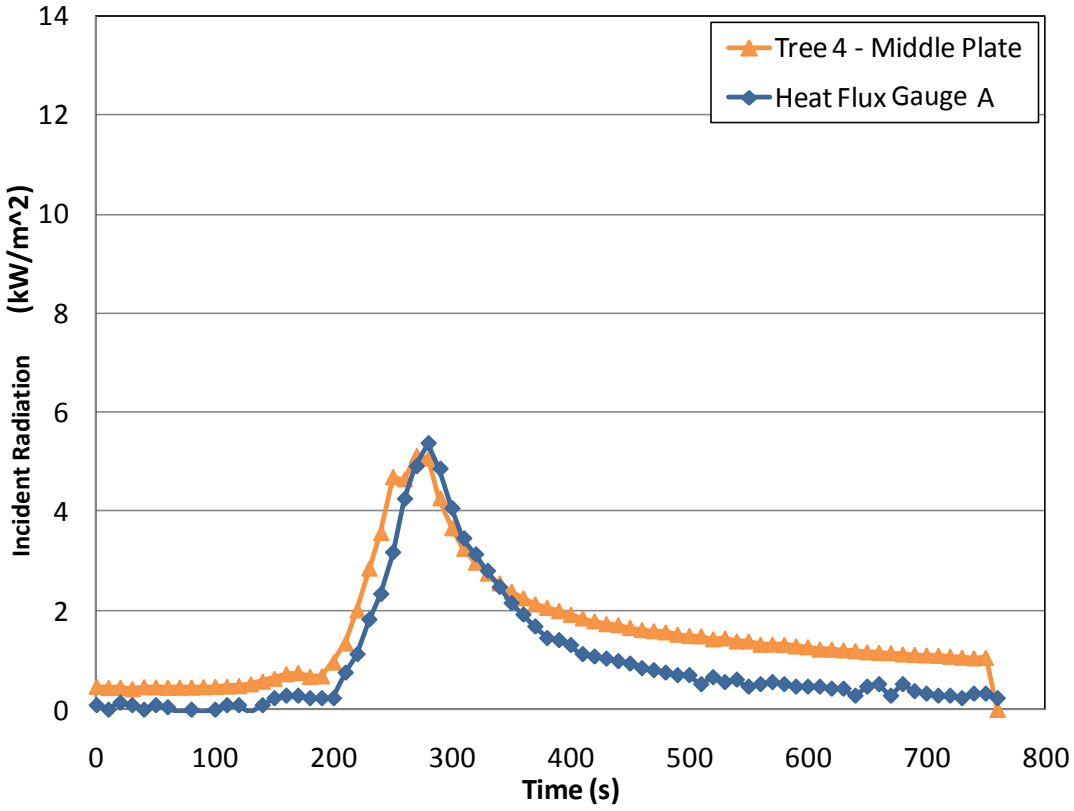

(a)

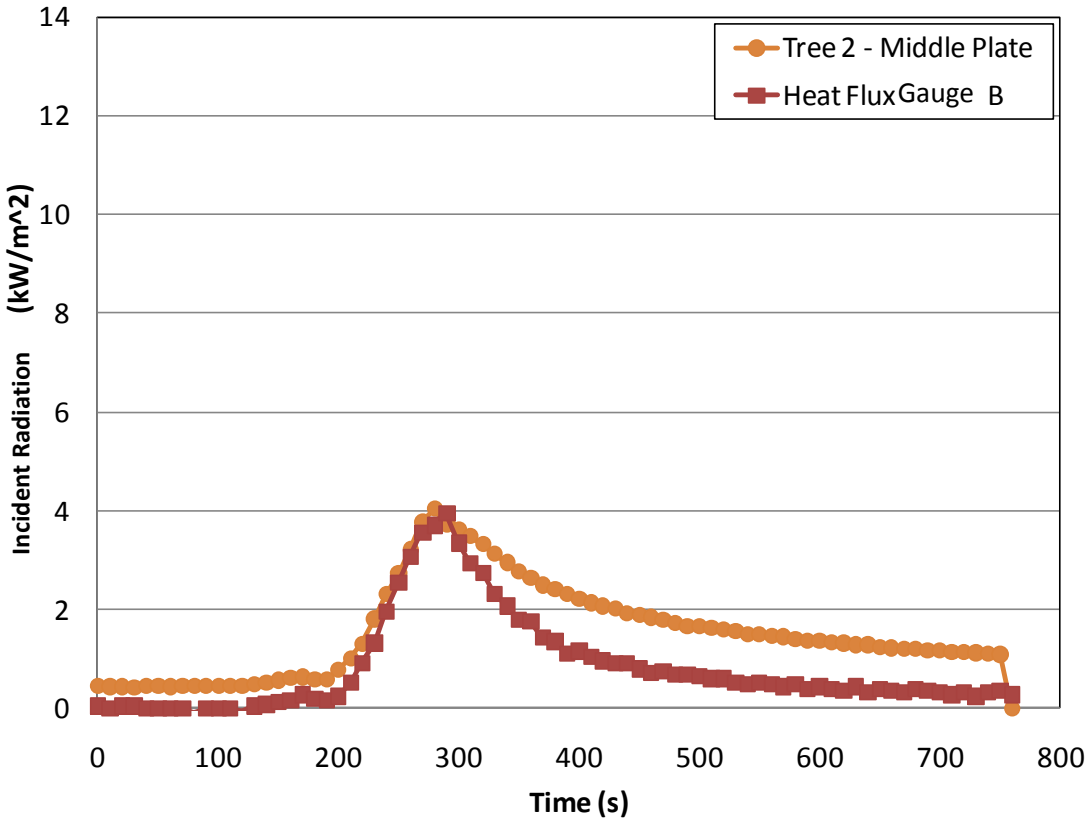

(b)

Figure 68: Estimates of the incident radiative heat flux at the (a) middle plate location of tree 4 and (b) middle plate location of tree 2 from plate thermometer and Gardon gauge measurements.

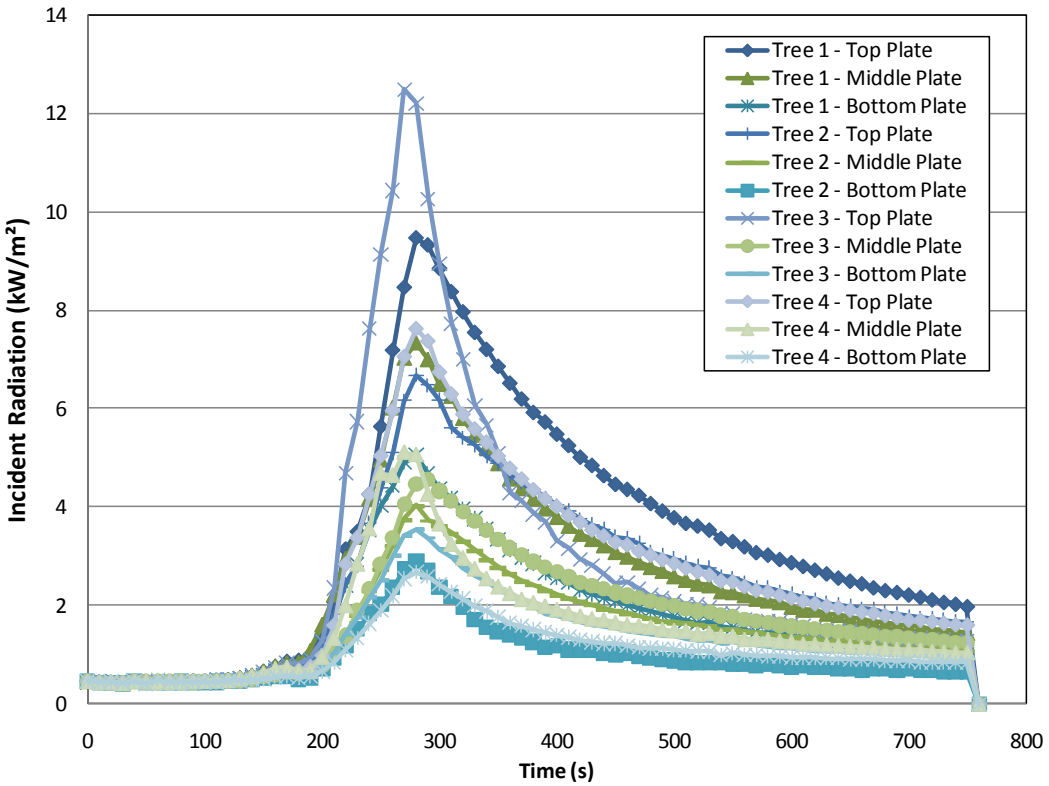

Figure 69: Estimates of the incident radiative heat flux from the plate thermometer measurements at each location on each tree.

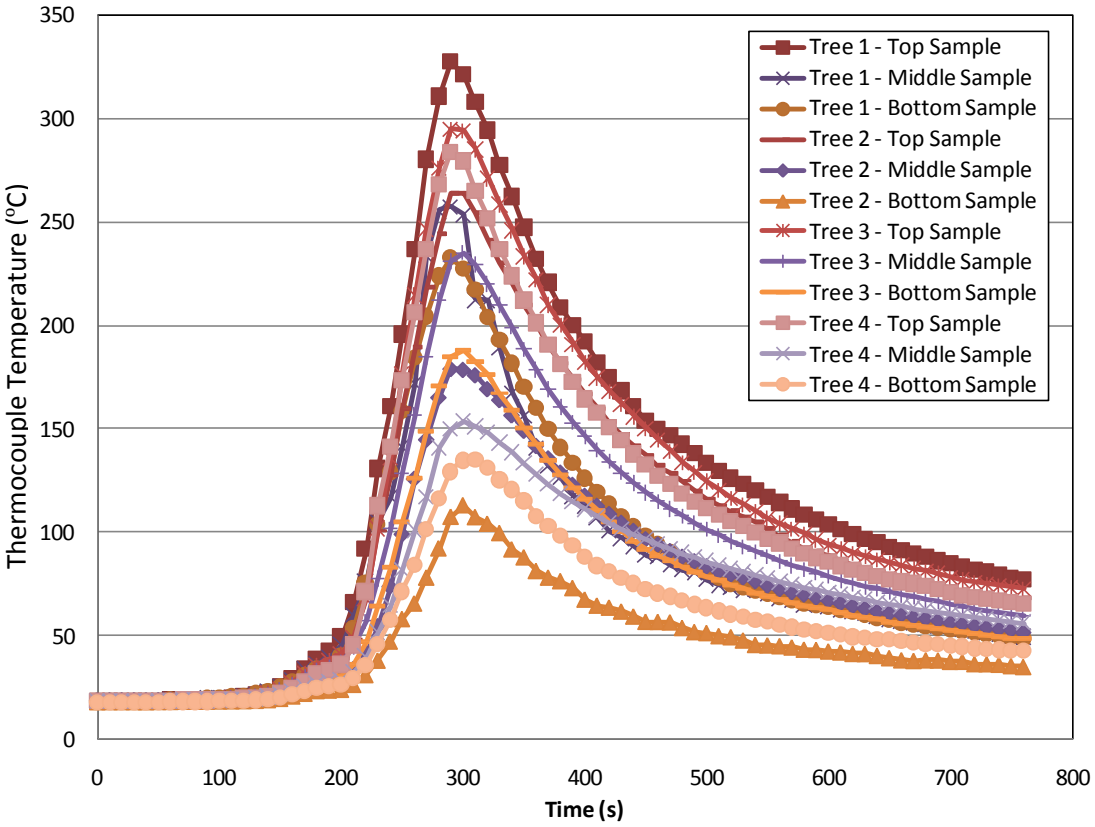

Figure 70: Thermocouple measurements at each sample location on each tree.

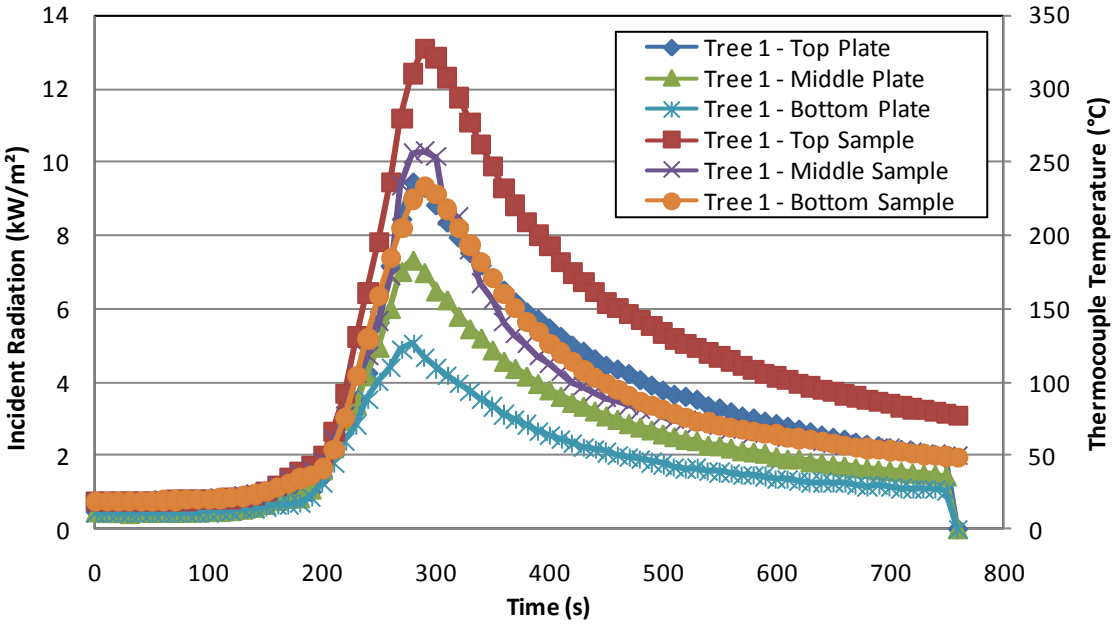
Tree 1 - Top Plate
Tree 1 - Middle Plate
Tree 1 - Bottom Plate
Tree 1 - Top Sample
Tree 1 - Middle Sample
Tree 1 - Bottom Sample
Incident Radiation (kW/m²)
Thermocouple Temperature (°C)
Time (s)
0
2
4
6
8
10
12
14
0
50
100
150
200
250
300
350
0
100
200
300
400
500
600
700
800

(a)

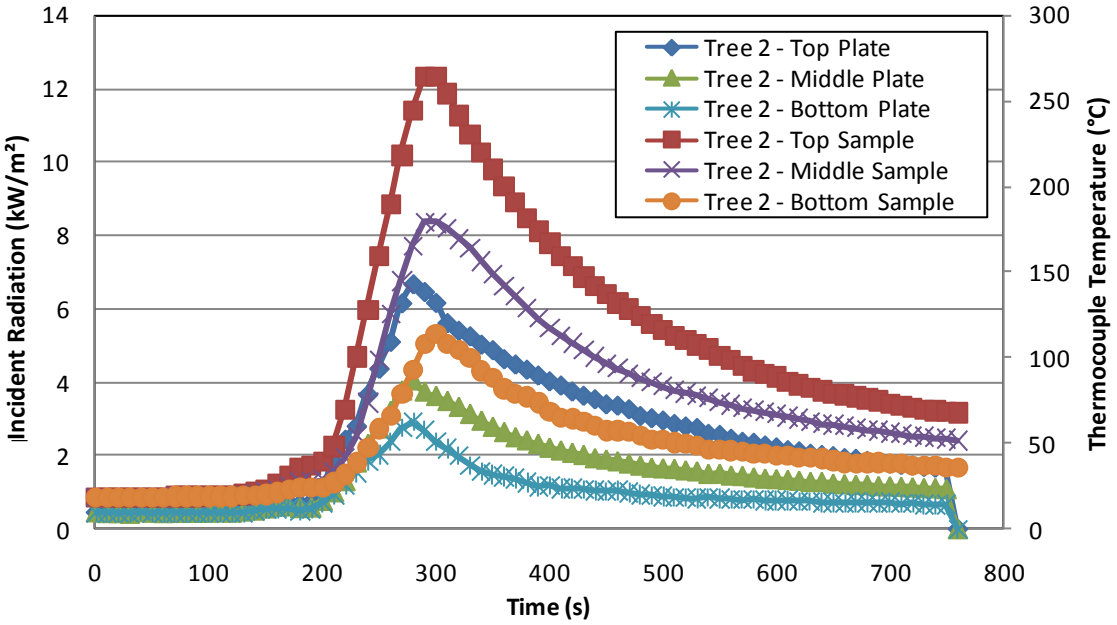
Tree 2 - Top Plate
Tree 2 - Middle Plate
Tree 2 - Bottom Plate
Tree 2 - Top Sample
Tree 2 - Middle Sample
Tree 2 - Bottom Sample
Incident Radiation (kW/m²)
Thermocouple Temperature (°C)
Time (s)
0
2
4
6
8
10
12
14
0
50
100
150
200
250
300
0
100
200
300
400
500
600
700
800

(b)

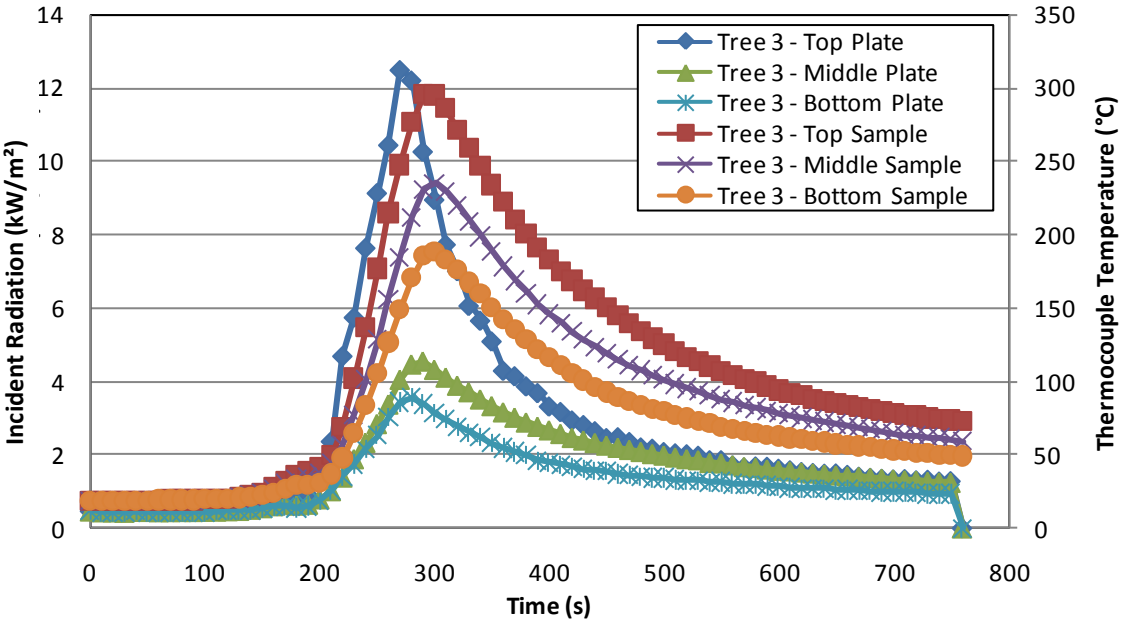

(c)

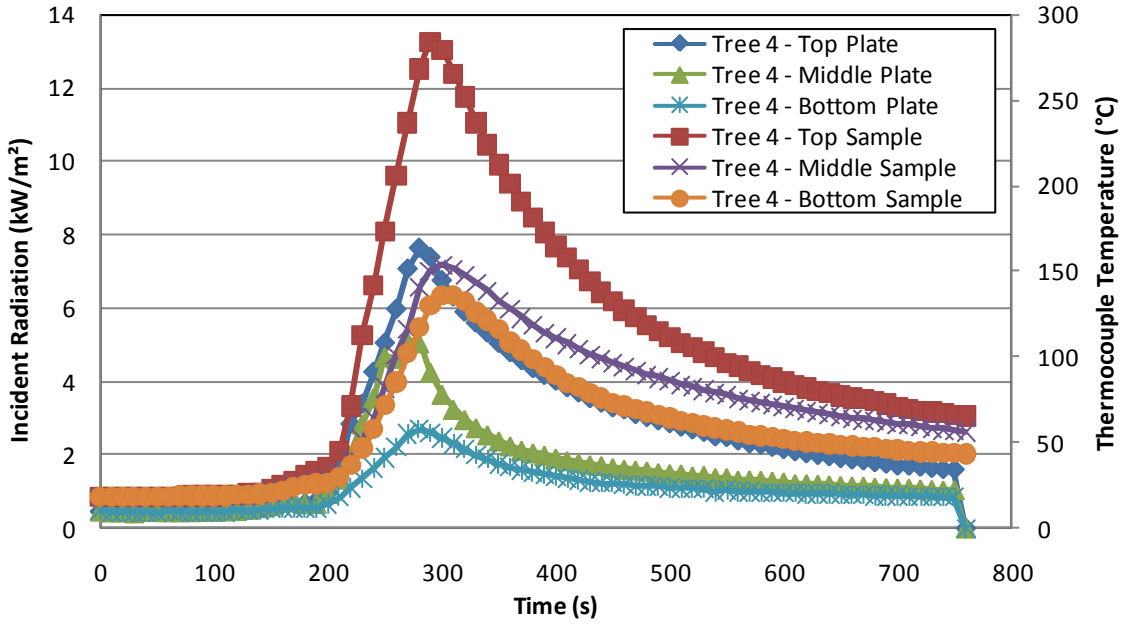

(d)

Figure 71: Thermocouple measurements and estimates of the incident radiation calculated from plate thermometer measurements for each location on each equipment tree: (a) tree 1, (b) tree 2, (c) tree 3 and (d) tree 4.

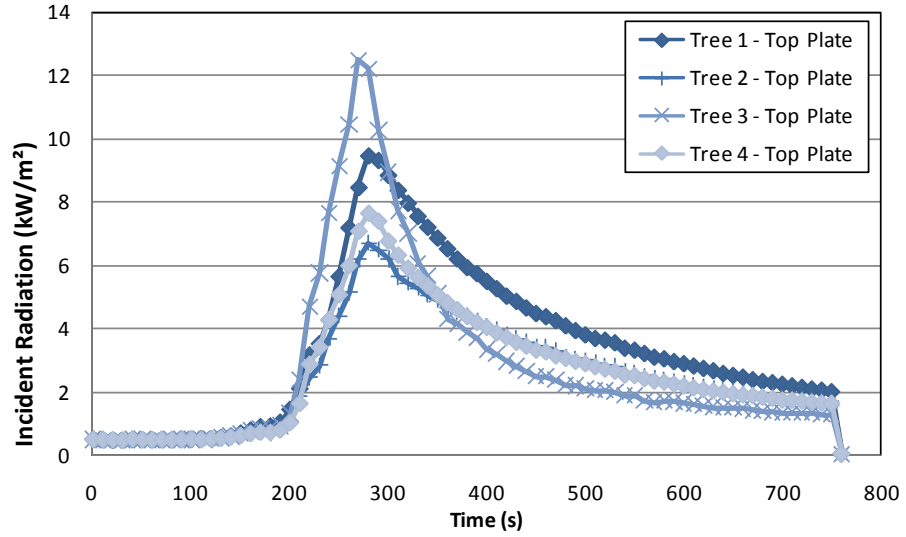

(a)

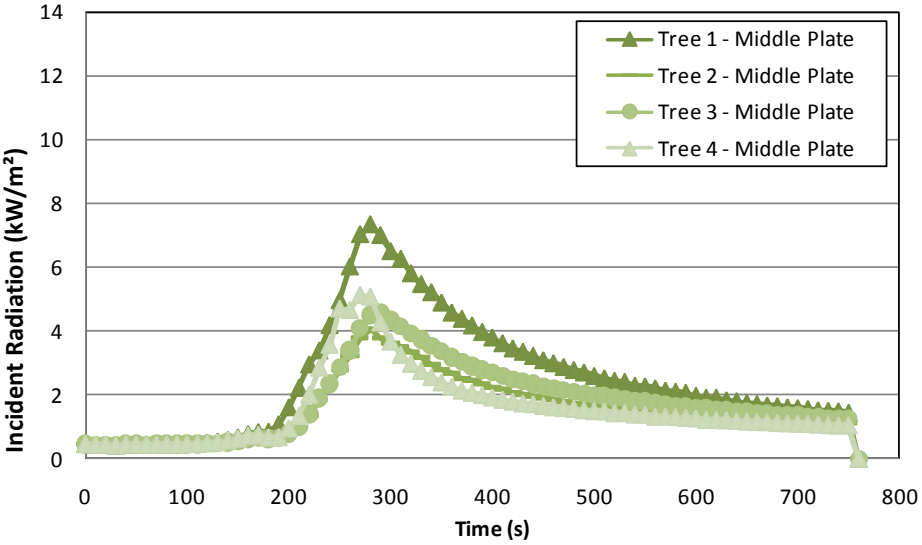

(b)

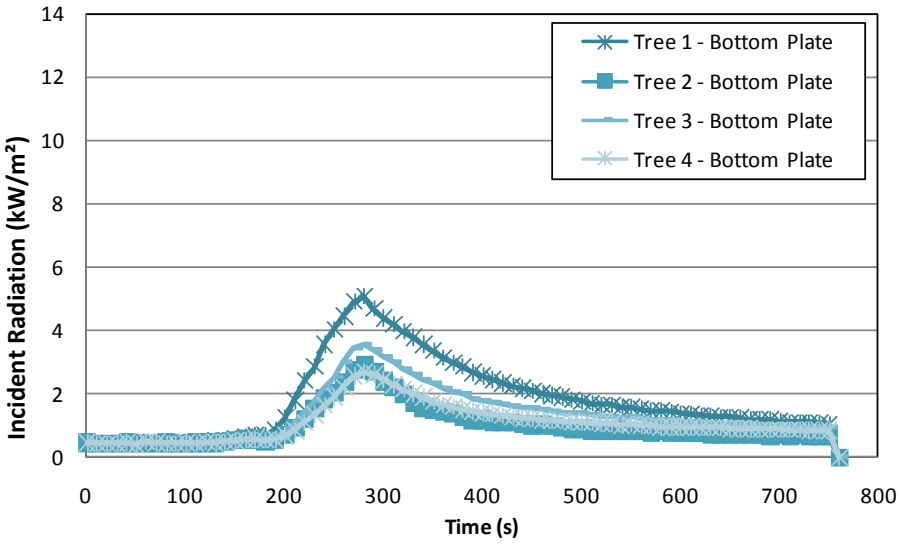

(c)

Figure 72: Estimates of the incident radiation flux calculated from plate thermometer measurements for the (a) top, (b) middle and (c) bottom locations of each of the equipment trees.

6.7 Closed ISO room experiments with mattress

Examples of the results of the tests using the ISO room and a burning mattress on a load cell in the corner with the door of the room sealed shut, as discussed in Section 5.2.7, are presented in this section. Detailed results are presented in Appendix A.

6.7.1 Test 1

This ISO room test with a folded mattress example had the equipment trees in the Orientation C set-up (Figure 11). The door of the ISO room was sealed off during the test.

From the temperature measurements in the corner of the ISO room (Figure 74), the layer height and average upper and lower layer temperatures were estimated, as shown in Figure 73. Temperatures just below the ceiling were also measured (Figure 75).

Where plate thermometers were in adjacent locations to the two Gardon gauges, estimates of the incident radiative heat flux from plate thermometer measurements were compared to the Gardon gauge measurements, as shown in Figure 76. In this case the middle plate locations of equipment tree 4 and 2 were directly below the locations of the Gardon gauges.

For all the plate thermometer measurements at each location on each equipment tree, the estimates of the incident radiative heat flux are shown in Figure 77 and the temperatures over each of the adjacent sample materials are shown in Figure 78. For clarity these results are shown for each of the equipment trees in Figure 79. The estimated incident radiative heat fluxes at each of the heights above the floor of the ISO room are shown in Figure 80.

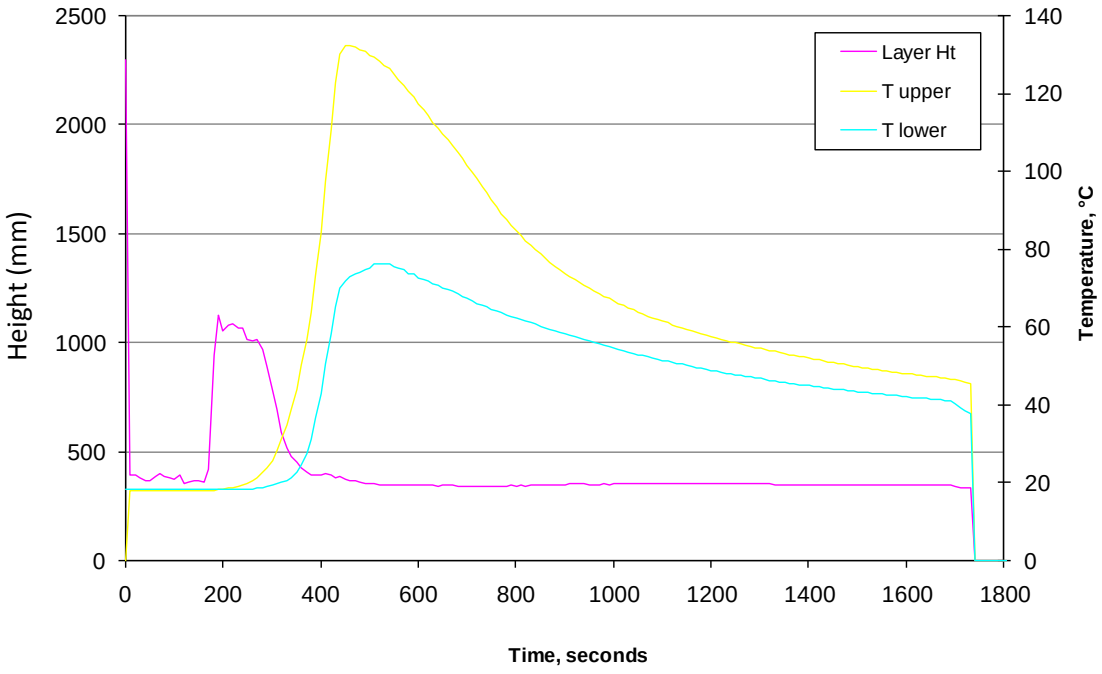

Figure 73: Estimate of the interface height and average upper and lower layer temperatures.

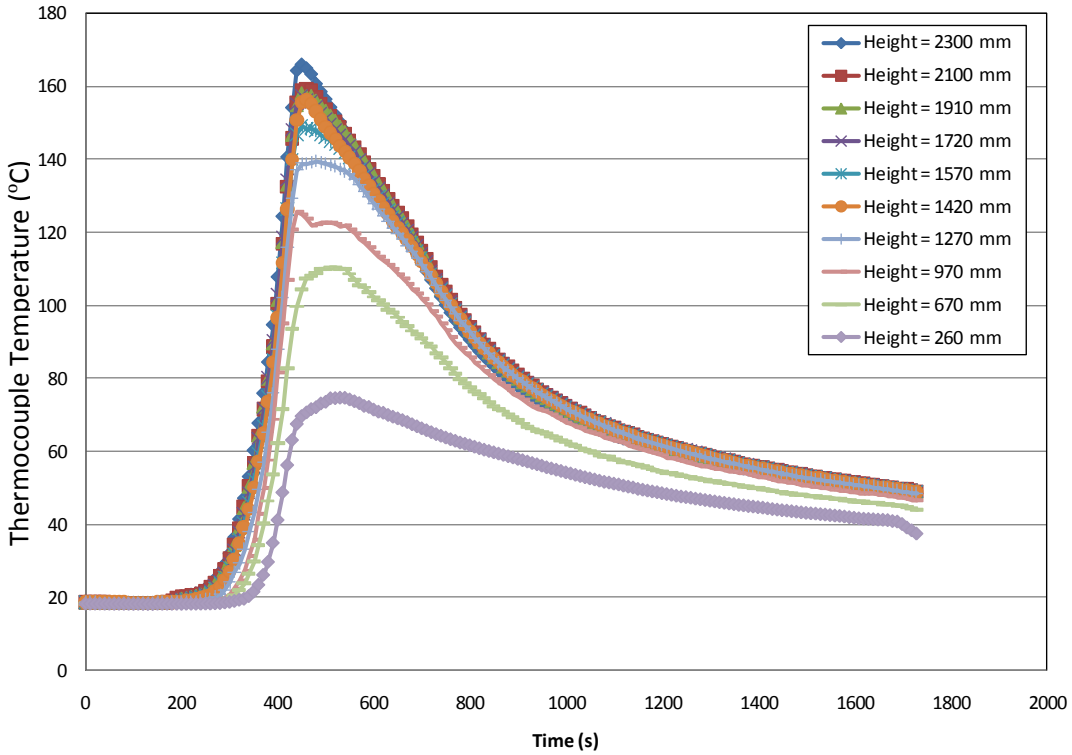

Figure 74: ISO room corner temperatures (°C) at various heights.

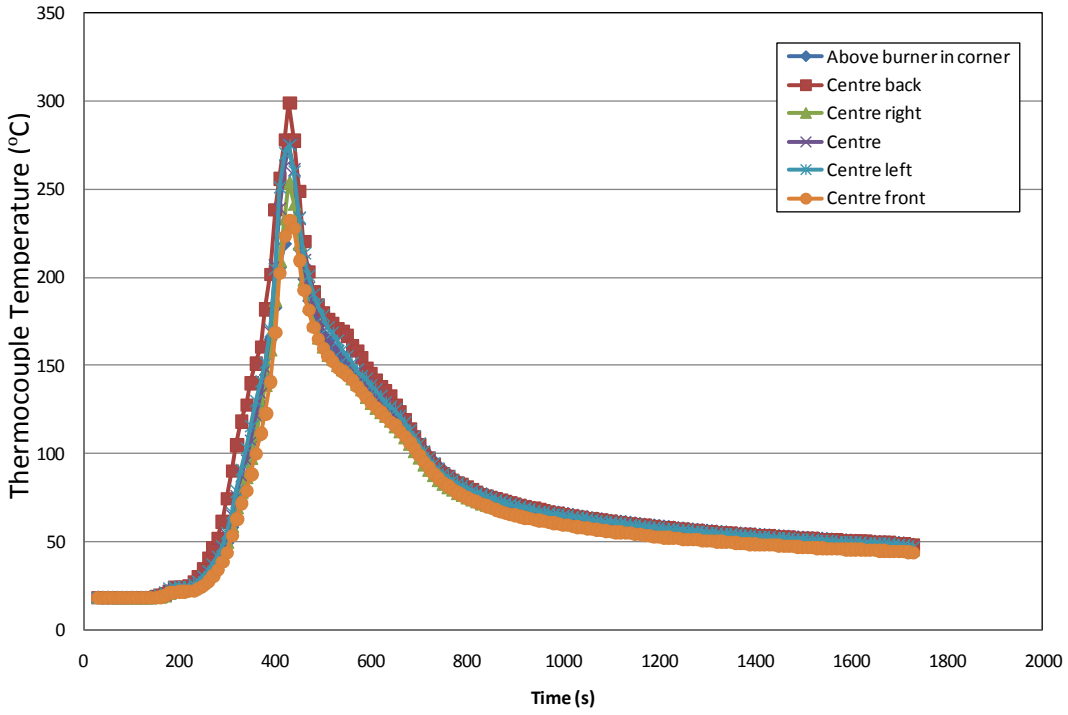

Figure 75: ISO room ceiling temperatures (°C).

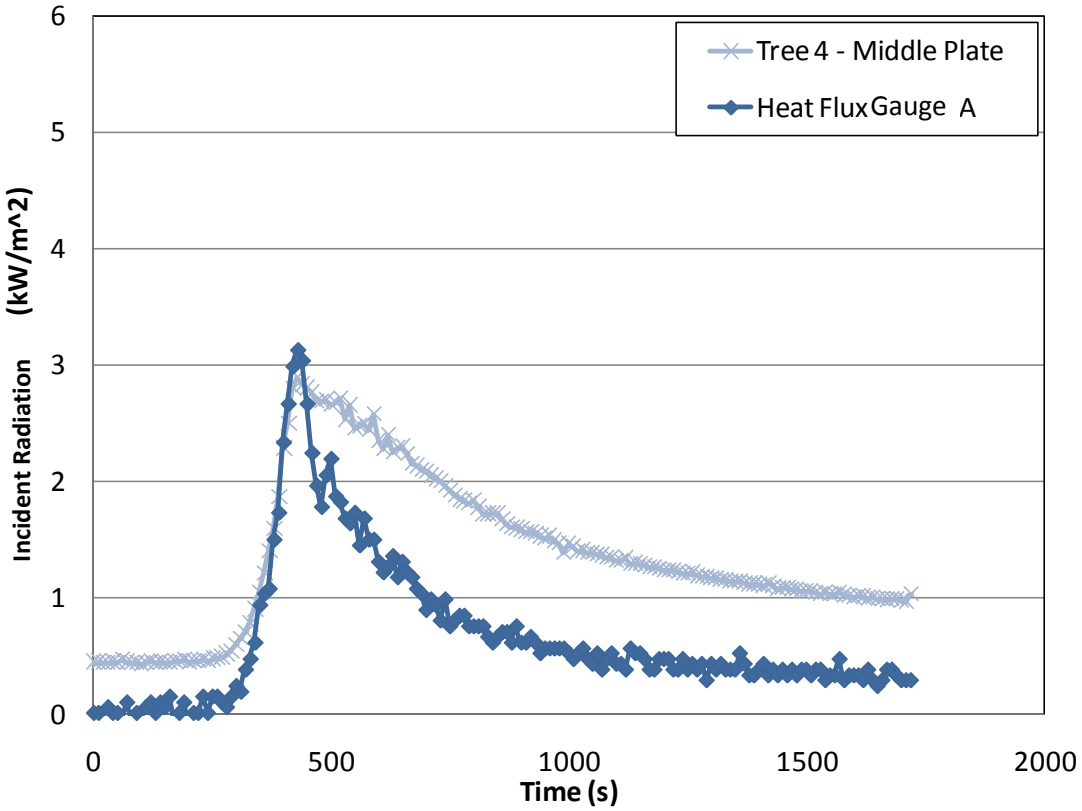

(a)

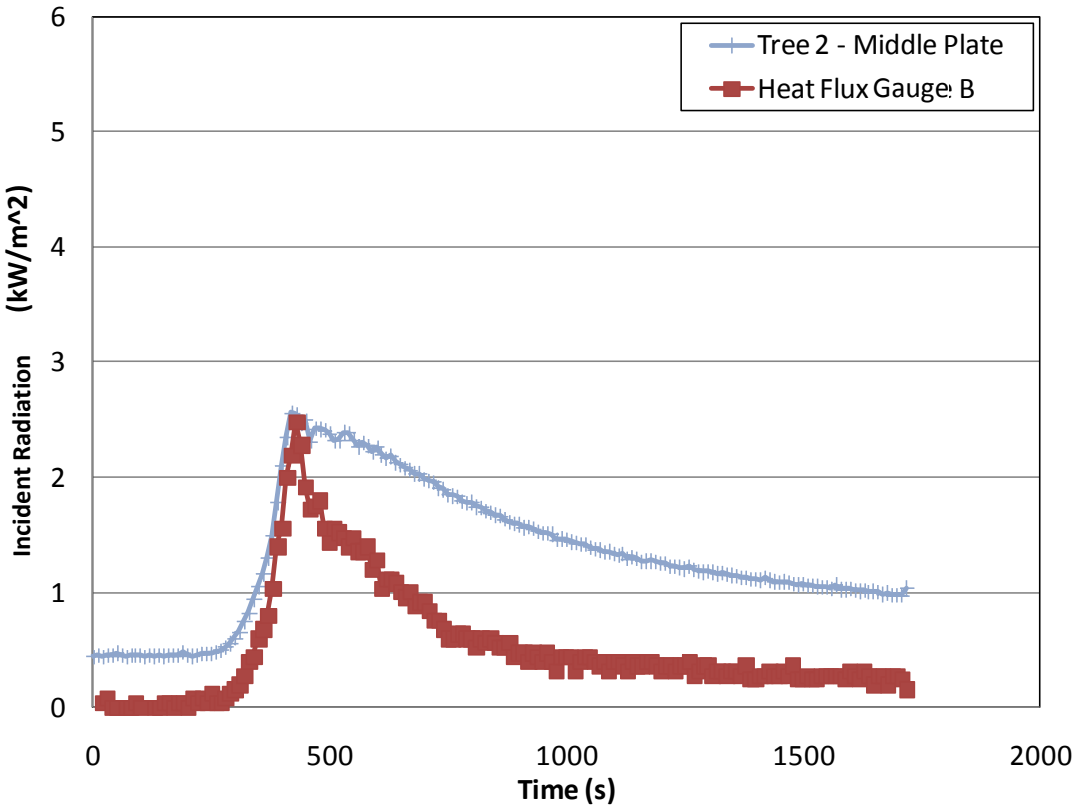

(b)

Figure 76: Estimates of the incident radiative heat flux at the (a) middle plate location of tree 4 and (b) middle plate location of tree 2 from plate thermometer and Gardon gauge measurements.

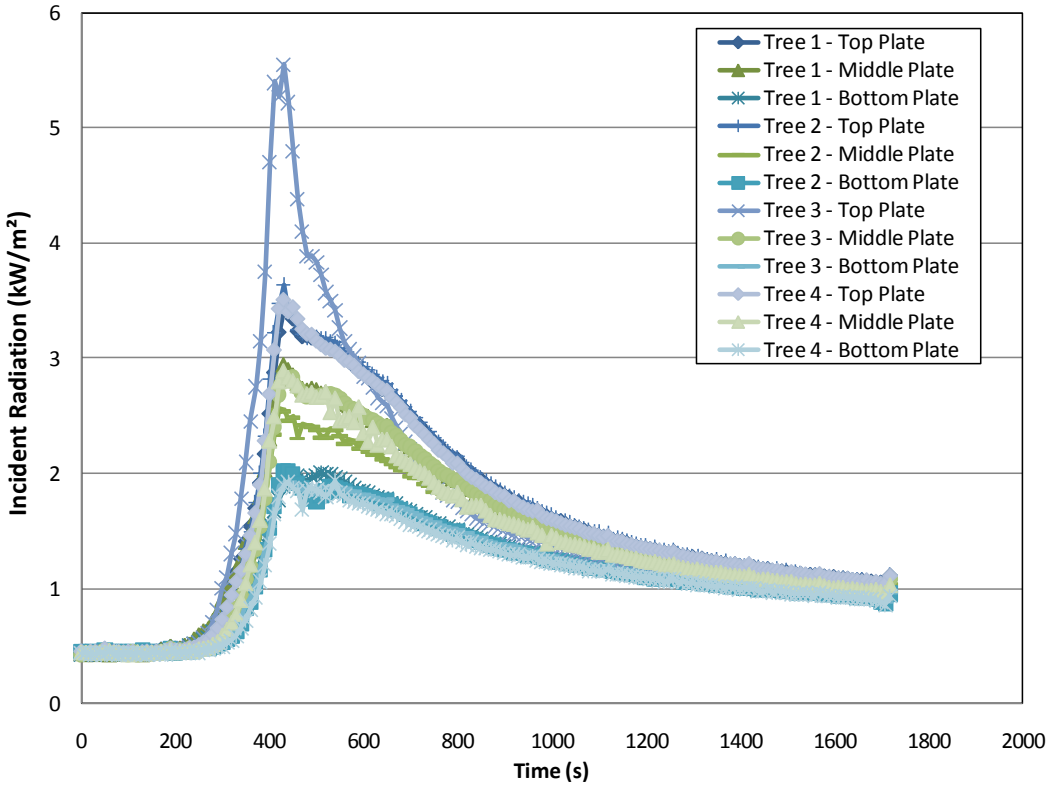

Figure 77: Estimates of the incident radiative heat flux from the plate thermometer measurements at each location on each tree.

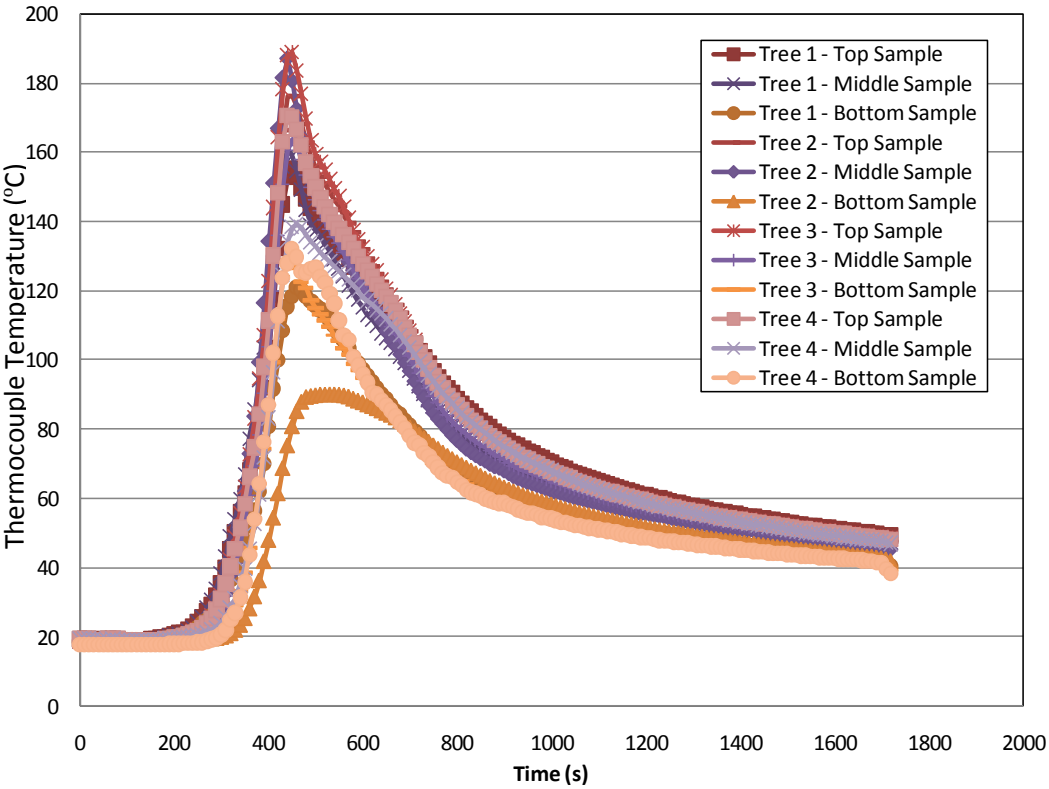

Figure 78: Thermocouple measurements at each sample location on each tree.

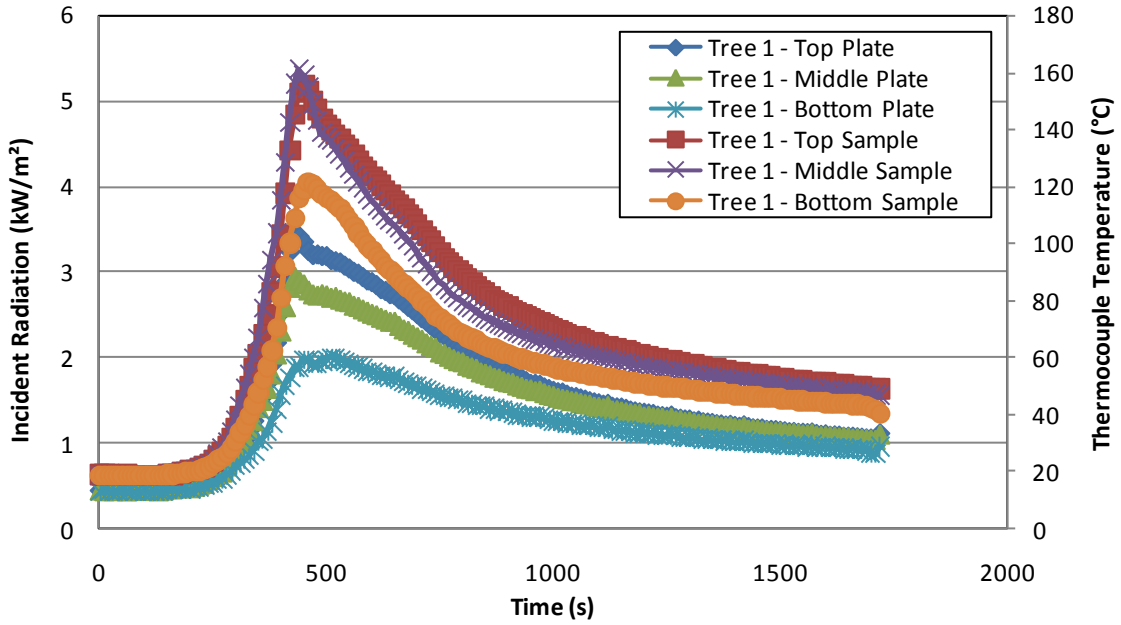
Tree 1 - Top Plate
Tree 1 - Middle Plate
Tree 1 - Bottom Plate
Tree 1 - Top Sample
Tree 1 - Middle Sample
Tree 1 - Bottom Sample
Incident Radiation (kW/m²)
Thermocouple Temperature (°C)
Time (s)
0
1
2
3
4
5
6
0
20
40
60
80
100
120
140
160
180
0
500
1000
1500
2000

(a)

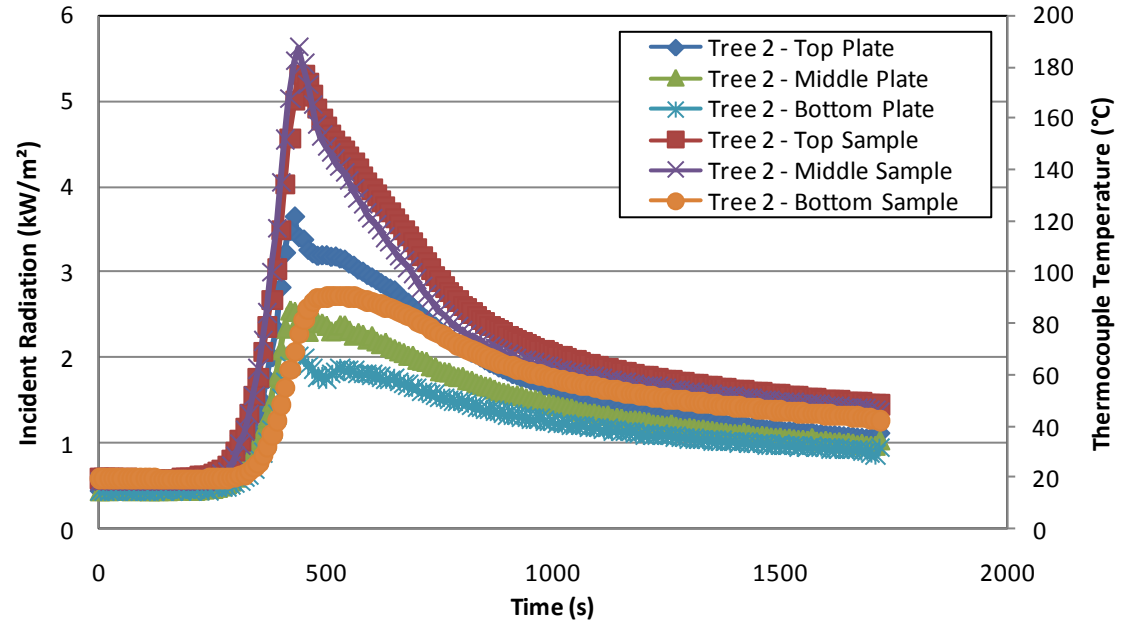
Tree 2 - Top Plate
Tree 2 - Middle Plate
Tree 2 - Bottom Plate
Tree 2 - Top Sample
Tree 2 - Middle Sample
Tree 2 - Bottom Sample
Incident Radiation (kW/m²)
Thermocouple Temperature (°C)
Time (s)
0
1
2
3
4
5
6
0
20
40
60
80
100
120
140
160
180
200
0
500
1000
1500
2000

(b)

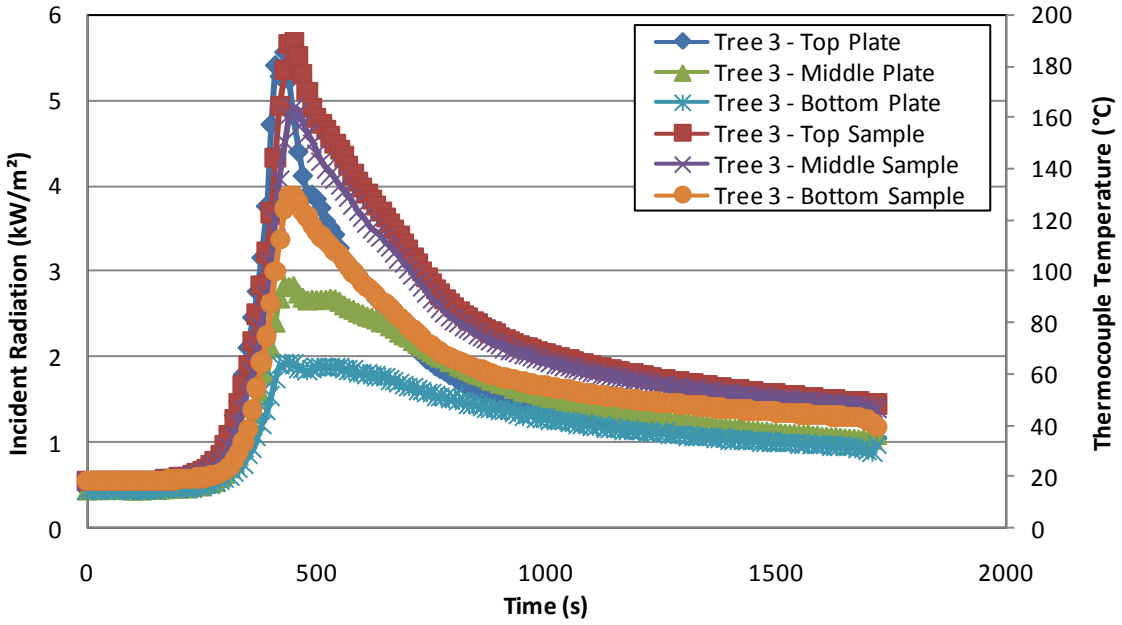

(c)

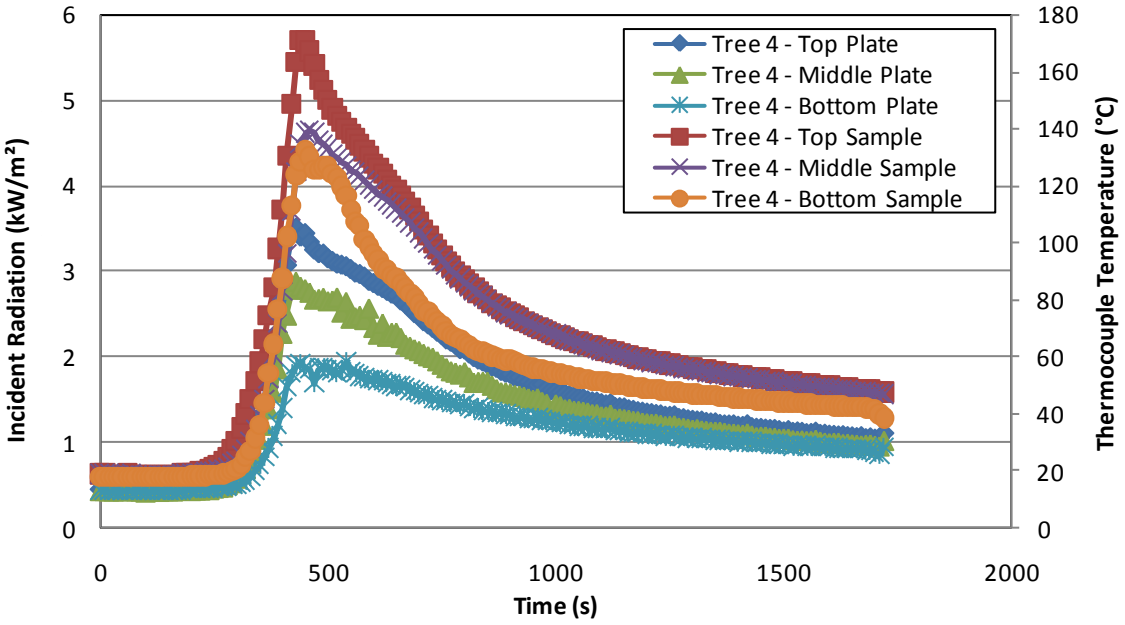

(d)

Figure 79: Thermocouple measurements and estimates of the incident radiation calculated from plate thermometer measurements for each location on each equipment tree: (a) tree 1, (b) tree 2, (c) tree 3 and (d) tree 4.

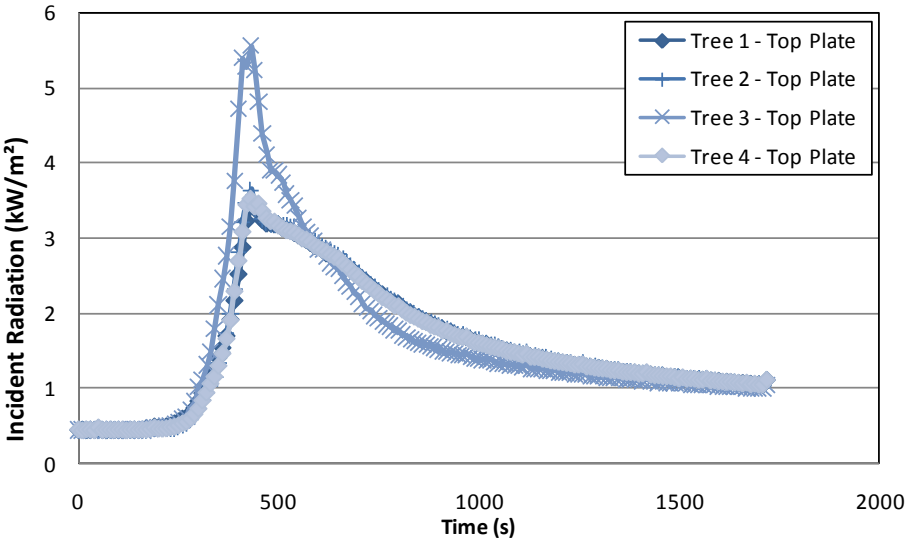

(a)

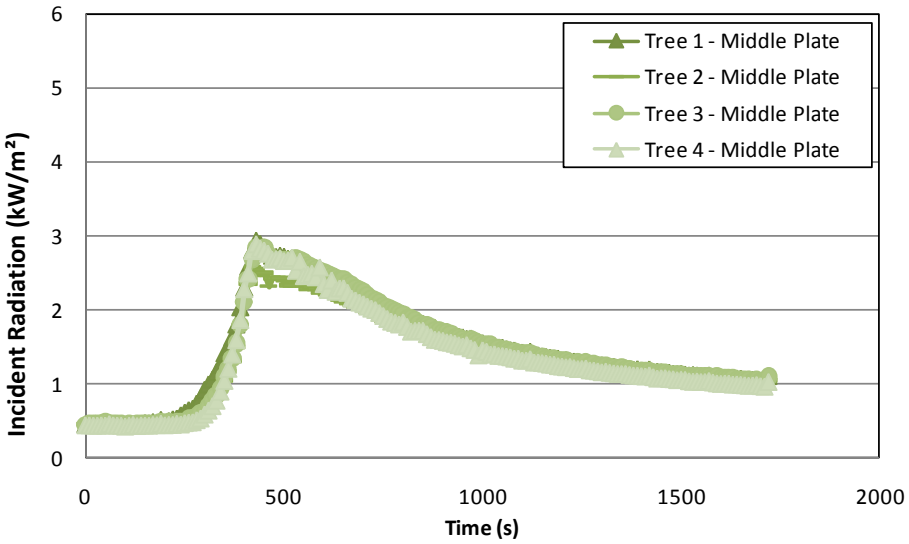

(b)

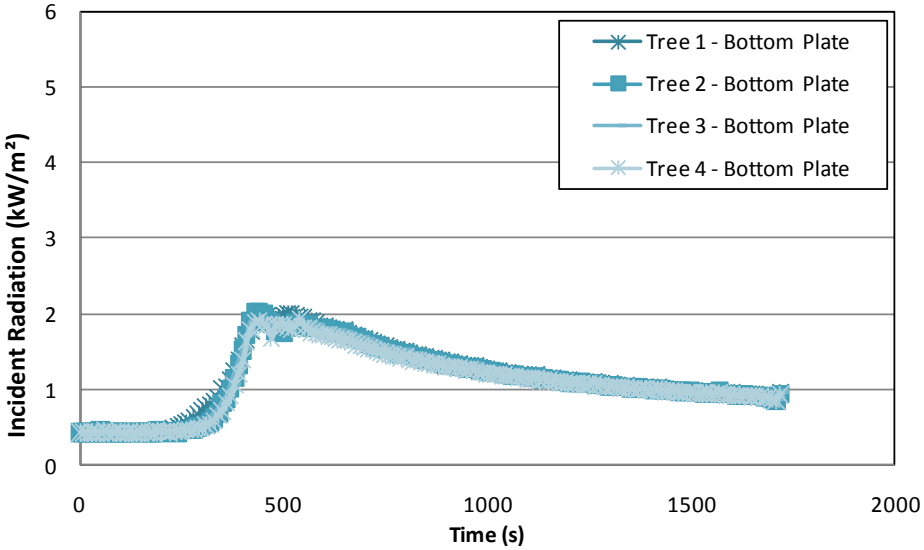

(c)

Figure 80: Estimates of the incident radiation flux calculated from plate thermometer measurements for the (a) top, (b) middle and (c) bottom locations of each of the equipment trees.

6.7.2 Test 3

Similarly to Test 1 presented in the previous section, this ISO room test with a folded mattress example had the equipment trees in the Orientation C set-up (Figure 11). The door of the ISO room was sealed off during the test.

From the temperature measurements in the corner of the ISO room (Figure 82), the layer height and average upper and lower layer temperatures were estimated, as shown in Figure 81. Temperatures just below the ceiling were also measured (Figure 83).

Where plate thermometers were in adjacent locations to the two Gardon gauges, estimates of the incident radiative heat flux from plate thermometer measurements were compared to the Gardon gauge measurements, as shown in Figure 84. In this case the middle plate locations of equipment tree 4 and 2 were directly below the locations of the Gardon gauges.

For all the plate thermometer measurements at each location on each equipment tree, the estimates of the incident radiative heat flux are shown in Figure 85 and the temperatures over each of the adjacent sample materials are shown in Figure 86. For clarity these results are shown for each of the equipment trees in Figure 87. The estimated incident radiative heat fluxes at each of the heights above the floor of the ISO room are shown in Figure 88.

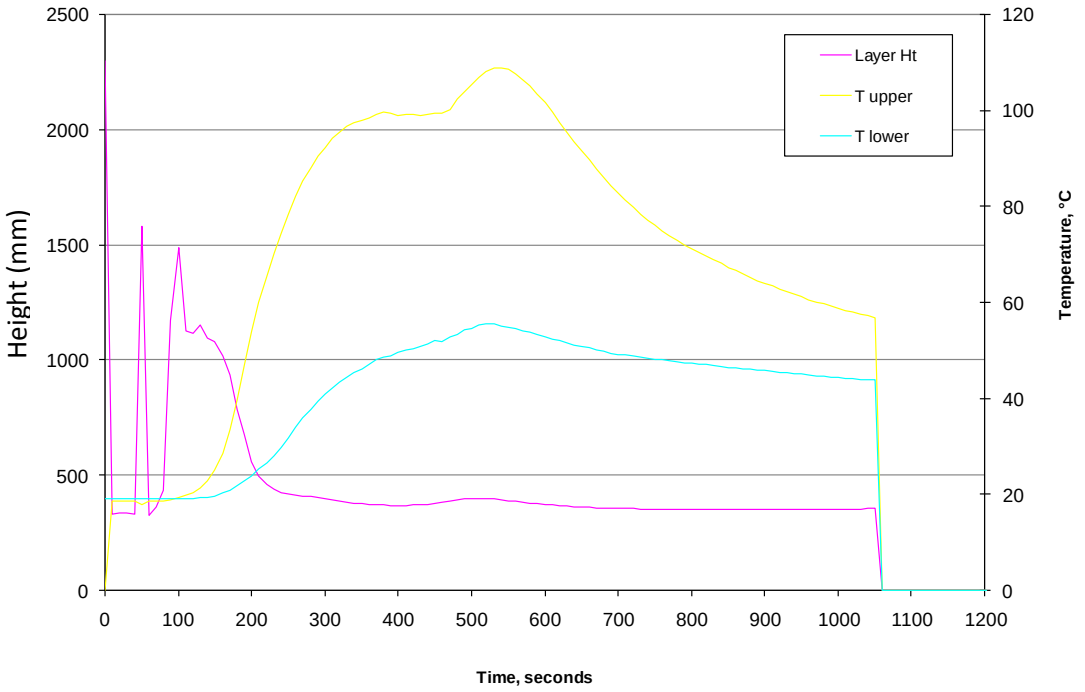

Figure 81: Estimate of the interface height and average upper and lower layer temperatures.

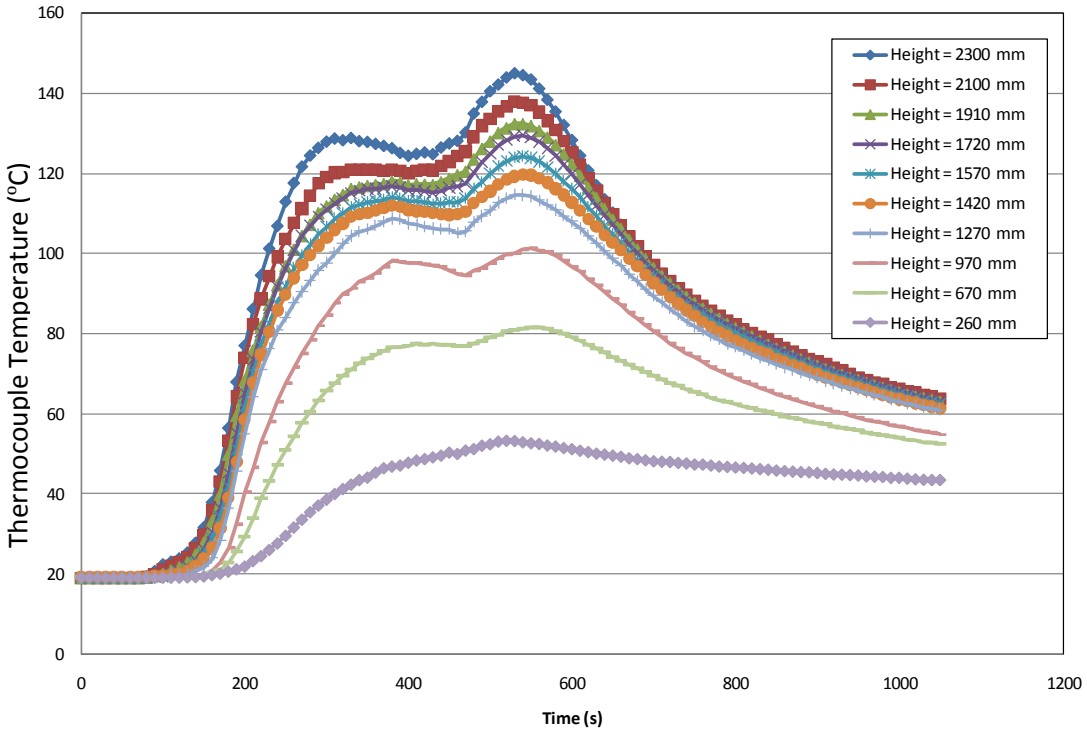

Figure 82: ISO room corner temperatures (°C) at various heights.

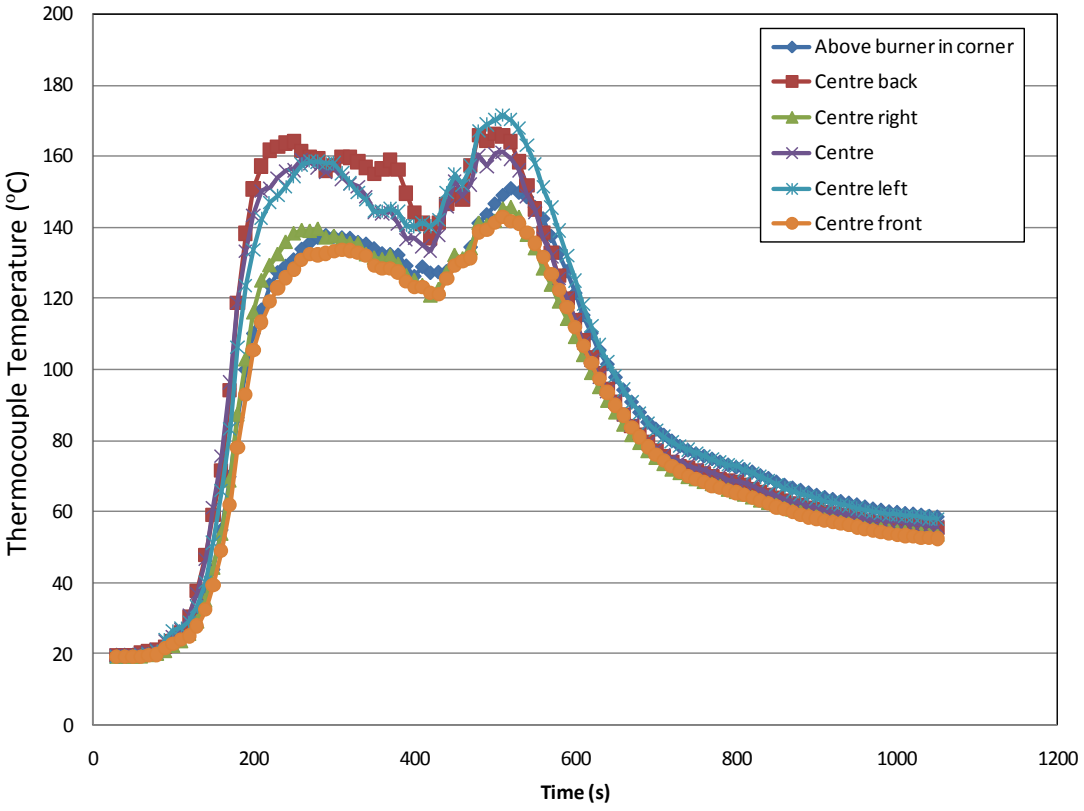

Figure 83: ISO room ceiling temperatures (°C).

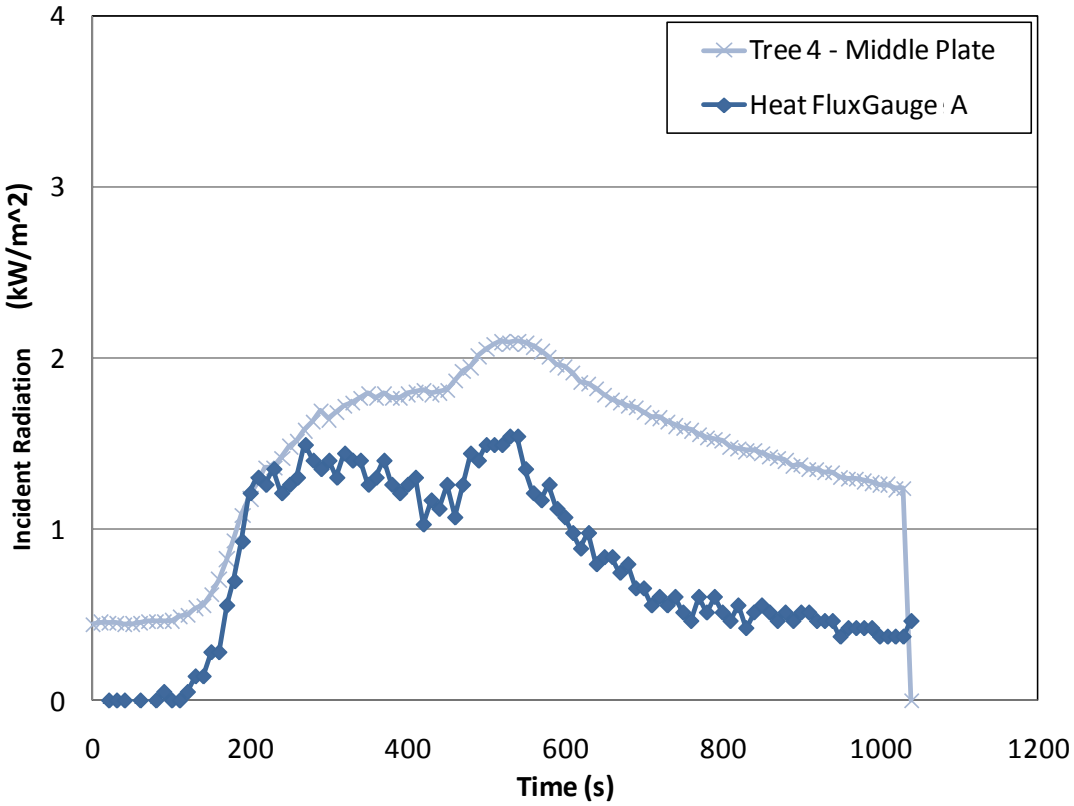

(a)

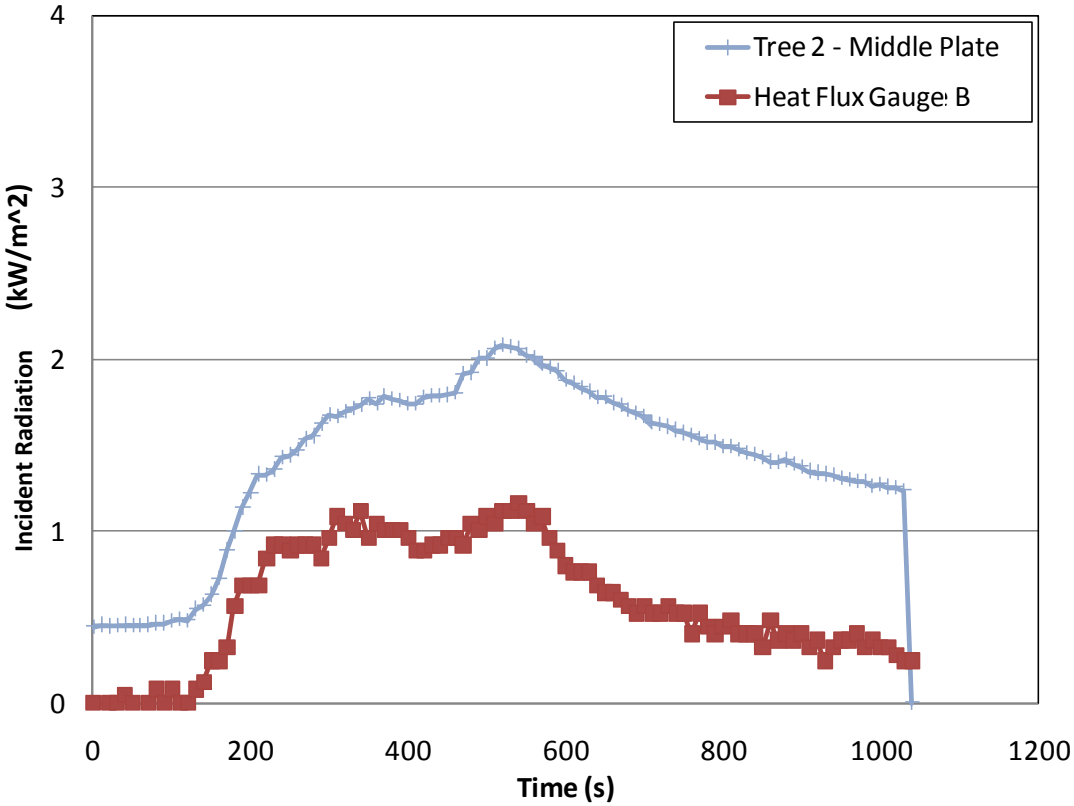

(b)

Figure 84: Estimates of the incident radiative heat flux at the (a) middle plate location of tree 4 and (b) middle plate location of tree 2 from plate thermometer and Gardon gauge measurements.

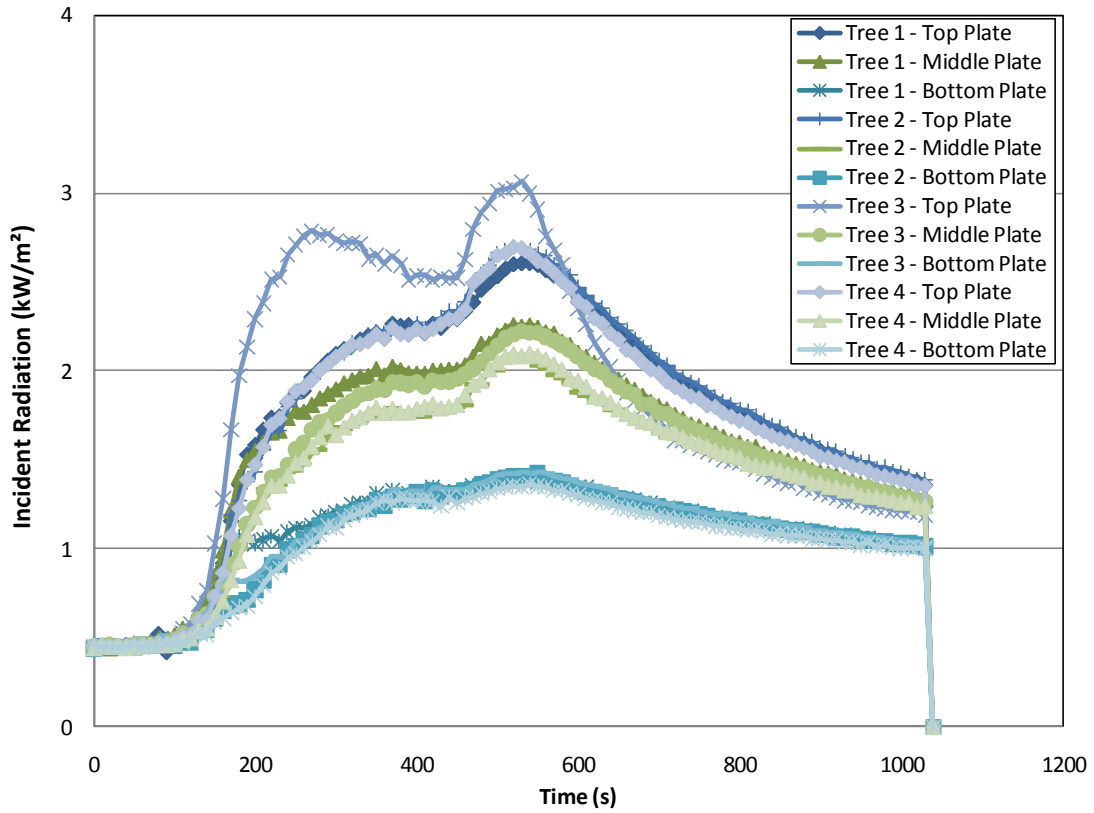

Figure 85: Estimates of the incident radiative heat flux from the plate thermometer measurements at each location on each tree.

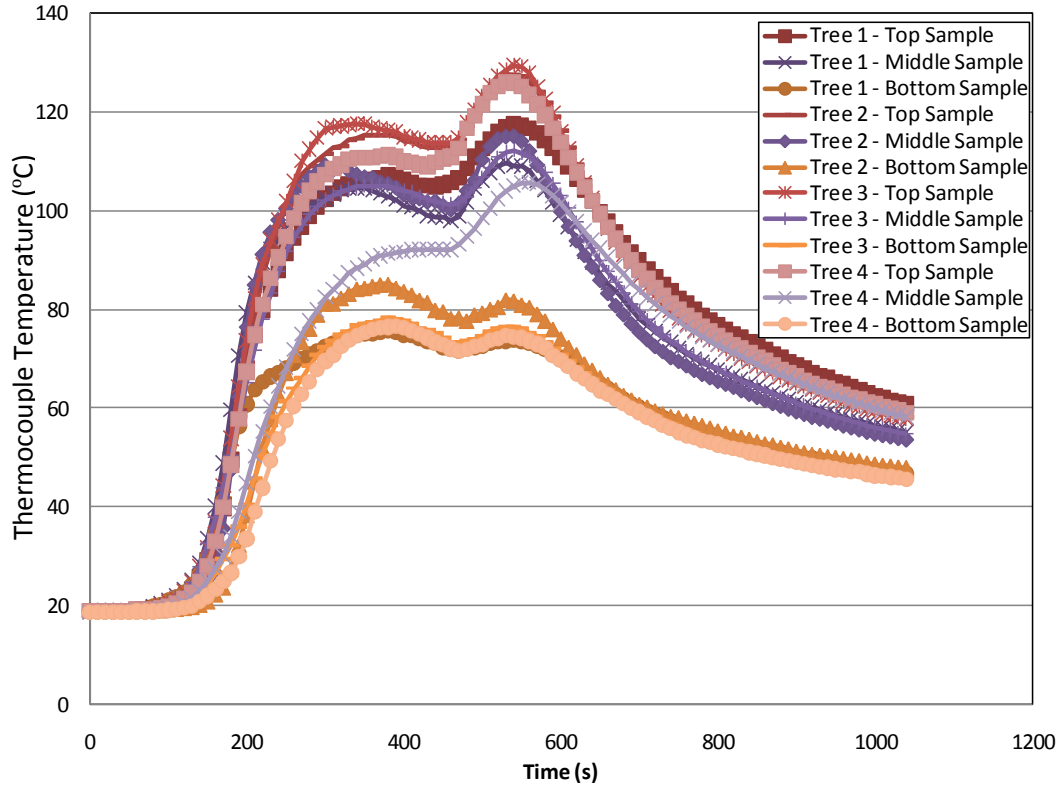

Figure 86: Thermocouple measurements at each sample location on each tree.

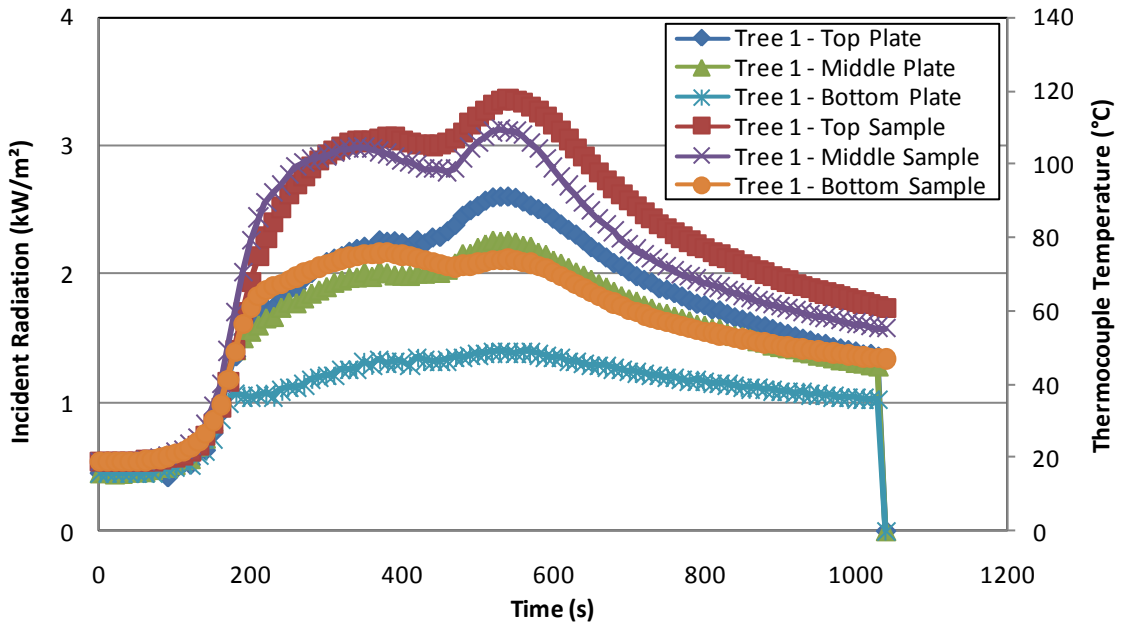
Tree 1 - Top Plate
Tree 1 - Middle Plate
Tree 1 - Bottom Plate
Tree 1 - Top Sample
Tree 1 - Middle Sample
Tree 1 - Bottom Sample
Incident Radiation (kW/m²)
Thermocouple Temperature (°C)
Time (s)
0
1
2
3
4
0
20
40
60
80
100
120
140
0
200
400
600
800
1000
1200

(a)

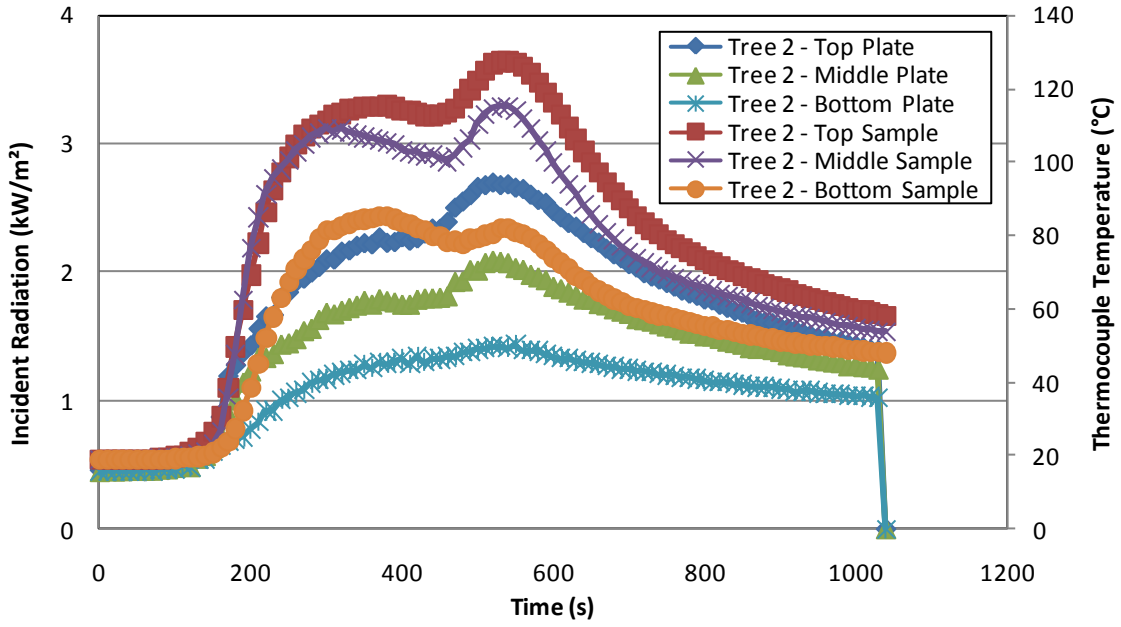
Tree 2 - Top Plate
Tree 2 - Middle Plate
Tree 2 - Bottom Plate
Tree 2 - Top Sample
Tree 2 - Middle Sample
Tree 2 - Bottom Sample
Incident Radiation (kW/m²)
Thermocouple Temperature (°C)
Time (s)
0
1
2
3
4
0
20
40
60
80
100
120
140
0
200
400
600
800
1000
1200

(b)

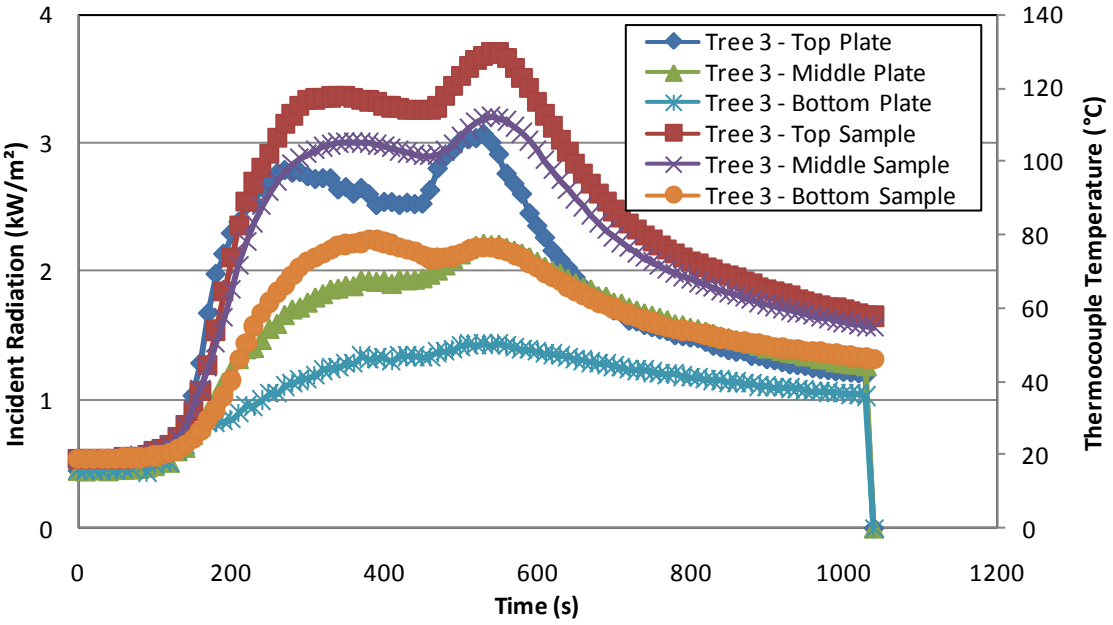

(c)

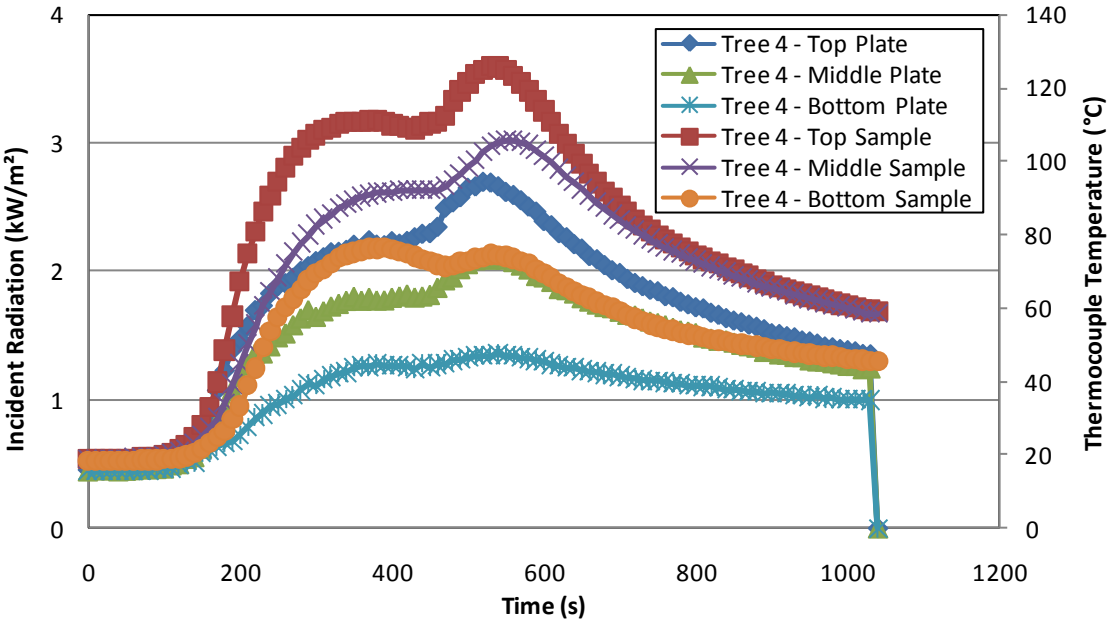

(d)

Figure 87: Thermocouple measurements and estimates of the incident radiation calculated from plate thermometer measurements for each location on each equipment tree: (a) tree 1, (b) tree 2, (c) tree 3 and (d) tree 4.

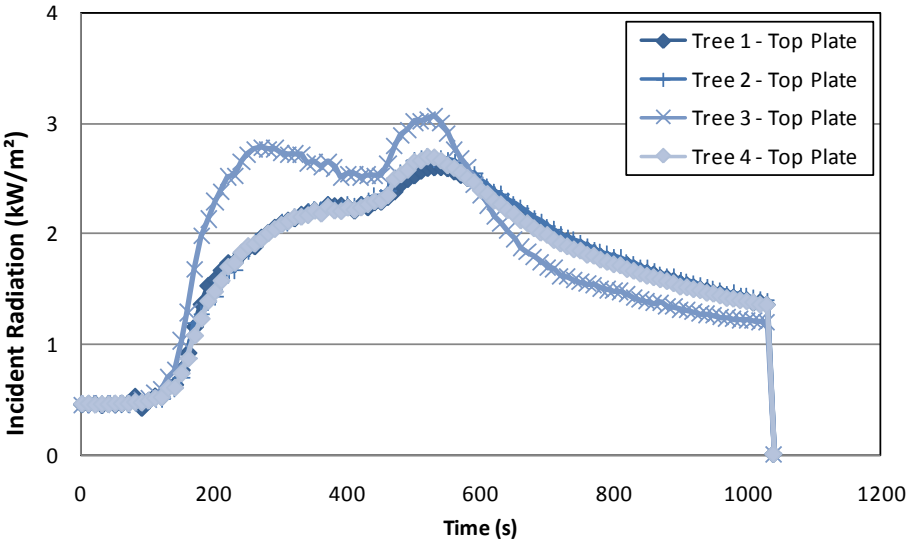

(a)

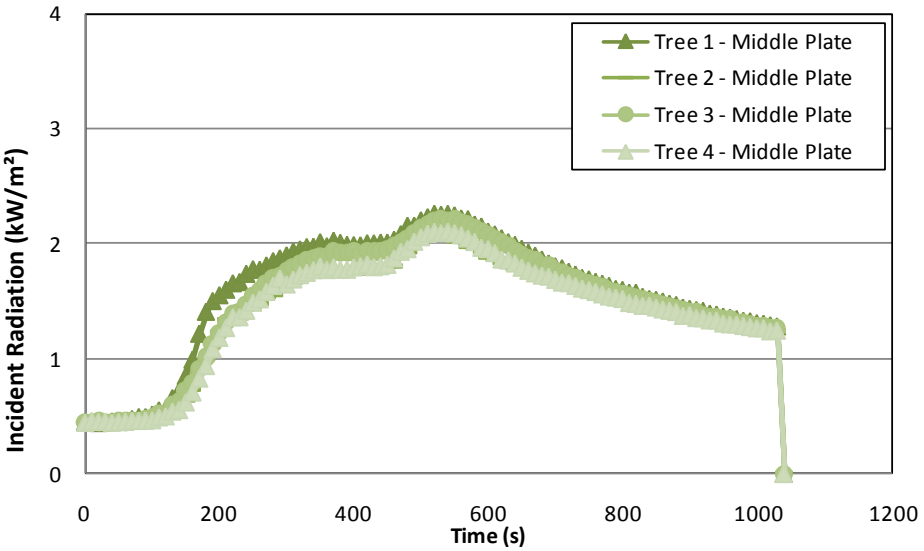

(b)

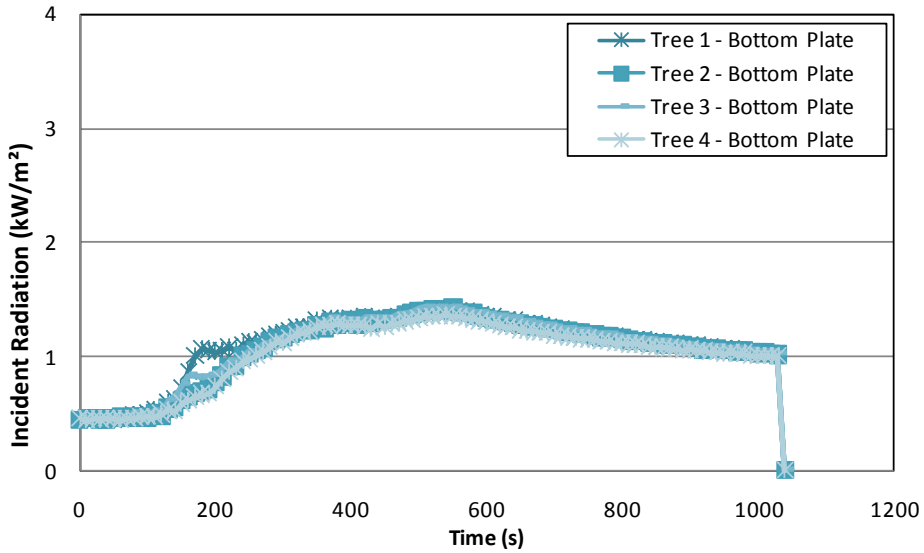

(c)

Figure 88: Estimates of the incident radiation flux calculated from plate thermometer measurements for the (a) top, (b) middle and (c) bottom locations of each of the equipment trees.

7. ANALYSIS OF EXPERIMENTAL RESULTS

7.1 Calibrating plate thermometers – Influence of parameter values

An analysis was performed to assess the range of heat flux values and sensitivities using PERT distributions for input parameters values (of Equation 7 with values presented in Table 3) using @Risk. The sampling of the input parameters was performed using the Latin Hypercube technique with a randomly generated seed and 10,000 iterations were used to calculate the results.

An example of the analysis of the results of the tests used in the calibration of the plate thermometers is presented in this section. Detailed results are included in Appendix A.

7.1.1 Test 3

An example of the calculated incident radiative heat flux based on plate thermometer measurements based on the range of input parameter values presented in Table 3 is shown in Figure 89 for each of the three plates tested in the horizontal orientation in the cone calorimeter. The results show the mean, 5th and 95th percentiles of the results for the distributed input parameter values calculated using @Risk (as described in Section 5.2.1) for each of the plates. The target incident radiative heat flux was 19 kW/m².

A measure of the sensitivity of the results to each of the input parameters is shown in Figure 90, Figure 91 and Figure 92 for Plates A, B and C respectively. These are the linear regression analysis results for the calculation of the incident radiative heat flux at three point that correspond to the initial rapid rise (a), the quasi steady state (c) and the midpoint between these two (c).

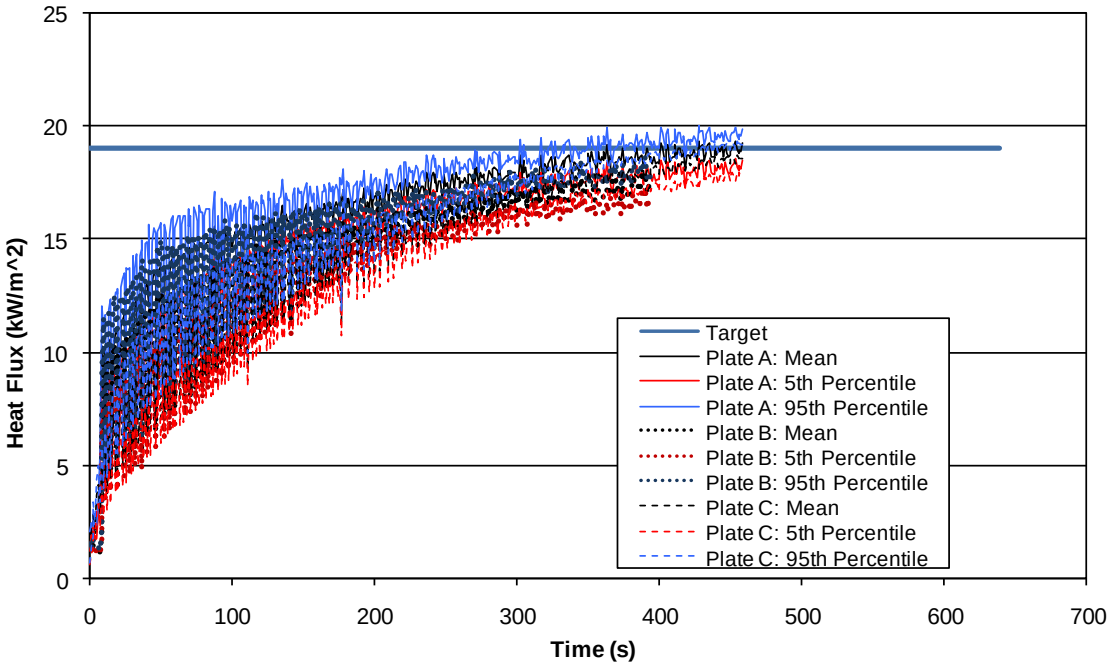

(a)

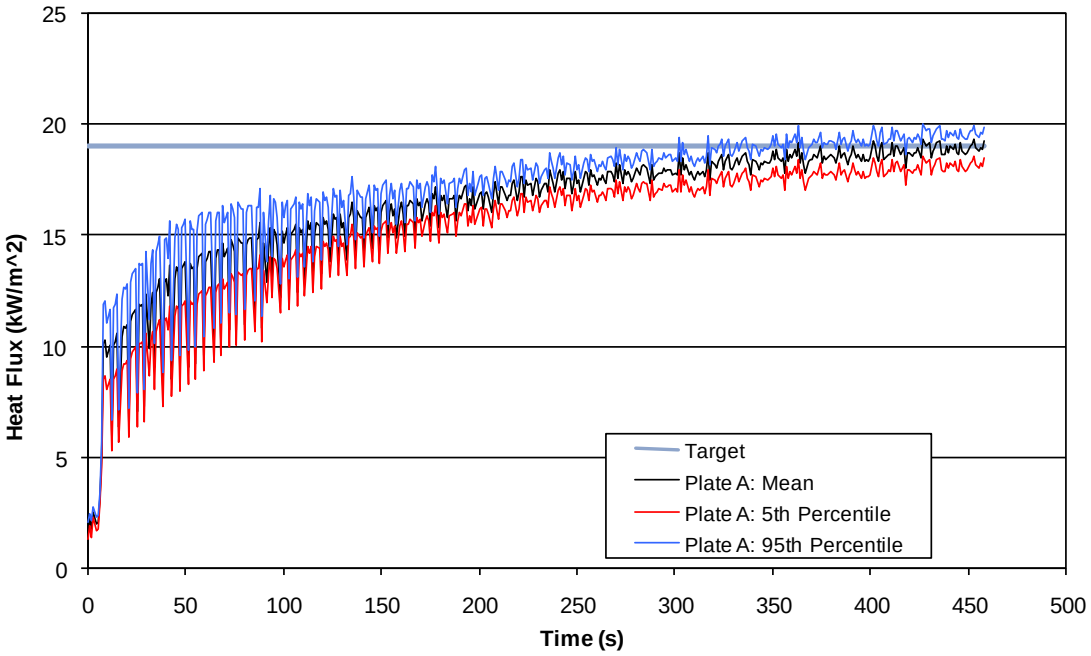
25
20
15
10
5
0
Heat Flux (kW/m^2)
0
50
100
150
200
250
300
350
400
450
500
Time (s)
Target
Plate A: Mean
Plate A: 5th Percentile
Plate A: 95th Percentile

(b)

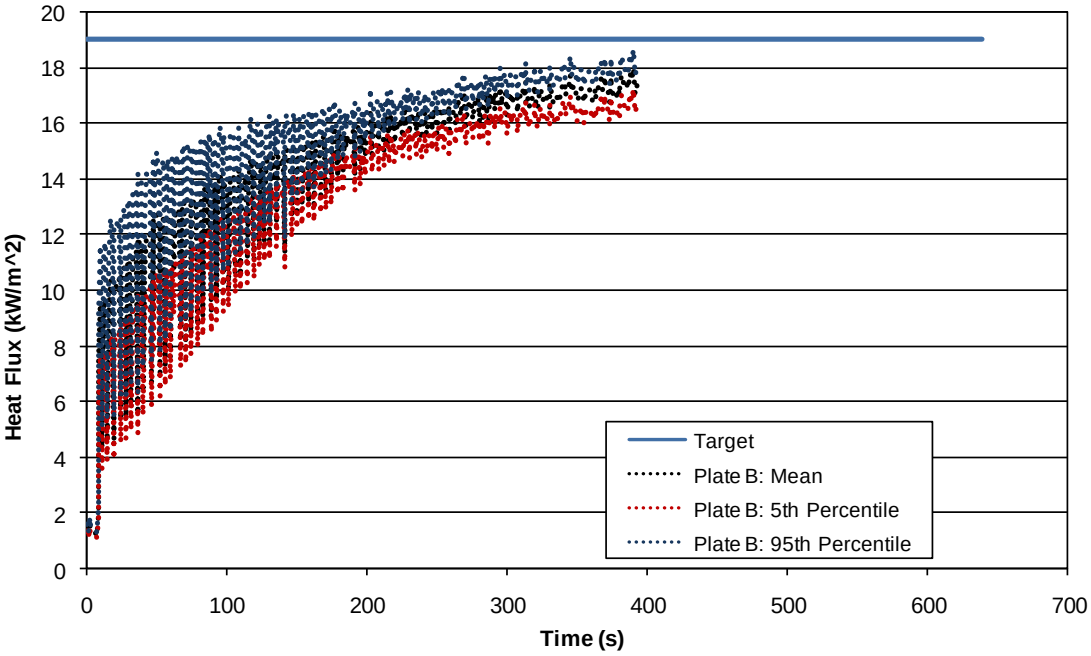
20
18
16
14
12
10
8
6
4
2
0
Heat Flux (kW/m^2)
0
100
200
300
400
500
600
700
Time (s)
Target
Plate B: Mean
Plate B: 5th Percentile
Plate B: 95th Percentile

(c)

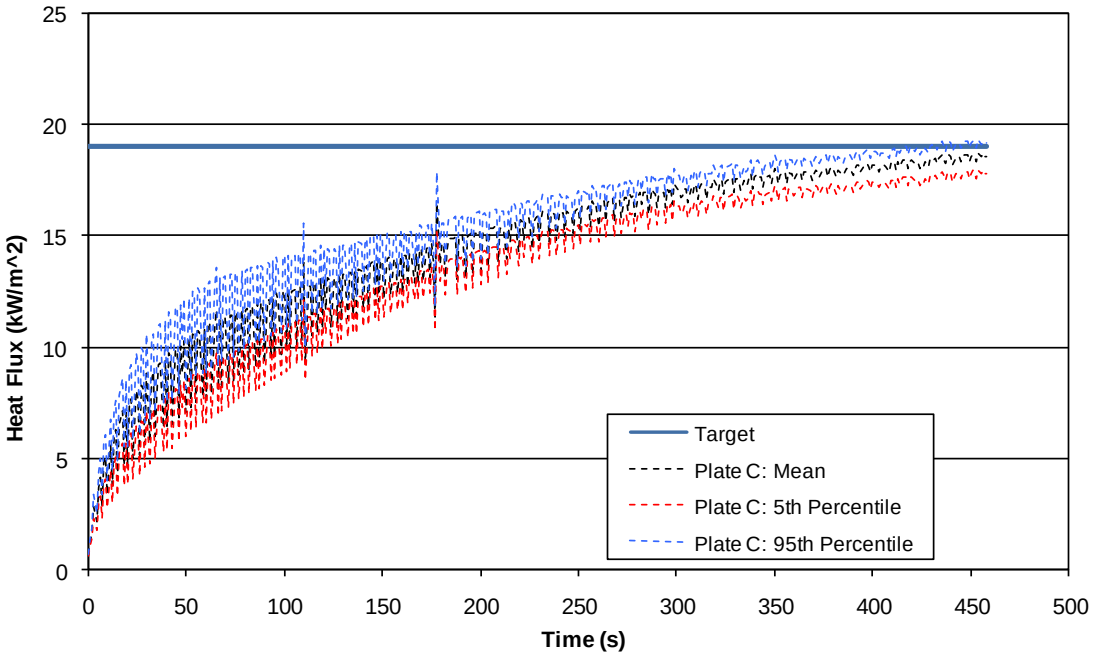

(d)

Figure 89: Calculated heat flux based on plate thermometer measurements for (a) all plates tested, (b) Plate A, (c) Plate B and (d) Plate C for the mean, 5th and 95th percentiles, based on input parameters presented in Table 3, with a target radiation level of 19 kW/m².

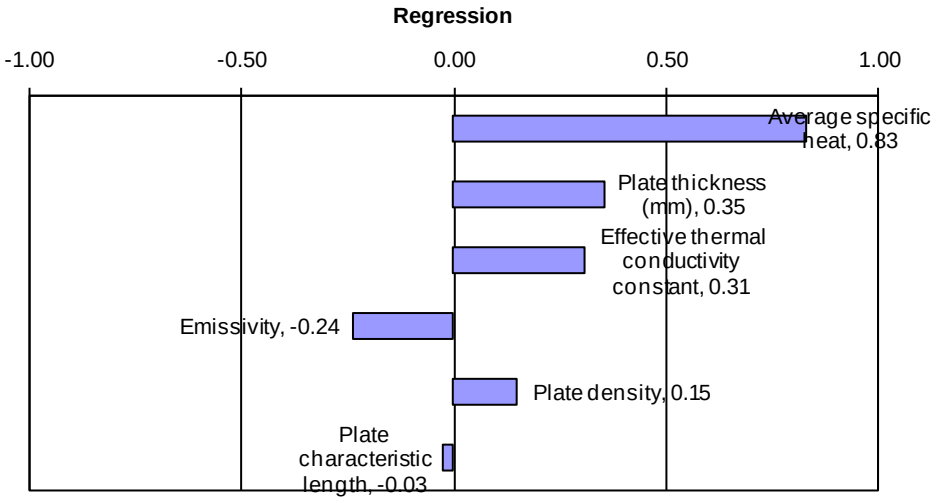

(a)

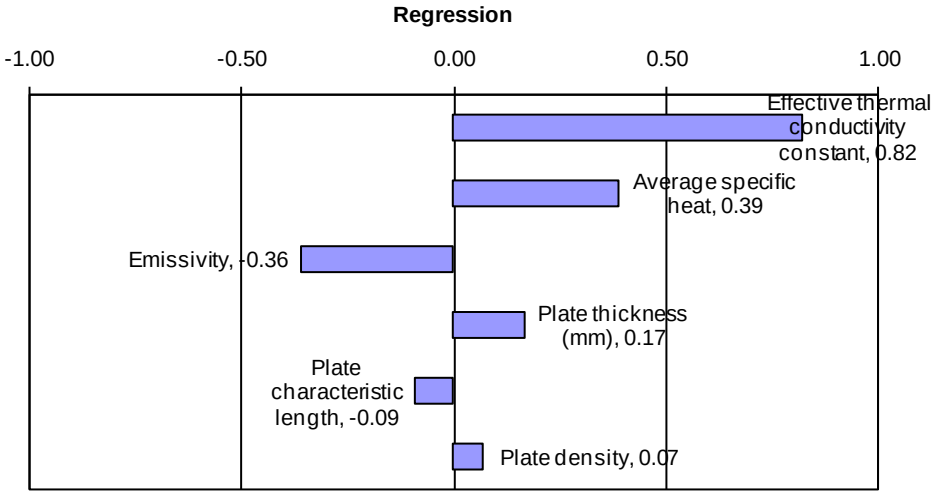

(b)

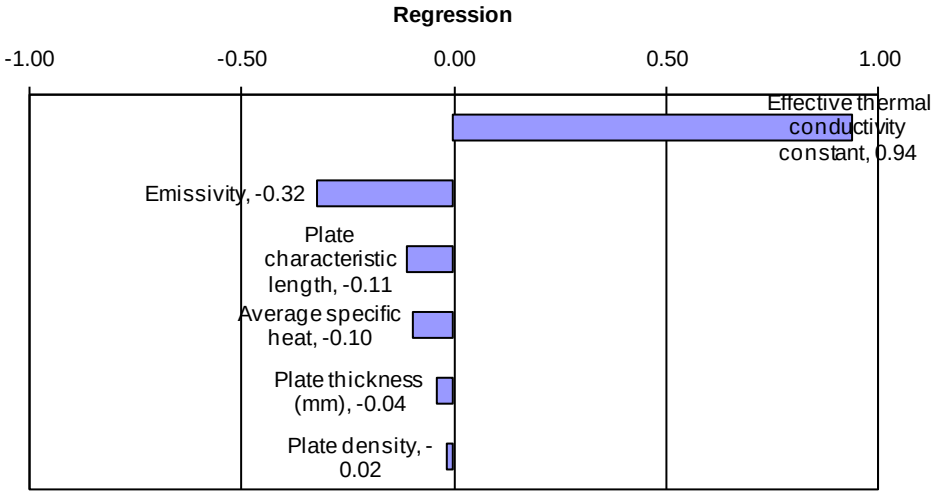

(c)

Figure 90: Linear regression analysis results for Plate A with a target radiation level of 19 kW/m², where (a), (b) and (c) relate to the times 2, 76 and 485 s in Figure 12 respectively.

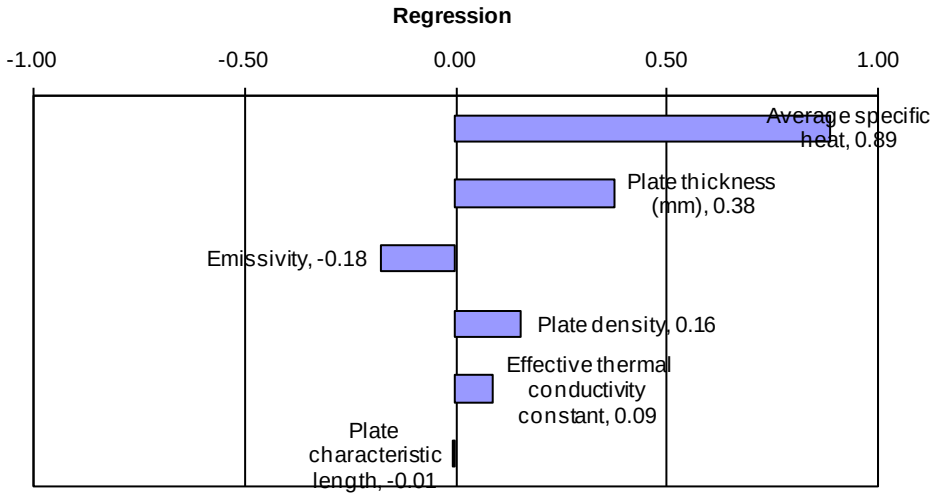

(a)

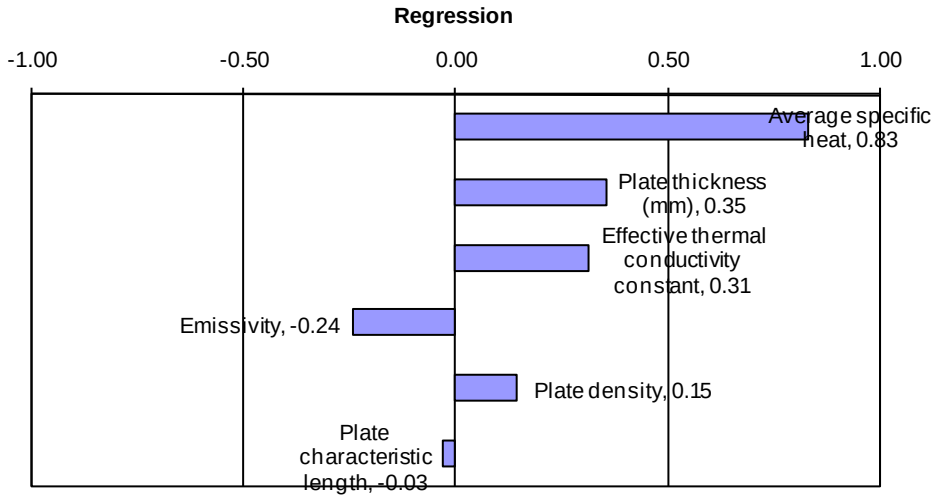

(b)

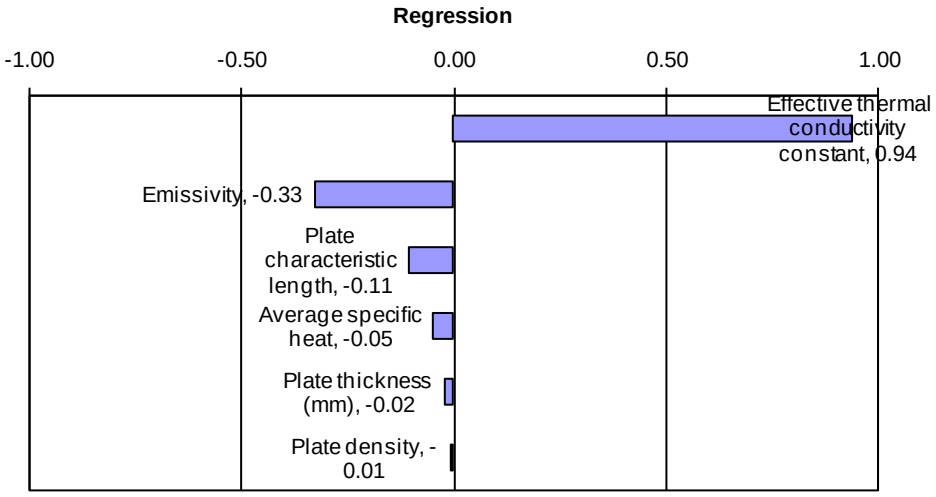

(c)

Figure 91: Linear regression analysis results for Plate B with a target radiation level of 19 kW/m², where (a), (b) and (c) relate to the times 3, 52 and 346 s in Figure 12 respectively.

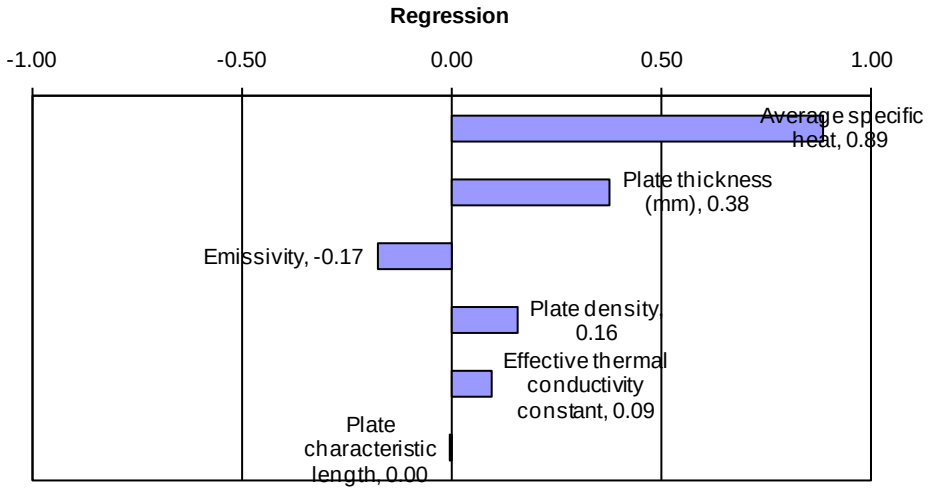

(a)

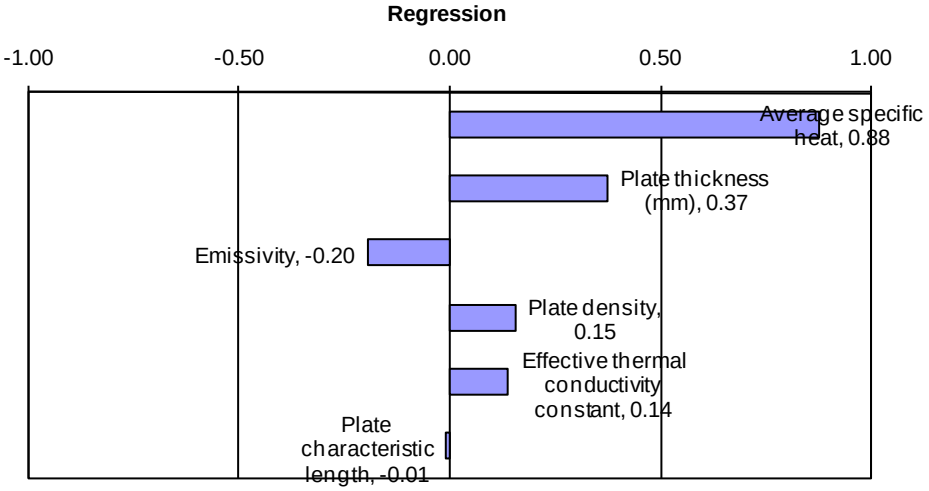

(b)

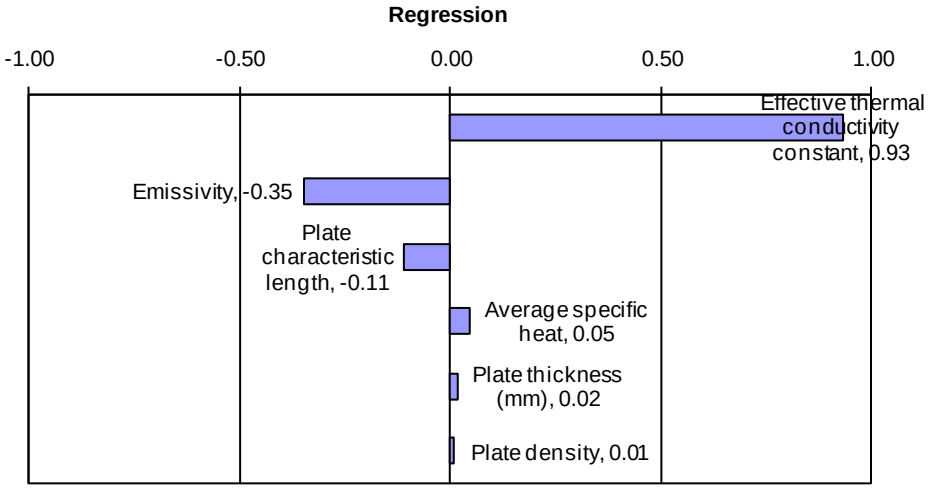

(c)

Figure 92: Linear regression analysis results for Plate C with a target radiation level of 19 kW/m², where (a), (b) and (c) relate to the times 2, 181 and 471 s in Figure 12 respectively.

7.2 Calibrating plate thermometers – Response

A simple stability analysis was performed to assess the behaviour of the system during the response of a plate thermometer to a constant incident heat flux (during the cone calorimeter tests, Section 5.2.1). The rate of change of the recorded data between sequential time steps provides a measure of the stability of the system. That is, whether the system is smoothly approaching a quasi steady state or whether there is oscillation about points or other combinations of behaviour.

An example of the analysis of the response of the plate thermometers to an incident heat flux during the calibration tests, as discussed in Section 5.2.1, is presented in this section. Detailed results are presented in Appendix A.

7.2.1 Test 3

The example results of cone calorimeter Test 3, with a target incident radiative heat flux level of 19 kW/m², are shown here.

The estimated incident radiative heat flux based on plate thermometer measurements and the 'best' input parameter values presented in Table 3 is shown in Figure 93 for each of the three plates tested. The fraction difference between sequential time steps for the estimated incident radiation is also shown in Figure 93. The fraction difference of estimated incident radiation between sequential time steps $\left(\frac{\dot{q}_{inc,t=n}-\dot{q}_{inc,t=n-1}}{\dot{q}_{inc,t=n}}\right)$ versus the estimated incident radiation $\left(\dot{q}_{inc,t=n}\right)$ is shown in Figure 94.

The results of Plate C are presented here as an example of the analysis of the stability of the data set collected. The temperature measurements of the plate thermometer $\left(T_{TP,t=n}\right)$ and the fraction of the temperature difference between time steps to the plate temperature $\left(\frac{T_{TP,t=n}-T_{TP,t=n-1}}{T_{TP,t=n}}\right)$ is shown in Figure 95. The difference in the temperature of the plate thermometer between time steps versus the plate temperature is shown in Figure 96. The difference in the temperature of the plate thermometer between time steps as a fraction of the plate temperature versus the plate temperature is shown in Figure 97.

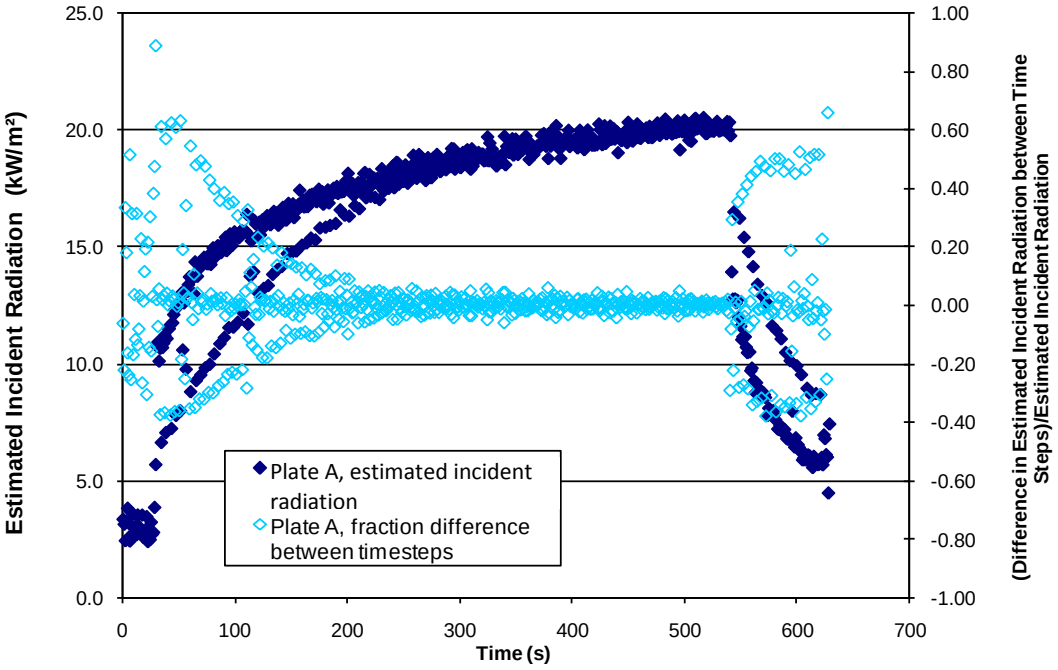
Estimated Incident Radiation (kW/m²)
(Difference in Estimated Incident Radiation between Time Steps)/Estimated Incident Radiation
Time (s)
Plate A, estimated incident radiation
Plate A, fraction difference between timesteps
25.0
20.0
15.0
10.0
5.0
0.0
1.00
0.80
0.60
0.40
0.20
0.00
-0.20
-0.40
-0.60
-0.80
-1.00
0
100
200
300
400
500
600
700

(a)

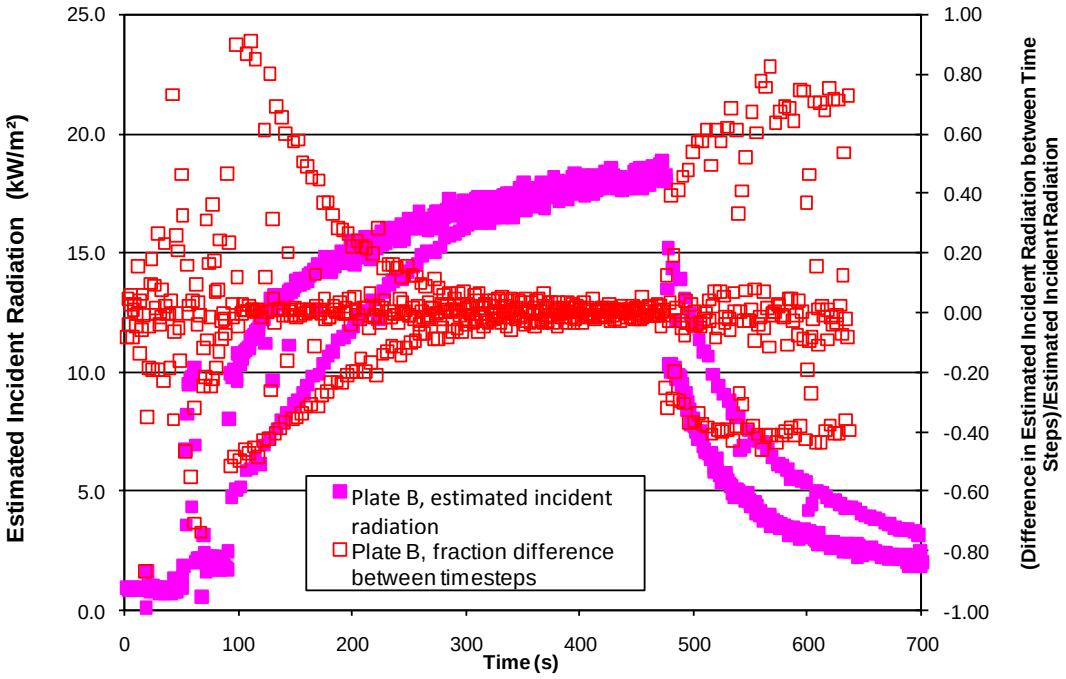
Estimated Incident Radiation (kW/m²)
(Difference in Estimated Incident Radiation between Time Steps)/Estimated Incident Radiation
Time (s)
Plate B, estimated incident radiation
Plate B, fraction difference between timesteps
25.0
20.0
15.0
10.0
5.0
0.0
1.00
0.80
0.60
0.40
0.20
0.00
-0.20
-0.40
-0.60
-0.80
-1.00
0
100
200
300
400
500
600
700

(b)

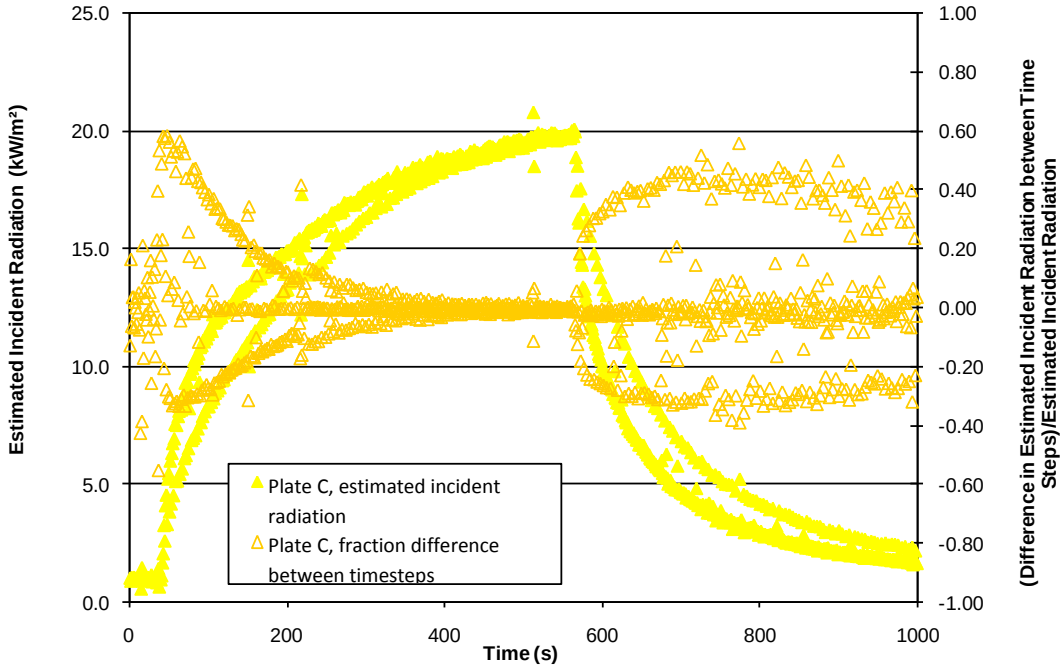

(c)

Figure 93: Calculated heat flux based on plate thermometer measurements and the fraction difference of estimated incident radiation between time steps for (a) Plate A, (b) Plate B and (c) Plate C, based on 'best' input parameters presented in Table 3, with a target radiation level of 19 kW/m².

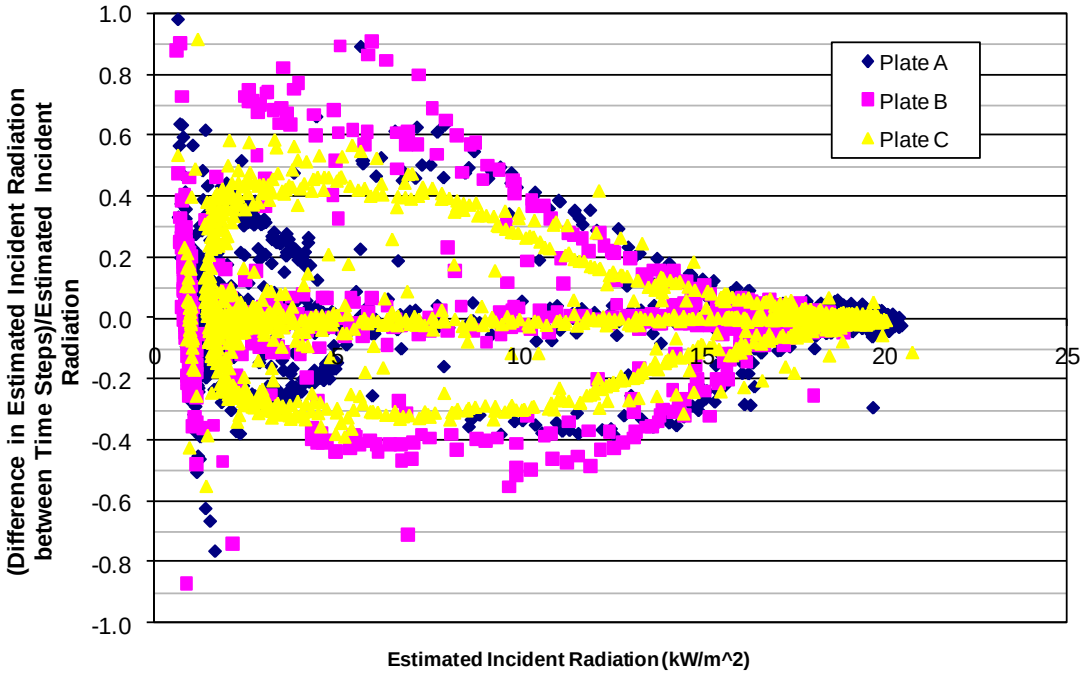

Figure 94: The fraction difference of estimated incident radiation between sequential time steps versus the estimated incident radiation.

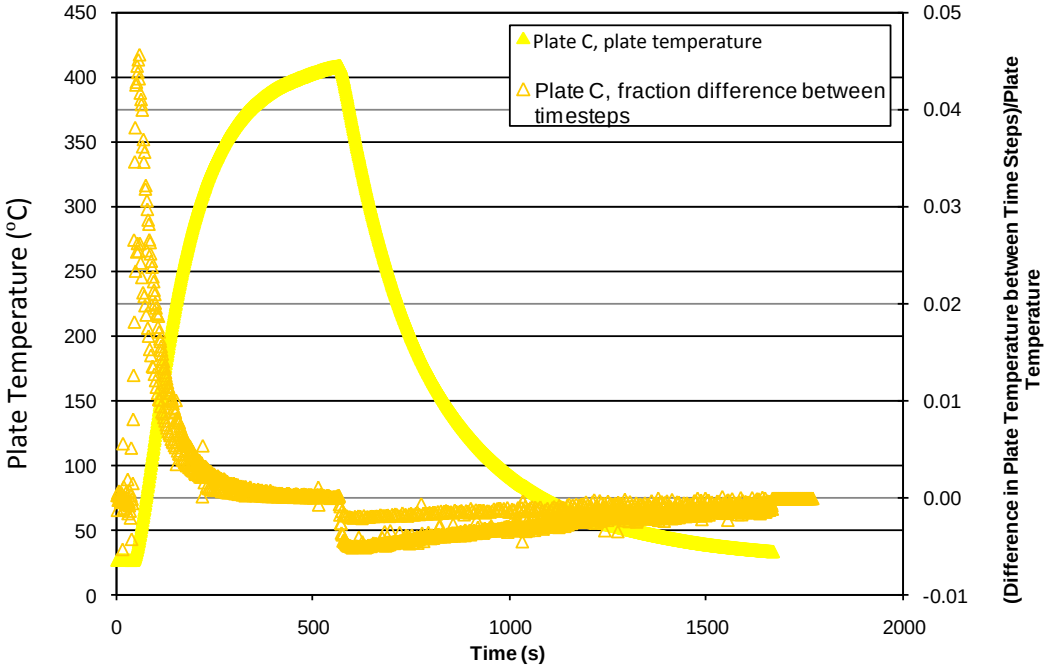

Figure 95: Temperature measurements of the plate thermometer compared with the fraction of the temperature difference between time steps to the plate temperature for Plate C.

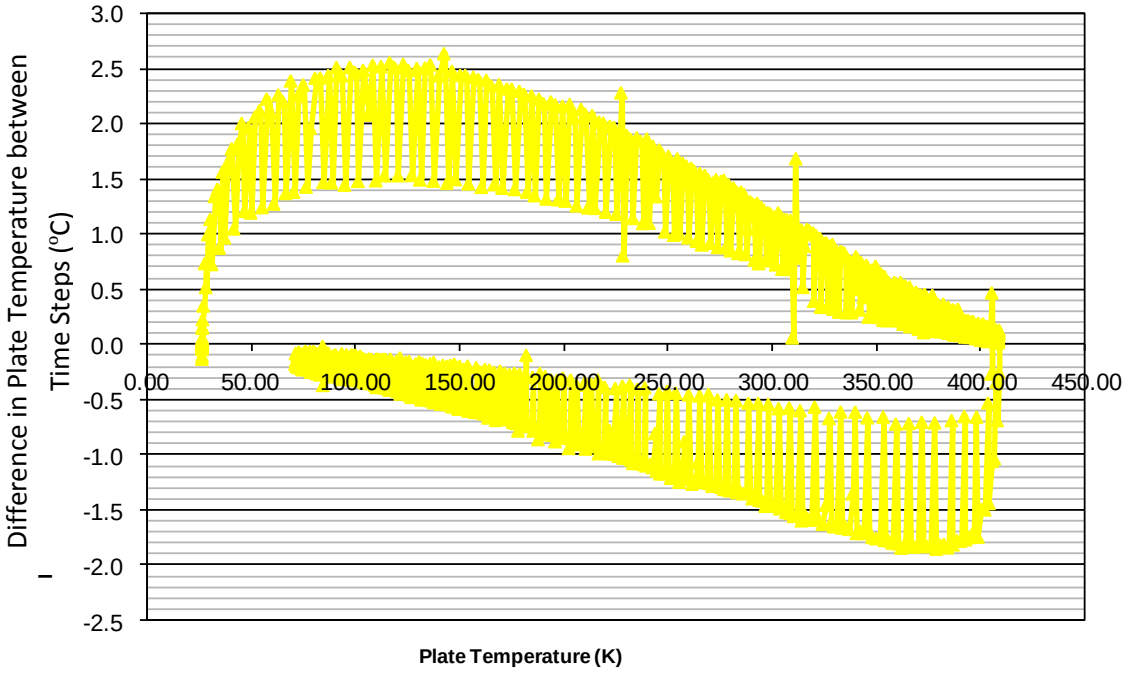

Figure 96: Difference in the temperature of the plate thermometer between time steps versus the plate temperature for Plate C.

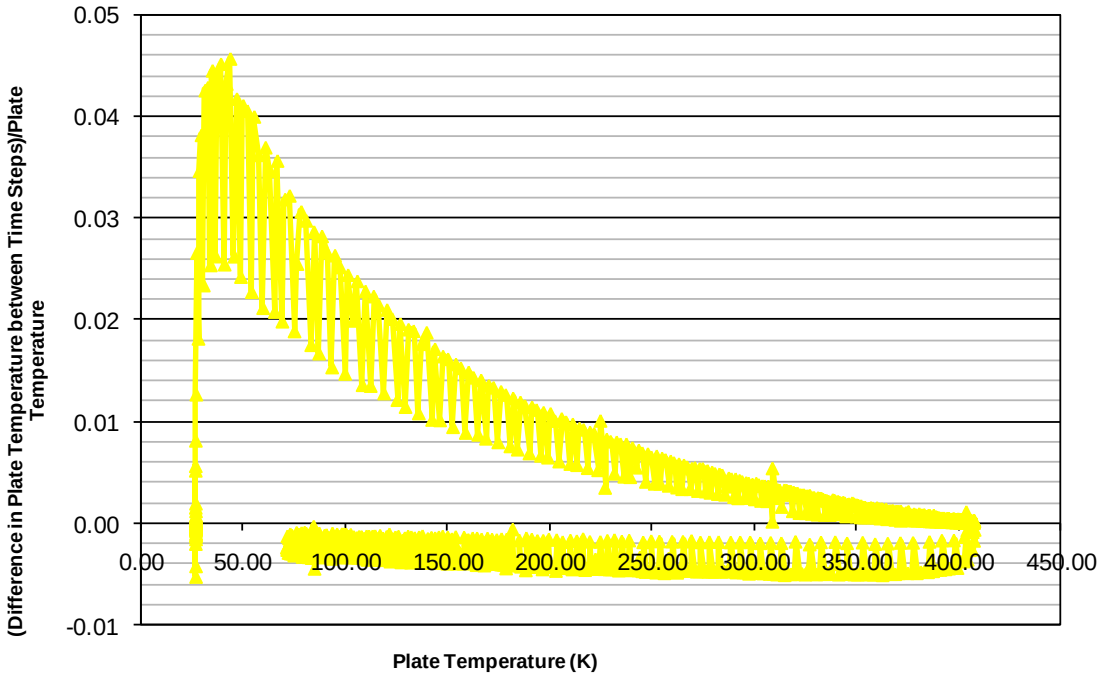

Figure 97: Difference in the temperature of the plate thermometer between time steps as a fraction of the plate temperature versus the plate temperature for Plate C.

7.3 Comparison of Gardon gauge and plate thermometer results

7.3.1 Furniture calorimeter with burner only Test 5

The analysis of the results of Test 5 of the furniture calorimeter using only the propane burner (as presented in Section 6.3.1) is presented here as an example. During this test Gardon gauge (A) was located directly above the plate thermometer at the middle location of equipment tree 4.

A comparison of the incident radiative heat flux as calculated from the plate thermometer and Gardon gauge results is shown in Figure 98 to provide a time-base comparison with the analysis also presented. The difference between the results for each time step as a fraction of the incident radiation estimates $\left(\frac{\dot{q}_{inc,t=n}-\dot{q}_{inc,t=n-1}}{\dot{q}_{inc,t=n}}\right)$ are also shown Figure 98.

The difference between sequential time steps for the estimated incident radiation $\left(\dot{q}_{inc,t=n}-\dot{q}_{inc,t=n-1}\right)$ is plotted against the estimated incident radiation $\left(\dot{q}_{inc,t=n}\right)$ for Gardon gauge A and the plate thermometer at the middle location of equipment tree 4, as shown in Figure 99.

The fraction difference of estimated incident radiation between sequential time steps $\left(\frac{\dot{q}_{inc,t=n}-\dot{q}_{inc,t=n-1}}{\dot{q}_{inc,t=n}}\right)$ is plotted against the estimated incident radiation $\left(\dot{q}_{inc,t=n}\right)$ for Gardon gauge A and the plate thermometer at the middle location of equipment tree 4 is shown in Figure 100.

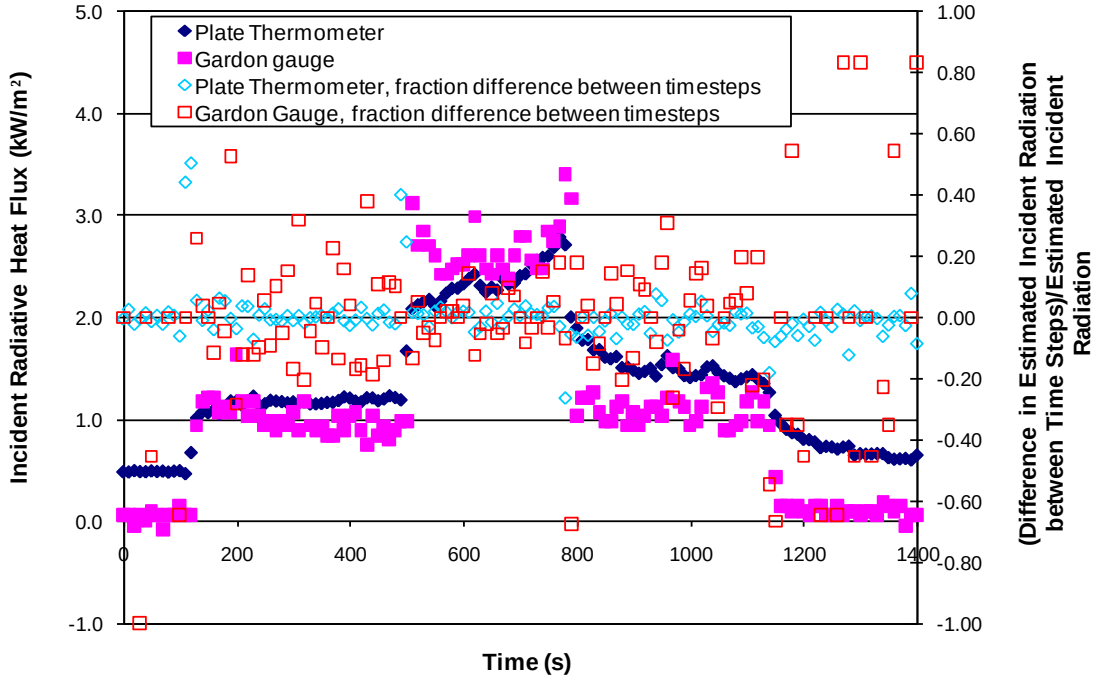

Figure 98: Comparison of the incident radiative heat flux results and the difference between results for each time step as a fraction of the incident radiation for Gardon gauge A and the plate thermometer at the middle location of equipment tree 4.

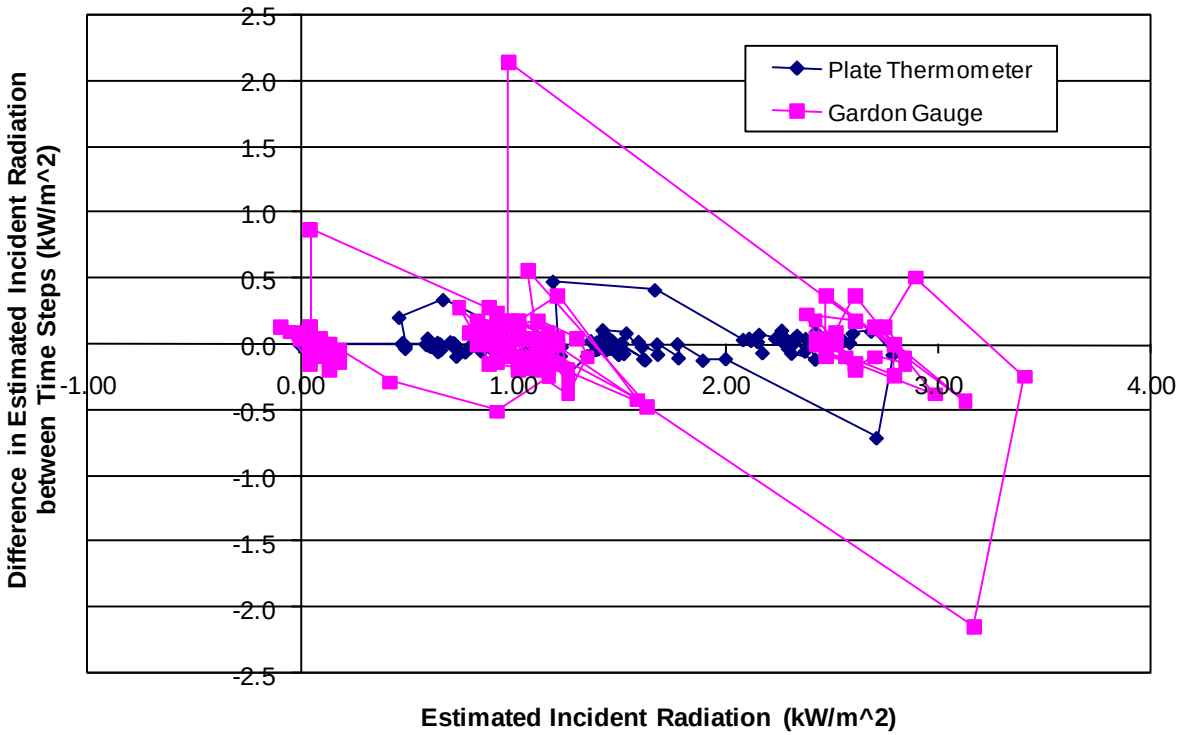

Figure 99: The difference of estimated incident radiation between sequential time steps versus the estimated incident radiation for Gardon gauge A and the plate thermometer at the middle location of equipment tree 4.

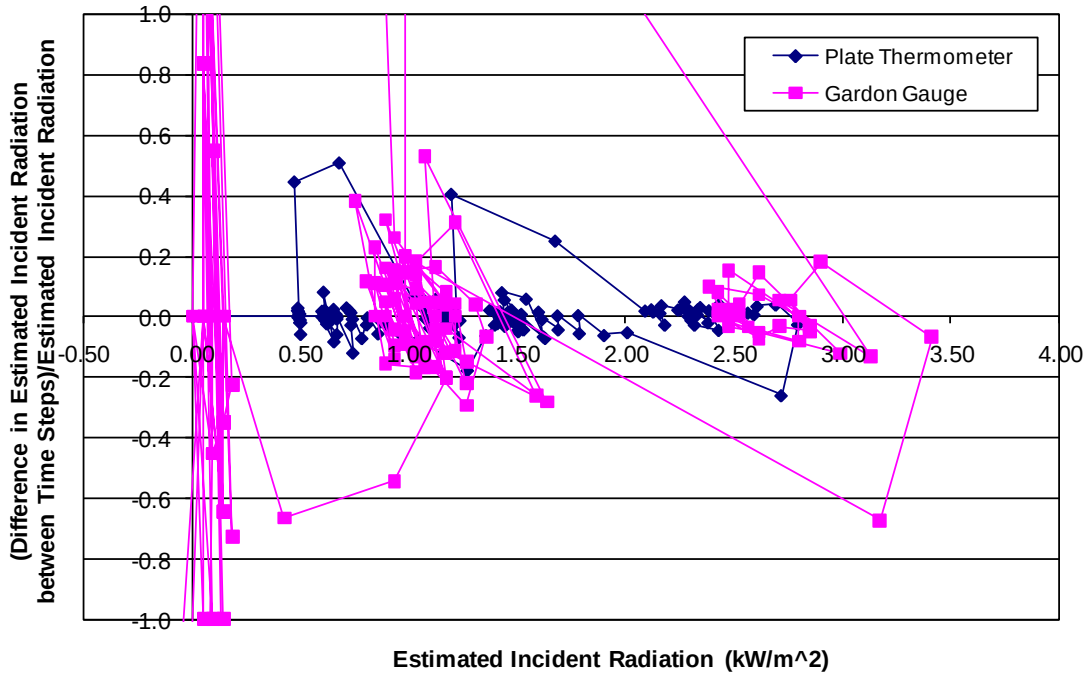

Figure 100: The fraction difference of estimated incident radiation between sequential time steps versus the estimated incident radiation for Gardon gauge A and the plate thermometer at the middle location of equipment tree 4.

7.3.2 Furniture calorimeter with burner only Test 6

The analysis of the results of Test 6 of the furniture calorimeter using only the propane burner (as presented in Section 6.3.2) is presented here as an example. During this test Gardon gauge A was located directly above the plate thermometer at the top location of equipment tree 4, Gardon gauge B was located directly above the plate thermometer at the top location of equipment tree 2.

A comparison of the incident radiative heat flux as calculated from the plate thermometer and the Gardon gauge results is shown in Figure 101 for gauge A and in Figure 104 for gauge B. This is to provide a time-base comparison with the analysis also presented. The difference between the results for each time step as a fraction of the incident radiation estimates $\left(\frac{\dot{q}_{inc,t=n}-\dot{q}_{inc,t=n-1}}{\dot{q}_{inc,t=n}}\right)$ are also shown Figure 101 and Figure 104.

The difference between sequential time steps for the estimated incident radiation $\left(\dot{q}_{inc,t=n}-\dot{q}_{inc,t=n-1}\right)$ is plotted against the estimated incident radiation $\left(\dot{q}_{inc,t=n}\right)$ for the Gardon gauge And the plate thermometer at the top location of the associated equipment tree, as shown in Figure 102 for gauge A and in Figure 105 for gauge B.

The fraction difference of estimated incident radiation between sequential time steps $\left(\frac{\dot{q}_{inc,t=n}-\dot{q}_{inc,t=n-1}}{\dot{q}_{inc,t=n}}\right)$ is plotted against the estimated incident radiation $\left(\dot{q}_{inc,t=n}\right)$ for the Gardon gauge And the plate thermometer at the top location of the associated equipment tree is shown in Figure 103 for gauge A and in Figure 106 for gauge B.

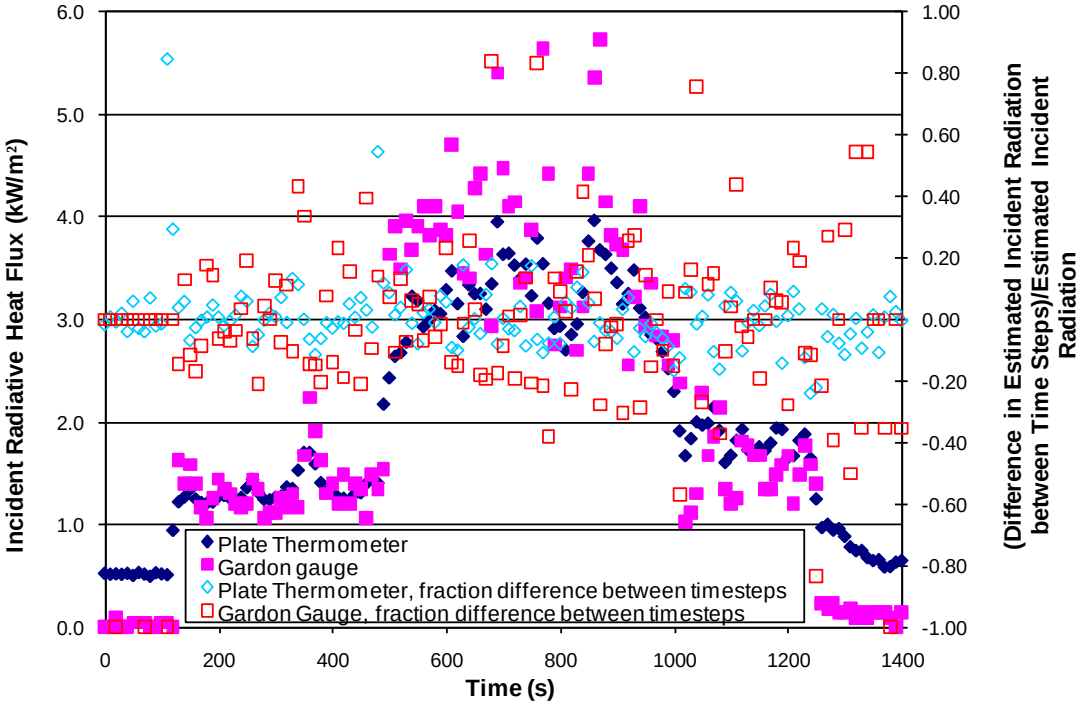

Figure 101: Comparison of the incident radiative heat flux results and the difference between results for each time step as a fraction of the incident radiation for Gardon gauge A and the plate thermometer at the top location of equipment tree 4.

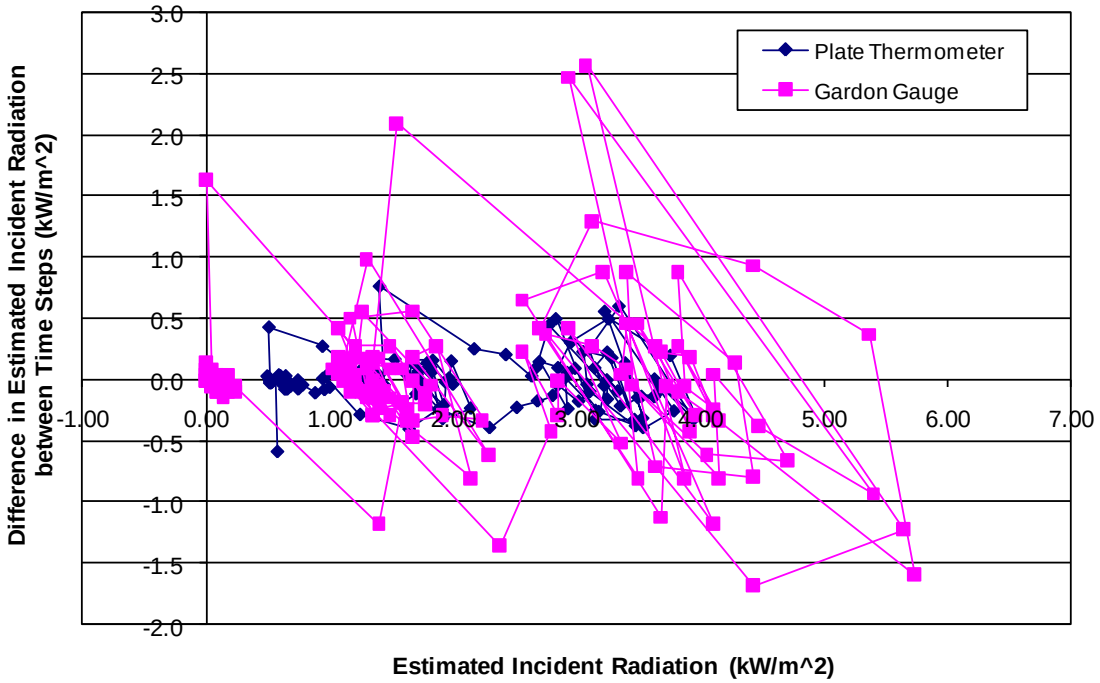

Figure 102: The difference of estimated incident radiation between sequential time steps versus the estimated incident radiation for Gardon gauge A and the plate thermometer at the top location of equipment tree 4.

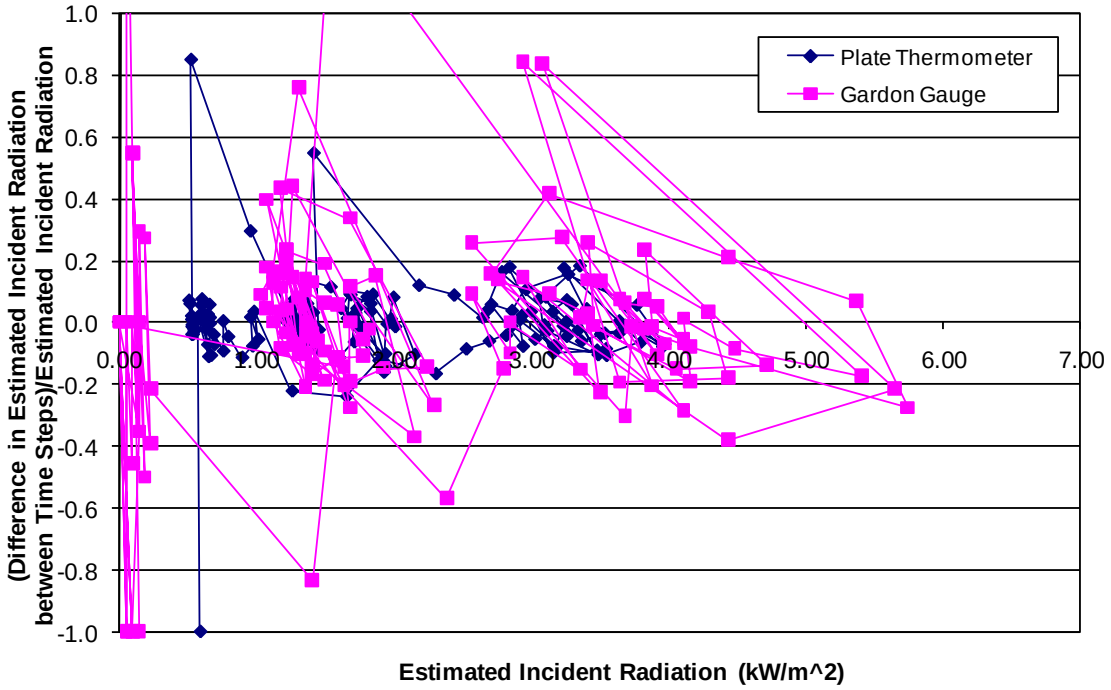

Figure 103: The fraction difference of estimated incident radiation between sequential time steps versus the estimated incident radiation for Gardon gauge A and the plate thermometer at the top location of equipment tree 4.

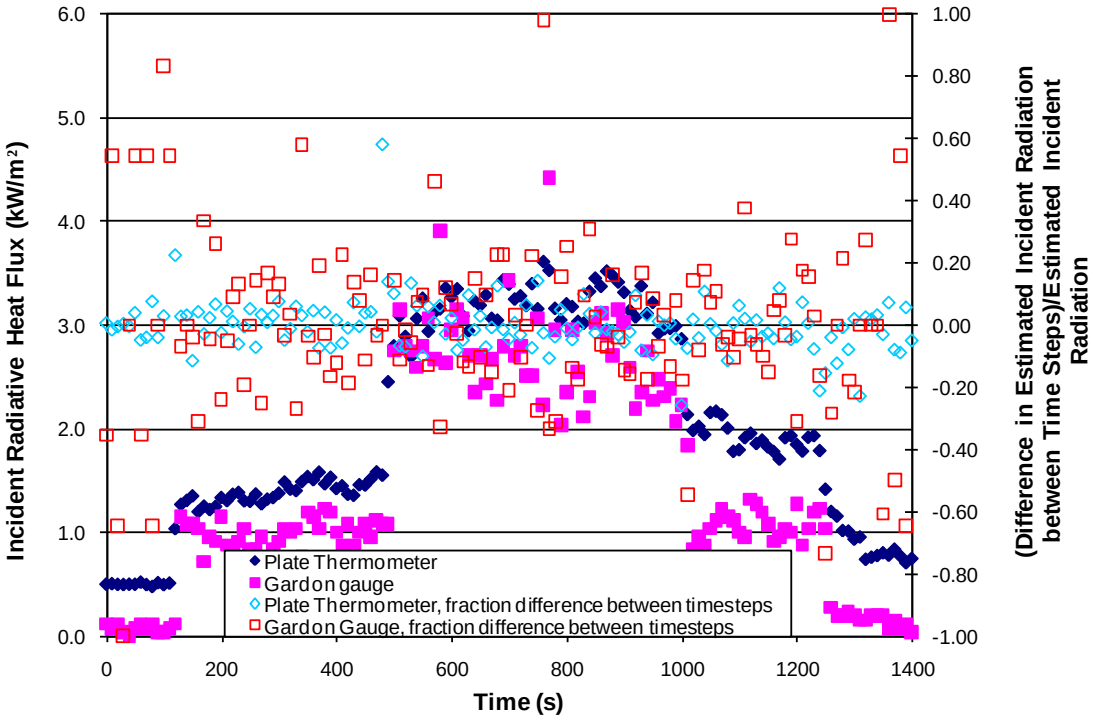

Figure 104: Comparison of the incident radiative heat flux results and the difference between results for each time step as a fraction of the incident radiation for Gardon gauge B and the plate thermometer at the top location of equipment tree 2.

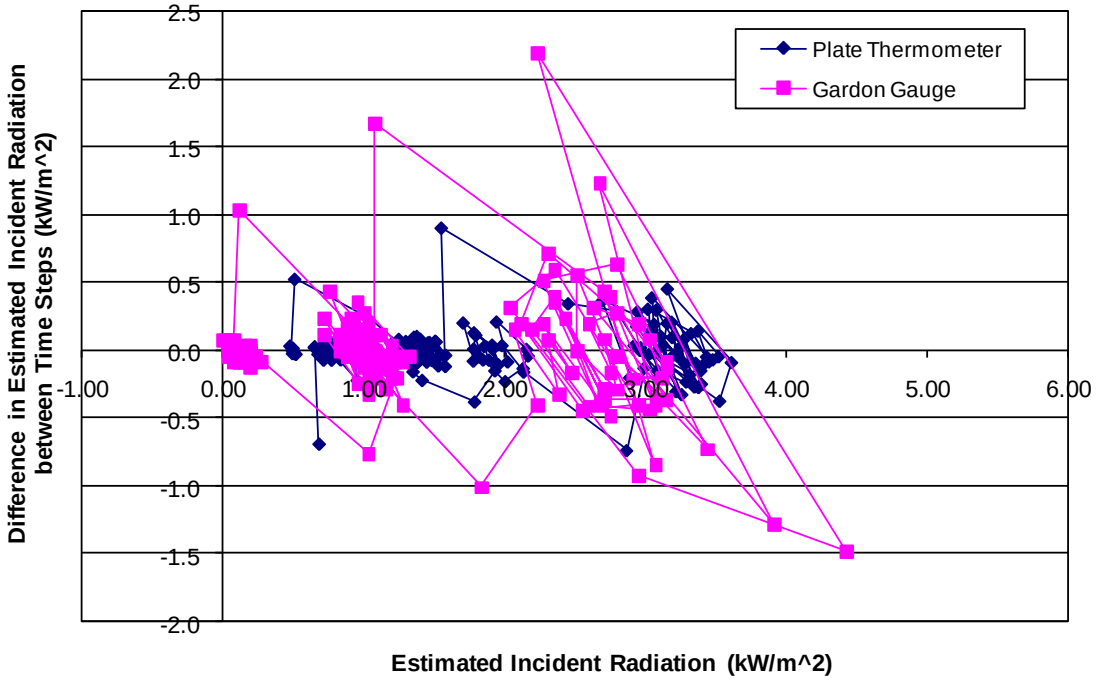

Figure 105: The difference of estimated incident radiation between sequential time steps versus the estimated incident radiation for Gardon gauge B and the plate thermometer at the top location of equipment tree 2.

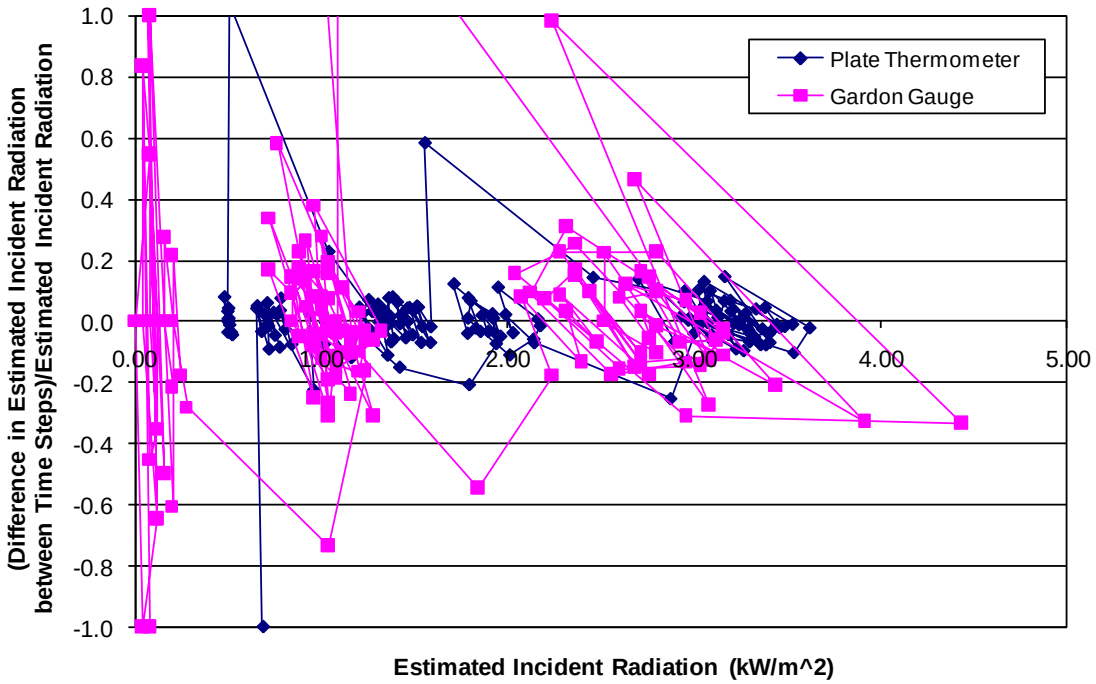

Figure 106: The fraction difference of estimated incident radiation between sequential time steps versus the estimated incident radiation for Gardon gauge B and the plate thermometer at the top location of equipment tree 2.

7.3.3 ISO Room with burner only Test 1

The analysis of the results of Test 1 of the ISO room using the propane burner (as presented in Section 6.5.1) is presented here as an example. During this test Gardon gauge A was located directly above the plate thermometer at the top location of equipment tree 4, Gardon gauge B was located directly above the plate thermometer at the top location of equipment tree 2.

A comparison of the incident radiative heat flux as calculated from the plate thermometer and the Gardon gauge results is shown in Figure 107 for gauge A and in Figure 110 for gauge B. This is to provide a time-base comparison with the analysis also presented. The difference between the results for each time step as a fraction of the incident radiation estimates $\left(\frac{\dot{q}_{inc,t=n}-\dot{q}_{inc,t=n-1}}{\dot{q}_{inc,t=n}}\right)$ are also shown Figure 107 and Figure 110.

The difference between sequential time steps for the estimated incident radiation $\left(\dot{q}_{inc,t=n}-\dot{q}_{inc,t=n-1}\right)$ is plotted against the estimated incident radiation $\left(\dot{q}_{inc,t=n}\right)$ for the Gardon gauge And the plate thermometer at the top location of the associated equipment tree, as shown in Figure 108 for gauge A and in Figure 111 for gauge B.

The fraction difference of estimated incident radiation between sequential time steps $\left(\frac{\dot{q}_{inc,t=n}-\dot{q}_{inc,t=n-1}}{\dot{q}_{inc,t=n}}\right)$ is plotted against the estimated incident radiation $\left(\dot{q}_{inc,t=n}\right)$ for the Gardon gauge And the plate thermometer at the top location of the associated equipment tree is shown in Figure 109 for gauge A and in Figure 112 for gauge B.

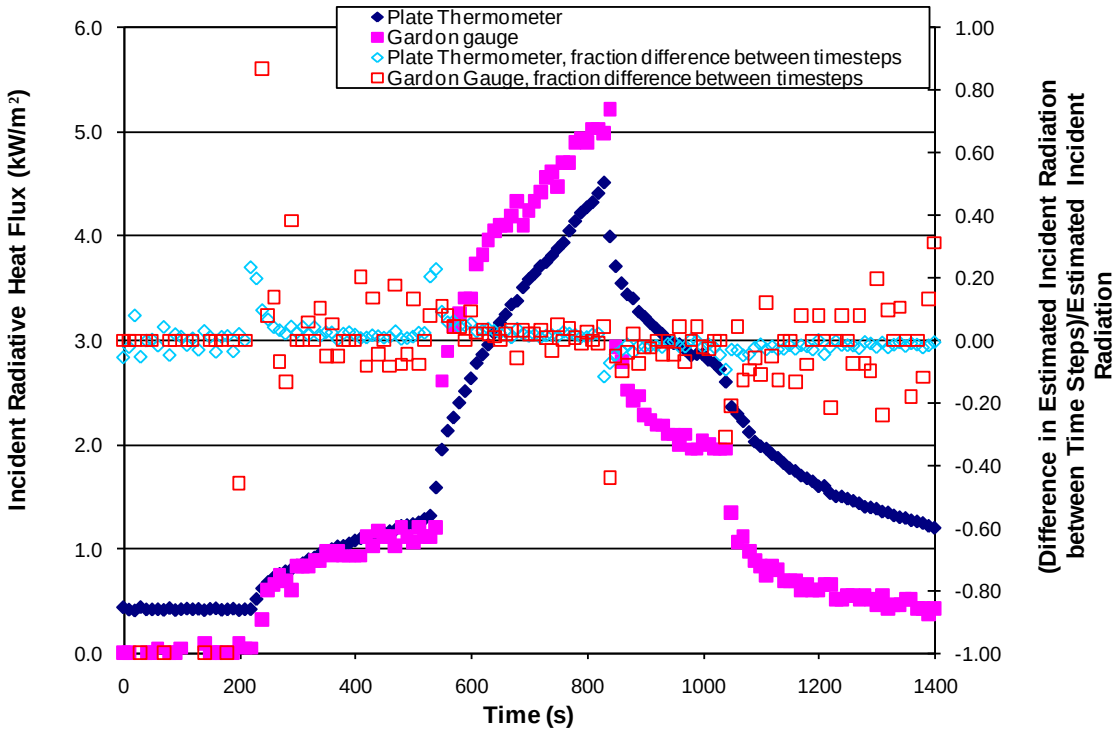

Figure 107: Comparison of the incident radiative heat flux results and the difference between results for each time step as a fraction of the incident radiation for Gardon gauge A and the plate thermometer at the top location of equipment tree 4.

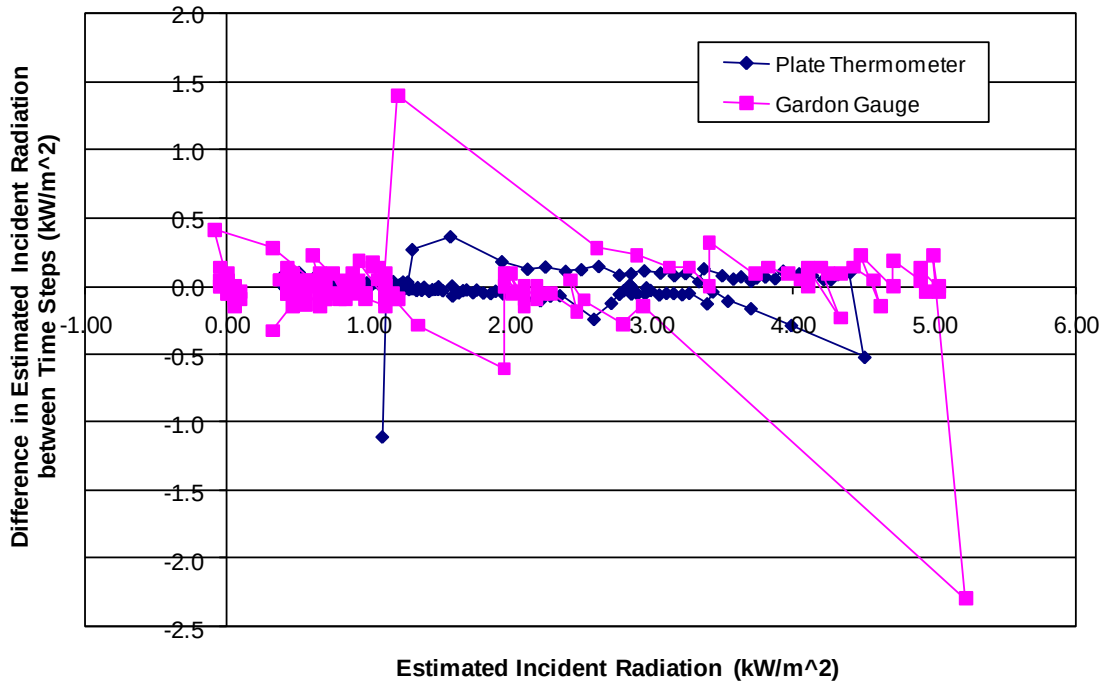

Figure 108: The difference of estimated incident radiation between sequential time steps versus the estimated incident radiation for Gardon gauge A and the plate thermometer at the top location of equipment tree 4.

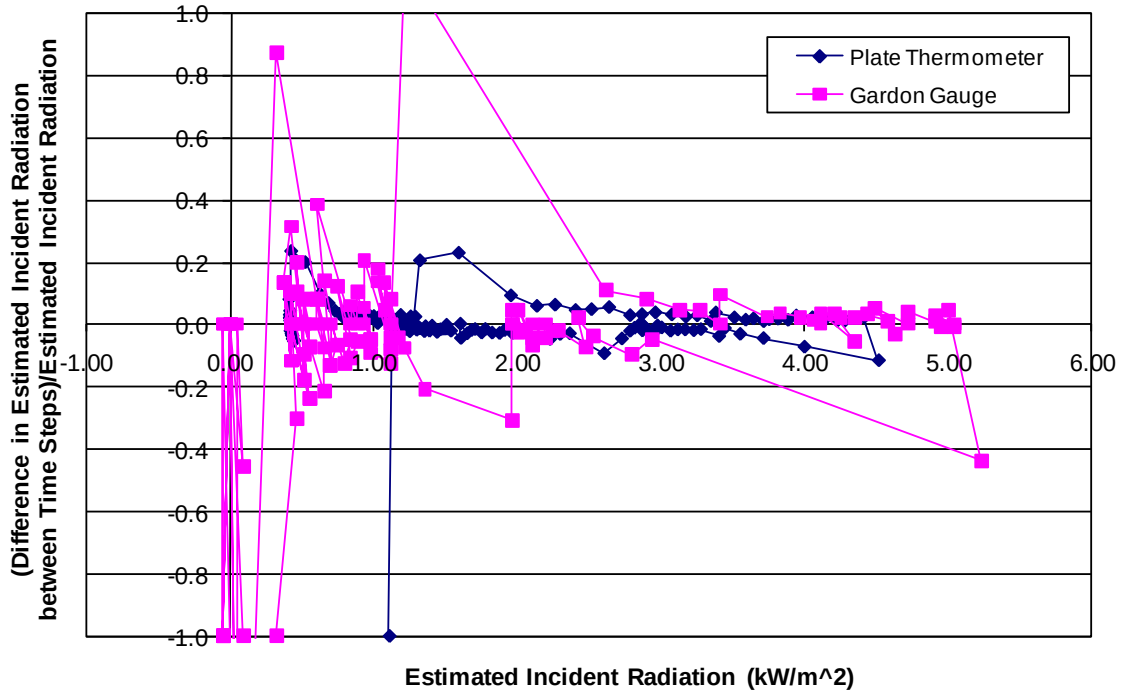

Figure 109: The fraction difference of estimated incident radiation between sequential time steps versus the estimated incident radiation for Gardon gauge A and the plate thermometer at the top location of equipment tree 4.

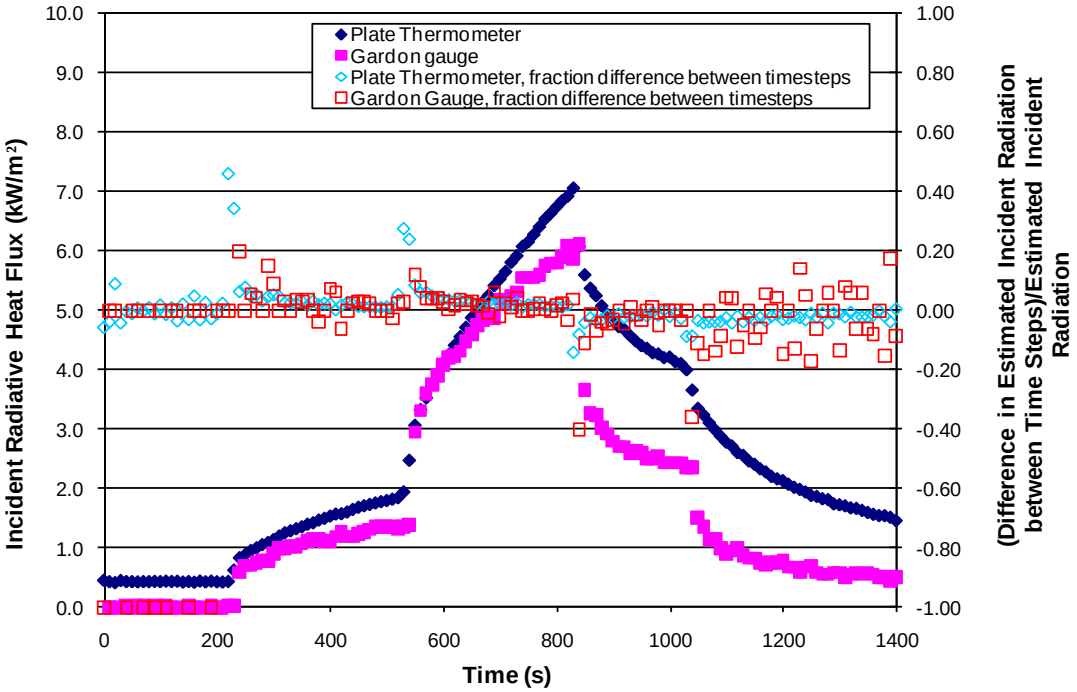

Figure 110: Comparison of the incident radiative heat flux results and the difference between results for each time step as a fraction of the incident radiation for Gardon gauge B and the plate thermometer at the top location of equipment tree 2.

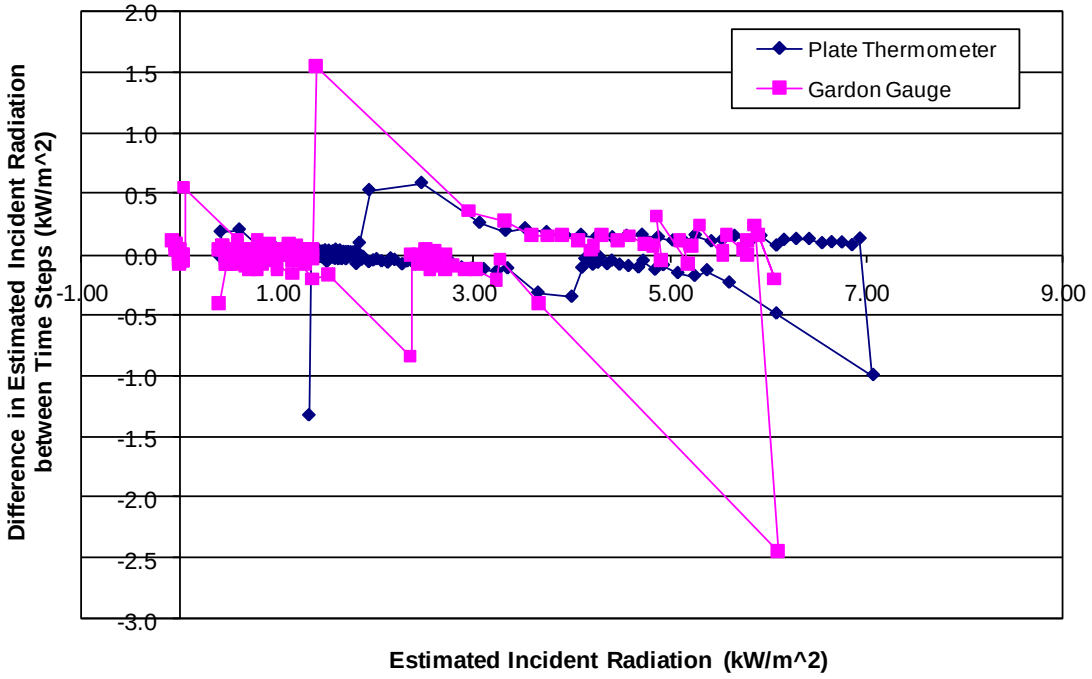

Figure 111: The difference of estimated incident radiation between sequential time steps versus the estimated incident radiation for Gardon gauge B and the plate thermometer at the top location of equipment tree 2.

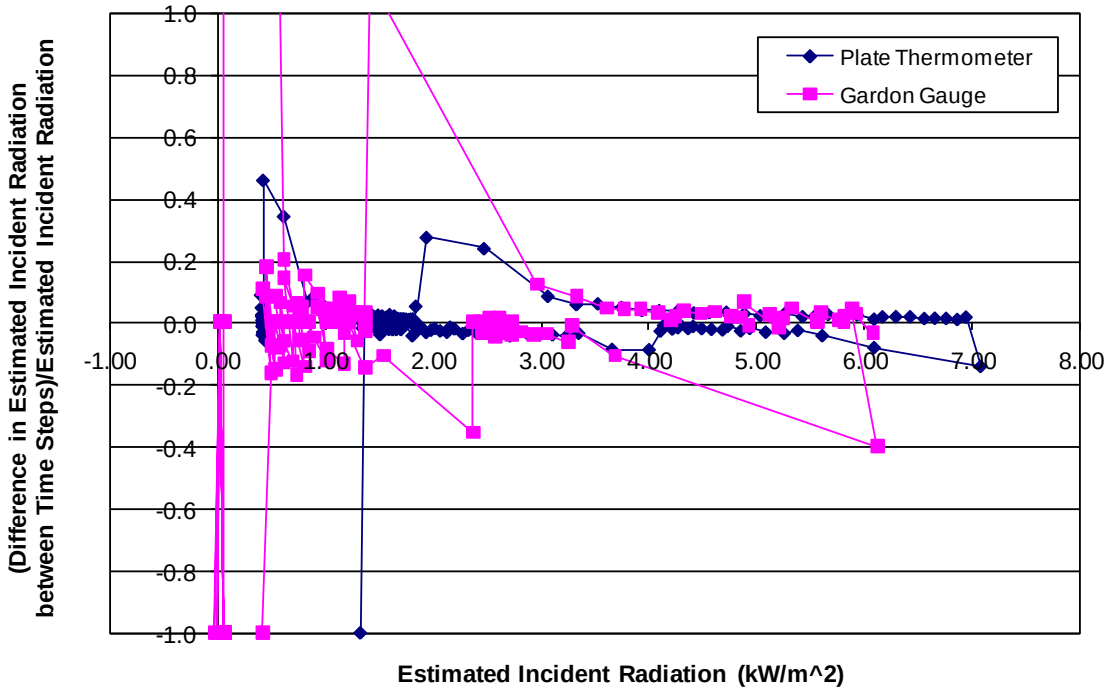

Figure 112: The fraction difference of estimated incident radiation between sequential time steps versus the estimated incident radiation for Gardon gauge B and the plate thermometer at the top location of equipment tree 2.

8. DISCUSSION OF EXPERIMENTAL RESULTS

8.1 Discussion of calibration results

Three plate thermometers were calibrated using cone calorimeter tests (as described in Section 5.2.1). Each plates was subjected to the target incident heat flux sequentially. Three plates with varying surface condition were selected to assess the influence of the surface condition on the plate thermometer response. The results of these tests were used to estimate a set of parameter values appropriate to be used with the 12 plate thermometers used in the subsequent tests.

The basic results for the estimate of incident radiation showed negligible differences between the three results (e.g. Figure 12 and in Appendix A.1). However the surface conditions of each of the three plates used in the calibration tests were visibly different (Figure 9), with Plate C in particular showing extensive signs of surface corrosion. Therefore it was assumed that the surface condition did not significantly influence the measurement.

It is noted that no plates used in the subsequent tests show as extensive surface corrosion as was present for Plate C, which was intentionally selected for the calibration tests to represent an extreme potential case. The maximum extent of surface damage of the plate thermometers used in the subsequent tests was of the order of that shown for Plate B.

The ambient incident radiation was approximately 0.6 kW/m² (as can be seen at the beginning of the tests, e.g. Figure 21), which is consistent with the ambient temperatures of approximately 16 to 19°C that were measured for the tests performed. This ambient incident radiation can be seen at the beginning of each test before an

external incident radiation is applied. Since the cone calorimeter incident radiation was set with a water-cooled Gardon gauge, it is expected that the target incident radiation is the ambient incident radiation plus the Gardon gauge measurement. That is, the Gardon gauge is a gauge measurement of the incident radiation, where the water temperature is ambient conditions and the water flow is sufficient to keep the body of the gauge At approximately ambient temperature. Therefore the differential temperature measured by the Gardon gauge is relative to ambient temperature. The plate thermometer uses only a single temperature measurement and thus the resulting estimate of incident radiation is an absolute measure of the incident radiative heat flux.

The time taken to achieve a relative steady state for the estimate of incident radiative heat flux was approximately 250 to 350 s.

The range of incident radiation levels for which these plates were calibrated to and found to be without significant noise was 1 to 28 kW/m^2. Higher incident radiation levels were associated with a lower percentage of noise. A maximum of ±10% error was associated with the quasi steady state estimates for incident radiative heat flux for the set of best fit input parameters.

8.1.1 Estimation of effective conductivity for losses

Of the input parameters the least known one is the effective thermal conductivity associated with the losses through the mineral insulation at the back of the plate. Therefore this parameter value is estimated using a best fit for the range of target incident radiation, as shown in the examples of Figure 12 and Figure 89 and Appendix A.1. For the horizontal plate thermometer orientation, as used in the cone calorimeter tests, a range of values for the effective conductivity coefficient of 0 to 7 W/m^{2}K was investigated. Values of 2 to 5 W/m^{2}K were found to be the best fit for the range of calibration tests performed in the horizontal orientation. Lower target incident radiative heat fluxes were associated with lower values for the effective thermal conductivity associated with the losses through the mineral insulation. For cone calorimeter tests performed in the vertical orientation, values of 1 to 8 W/m^{2}K were found to be the best fit for the range of calibration tests performed. For the range of target incident heat fluxes in the range observed for the remainder of the testing (of approximately < 10 kW/m^2) the best fit was 1 to 5 kW/m^2.

Little difference is observed when comparing the results for the estimated best value for the effective thermal conductivity coefficient related to the losses of the plate thermometer in the horizontal and vertical orientations. Although, as expected, the results associated with the vertical orientation were higher than for the horizontal orientation. In both cases, only natural convection was present. The turbulent mixing present when near a fire plume, submerged in the hot layer or near the layer interface, was outside the scope of these experiments. Higher values would be expected to be associated with more turbulent local conditions.

A value of 4 W/m^{2}K was chosen as the best fit as a single value for the range of target incident radiative heat fluxes used in the calibration tests. This is in agreement with previous experiments to determine other plate thermometers using cone calorimeter tests, where the correction factor associated with the conductive losses through the mineral insulation was reported as 5 W/m^{2}K (Ingason and Wickstrom 2007).

The influence of the effective thermal conductivity associated with the losses via the mineral insulation is discussed in Section 8.5.3.

8.1.2 Input parameter influence

The influence of each of the parameter values used as input to estimate the incident radiative heat flux (as discussed in Section 3.2.1 and included in Table 3) was assessed, as shown in the example in Section 7.1 and the detailed results included in Appendix A.1. Three times on the curves were selected to represent snapshots of the three obvious parts of each curve:

1. The initial rapid rise,
2. The middle of the moderate rise between the initial rapid rise and the quasi steady state, and
3. The quasi steady state.

The results for the input parameters with the most influence on the result for the initial rapid rise were consistent across the tests performed, indicating the most influential parameter as the average specific heat of the INCONEL® plate (with a linear regression of ~0.8 to 0.9) and for the second as the plate thickness (with a linear regression of ~0.3 to 0.4), as shown in Figure 90(a), Figure 91(a), Figure 92(a) and Appendix A.1. The next three most influential input parameters are the effective thermal conductivity constant associated with the conduction losses through the mineral insulation, the emissivity and the density of the INCONEL® plate.

The most influential parameters for the initial rapid rise of the curves are associated with the storage term, which is expected as most energy will be initially used to increase the plate temperature from ambient conditions and is consistent with the example shown in Figure 16 (and for other tests in Appendix A.2). It follows that these parameters are also highly influential in the response time of a plate thermometer to report the incident radiative heat flux experienced by the plate.

The results for the input parameters with the most influence on the result for the middle of the moderate rise were mixed across the tests performed. This depended on whether the data point chosen was at the slightly earlier time (associated with the initial rapid rise) or at a slightly later time (associated more closely with heading towards a quasi steady state). The most influential top four parameters across the tests performed were the effective thermal conductivity constant associated with conduction losses through the mineral insulation, the average specific heat of the INCONEL® plate, the emissivity of the plate and the plate thickness, as shown in Figure 90(b), Figure 91(b), Figure 92(b) and Appendix A.1. These parameters are associated with the top influential parameters associated with the other two parts of the curve considered.

The mid-sections of the curves are transitions between the controlling influences of the section of rapid rise to the approach of a quasi steady state. Therefore it is expected that there is a mixture of influential input parameters for this section of the curve.

The results for the input parameters with the most influence on the result for the quasi steady state section of the curve were consistent across the tests performed, indicating the most influential parameters from highest to lowest influence as the effective thermal conductivity constant for conductive losses via the mineral insulation, the emissivity of the plate, the Plate Characteristic length, the average specific heat, plate thickness and plate density. These results are shown in Figure 90(c), Figure 91(c), Figure 92(c) and Appendix A.1.

The most influential parameters for the quasi steady state sections of the curves are associated with the conductive losses, radiative heat transfer, convective losses, which is expected as once the plate is brought up to near a steady state temperature, then the steady state value depends on the balance of incident and loss of energy and is consistent with the example shown in Figure 16 (and for other tests in Appendix A.2). It

follows that these parameters are also highly influential in the value to which the estimate of the incident radiative heat flux tends.

8.1.3 Response

It was noted for each test that the plate thermometer temperature and the subsequent estimate of incident radiation followed two distinct curves that approached an asymptote of the same plate temperature or estimate of incident radiation level. This is obvious in the results of each test and is particularly apparent in the results of the calibrations, e.g. Figure 12 and Figure 93. This was investigated further, as shown in the example of Section 7.2. Interest in this observation of the data was related to determining whether this is an artefact of the equipment set-up and/or whether this can be exploited to reduce the effective time for the estimated incident radiative heat flux to come to a quasi steady state estimate. This would be particularly useful in non-steady state incident heat flux scenarios.

When the plate thermometer is initially subjected to the target heat source, the difference between time steps of the estimated values for the incident radiation suddenly increases, as shown in Figure 93. The estimated incident radiation oscillates between two temperature-versus-time curves as both curves increase. As both curves approach the same quasi steady state value the variation between the curves decreases, as shown in Figure 94.

The plate temperature (from which the estimate of the incident radiative heat flux is calculated) shows similar oscillatory behaviour for each of the experiments in this study, as shown in the example included in Section 7.2.1 (Figure 95, Figure 96 and Figure 97).

It is currently not clear as to what is the fundamental cause for this oscillatory behaviour. However this behaviour is consistently observed throughout all of the calibration tests (Sections 6.1, 6.2, Appendix A.1 and Appendix A.2).

If this oscillatory behaviour is found to be fundamental to the system, and is deemed not to be an artefact of the data acquisition or other part of the equipment set-up, then there may be opportunity to exploit this feature to determine the appropriate estimate of the incident radiative heat flux value for non-steady state heat source scenarios.

The time taken for the estimated incident radiative heat flux to report a quasi steady state values is discussed further in relation to the assumptions of the theory used in the calculations in Sections 8.1.4.2 and 8.5.

8.1.4 Plate thermometer set-up

In regards to assessing what assumptions were used in the calculation of the estimate of the incident radiative heat flux, the plate thermometer set-up was further investigated in terms of:

- the temperature difference across the INCONEL® plate,
- the influence of the metal strip locating the thermocouple compared to using a spot weld, and
- the heat flux exiting the back of the instrument.

An example of these results is shown in Section 6.2 for a target incident radiation of 19.4 kW/m², and the total results are included in Appendix A.2.

8.1.4.1 Temperature difference across plate

The difference in temperature between the front and the back of the plate (e.g. Figure 15 and included in Appendix A.2) is consistently negligible, with a maximum of up to 3 K for any of the range of incident radiation tested as part of this study. This temperature difference relates to a difference in the estimated incident radiative heat flux between using both the temperature measurements from the front and back of the plate to using the temperature of the back of the plate only (assuming the front of the plate is the same temperature) of up to ±1 kW/m². This excludes single data point spikes in the results, which if included would increase this to ±3 kW/m². This difference could be significant depending on the accuracy of the measurement required. However relative to the target radiative heat flux this difference is approximately 4 to 6%, as presented in Table 14.

Table 14: Difference in estimated incident radiative heat flux between using front and back surface temperatures and only back temperatures of a plate thermometer.

Test Number	Target Radiative Heat Flux (kW/m²)	Maximum Difference in Estimated Incident Radiative Heat Flux between Calculation Methods (± kW/m²)	Difference as a Percentage of the Target Radiation (%)
Test 1	5.0	0.25	5
Test 2	7.2	0.4	6
Test 3	9.3	0.6	6
Test 4	14.4	0.9	6
Test 5	19.4	1.0	5
Test 6	22.9	1.1	5
Test 7	27.3	1.2	4

8.1.4.2 Influence of thermocouple location method

The difference observed in the estimated incident radiative heat flux, as shown in Figure 17, is significant during the initial steep rise when the plate thermometer is first exposed to the target source. The quasi steady state section of both results is in reasonable agreement. The plate thermometer with the thermocouple located using a spot-weld shows a steeper initial increase in temperature and, subsequently, also a steeper initial increase in the estimated incident radiative heat flux. This indicates that the metal strip and two screws used to locate the thermocouple (Section 3.1) influence the performance of a plate thermometer. The small metal strip and two screws would influence the storage term of the theory used in this study (Section 3.2.1).

This additional mass located directly over the thermocouple is not included in the theory used to calculate the estimates of the incident radiative heat flux. This will be discussed further in Section 8.5.

8.1.4.3 Heat losses from back of plate thermometer

The incident heat flux from the back of a plate thermometer was estimated using a second plate thermometer placed directly under the first plate thermometer. An example for the results for a target incident radiative heat flux of 19 kW/m² is shown in Figure 18, where Plate A was placed directly below Plate B during the cone calorimeter test and a value of 4 W/m²K was used for the effective conductivity for the losses through the mineral insulation. A comparison of the components that make up the estimate of the incident radiative heat flux for Plate B and the incident heat flux (where convective heat transfer was not included in the estimation) of Plate A is shown in

Figure 19. The conduction losses component of Plate B and the incident heat flux of Plate A show reasonable agreement. Examples of results for a range of effective conductivity coefficient value are included in Appendix A.2.8.

8.2 Comparison of Gardon gauge And Plate Thermometer Results in a Vertical Orientation

8.2.1 General

A difference is expected between the incident radiation flux estimates based on the measurements from a Gardon gauge And a plate thermometer, since both have different assumptions in the calculation methods for the incident radiation flux estimate.

For example, at low incident heat flux conditions (~0.6 kW/m²) the Gardon gauges produce an estimate of the incident radiation flux that is lower than the estimate calculated from plate thermometer measurements. This is expected because at ambient conditions the Gardon gauges have no temperature difference between the centre and edge locations on the foil. Thus the measured voltage is zero and subsequently the net radiation flux is zero, since the incident radiation flux minus the reflected radiation flux equals the emitted radiation flux. Whereas the plate thermometers provide an estimation of the incident radiation based on a single temperature reading rather than a temperature difference. Therefore at ambient conditions, estimates of the incident radiation calculated from the plate thermometer measurements are not zero.

At moderate incident heat fluxes (~5 – 25 kW/m²), where the plate thermometer has been calibrated relative to Gardon gauge readings in the cone calorimeter, the estimates of the incident radiation flux from the two methods is comparable because of the method of calibration.

At higher incident heat fluxes, it is expected that the calculation methods for the estimates of the incident radiation would be influenced by convection. With different geometries (related to surfaces exposed to convective heat transfer) and base temperatures (i.e. no water cooling for plate thermometers), the different methods of estimating incident radiative heat flux would be affected to different extents.

The lack of cooling of the insulation material of a plate thermometer means that an assumed ambient temperature is less accurate for longer duration tests where the materials of the sensors can increase significantly above initial ambient conditions (as estimated in Equation 7). Increasing temperatures of the insulation material of the plate thermometer may provide over-estimates of the incident radiation.

Similarly the assumption that the local gas is at ambient temperature for the estimation of the convection heat transfer component of the plate thermometer estimate of the incident radiation (as estimated in Equation 6 and Equation 7) may not be appropriate when the sensor is near to (and subject to local turbulence caused by mixing at the layer interface) or within the hot smoke layer.

8.2.2 Furniture calorimeter results

Comparison of Gardon gauge results and estimates using plate thermometer results is shown in the example of Figure 21. The initial difference in the incident radiation values is not consistent throughout the test. The time taken for the plate thermometer to reach a quasi steady state may be the reason for this, as the plate thermometer results are observed to increase over the periods of steady burner HRR.

Consistently reasonable agreement is observed between the Gardon gauge and plate thermometer results for the initial step from ambient conditions to 100 kW burner HRR, then the plate thermometer results show a distinct lag in reaching a quasi steady state during the 300 kW period of each burn and the plate thermometer values are consistently lower than the Gardon gauge measurements. In addition, during the stepping down of the HRR, the plate thermometer results also show a distinct lag in reaching a quasi steady state value and are higher than the Gardon gauge results.

However the results show reasonably good agreement overall considering the levels of measurement error involved for each method of measurement, the time taken for a plate thermometer to reach a quasi steady state and, to a lesser extent, for the change in convection losses associated with the vertical orientation of the plate thermometers with increased local flow velocities that had not been included in the calibration using the cone calorimeter test results (that only included natural convection when challenged with a heated coil instead compared to a naked flame). The lag associated with the value for the estimate of the incident radiative heat flux is difficult to assess because of the transient nature of the applied incident heat flux associated with movement of the flame due to air movement in the laboratory (as is discussed in Section 8.3). Subsequently it is difficult to ascertain a temperature-independent correction factor associated with the increased convective heat losses from these tests.

For comparison, a similar analysis of the results of Test 6 (Figure 27) are also included as an additional example. The difference is that this test had a linear decrease in the HRR provided by the gas burner during the higher level heat output, as shown in Figure 26.

Vertically orientated cone calorimeter tests (e.g. as summarised in Section 6.1.2) assisted in determining the change in convection coefficient associated with the change in orientation from the horizontal position. The resulting estimates for the effective convection coefficient to account for the losses through the mineral insulation (Table 13) were similar to the results for the horizontal orientation of the plate thermometers. However these tests did not include the effects of forced convection conditions that would occur in situations where the plate is in or near to the plume, or the turbulent conditions at the interface or in the hot layer of an enclosure. Therefore caution must be applied when estimating appropriate coefficients and the application of the incident radiative heat flux results and the associated errors.

An estimate for an increase in the conductive coefficient was suggested to account for plate thermometers used in a set of experiments where the plates were within the flaming zone of the burner (Ingason and Wickstrom 2007). This is discussed in Section 8.5.3.

8.3 General discussion of furniture calorimeter results

Observations of the burner during furniture calorimeter tests indicated that the flame orientation was significantly influenced by draughts within the laboratory. This is shown by the variation of the incident radiative heat flux estimates for the plate thermometers when they were placed the same distance from the burner. For example, in Test 5 where equipment trees 1 and 4 were diametrically opposite and equipment trees 2 and 3 were diametrically opposite, and all equipment trees were located 1.3 m from the centre of the burner. The variation in the incident radiative heat flux at the same heights above floor level is shown in Figure 25. Similarly, results for the example of Test 6, where the equipment trees are at a distance of 1 m from the centre of the burner, are shown in Figure 31.

When comparing each of the heights on the equipment trees, for tests where all of the equipment trees are located at the same distance from the centre of the flame, it is

obvious that as one or two equipment trees provide higher estimates of the incident radiative heat flux, as the burner flame leans towards their location, then conversely one or two equipment tree results provide lower values for the estimate of the incident radiation. Therefore the results for each of the heights above the floor can be combined to provide an average and range for the set-up. This average and range is of more use than experimental results from any one location when compared to modelling results that do not include the transient laboratory air movement.

8.4 General discussion of ISO room results

Comparisons of the Gardon gauge And plate thermometer results for the example of ISO room tests are shown in Figure 41 for Test 1 and Figure 50 for Test 6. Similar to the results from the furniture calorimeter tests, as discussed in Section 8.2.2, where a stepped HRR of ambient, 100 and 300 kW was used during the tests (e.g. as shown in Test 1) the initial step of the test showed lag in plate thermometer values reaching a quasi steady state but the results still showed reasonable agreement with Gardon gauge measurements. Similarly the plate thermometer values are consistently lower than the Gardon gauge measurements for the highest HRR value step used, and then the plate thermometer values are greater than the Gardon gauge measurements during the step-down of the HRR as the plate thermometer values still lag behind the Gardon gauge measurements.

During the initial linear ramp-up and ramp-down of the example shown in Test 6 (Figure 46), the plate thermometer results more closely follow the Gardon gauge results (Figure 50) than when a stepped HRR is applied (e.g. Figure 41).

Overall, the Gardon gauge And the plate thermometer values for the incident radiative heat flux are in reasonable agreement. The effects of the hot upper layer and heating the room become more pronounced over the duration of each test and are observed in both forms of incident radiative heat flux measurement.

The distributions of the incident radiative heat flux at each equipment tree at each height are shown in Figure 44 and Figure 53. These indicate the variation of incident heat flux based on height at these locations. Used in conjunction with the results of the thermocouples on the surface of the material samples (also shown in Figure 44 and Figure 53) and the estimate of the height of the hot and cool layer interface (Figure 38 and Figure 50), a more complete description of the environment within the enclosure emerges. For instance the small spike at the beginning of the 300 kW step (Figure 37) was picked up by the thermocouple directly above the burner (Figure 40), and was also related to a small spike in the results of the thermocouple over the sample material at the top of equipment tree 1 (Figure 43 and Figure 44). The estimate of the layer interface height also shows that it was approaching the top of the equipment trees about this time (Figure 38). All of this aids in the interpretation of the incident radiative heat flux (Figure 44 and Figure 45) and what conditions may be influencing these values.

8.5 Impact of assumptions on the estimate incident radiation flux

Each of the assumptions used to develop the estimate of the incident radiative heat flux based on the plate thermometer temperature measurement (as presented in Section 3.2.1) are considered here in turn.

8.5.1 Uniform plate thermometer temperature

It is assumed that the surface temperature is the same as the temperature between the metal plate and the backing insulation ($T_S = T_{PT}$).

The experimental results of this study show that in general the assumption that thermocouples located on the front and back surfaces of the metal plate measure similar temperatures (e.g. Figure 15 and Section 8.1.4.1). However it is noted that the front and back thermocouple temperatures show the most difference when initially exposed to the heat source and then initially when removed from the heat source. Therefore when a variable heat source is of interest this assumption may break down.

8.5.2 Convective heat transfer coefficient

The convection heat transfer coefficient (H_{conv}) was estimated for a horizontal plate under natural convection conditions (Equation 6). This assumption is expected to be valid for the cone calorimeter tests, where the plate thermometers were oriented in a horizontal position with natural convection conditions. However the experiments performed in the furniture calorimeter or the ISO room used the plate thermometers in a vertical orientation. Mixing of hot and cooler gases, resulting in localised turbulent flow, is expected in the ISO room experiments compared to a plate located in a large open space.

Dillon (1998) proposed a convective heat transfer coefficient for vertically orientated plate thermometers that was suggested as 8.6 W/m^{2}K for natural convection within a one-fifth-scale ISO room. Values of 13.8 and 15.9 W/m^{2}K were suggested for regions within the flame, where forced convection was assumed, for 100 and 300 kW HRRs respectively (Dillon 1998).

8.5.3 Conduction correction factor

The loss of heat to the insulation and the non-one-dimensional heat transfer through the metal plate was estimated by an effective lumped conduction heat transfer coefficient (K_{cond}). This lumped coefficient was assumed to be temperature independent and was estimated as approximately 4 W/m^{2}K using experimental data from the calibration phase using cone calorimeter test results.

However the results from the calibration using cone calorimeter test showed that the value for this effective conduction coefficient varied over the target incident fluxes tested, with lower values generally associated with lower target incident fluxes compared to higher target incident fluxes.

The effective conduction coefficient value of 4 W/m^{2}K is consistent with the value of 5 kW/m^{2}K previously suggested to provide sufficiently accurate results compared to water-cooled Gardon gauge results (Ingason and Wickstrom 2007). Whereas a higher value for the effective conduction coefficient of ~22 kW/m^{2}K was estimated for the use of plate thermometers in vertical orientation with fire plume impingement (Ingason and Wickstrom 2007).

Since the plate thermometers in these set of experiments were not in the plume except for short durations during some furniture calorimeter tests where the burner flame was observed to lean in a direction of an equipment tree, a value as high as 22 kW/m^{2}K would not be expected. However the local turbulent conditions observed during the ISO room experiments where plate thermometers were either submerged in the hot layer or near the layer interface is expected to provide conditions related to an increase in the

effective thermal conductivity coefficient value estimated in natural convection conditions.

Comparison of estimates of incident radiative heat flux from plate thermometer measurement and Gardon gauge results from the furniture calorimeter tests provides more insight into this, as discussed in Section 8.2.2.

8.5.4 Local gas and backing insulation temperature

The local gas temperature was assumed to be ambient $\left(T_{local\ gas} = T_{\infty}\right)$ as was the temperature of the backing insulation $(T_{insluation} = T_{\infty})$. These assumptions affect the heat transfer losses by convection and conduction (Equation 7).

These are likely to be reasonable assumptions for the cases of the cone calorimeter tests and furniture tests, where a hot layer is not maintained and the total test duration is not long enough for the backing insulation to heat up. However when the plate thermometer is submerged in the hot layer during a compartment test, then the assumption of the local gas being ambient temperature is no longer valid. In addition, test durations may be long enough for the backing insulation to heat up.

For the furniture calorimeter and ISO room tests, temperatures of the surface of sample materials adjacent to each plate thermometer were recorded. Thermocouples were also used across the ceiling and in a tree near the door of the ISO room. These measurements could be used to estimate a local gas measurement in future analyses. The impact of the assumption of ambient local gas temperatures could then be assessed at this time in comparison with results using an estimate of the local gas temperature.

8.5.5 Lumped parameter model approach

The average response time for a plate thermometer to reach a quasi steady state estimate of the incident radiative heat flux when subjected to a steady state incident heat flux of 250 to 350 s indicates that the assumptions used to develop the theory may not be as appropriate as possible. The appropriateness of the assumptions presented in Section 3.2.1 is related to the scenario. That is, if the incident heat flux is known to be quasi steady state or changes with time relatively slowly, then these assumptions are appropriate for estimating the incident radiative heat flux from the temperatures measured at the plate thermometers. However if the plate thermometers are required to provide an estimate of the incident radiative heat flux for scenarios where the heat source is variable, then another approach may be more appropriate.

The analysis assumption that the plate thermometer is a lumped parameter system contributes to the rise time of the plate thermometer to incident radiation changes. Taking more transitive aspects into account in the theory used for analysis may reduce the rise time. Alternative theory or estimate approaches are discussed in Section 8.5.6.

8.5.6 Alternative theories or estimate approaches

From the results of the experiments and the analysis presented here it is suggested that, for scenarios where the incident heat flux is not expected to be constant or to change smoothly and relatively slowly, then an alternative approach would be required to provide a more accurate estimate of the incident radiative heat flux. Suggestions for future work in this area include:

- Investigation of dimensional approaches to heat transfer to replace the lumped parameter assumption.
- Investigation of the use of stability analysis to interpret when the measurement of the plate temperatures is approaching a quasi steady state or not and to estimate the value of the quasi steady state that is being approached.

9. MODELLING OF BURNER AND ISO ROOM

An example was used to compare the results of the computational fluid dynamics (CFD) package, Fire Dynamics Simulator (FDS) (McGrattan et al 2007) to experimental values obtained using plate thermometers and Gardon gauges for incident radiative heat flux values.

The example presented here is based on Test 1 of the set of tests performed in an unlined ISO room using a propane burner as the heat source.

The FDS model was used to solve a low March number form of the Navier-Stokes equations for a Cartesian grid using a large eddy simulation approximation for turbulence. Combustion was calculated using a mixture fraction approach. Radiative heat transfer was calculated using a finite volume method and the gray gas approximation (McGrattan et al 2008).

9.1 Model set-up

The model comprised of a section of the laboratory with the ISO room and extraction hood located within it. The model geometry is shown in Figure 113. The model location of the heat flux gauges and the plate thermometers was limited by the Cartesian coordinate system used. So the orientation of the modelled heat flux surfaces, depending on the model device used, with respect to the burner was sometimes related to the closest Cartesian coordinate axis rather than using a vector between the gauge And the burner locations. This becomes apparent in the comparison of the results in the following section.

The code used for this example modelled scenario is included in Appendix B.1 for completeness. All details used in the model are included at this location.

The only result from the experiment that was used as input to the modelled scenario was the HRR versus time of the propane burner (Figure 114).

Two types of variables were of primary consideration for the comparison of computer and experimental results:

- Incident heat fluxes at each location of the equipment trees and the Gardon gauges (for this example, Orientation A was used, with the set-up shown in Figure 10(a)), and
- Gas temperatures for comparison with experimental results for the thermocouples on the ceiling and in a tree configuration near the door opening of the ISO room, as well as the locations of the thermocouples used on the surface of the material samples (all in the same locations as used in the experiments).

The incident heat fluxes were of primary interest for comparison and evaluation of the calculated values based on the plate thermometer results. The results for the gas temperatures are for comparison with the thermocouple temperatures to evaluate the overall appropriateness of the modelling approach taken.

Firstly, two grid sizes (50 x 50 x 50 mm and 100 x 100 x 100 mm) were used to establish the influence of the chosen grid on the modelled scenario results. The 100 x 100 x 100 mm grid was found to be sufficient for the estimation of heat fluxes and gas temperatures for this scenario.

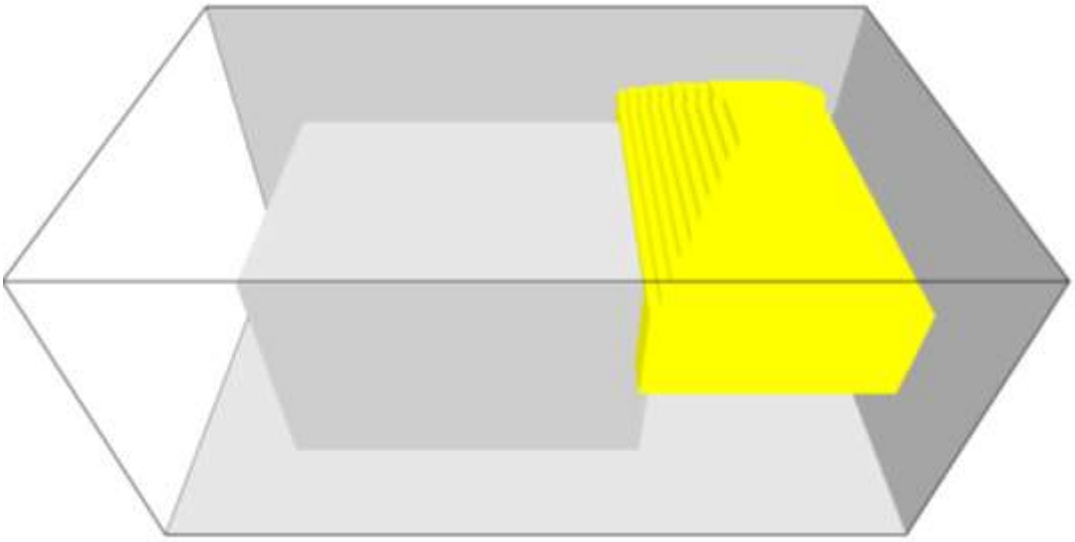

(a)

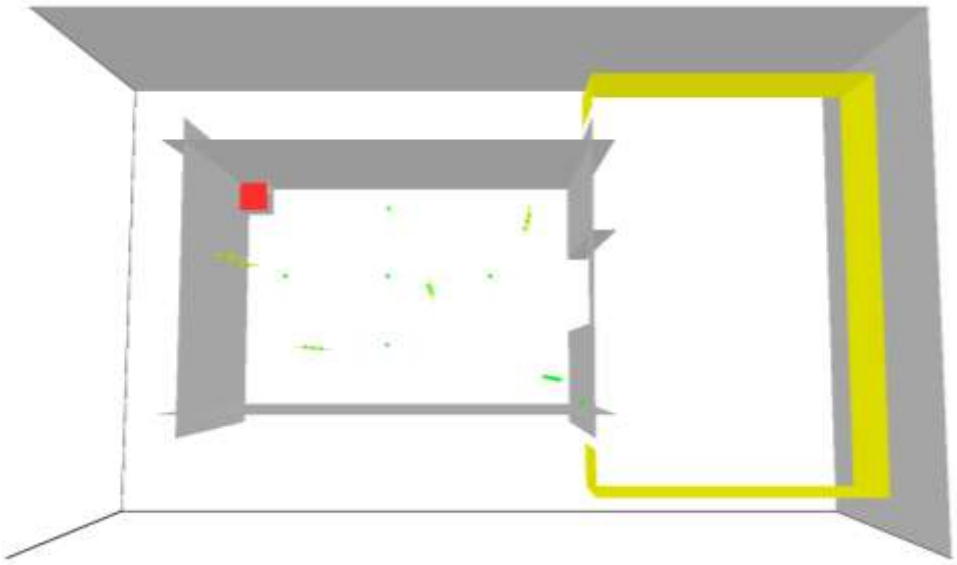

(b)

Figure 113: Visual representation of the ISO room and hood as modelled, where (a) shows the whole section modelled, and (b) shows the section with the top clipped to show the inside of the ISO room (the locations of thermocouples and heat flux meters are the same as Orientation A, Figure 10(a)).

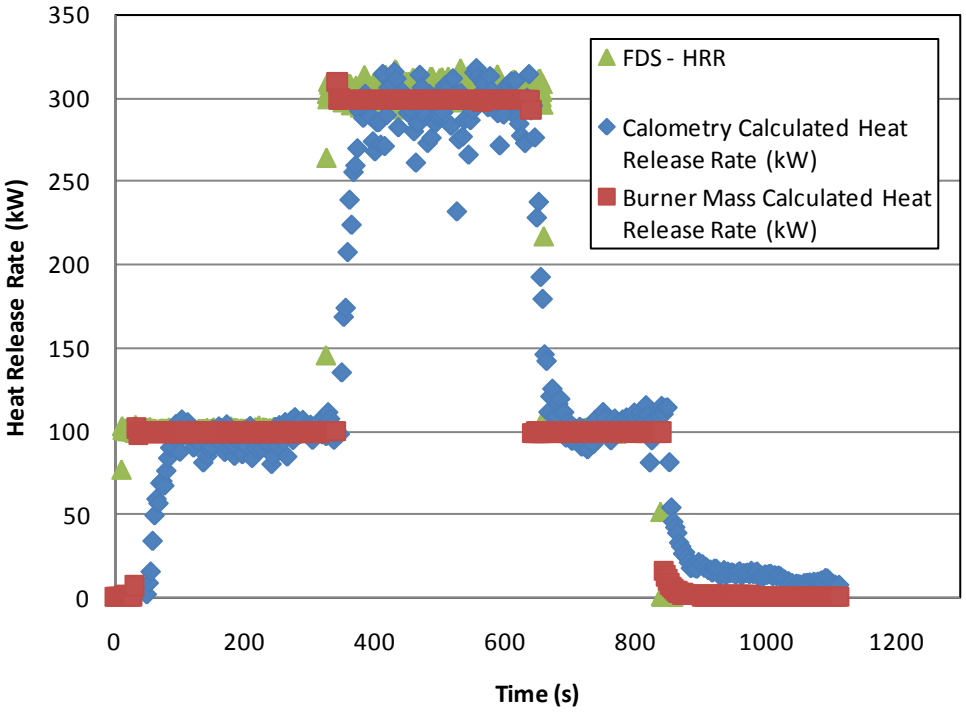

Figure 114: Comparison of FDS and experimental HRR values.

10. COMPARISON OF EXPERIMENT AND MODELLING RESULTS

The differences between experimental measurements and modelling estimates are summarised here. More detailed modelling results are included in Appendix C.

The predicted temperatures within the ISO room are in good agreement with experimental results, as shown in Figure 115 and Figure 116.

The comparison of experimental results and heat flux results for a modelled “gauge heat flux”, which is an estimate of the rate at which energy is absorbed at a surface at ambient temperature, is shown in Figure 117. This particular model variable must be located on the surface of a solid obstacle and can only be oriented parallel to one of the Cartesian coordinate axes. With this limitation of the orientation of the heat flux estimates, results for equipment tree 1 would be expected to be reasonable. However for equipment tree 4 there would be a slight difference because of the experimental orientation being just off parallel to the y-axis. Further deviation would be expected for equipment tree 2 and 3 because of the large angles between the experimental orientation of the gauges and the coordinate axes (as obvious when comparing Figure 10(a) and Figure 113). The comparisons shown in Figure 117 reflect this difference in orientation.

The comparison of experimental results and heat flux results for a modelled “radiometer”, which estimates the incoming radiative flux and integrates over 2π solid angles about a chosen axis of the coordinate system, is shown in Figure 118. Similar to the gauge heat flux, this model variable must also be located on the surface of a solid obstacle and can only be oriented parallel to one of the Cartesian coordinate axes.

The comparison of experimental results and heat flux results for a modelled “radiative heat flux”, which estimates the incoming radiative flux integrated over 2π solid angles about a vector between the gauge And burner locations, is shown in Figure 119. Since

a three-dimensional vector was used to orientate the modelled direction for the heat flux to be estimated for, model result estimates were closer to the experimental results for each of the equipment trees. However there is still a trend of lower estimates for the equipment trees located further away from the burner. This may be attributed to the effect of the hot layer and the heated surfaces within the ISO room during the experiment.

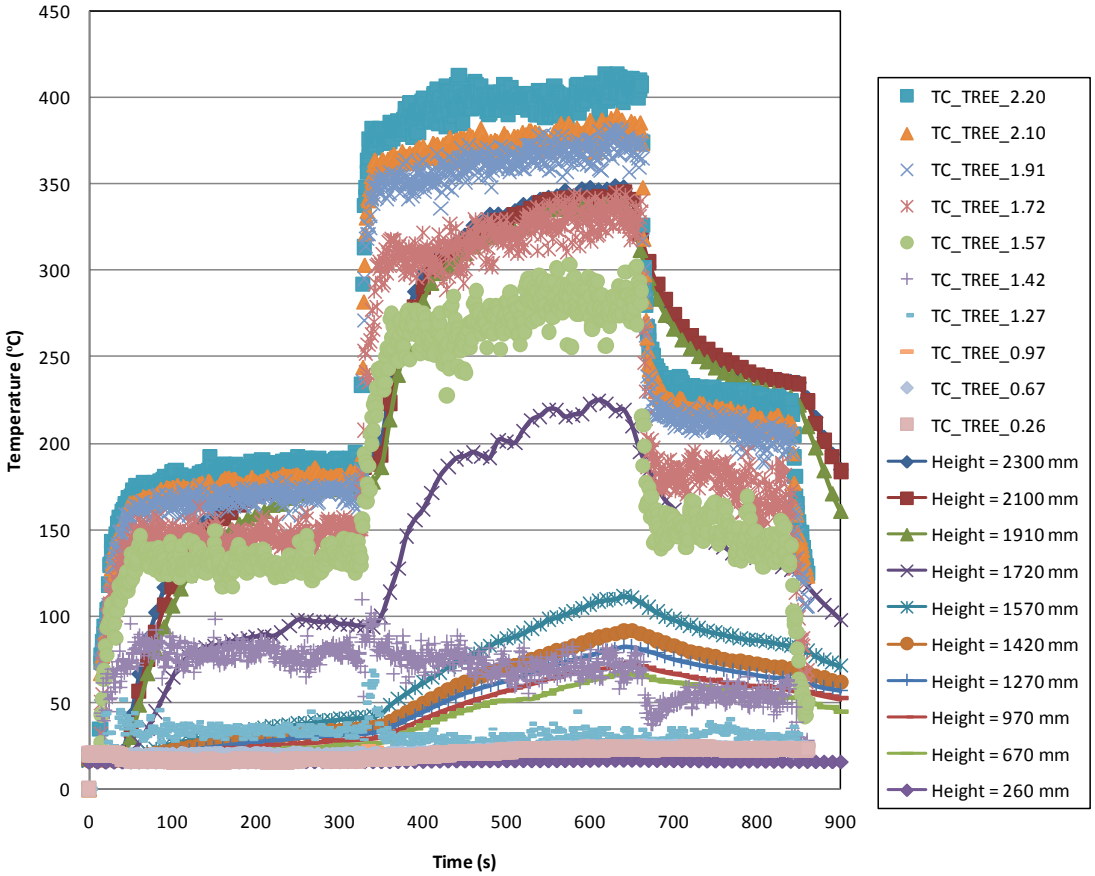

Figure 115: Comparison of temperatures for the thermocouple tree in the corner of the ISO room for the predictions using the FDS example (represented by the 'TC_TREE_x' series, where x represents the height of the thermocouple) and the experimental results.

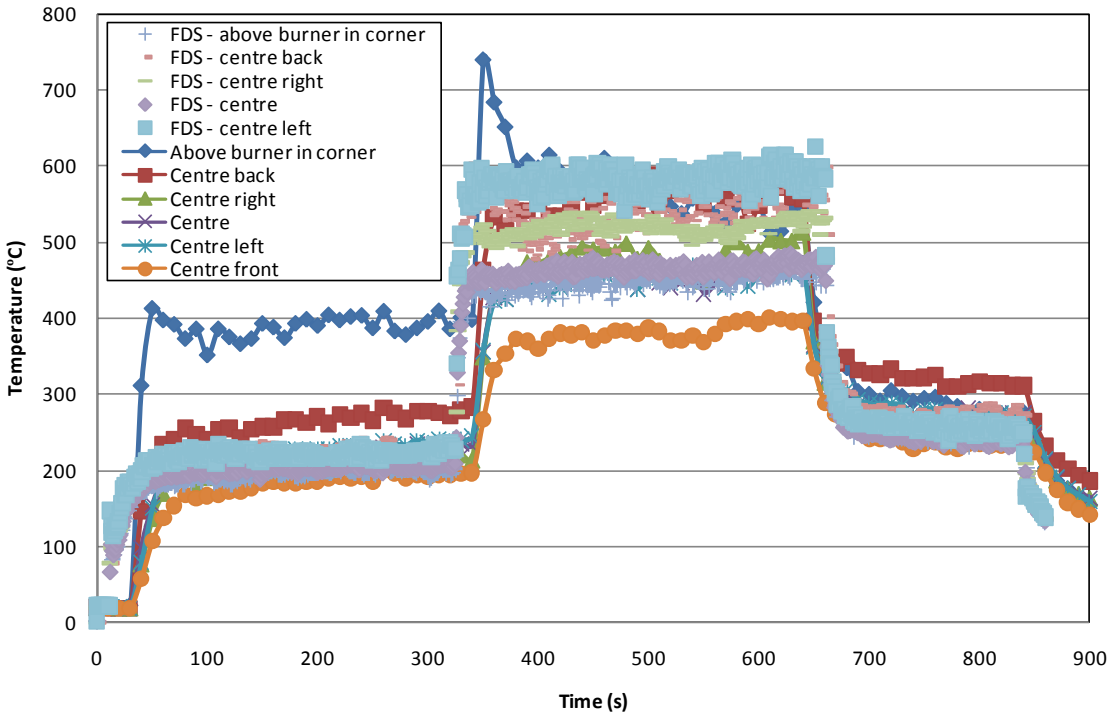

Figure 116: Comparison of the temperatures estimated for the FDS modelled example and the experimental results.

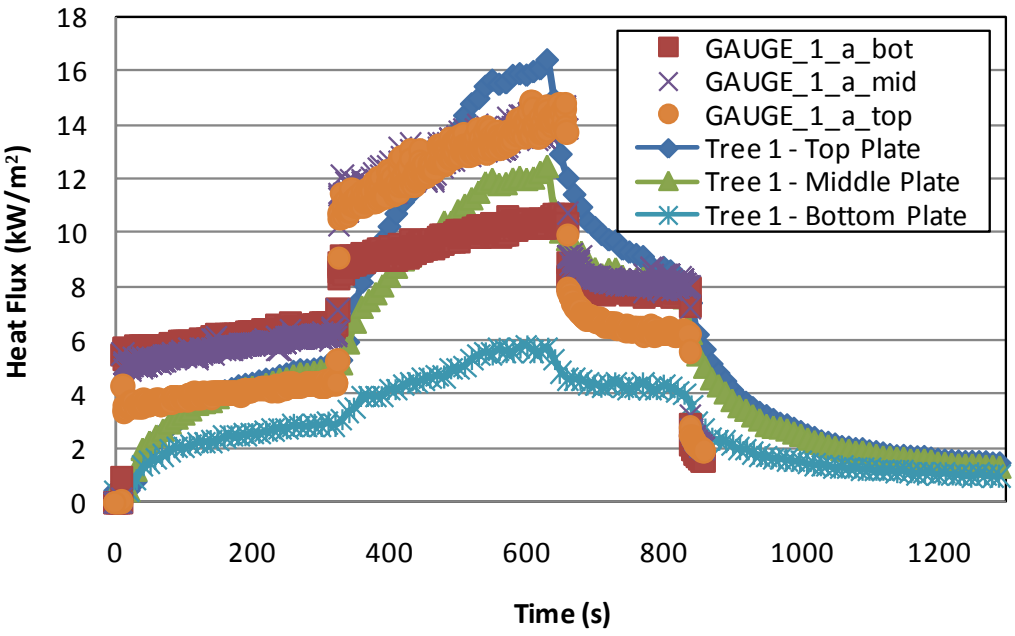
Heat Flux (kW/m²)
Time (s)
GAUGE_1_a_bot
GAUGE_1_a_mid
GAUGE_1_a_top
Tree 1 - Top Plate
Tree 1 - Middle Plate
Tree 1 - Bottom Plate

(a)

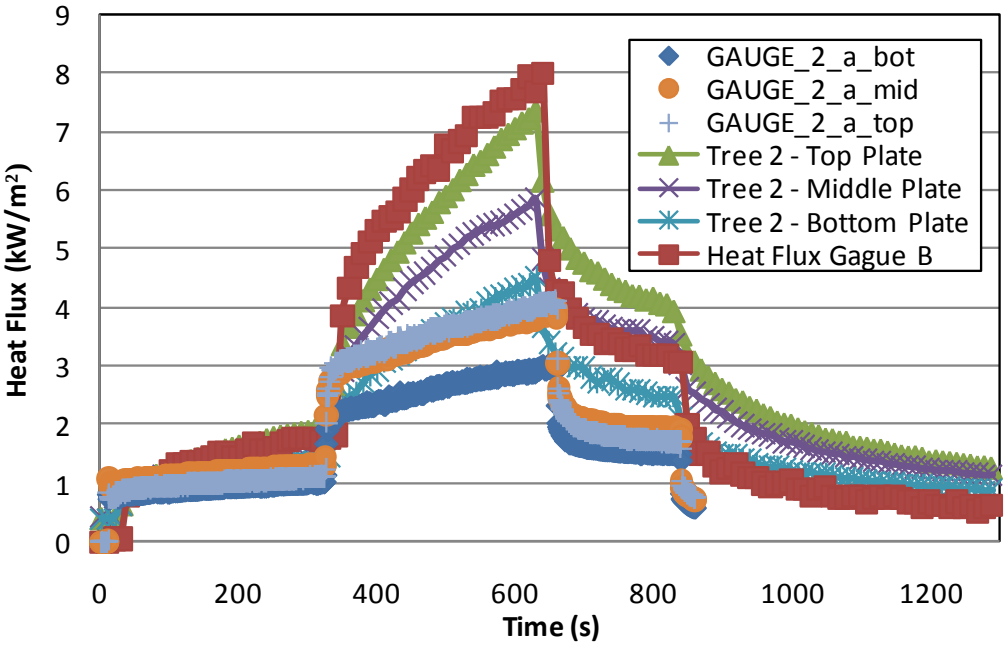
Heat Flux (kW/m²)
Time (s)
GAUGE_2_a_bot
GAUGE_2_a_mid
GAUGE_2_a_top
Tree 2 - Top Plate
Tree 2 - Middle Plate
Tree 2 - Bottom Plate
Heat Flux Gague B

(b)

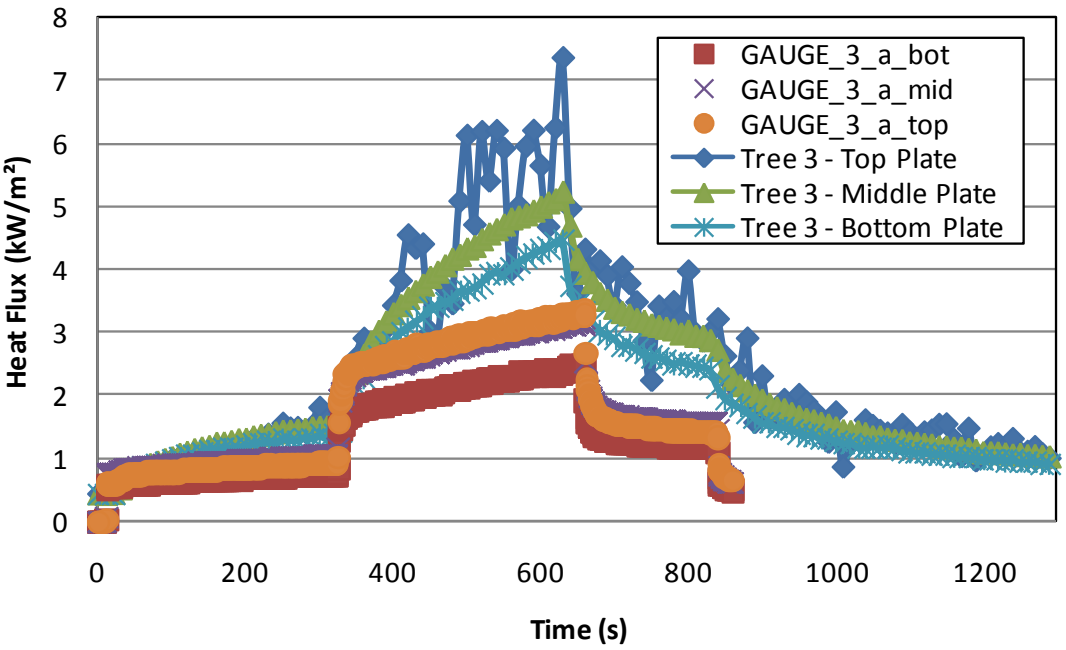

(c)

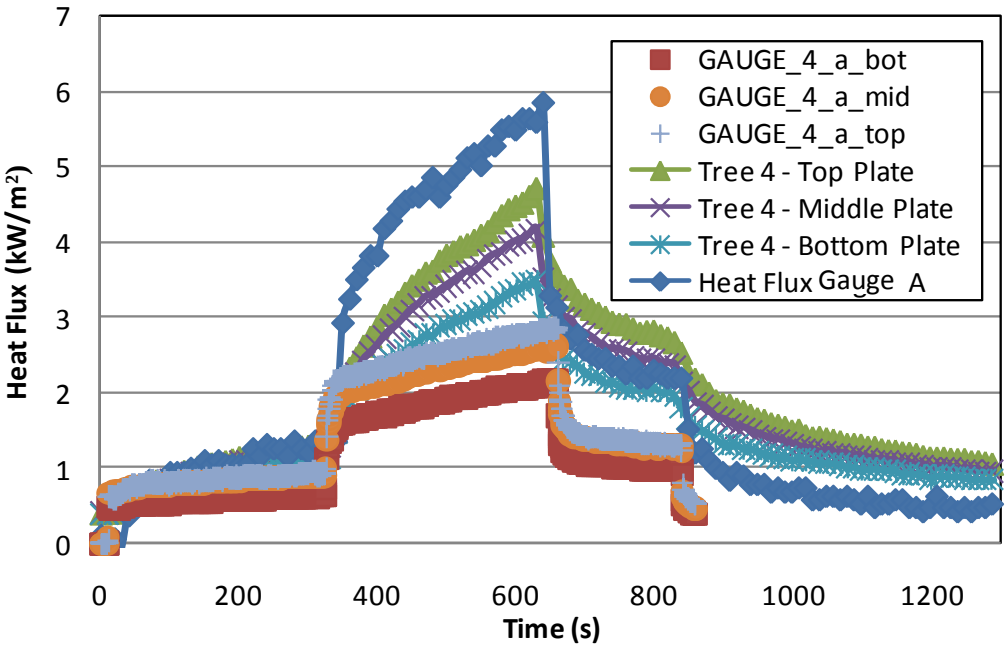

(d)

Figure 117: Modelled gauge heat flux (the rate at which energy is absorbed at a surface at ambient temperature) estimates for (a) equipment tree 1, (b) equipment tree 2, (c) equipment tree 3 and (d) equipment tree 4.

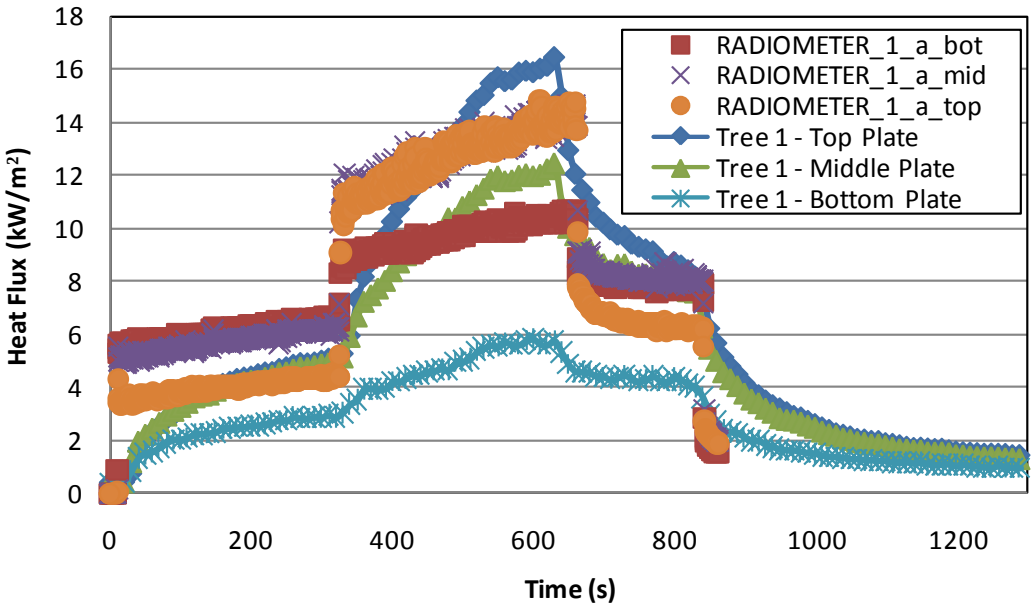
Heat Flux (kW/m²)
Time (s)
RADIOMETER_1_a_bot
RADIOMETER_1_a_mid
RADIOMETER_1_a_top
Tree 1 - Top Plate
Tree 1 - Middle Plate
Tree 1 - Bottom Plate

(a)

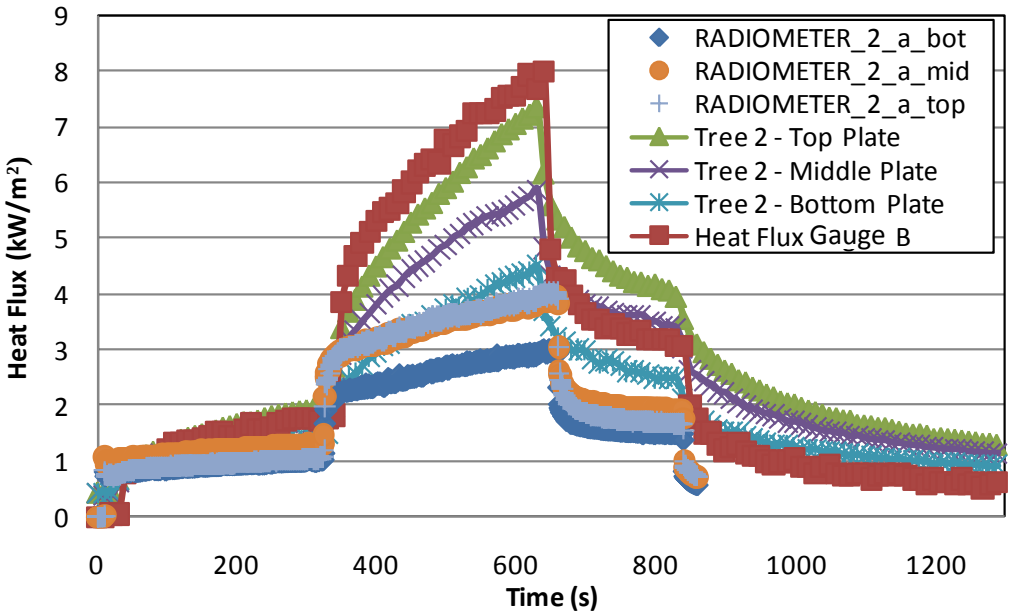
Heat Flux (kW/m²)
Time (s)
RADIOMETER_2_a_bot
RADIOMETER_2_a_mid
RADIOMETER_2_a_top
Tree 2 - Top Plate
Tree 2 - Middle Plate
Tree 2 - Bottom Plate
Heat Flux Gauge B

(b)

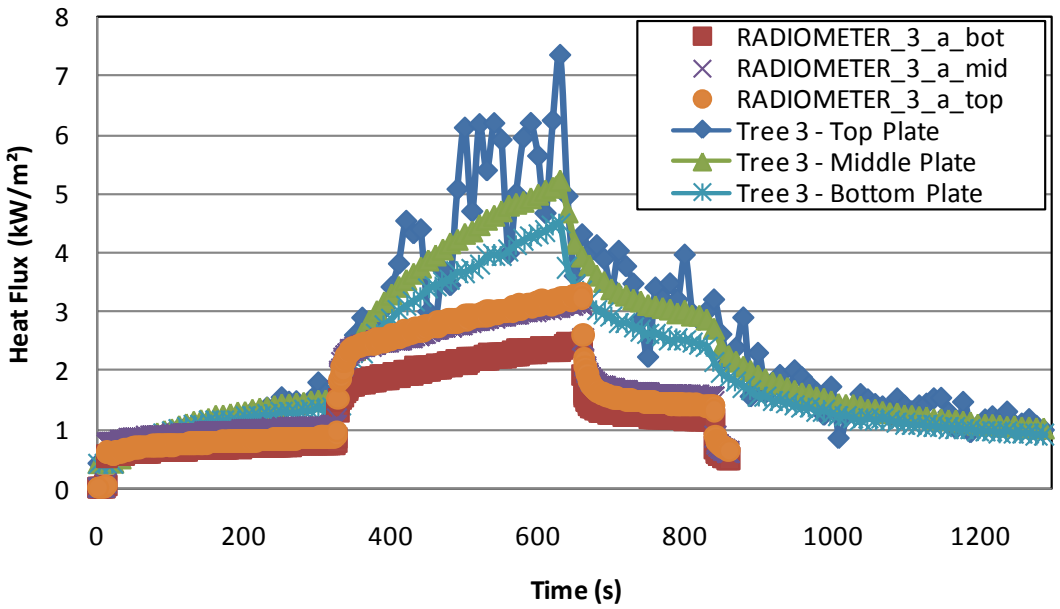

(c)

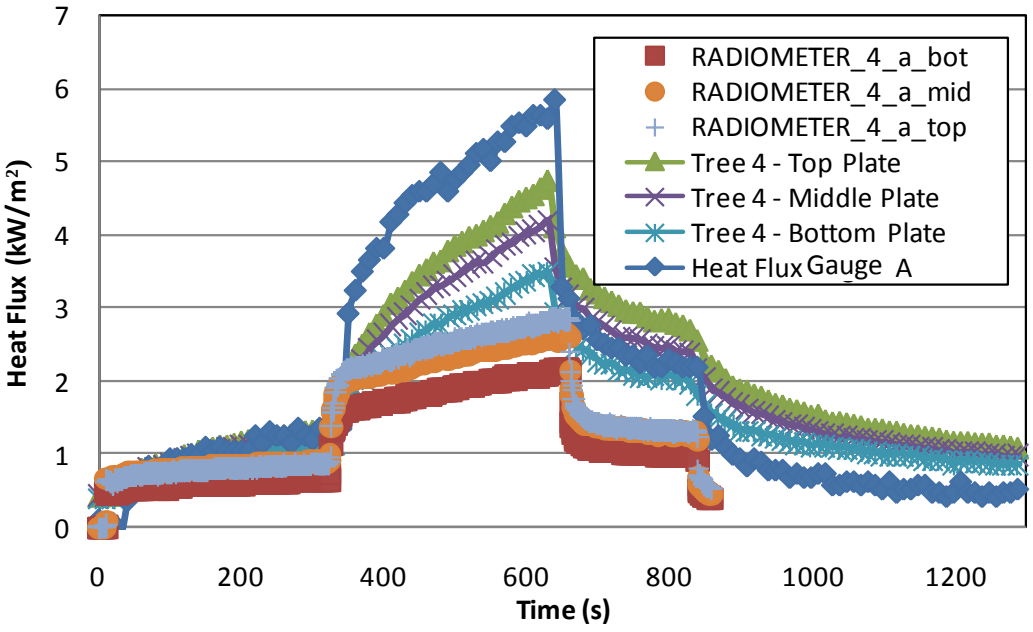

(d)

Figure 118: Modelled radiometer (incoming radiative flux is integrated over 2π solid angles about a chosen axis of the coordinate system) estimates for (a) equipment tree 1, (b) equipment tree 2, (c) equipment tree 3 and (d) equipment tree 4.

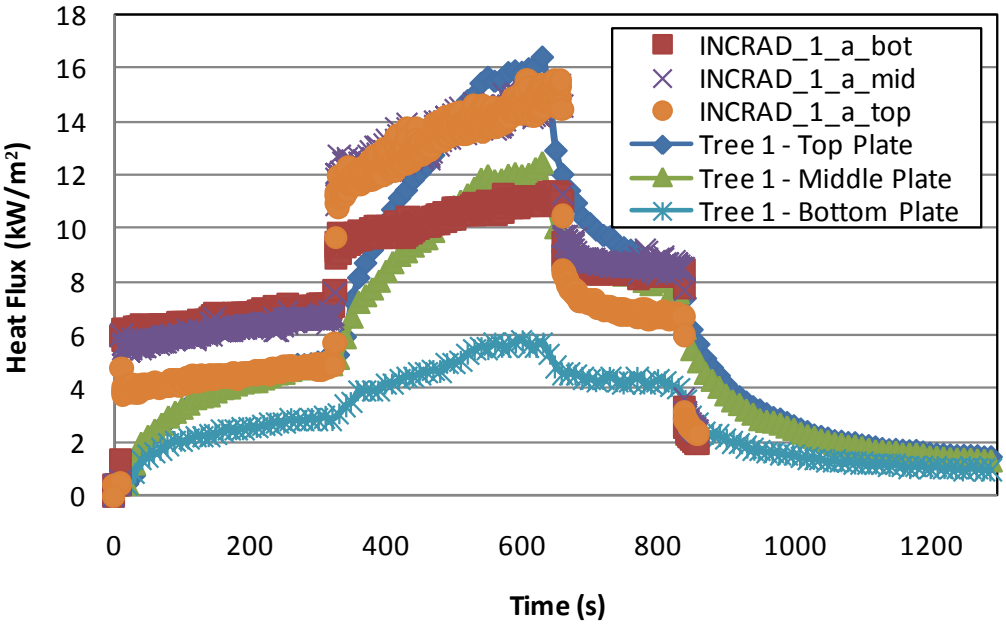
Heat Flux (kW/m²)
18
16
14
12
10
8
6
4
2
0
0
200
400
600
800
1000
1200
Time (s)
INCRAD_1_a_bot
INCRAD_1_a_mid
INCRAD_1_a_top
Tree 1 - Top Plate
Tree 1 - Middle Plate
Tree 1 - Bottom Plate

(a)

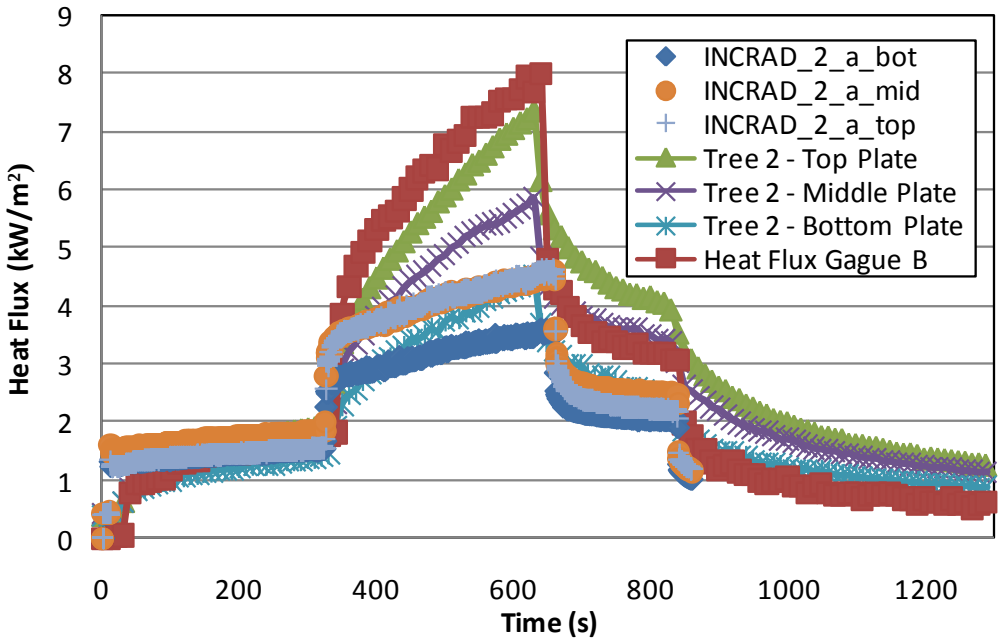
Heat Flux (kW/m²)
9
8
7
6
5
4
3
2
1
0
0
200
400
600
800
1000
1200
Time (s)
INCRAD_2_a_bot
INCRAD_2_a_mid
INCRAD_2_a_top
Tree 2 - Top Plate
Tree 2 - Middle Plate
Tree 2 - Bottom Plate
Heat Flux Gague B

(b)

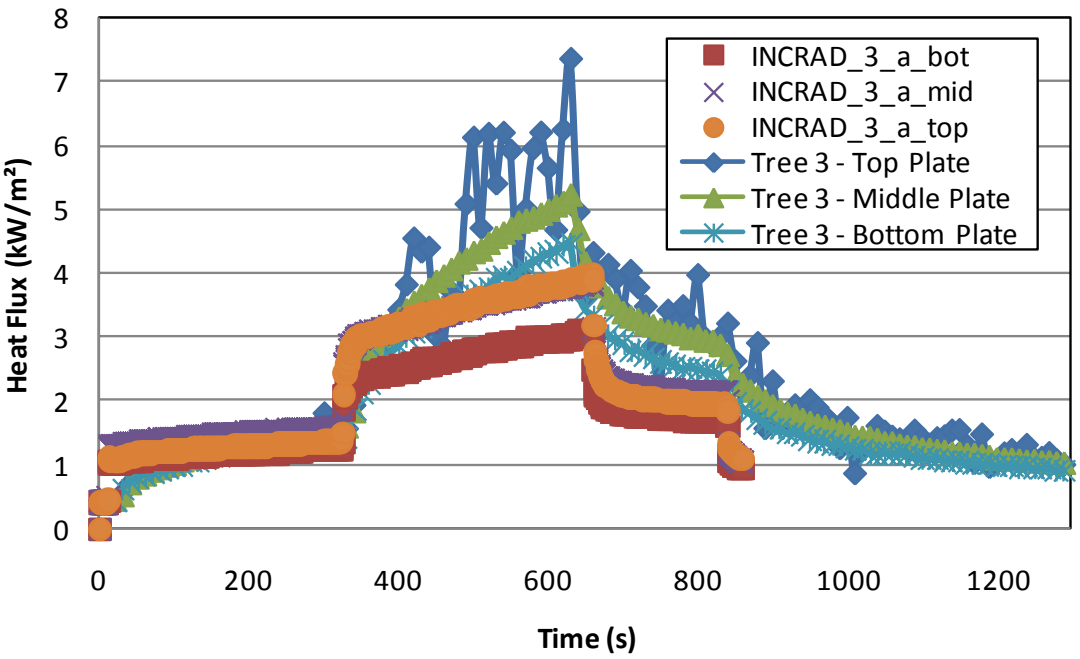

(c)

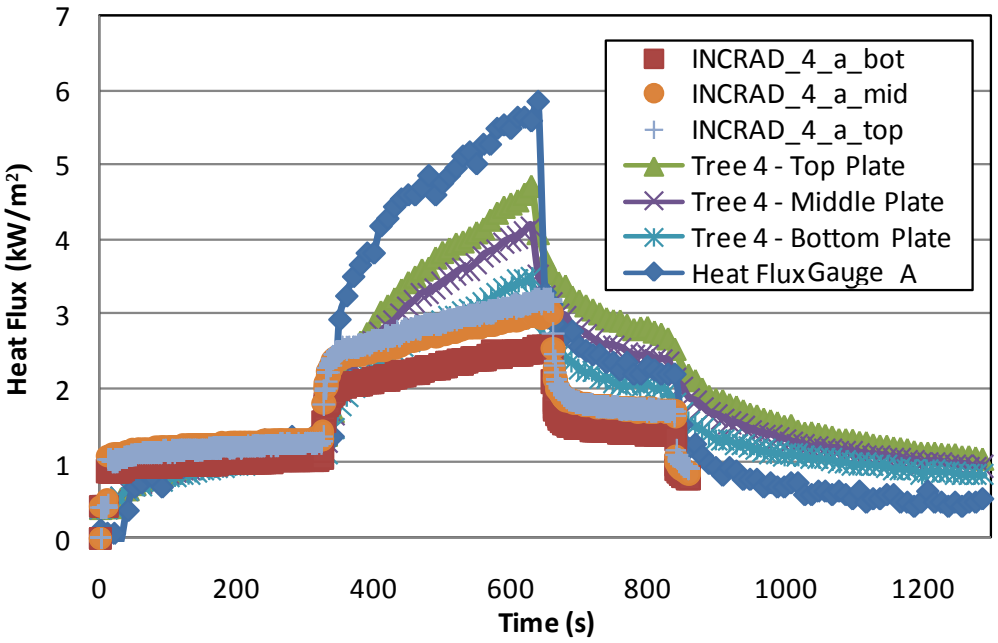

(d)

Figure 119: Modelled radiative heat flux (incoming radiative flux is integrated over 2π solid angles about a vector between the gauge locations and the burner) estimates for (a) equipment tree 1, (b) equipment tree 2, (c) equipment tree 3 and (d) equipment tree 4.

11. SUMMARY AND CONCLUSIONS

Plate thermometers for estimating incident radiative flux were investigated using a range of experiments: cone calorimeter tests, furniture calorimeter tests using a burner or a mattress as the heat source, and ISO room experiments also using a burner or a mattress as the heat source. A series of experiments in the ISO room were also performed with the door of the ISO room sealed off. The results from these experiments and the subsequent analysis are summarised here.

Results from these tests revealed:

- Response time for plate thermometer estimates of the incident radiative flux to reach a quasi steady state value was found to be approximately 250 to 350 s for the tests performed in the cone calorimeter.
- A maximum of ±10% error was associated with the quasi steady state estimates of incident radiative heat flux. Larger error was associated with the estimates before a quasi steady state was reached.
- Values of 2 to 5 kW/m^{2}K for the effective conductivity coefficient (associated with the losses through the mineral insulation) were found to be the best fit for the range of calibration tests performed. Lower target incident radiative heat fluxes were associated with lower values for the effective conductivity coefficient. A value of 4 kW/m^{2}K was chosen as the best fit for a single value of the effective conductivity coefficient for the range of target incident radiative fluxes tested. This is in agreement with previous experiments (Ingason and Wickstrom 2007). This was also found to be a reasonable assumption when the component of the conduction losses was compared to heat flux estimates from a plate thermometer located directly below the Plate Being tested in the cone calorimeter.
- Curves of the estimated incident radiative heat flux versus time followed the same trend: an initial steep rise that settled out until eventually reaching a quasi steady state value.
- The influence of each of the input parameter values used in the calculation to estimate the incident radiative heat flux from the plate thermometer temperatures was assessed:
    - During the initial rise of the curves, the most influential parameters were found to be associated with the storage term. This is expected since most of the energy will be initially used to increase the plate temperature from ambient conditions. It follows that the parameters associated with the storage term are also highly influential in the response time of a plate thermometer to report the incident radiative heat flux experienced by the plate.
    - During the quasi steady state section of the curves, the most influential parameters were found to be associated with the conductive losses, radiative heat transfer and convective losses. This is expected since the balance of these heat transfer components are expected to dominate the value of the incident radiative heat flux once the plate has been initially heated.
- Temperature data from the plate thermometers (and subsequently the estimates of the incident radiative heat flux) was found to oscillate between two distinct curves during the initial rise and then these two curves approached the same quasi steady state value (e.g. Figure 93 and Figure 95):

    - It is currently not clear as to what is the fundamental cause of this oscillatory behaviour.
    - If this oscillatory behaviour is found to be fundamental to the system, and is not an artefact of the data acquisition or the equipment set-up, then this feature may be exploited in the analysis of the estimation of the incident radiative heat flux for non-steady state heat source scenarios.

- The lumped parameter assumption of a uniform temperature within the metal plate provides quasi steady state estimates of the incident radiative heat flux within approximately ±1 kW/m^2 compared to the estimates that would be calculated using temperatures of thermocouple on both surfaces of the plate for the range of target incident radiative heat fluxes investigated.
- The small metal strip used to locate the thermocouple to the back of the plate was found to influence the initial rise time of the estimated incident radiative heat flux. This indicates that this additional mass needs to be included in the theory used to estimate the incident radiative heat flux from plate thermometer temperatures.
- In general, the results from Gardon gauges and the plate thermometers provided agreement of the incident radiative heat flux. However the Gardon gauge results show a faster initial rise, therefore the slower initial rise associated with the plate thermometers needs to be taken into account during the analysis. In addition the plate thermometers do not use a reference temperature, unlike the water-cooled Gardon gauges. Therefore this initial difference in incident radiative heat flux must also be considered when comparing the results from these two instruments.
- Results from the furniture calorimeter tests indicate the amount of movement of the burner flame during a test in the laboratory under the extraction hood. Using equipment trees located around the burner, with trees directly opposite one another, the range of heat fluxes experienced at a certain distance from the centre of the burner can established. Also the arrangement of equipment trees can assist in the assessment of spikes in the data of any individual sensor.
- When the heat source was increased linearly compared to using a stair-step increase, the results from the plate thermometers and the Gardon gauges showed better agreement for both the ISO room and the furniture calorimeter tests.

From example comparison of the ISO room results for the modelled scenario and the experimental results, reasonable agreement was found for the incident radiative heat flux.

11.1 Future work

From the results of the experiments and the analysis presented here it is suggested that for scenarios where the incident heat flux is not expected to be constant or to change smoothly and relatively slowly, then an alternative approach would be required to provide a more accurate estimate of the incident radiative heat flux. Suggestions for future work in this area include:

- Investigation of dimensional approaches to heat transfer to replace the lumped parameter assumption.
- A potentially more appropriate way to include the additional mass used to locate the thermocouples to the back of the metal plate.

- Investigation of the use of stability analysis to interpret when the measurement of the plate temperatures is approaching a quasi steady state or not and to estimate the value of the quasi steady state that is being approached:
    - The fundamental reasons for the oscillatory behaviour observed for the plate thermometer temperature and subsequent estimate of the incident radiative flux must be identified before further use of a stability analysis can be potentially used.

12. REFERENCES

64 Series, Heat Flux Transducers and Infrared Radiometers for the Direct Measurement of Heat Transfer Rates, Bulletin 118. 2002. MEDTHERM Corporation, Hunstville, AL, USA.

AS/NZS 3837: Method of Test for Heat and Smoke Release Rates for Materials and Products Using an Oxygen Consumption Calorimeter. 1998. Standards Australia, Homebush, Australia.

ASTM E119-88, Standard Methods of Fire Tests of Building Constructions and Materials. 1995. American Society for Testing and Materials, Philadelphia, PA.

Ballestrin J, Estrada CA, Rodriguez-Alonso M, Perez-Rabago C, Langley LW and Barnes A. 2006. 'Heat Flux Sensors: Calorimeters or Radiometers?' *Solar Energy* 80: 1314-1320.

Bundy M, Hamins A, Johnsson EL, Kim SC, Ko GH and Lenhert DB 2007. *Measurements of Heat and Combustion Products in Reduced-Scale Ventilation-Limited Compartment Fires, Nist Technical Note 1483*. National Institute of Standards and Technology, Gaithersburg, MD, USA.

CAN/ULC-S101-M89, Standard Methods of Fire Endurance Tests of Building Construction and Materials. 1989. Underwriters' Laboratory of Canada, Ontario, Canada.

Dillon SE 1998. *Analysis of the ISO 9705 Room/Corner Test: Simulations, Correlations and Heat Flux Measurements, NIST GCR 98-756*. National Institute of Standards and Technology, Gaithersburg, MD, USA.

EN 1363 Fire Resistance Tests, Part 1: General Requirements. 1999. British Standards Institute, London, UK.

Gross D and Robertson AF 1965. Experimental Fires in Enclosures. *10th International Symposium on Combustion* Pittsburgh, PA, USA.

Harmathy TZ 1993. *Fire Safety Design and Concrete*. John Wiley & Sons Ltd, New York, NY, USA.

Inconel® Alloy 600. 2008. Special Metals Corporation. Accessed on 6 January 2009. http://www.specialmetals.com/documents/Inconel%20alloy%20600%20(Sept%202008).pdf.

Ingason H and Wickstrom U. 2007. 'Measuring Incident Radiant Heat Flux Using the Plate Thermometer'. *Fire Safety Journal* 42: 161-166.

ISO 834 Fire-Resistance Rests - Elements of Building Construction - Part 1: General Requirements. 1999. International Organisation for Standardization, Geneva, Switzerland.

ISO 5660 Reaction to Fire Tests - Heat Release, Smoke Production and Mass Loss Rate - Part 1: Heat Release Rate (Cone Calorimeter Method). 2002. International Organisation for Standardization, Geneva, Switzerland.

ISO 9705 Fire Tests - Full-Scale Room Test for Surface Products. 1993. International Organization for Standardization, Geneva, Switzerland.

Johnsson EL, Bundy MF and Hamins A 2007. Reduced-Scale Ventilation-Limited Enclosure Fires - Heat and Combustion Product Measurements. *Interflam 2007* London, UK.

Lennon PF and Silcock GWH. 2006. 'A Preliminary Investigation into the Partitioning of the Convective and Radiative Incident Heat Flux in Real Fires'. *Fire Technology* 42: 109-129.

McGrattan K, Hostikka S, Floyd J, Baum H, Rehm R, Mell W and McDermott R 2008. *Fire Dynamics Simulator (Version 5) Technical Reference Guide. Volume 1: Mathematical Model. NIST Special Publication 1018-5*. National Institute of Standards and Technology, Washington D.C., MD, USA.

McGrattan K, Klein B, Hostikka S and Floyd J 2007. *Fire Dynamics Simulator (Version 5). User's Guide. NIST Special Publication 1019-5*. National Institute of Standards and Technology, Washington D.C., MD, USA.

Pitts WM, Murthy AV, de Ris JL, Filtz J-R, Nygard K, Smith D and Wetterlund I. 2006. 'Round Robin Study of Total Heat Flux Gauge Calibration at Fire Laboratories'. *Fire Safety Journal* 41: 459-475.

Wickstrom U. 1994. 'The Plate Thermometer - a Simple Instrument for Reaching Harmonized Fire Resistance Tests'. *Fire Technology* 30(2): 195-208.

Wickstrom U. 2004. 'Short Communication: Heat Transfer by Radiation and Convection in Fire Testing'. *Fire and Materials* 28(5): 411-415.

Wickstrom U 2008. Personal Communication concerning *Heat Transfer and Temperature Calculations Based on Plate Thermometer Measurements*.

Wickstrom U, Duthinh D and McGrattan K 2007. Adiabatic Surface Temperature for Calculating Heat Transfer to Fires Exposed Structures. *Interflam 2007* London, UK.